UNIVERSITÀ DEGLI STUDI DI PADOVA

SCUOLA DI SCIENZE

DIPARTIMENTO DI SCIENZE CHIMICHE

SCUOLA DI DOTTORATO IN SCIENZE CHIMICHE

XXIX CICLO

PhD Thesis

Nanoproteomics. Interaction of gold nanoparticles with proteins

Dottorando: ALVARO MARTINEZ CEBALLOS

Supervisore: PROF. PAOLO M. SCRIMIN

Gennaio 2017

If a man can keep alert and imaginative, an error is a possibility
a chance at something new;
to him, wandering and wondering are part of the same process,
and he is most mistaken, most in error, whenever he quits exploring."

William Least Heat-Moon: Blue Highways

Acknowledgements

When I was an undergraduate student I used to argue that it was not fair to call us *students* forever while we were conducting full-time research during our Masters or Ph.D. Now I not only consider it fair but I feel like I have been a student these last years more than ever. I realize how much I have learned and, what is more important, I will still learn in the next stages of my life.

I find extremely difficult to express in these lines how grateful I am to my supervisors Prof. Paolo Scrimin and Prof. Fabrizio Mancin. They have been a source of fruitful discussions, availability, patience, inspiration and understanding. I could not have asked for anything better either from the scientific or the human point of view. Thank you so much.

To the great students we had in our group. Typically they believe that we are supposed to teach them, but ignore that we get as much feedback from them as what they get from us. Movilli, Muraca, Tannorella, Nick, le varie Giulie, Elena, Leoni (although he was not from our group we adopt you somehow) but especially Enrica and Fede. It was a great experience supervising you both and I have learned tons of things from it.

To all the great people that shared the lab or the building. Sergio and Simo, tolerating my peptides spinning forever; Sara and the never-ending questions about NMR; Kuba and Luca, the best possible office colleagues and the discussions we had that help to solve so many issues with everyone's projects; Bartox, Maiti, Matteo, Squarc, Faresin, Nicola, Carlo, Vivi, Claudia...We all made our building a great place, you made it feel like home in here.

To Marta and Giovanni. One brought me here without knowing me and the other was the first one I met. You already know everything I could write here.

To my parents and my family. I would have never make it so far without their support.

To all of you, some people that I keep for myself and the ones that for sure are missing,

Thank you.

Summary

Specific and reliable protein sensing and detection is a challenge of increasing interest due to their role as biomarkers in many diseases. Classical proteomics require time-consuming separation techniques and lacks the capability to assess protein activity variations uncorrelated to expression levels. Activity-based protein profiling (ABPP) is a strategy in which chemical probes (irreversible protein inhibitors) are covalently bound to target proteins with a shared activity and some signal arising from the probe is quantified, being sensitive to protein activity due to the binding step. Nonetheless, protein separation is still expensive in terms of time or requires the use of high-cost instrumentation.

Our proposal was to employ gold nanoparticles as a tool for covalently capturing proteins of interest and separating them with ease from the remaining proteome by size-differentiation.

Mixed monolayer nanoparticles have been obtained by two different methods, by direct substitution on an homogeneous monolayer or by supramolecular click-coupling reactions onto azido-functionalized derivatives. The two strategies were shown to be complementary; thiol exchange is simpler but substitution yields are difficult to predict when new thiols are tested whereas reliable click-coupling onto pre-substituted azido-nanoparticles requires the use of dibenzocyclooctyne derivatives to obtain high yields.

We have developed and fully characterized supramolecular conjugates of gold nanoparticles with a thiol-based mixed-monolayer that endow the nanoparticles with high water solubility but also the capability to expose the targeting moiety on their surface.

Avidin-biotin interaction has been chosen as model system to prove the capability of functionalized nanoparticles to effectively reach protein active sites and displace small molecules from their binding site in competition assays.

On the other hand, supramolecular architectures based on chain-like arrays of nanoparticles have been prepared and shown to fuse in water to form nanorods or nanowires by treatment with glucosamine phosphate. Addition of thiol during the incubation stop nanoparticle fusion, opening the possibilities for a potential synthetic method to obtain anisotropic systems for NIR sensing.

Table of Contents

List of Abbreviations

^{1}H NMR Proton Nuclear Magnetic Resonance

^{13}C{^{1}H } NMR Proton-decoupled ^{13}C Nuclear Magnetic Resonance

DBCO Dibenzocyclooctyne derivative

DIPEA *N*,*N*-Diisopropylethylamine

DMAP 4-Dimethylaminopyridine

DMF Dimethylformamide

DMSO Dimethylsulfoxide

EDC *N*-(3-Dimethylaminopropyl)-*N*′-ethylcarbodiimide hydrochloride

ESI–MS Electron Spray Ionization Mass Spectrometry

GAP D-Glucosamine-6-phosphate sodium salt

HR–MS High Resolution Mass Spectrometry

LED Light-Emitting Diode

MS Mass Spectrometry

NIR Near Infrared

NPs Nanoparticles

PEG Polyethyleneglycol

PMMA Poly(methyl methacrylate)

TBTA Tris[(1-benzyl-1*H*-1,2,3-triazol-4-yl)methyl]amine

TEG Triethyleneglycol-based thiol (9)

TEM Transmission Electron Microscopy

TGA Thermal Gravimetric Analysis

THF Tetrahydrofuran

THPTA Tris(3-hydroxypropyltriazolylmethyl)amine

TLC Thin Layer Chromatography

TMA Trimethylammonium-based thiol (10)

UV Ultraviolet

ZW Phosphorylcholine-based zwitterionic thiol (1)

List of Figures

List of Tables

List of Schemes

Chapter 1 Introduction

1.1 Biomarkers and diseases

Biomarkers were originally defined as "a characteristic that is objectively measured and evaluated as an indicator of normal biological processes, pathogenic processes, or pharmacologic responses to a therapeutic intervention."[1] However, it can be extended to "almost any measurement reflecting an interaction between a biological system and a potential hazard, which may be chemical, physical, or biological. The measured response may be functional and physiological, biochemical at the cellular level, or a molecular interaction"[2] as indicated by Strimbu and Tavel.[3]

Detecting biomarkers before symptoms are present has attracted a lot of effort in the recent years, especially in those cases in which an early detection increases significantly the probability of tackling the disease or makes the treatment easier in many cases as occurs with several cancers[4] or Alzheimer's disease.[5] On the other hand, specificity of these biomarkers is also challenging; to ensure a reliable diagnosis the changes observed should respond, ideally, to only one factor or condition, which is not always the case. To fulfil that requirement two main approaches can be followed: a) measuring more than one biomarker simultaneously, looking for global patterns that define a specific situation or b) employing more specific markers which are altered only by a reduced number of factors.

Two examples of the first approach would be the quantification of the relative levels (concentration ratios) of some fatty acids to arachidonic acid[6] or asymmetric dimethylarginine to nitric oxide[7] in blood serum to identify potential cardiovascular risks. This presents the advantage of small probability of a false positive at the expense of multiple analysis, what requires time and instrumentation. If less analytical measurements are required or desired, more specific markers must be chosen. Among the different possibilities, proteins are the most extensively used, with no close competitors.

1.2 Genomics and proteomics

These studies were initially performed via classical genomics, quantifying the expression of some genes that code for the proteins of interest, but more sophisticated techniques were required to take into account additional factors such as dynamic protein degradation or post-translational modifications.[8]

The comprehensive study of a set of proteins is usually called *proteomics*. It includes finding about protein abundances, modifications, functions and interactions inside a *proteome*, defined as the entire set of proteins produced by a living organism, including single cells (Figure 1).

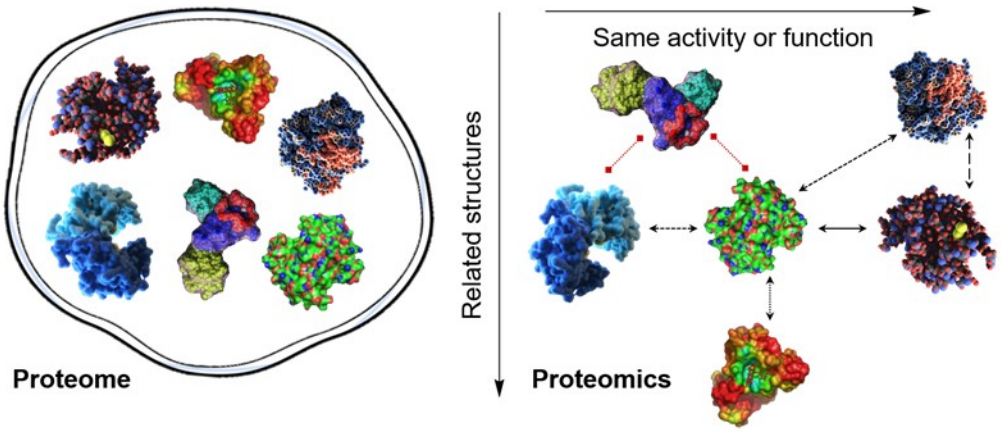

Figure 1 – Representation of a proteome (left) and the sorted outcome of a proteomic study (right). Global shapes define protein structures, holed shapes denote function/activity and colours represent generic modifications.

Despite the advantages of proteomics in comparison with genomic studies, one main drawback was still present, since the main quantification parameter was, in all cases, protein expression levels, this is, the actual concentration of protein in the sample. Several studies pointed out that not protein concentration but protein activity changes are indicators of anomalous processes and, in many cases, this can occur without altering the expression levels.[9]

Cravatt and co-workers have developed a modern technique called Activity-Based Protein Profiling (ABPP) that allows to perform proteomic studies within complex proteomes quantifying the total activity of a protein or family of proteins sharing the same activity, taking also into account the effect of post-translational and transductional modifications.[9] The strategy is based on covalently labelling the proteins by using a specific inhibitor that will react with the proteins of interest. Later, proteins are separated, typically by gel electrophoresis, and those that are labelled are then revealed (Figure 2). The most common labelling techniques include direct use of fluorescent tags or azide moieties for an additional click-functionalization step.

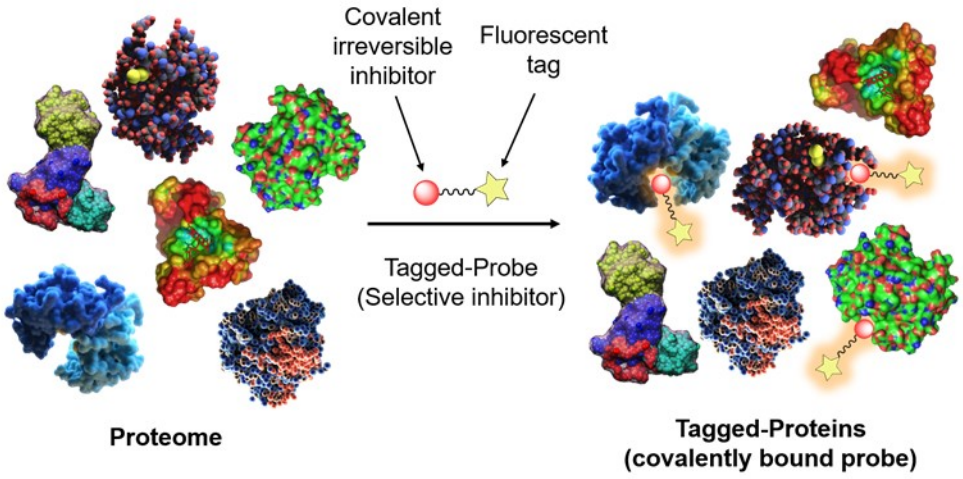

Figure 2 – Representation of the covalent irreversible inhibitor and the proteome before (left) and after (right) the Activity-Based Protein Profiling labelling step. Only those proteins that share the same activity are labelled. See Figure 1 for protein legend. Star denotes the fluorescent moiety and red ball the inhibitor structure that captures the desired protein.

Despite the usefulness of the ABPP studies in many fields, such as the discovery of metabolic pathways in malignant cells[10] or finding new enzyme inhibitors[11] or drugs,[12] it still presents one important drawback due to the fact that proteins must be separated from the complex mixture to allow identification and quantification, which is significantly time-consuming and very dependent on the sample complexity itself.

One alternative emerged recently in which polarized fluorescence is employed to avoid sample separation, being especially useful for enzyme inhibitor identification when the target proteins are not fully characterized.[13] It takes advantage of the fact that small fluorescent molecules lose the polarization of the absorbed radiation, emitting unpolarised light, but this polarization is maintained if the mobility of the molecules is somehow reduced (Figure 3).

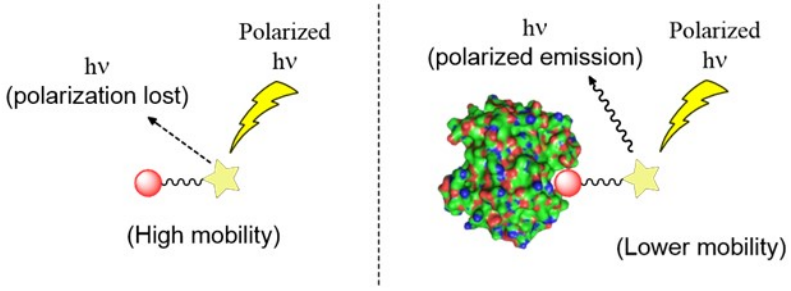

Figure 3 – Illustration of the effect of molecular mobility on the polarization of the emitted light.

Therefore, two possible outputs may come from irradiating with polarized light samples containing the following three components: i) the proteome, ii) a specific fluorescent inhibitor for the target protein (or protein family) and iii) the candidate inhibitors to screen; if the potential inhibitor is weak or inactive, the fluorescent tag will be bound to the target protein, its mobility will become that of the macromolecule and polarized fluorescence will be observed, on the other hand, if the candidate is strongly interacting with the protein, the fluorescent label will remain free in solution and polarization will be absent in the emission (Figure 4).

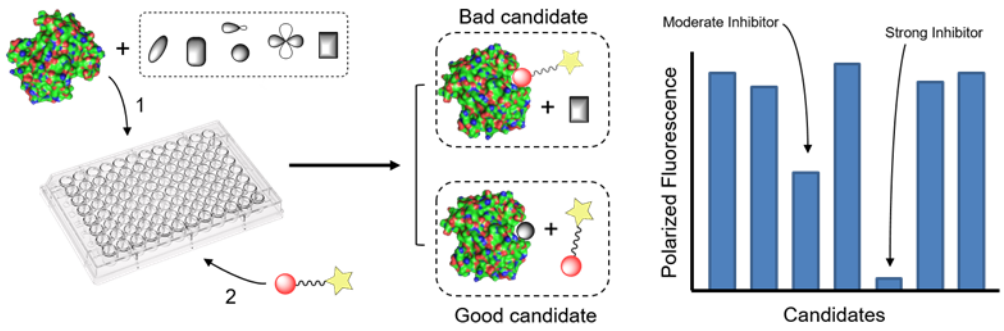

Figure 4 – Representation of an inhibitor screening for a protein using the polarized fluorescence experiment. Grey potential candidates are tested one by one (1) with the fluorescent tag for a specific protein (2). The output (right) represents a chart of polarization detection depending on the Candidate tested.

This proposal allowed for very fast high throughput screening of many candidates without performing individual protein separation, since target specificity was conferred by the chemical structure of the fluorescent tag. However, nowadays the cost of the equipment required for these experiments is still high compared with other optical devices.

1.3 Proposal and aim of our project

Gold nanoparticles have been widely used for biomedical applications such as imaging, sensing or drug delivery.[14,15] Studies based on surface enhancement Raman spectroscopy (SERS) have been used in protein detection[16–20] and although some alternatives have been proposed in which the plasmonic band is employed as the reporter, most of them are based on nonspecific interactions or employ antibodies for targeting.[21–24]

Our proposal consist in combining the plasmonic properties of gold nanoparticles with the activity-based protein profiling approach developed by Cravatt and co-workers to build a supramolecular protein-sensing system capable to capture the desired protein or protein family (Figure 5B), overcoming some of the main drawbacks of classic ABPP techniques.

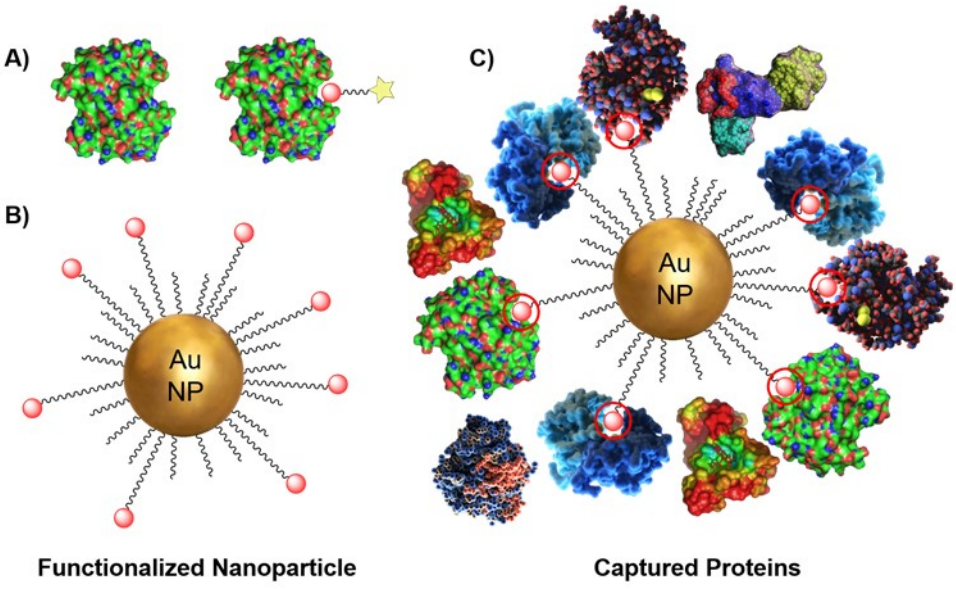

Figure 5 – A) Comparison in size of free and tagged proteins; B) Supramolecular construct proposed, gold core with filling thiol (wavy lines) and irreversible protein inhibitor (red balls); C) Illustration of the difference in size of the supramolecular complex with free proteins.

Due to the difference in size between the different components of the system, separation of the desired proteins from the proteome could be performed by filtration with a molecular-weight cut-off if necessary (see below). Using NPs plasmonic band as reporter of the protein capture, separation could be avoided and the system quantified *in situ*. Protein size can be estimated from their molecular weight,[25] For comparison purposes, a 100 kDa protein would have an approximate diameter of 5 nm. AuNPs plasmonic band intensity is increased in a logarithmic trend up to *c.a.* 20 nm in diameter.[26] Therefore the NPs employed should be, in all cases, at least equal and probably bigger than the proteins to detect. The use of big nanoparticles will improve both ease of separation and plasmonic intensity and sensitivity.

To prepare monodisperse gold nanoparticles of that size a modification of the classic citrate-reduction method was chosen.[27] These nanoparticles were then covered with the active thiol functionalized with the specific inhibitor and a phosphorycholine zwitterionic thiol as filling agent to confer water solubility but no net charge to the nanoparticle, to avoid nonspecific protein adsorption.[28] Two strategies were followed in parallel (Figure 6); Direct substitution of the filling thiols by the functional has the advantages of being is fast and reproducible but gives very different outputs when the structure of the thiol is modified, with required optimisation for each candidate inhibitor to use. In order to develop a general synthetic approach, we planned to implement a click-chemistry strategy, in this sense, a general azide-polyethylene glycol-alkyl thiol was attached to the NP surface *via* ligand exchange and then a convenient alkyne-functionalized inhibitor for the desired enzyme will be bound to it once the nanoparticle is formed. The inclusion of this additional step ensures reproducible nanoparticle loading when a battery of inhibitors want to be tested.

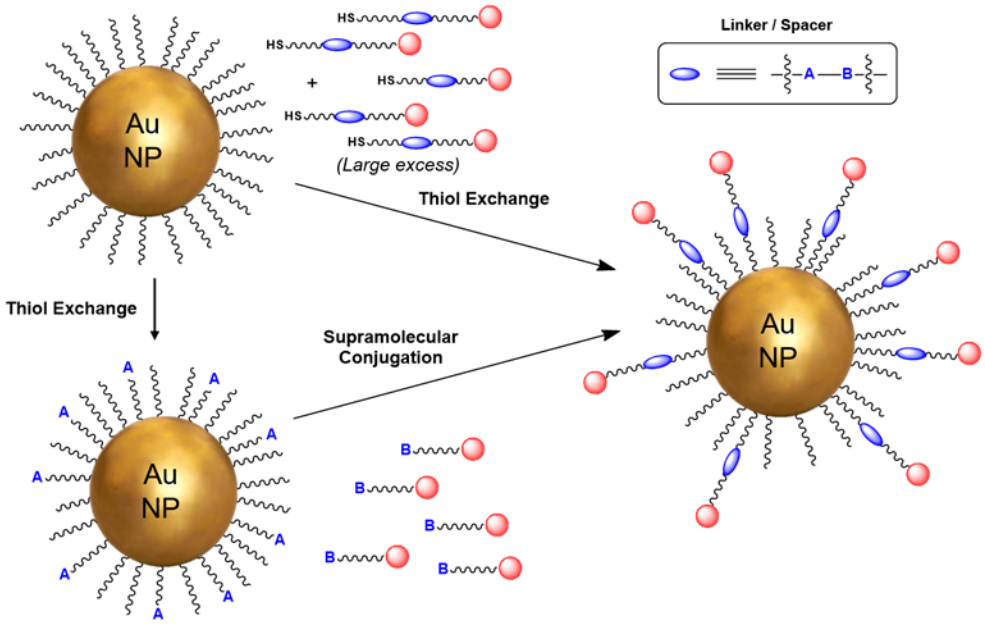

Figure 6 – Illustration of the supramolecular decoration strategies by both direct thiol exchange and click conjugation. The system can be modified to target any desired protein family by changing the chemical nature of the inhibitor and attaching it to the common azide-NP precursor or synthesise the complete thiol to exchange it.

The chemical structures of the chosen thiols are shown in Figure 7, biotin (**4**, **5**) and naproxen (**6**) motifs were chosen as proof-of-concept ligands for avidin and albumin respectively even though they do not interact covalently with the target proteins

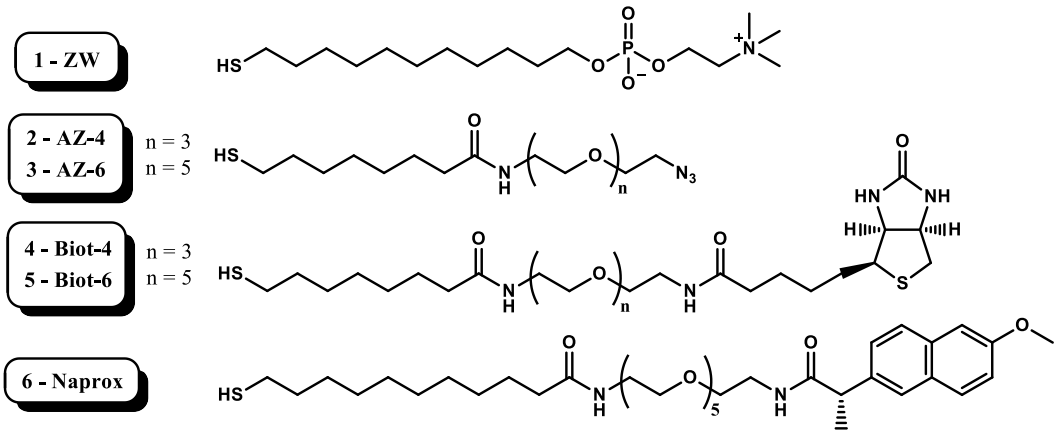

Figure 7 – Chemical structures of the zwitterionic, azide thiols selected and protein-binding thiols selected for this work.

Chapter 2 Thiol exchange on gold nanoparticles

2.1 Introduction

The chemical nature of the gold-sulfur interface has been deeply studied in the recent years from both theoretical and experimental points of view in many different systems, from self-assembled monolayers on perfectly defined crystalline faces to polydisperse gold nanoparticles and atomically-defined clusters.[29,30] Ligand-exchange reactions, in which one or more molecules bound to the gold surface are replaced by an alternative ligand, are still poorly understood in many ways although some common grounds have been established.

It has been well established that the exchange process occurs at two different rates depending on the organization level of the gold substrate, being much faster around boundaries and defects than on flat terraces.[31,32] This difference in substitution rate was observed when small and big clusters are compared, due to the higher abundancy of terraces in the latter[33] and this is also the reason why substitution on gold nanorods occurs much faster at the curved tips than on the cylindrical section.[34,35]

Small gold clusters present a particular behavior since no edges or terraces are present. Their atomic structures are well-known from single-crystal x-ray diffraction studies and some insights into the exchange mechanisms have been proposed.[36–39] However, they will not be discussed in detail here because they fall out of the scope of this thesis.

Ligand place exchange reaction with spin-labelled disulfides have been deeply studied through EPR spectroscopy.[40,41] Two main phenomena should be highlighted: a) both branches of the entering disulfide do not bind to the same nanoparticle, but one remains in solution upon formation of a mixed disulfide with the outgoing thiol[42] and b) a solution of two types of nanoparticles with only one thiol on each surface results in mixed monolayer nanoparticles upon incubation, so thiols can dynamically exchange from one nanoparticle to another.[43] In addition, when unsymmetrical disulfides were employed, a preferential substitution by one of the two subunits was observed.[44]

All the experimental evidence reported above clearly highlights the high complexity of the thiol exchange process and the difficulty of finding simple cause-effect correlations due to the high number of variables that influence the system final state.

On the contrary, we can build an ideal model of the ligand exchange process as shown on Scheme 1. It can be seen from the equation that if the initial amount of entering ($[E]_0$) and bound to the nanoparticles ($[SH]_{NP}$) thiol are controlled, by quantifying the degree of substitution ($[E]_B$) the equilibrium constant can be easily calculated from one single experimental parameter.

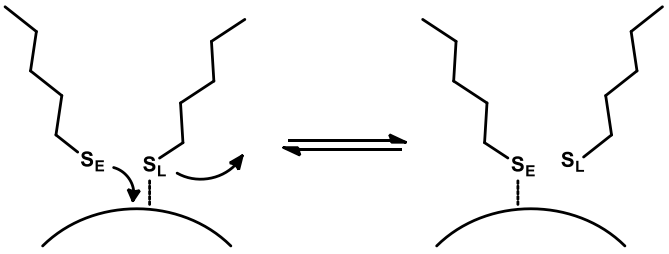

$$K = \frac{[L]\cdot[E]_B}{[E]\cdot[L]_B} = \frac{[E]_B^2}{[E]\cdot[L]_B} = \frac{[E]_B^2}{([E]_0-[E]_B)\cdot([SH]_{NP}-[E]_B)}$$

Scheme 1 – Representation of the thiol exchange reaction. Mathematical expression for the equilibrium constant of the process is included. E and L denote the entering and leaving thiol respectively. Subindexes 0 and B are referred to the initial and the nanoparticle bound concentration respectively. SH_{NP} denotes the total concentration of thiols attached to the nanoparticles.

In the ideal case scenario, the value of K should be equal to 1 and the final ratio on the nanoparticles surface becomes equal to the global ratio of concentration in the system between the two components. However, real values are typically smaller.[45]

2.2 Results

Results of exchange reaction on nanoparticles of 2 nm in diameter are shown on Table 1 for two different couples of leaving and entering thiols and three different reaction conditions in each case. To clarify results and discussion, the chemical structure of the thiols involved is shown on Figure 8.

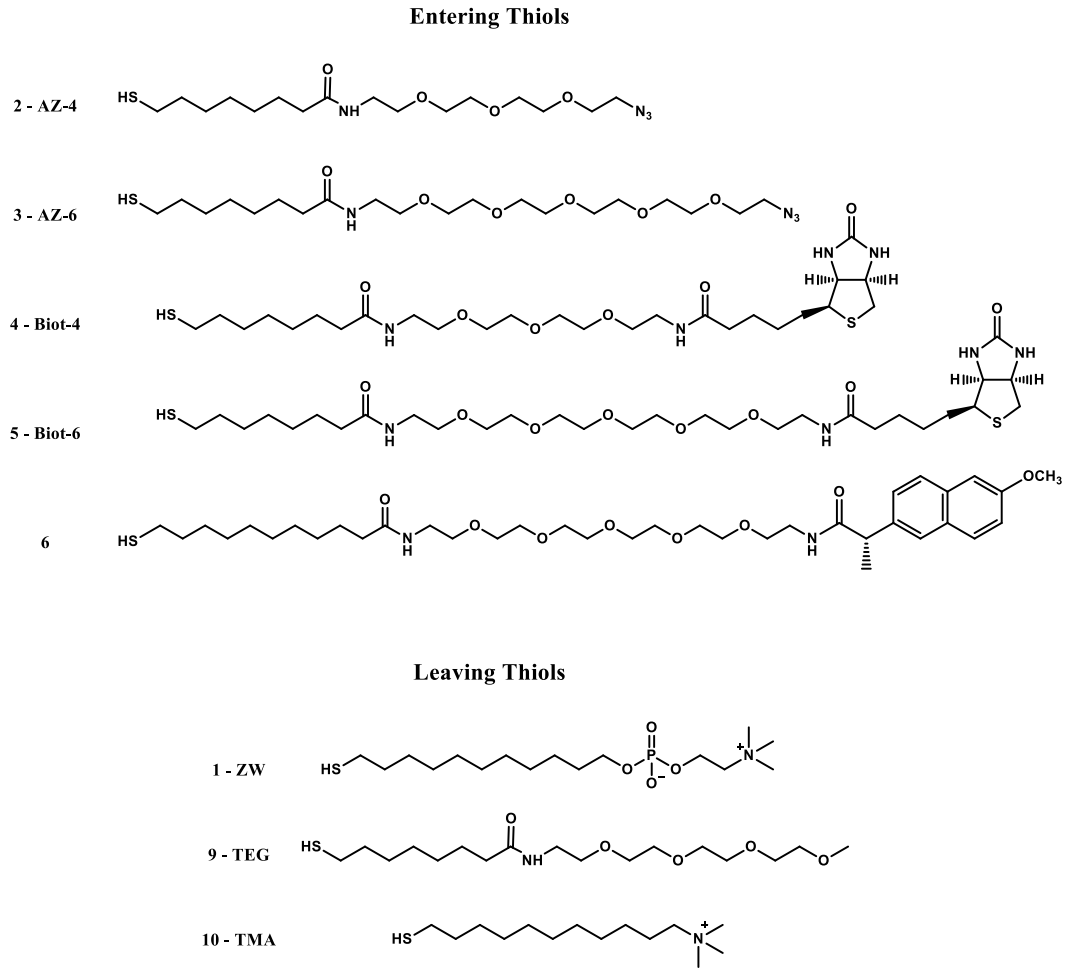

Figure 8 – Chemical structure of thiols involved in place-exchange reactions.

Table 1 – Percentage of leaving thiol substituted on 2 nm nanoparticles after 18 hours at 30 °C. Values in brackets represent the relative degree of substitution respect to the ideal equilibrium, this is, experimental K. [a]Reaction ratio represents the molar ratio between the entering and leaving thiols, percentage indicates the ideal degree of substitution if theoretical equilibrium with K=1 was achieved. [b]Quantification inaccurate due to signal overlapping.

Entering thiol	Reaction ratio[a]	Leaving Thiol	
		1 – ZW	**10 – TMA**
2 (AZ-4)	1:1 – 50%	25% (0.50)	52% (1.04)
	1:4 – 20%	9% (0.44)	21% (1.04)
	1:20 – 5%	2% (0.49)	~ 5%[b]
3 (AZ-6)	1:1 – 50%	30% (0.60)	40% (0.79)
	1:4 – 20%	11% (0.55)	16% (0.78)
	1:20 – 5%	~ 3% (0.55)	~ 4%[b]

On the whole, the degrees of substitution obtained were spread between 44 and 104% of the ideal values, remaining however almost invariant when the reaction ratio was modified. This trend was also observed when nanoparticle size was increased from 2 to 9 nm (see Table 2). It must be noticed that despite the spread of the values, thiol displacement was consistently more extended on nanoparticles exposing the cationic thiol **10** (yields 78-104%) than with the zwitterionic **1** (44-60%).

Table 2 – Percentage of entering thiol on 9 nm nanoparticles surface after 18 hours at 30 °C. Values in brackets represent the relative degree of substitution respect to the ideal equilibrium, this is, experimental K. [a]Reaction ratio represents the molar ratio between the entering and main thiols, percentage indicates the ideal degree of substitution if theoretical equilibrium with K=1 was achieved. [b]Nanoparticles became insoluble in water, quantification might not be accurate. [c]Quantification not possible, nanoparticles became insoluble.

Entering thiol	Reaction ratio[a]	Leaving Thiol	
		1 – ZW	9 – TEG
2 (AZ-4)	1:1 – 50%	22% (0.43)	—
	1:4 – 20%	8% (0.39)	—
	1:20 – 5%	2% (0.41)	—
3 (AZ-6)	1:1 – 50%	16% (0.31)	16% (0.31)
	1:4 – 20%	4% (0.18)	4% (0.22)
	1:20 – 5%	~ 2% (0.35)	—
4 (Biot-4)	1:1 – 50%	13% (0.27)	8% (0.16)[b]
5 (Biot-6)	1:1 – 50%	11% (0.22)	n.d.[c]
6	1:4 – 20%	13% (0.66)	—
	1:20 – 5%	<0.3% (<0.07)	—

Considering the little difference in substitution yield when varying the exchange reaction ratio, an average value for each entering-leaving thiol couple can be considered in order to facilitate the discussion (Table 3).

Table 3 – Average degree of substitution with respect to the ideal equilibrium (K=1). Data calculated by averaging results from different exchange ratios from Table 1 and Table 2.

Entering thiol	Nanoparticle diameter | Leaving Thiol			
	2 nm	**9 nm**	**2 nm**	**9 nm**
	1 – ZW		**10 – TMA**	**9 – TEG**
2 (AZ-4)	48%	41%	104%	—
3 (AZ-6)	57%	28%	78%	26%
4 (Biot-4)	—	27%	—	16%
5 (Biot-6)	—	22%	—	—

When studying the influence of nanoparticle diameter on substitution yield, by comparing the experiments where thiol **1** was displaced by either **2** or **3**, values typically decrease when increasing the nanoparticle diameter, although values for **2** did it by a small margin whereas substitution by **3** was almost halved.

Substitution on 9 nm nanoparticles typically proceeded with low yields (16-41%) with both **1** and **9** as leaving thiols, with the exception of thiol **6** (see Table 2 más atrás), that will be discussed later.

Results in Table 4 below show the data corresponding to the simultaneous exchange reaction with two entering thiols onto 9 nm nanoparticles with a monolayer of **1**.

Table 4 – Degree of substitution of mixed exchange reactions on 9 nm nanoparticles covered with ZW–1. Values in brackets represent the relative degree of substitution respect to the ideal equilibrium for each components considering only the individual equilibrium between each entering and leaving thiol. [a]Reaction ratio represents the molar ratio between the entering and leaving thiols, percentage indicates the ideal degree of substitution if theoretical equilibrium with K=1 was achieved considering all thiols present in the solution. [b]Nanoparticles became insoluble in water, number averaged between water soluble and methanol soluble fractions considering their relative proportions.

Entering thiol	Reaction ratio[a]	Final thiols on the surface	
		5 (Biot-6)	**6**
5 (Biot-6)	1:2 – 25%	3% (0.09)	33% (1.00)[b]
6	1:2 – 25%		
5 (Biot-6)	1:1.25 – 41%	7% (0.16)	5% (0.69)
6	~ 1:7 – 8%		

When both were introduced simultaneously in the same proportion (1:2 with respect to **1**), thiol substitution occurred almost exclusively for **6**, progressing beyond the ideal equilibrium for the mixture of all three thiols (33% instead of 25%), whereas for **5** the substitution yield decreased below 10%. When the ratio was tweaked aiming for a similar substitution by both of them, by employing an amount of **5** almost identical to the one reported on previous experiments and almost half of **6**, both thiols were capable to displace **1** from the surface with yields more or less similar to those reported independently in Table 2.

A particular behaviour was observed for thiol **6** during the exchanges, since it presented the highest exchange extend for electrically neutral nanoparticles. Furthermore it modified significantly its substitution degree when included in very small concentration or in a large one. Figure 9 illustrates the difference in trend between exchanges with thiol **6** and those with **2** and **3**.

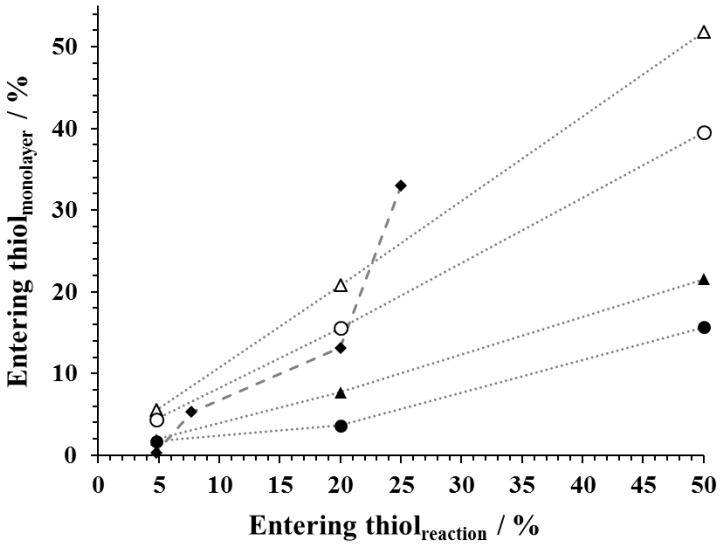

Figure 9 – Dependence of substitution yield upon entering thiol proportion corresponding to the exchange of 9 nm nanoparticles covered with 1–ZW (filled symbols) or 10–TMA (empty symbols) by thiol 2 AZ–4 (triangles), 3 AZ–6 (circles) or 6 (squares, dashed line).

All azido-functionalized thiols show a linear dependence of substitution with the initial amount employed whereas the substitution degree increases with the amount of reactant in the case of **6** in a non linear fashion. We can analyse the same phenomena by comparing the values of K calculated as shown in the equation shown previously on Scheme 1.

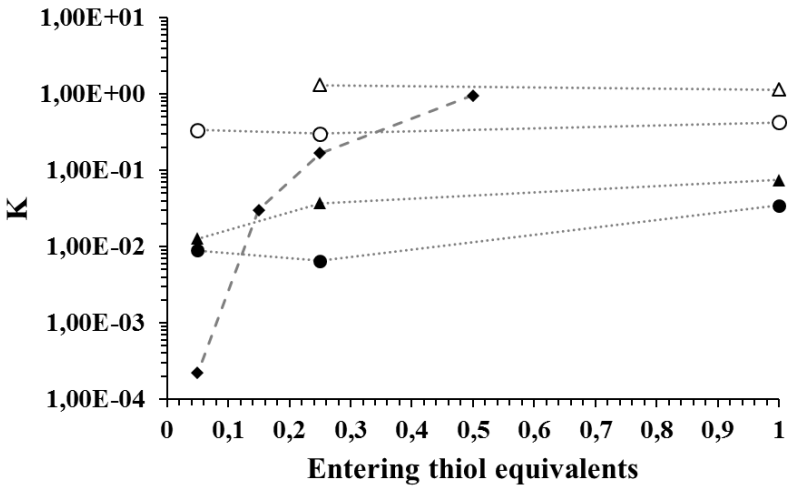

Figure 10 – Equilibrium constant of the ligand displacement during the thiol substitution corresponding to the exchange of 9 nm nanoparticles covered with 1–ZW (filled symbols) or 10–TMA (empty symbols) by thiol 2 AZ–4 (triangles), 3 AZ–6 (circles) or 6 (squares, dashed line). Notice the vertical logarithmic scale.

It can be observed that contrary to **2** and **3**, where the value of K is not significantly altered when the amount of thiol is modified, increasing the number of equivalents of **6** during the substitution process increases the equilibrium constant by up-to four orders of magnitude.

2.3 Discussion

When analyzing the influence of the chemical structure of the leaving thiol, the improvement in the degree of substitution when zwitterionic thiol **1** is replaced by cationic **10** can be easily explained considering that each substitution of **10** by a neutral entering thiol reduces the electrostatic repulsion between the trimethylamonium groups on the nanoparticle surface, whereas no effect on net charge occurs when the original monolayer is constituted by **1**. This will constitute a substantial driving force for the substitution process to occur.

The decrease in yield when increasing the nanoparticle diameter for the same couple of thiols can be understood on the basis of the nanoparticle curvature and its effect on the compactness of the monolayer. Since a thiol fingerprint on the gold surface is essentially constant and about of 0.2 nm^2 per thiol,[46] an increase in nanoparticle size constrain the chains of the ligands to be packed in a more compact arrangement (Figure 11), this could have a double effect; on one side it should diminish the ability of the entering thiol to reach the surface and successfully displace one of the existing ligands but, on the other hand, more sterically hindered entering thiols would struggle to find a suitable place in the monolayer. The balance between these two factors should dictate the global behavior for each particular case. For instance, an opposite trend to the one observed here has been reported in literature. However, this was referred to a particular case in which supramolecular interactions between the thiols were suspected to dictate the kinetic behavior,[47] being more favored in the more compact monolayer.

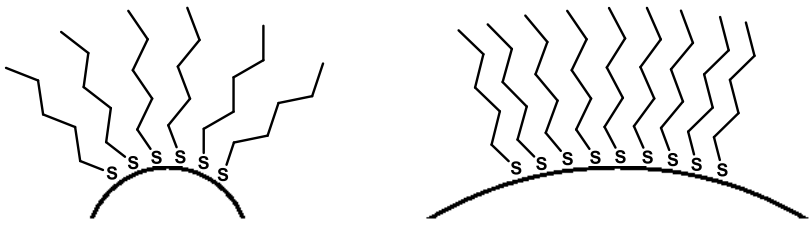

Figure 11 – Scale representation of curvatures for 2 and 9 nm nanoparticle surfaces and an ideal disposition of thiol molecules.

In addition, for very small sizes, the chain disposition is far from the ideal spherical shape illustrated before and they tend to group on two poles of the nanoparticles in a rugby-ball-like shape, leaving a highly exposed belt in which ligand displacement should be highly favored (Figure 12).[48]

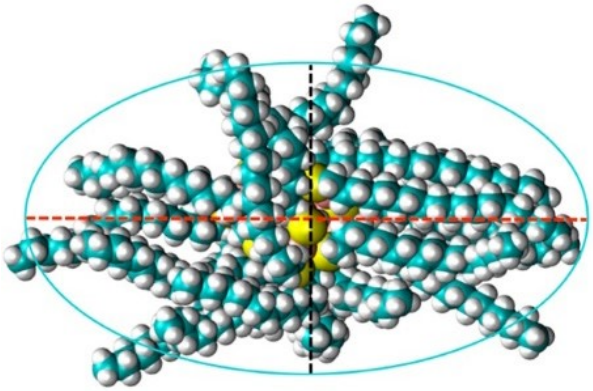

Figure 12 – Rugby ball shape of a monolayer protected gold cluster. Notice the deviation from the ideal spherical representation. Reproduced from reference.[48]

When I attempted to introduce two thiols simultaneously on the monolayer, the degrees of substitution remained similar to those of individual exchange in the case of biotinylated **5**. This is in good agreement with the results reported in literature, typically foreseeing similar degree of substitution for individual and simultaneous exchanges except for thiols that present steric hindrance effects.[45]. However, they presented a high variability in the degree of substitution of the naproxen functionalized **6**, which already presented an unusually high substitution capability on 9 nm nanoparticles compared with all other thiols (Table 2).

The non-linear behavior of thiol **6** when varying its concentration indicates a dependence of the equilibrium constant on the latter, as shown in Figure 10. The observed trend could be an indication of a cooperative mechanism, so the presence of a higher amount of the entering thiol on the nanoparticle surface facilitates subsequent substitutions. The hydrophobic nature of the head group could be responsible for this *via* π-π interactions of thiols free in solution with those already on the surface, as illustrated in Figure 13; however, more experimental data are required in order to confirm this

mechanism for this particular case. Similar interactions have been already reported in the literature,[47,49] being even capable to induce phase segregation on the nanoparticle surface upon substitution.[50]

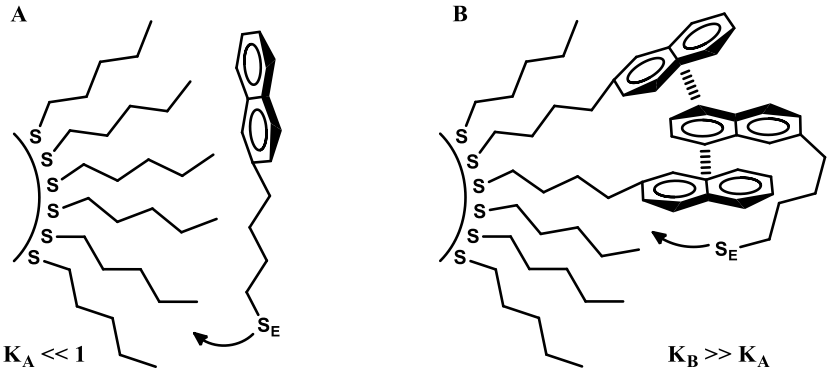

Figure 13 – Representation of the cooperative mechanism potentially responsible for the enhancement of the equilibrium constant when entering thiol concentration is modified from a low (A) to a high (B) value.

2.4 Conclusions

Mixed monolayer nanoparticles functionalized with both, azido clickable and protein binding groups have been successfully prepared in a highly reproducible way by means of thiol substitution of parent nanoparticles.

Despite the representation of the ideal thiol substitution equilibrium shown on Scheme 1, experimental data clearly show that many factors determine the actual values of K. Some of the factors that appear to play a role could be thiol solubility in the reaction medium, interaction between neighboring thiols on the nanoparticle monolayer and compactness of the latter.

In general, the degree of substitution obtained can be predicted and tuned due to the independence of the equilibrium constant on the molar ratio between entering and leaving thiols.

On the other hand, it is difficult to predict in advance what the equilibrium constant will be for an unknown couple of leaving and entering thiols, due to the high complexity of the process and the number of factors that influence the final result.

Substitution on smaller nanoparticles proceeded typically in larger extents, probably due to the less compact monolayer on their surface.

Mixed-monolayer nanoparticles with three different thiols have been prepared in a successful way in one single step by means of simultaneous thiol substitution.

Thiol **6**, bearing an aromatic head group, presented a particular behavior in which equilibrium constant increased up to four orders of magnitude when increasing the equivalents present in the reaction, contrary to any other thiol employed so far. A possible cooperative mechanism to explain these results has been suggested.

Chapter 3 Click-coupling on gold nanoparticles

3.1 Introduction

Click reactions and in particular copper catalyzed alkyne-azide cycloaddition (CuAAC)[51] are among the most extended methods employed nowadays for chemical conjugation due to their simplicity, selectivity, high yields, biological and chemical compatibility and low toxicity of the products. Although the reaction progresses by thermal activation, Cu(I)-mediated catalysis improved drastically reaction times and included also regiospecificity towards one of the two possible regioisomers of the triazole product.

Originally, it was typically carried out in the presence of $CuSO_4$ as copper source and a reducing agent, typically sodium ascorbate, to form the active copper(I) species. But in order to improve the reaction yield, copper-binding ligands capable to stabilize the Cu(I) oxidation state and protect it from oxidation were designed and implemented for both polar and non-polar solvents (Figure 14).

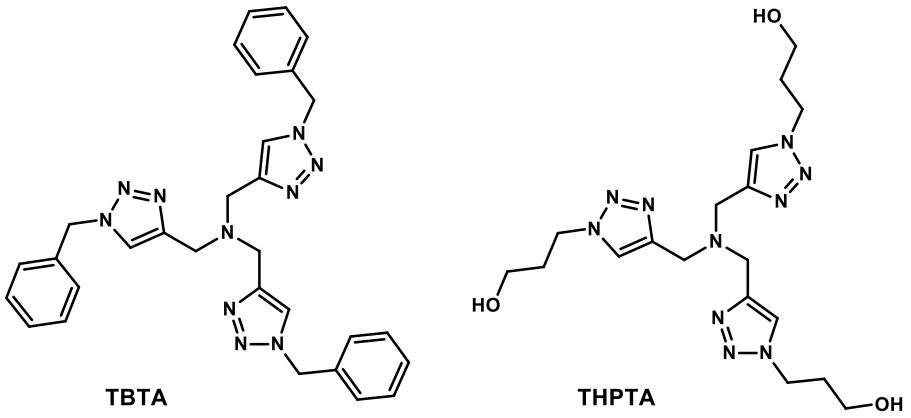

Figure 14 – Cu(I)-stabilizing ligands employed in non polar (left) and polar media (right).

Despite the great performance of CuAAC for small molecule synthesis, previous attempts onto gold nanoparticles have proven unsatisfactory, reporting low yields, typically between 1 and 22%,[52] or very long reaction times of up to several days.[53] This low yields were mainly attributed to the poor solubility of the nanoparticle chains and the low stability of the Cu(I) catalytic species in the non-polar media required to solubilize the azido-functionalized alkyl nanoparticles (dioxane, hexane). However, modified experiments employing toluene[54,55] or water:THF mixture[56] as a solvent showed higher yields ranging from 75% to virtually quantitative with a broad range of alkynes, disproving the original claims.

In the recent years, new catalytic systems in the absence of copper have been developed, employing strained cyclooctynes as coupling agents[57] (Figure 15), giving rise to the so-called strain-promoted alkyne azide cycloaddition (SPAAC). It has the advantage to avoid the use of copper and proceed at room temperature with no required purification. However, it must be noticed that regioselectivity is lost with this strategy.

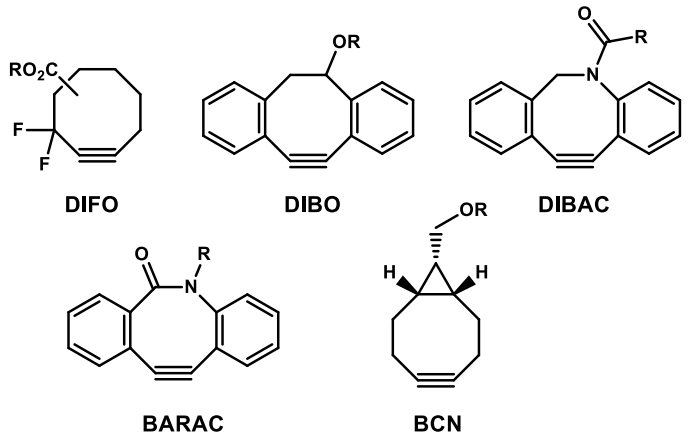

Figure 15 – Chemical structure of the most representative cyclooctynes derivatives employed in SPAAC.

Gold nanoparticles multivalency must be taken into account when referring to reaction yields on them. When several chemical transformations are carried out over a multivalent system element, if the yield of each coupling is considered to be constant throughout the transformation, the global reaction yield due to the propagation of *n* single steps would be equal to the yield of a single step raised to the number of steps.

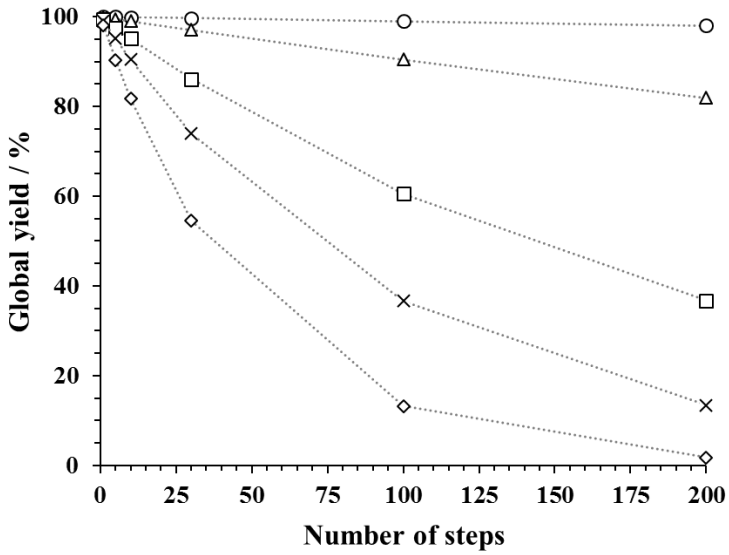

Figure 16 – Multivalent global yield dependence on the number of steps and the individual reaction yields: 99.99% (circles), 99.9% (triangles), 99.5% (squares), 99% (crosses) and 98% (diamonds).

As it can be seen in Figure 16, even with individual yields above 98%, the global yield decreases very fast when increasing the number of steps.

3.2 Results

When nanoparticles that undergone the click-coupling reaction were analyzed in search of the coupling product, no clear signals of the triazole signal were observed in the ^{1}H-NMR spectra. In addition despite the high homogeneity of the magnetic field (see orange signal in Figure 17 below), both signals of the methylene groups close to the phosphate were broad and low in intensity.

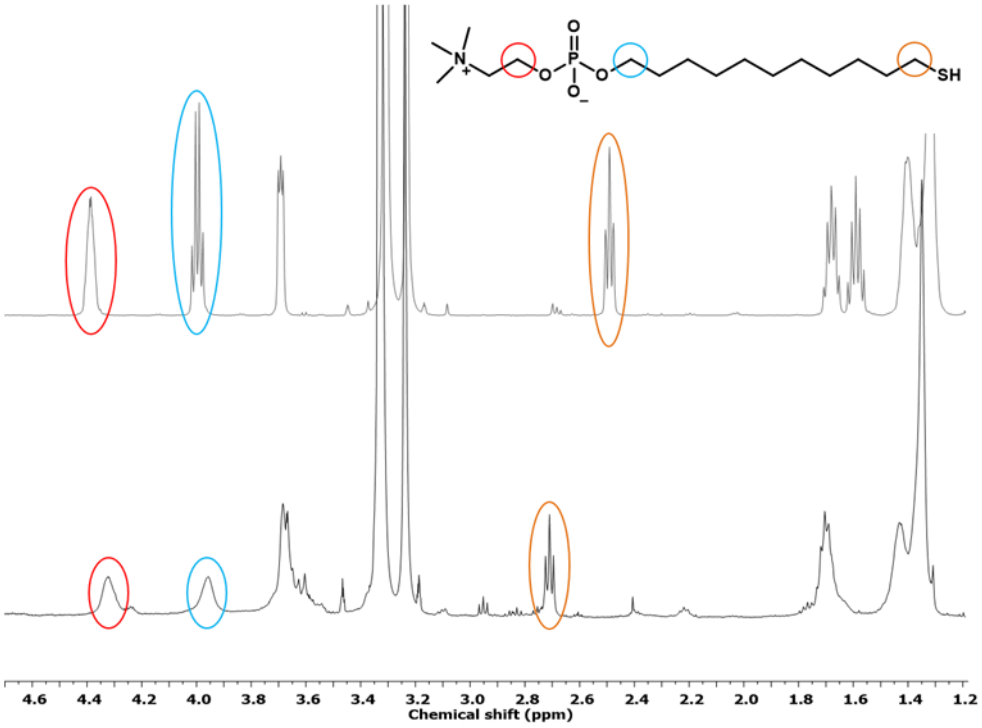

Figure 17 – ^{1}H-NMR spectra of ZW Thiol 1 (top) and an sample after click reaction with thiols detached from the nanoparticles surface. Relevant signals are highlighted.

Treatment of the cleaved mixture of thiols with Chelex® resin resulted in sharp spectra, proving that residual copper (Cu(II)) contamination was present in the final samples even after purification. Attempts to remove the copper by treating the exchanged nanoparticles with chelating resin before detaching the thiols from the nanoparticles proved to be unsuccessful. All results shown below were calculated after treatment of the detached mixture of thiols with chelating resin.

Chemical structures of the thiols constituting mixed-monolayer nanoparticles and alkynes employed in this section are shown in Figure 18 and Figure 19, respectively.

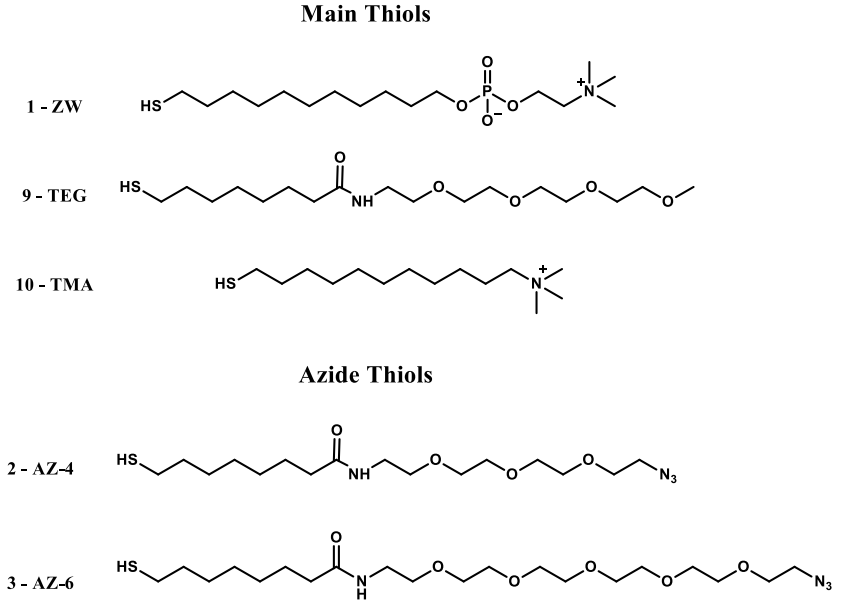

Figure 18 – Chemical structure of thiols constituting mixed monolayer nanoparticles employed in this chapter.

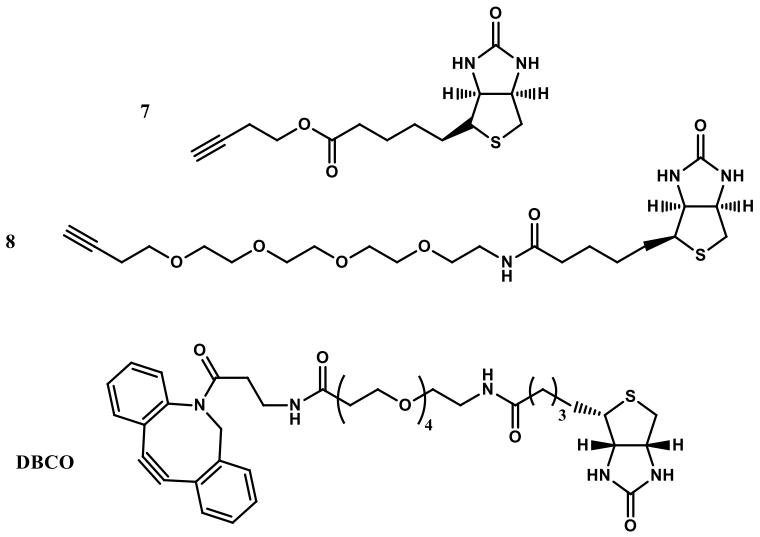

Figure 19 – Chemical structure of alkynes employed in this chapter.

Results shown in Table 5 below show the click-coupling yield under different conditions for nanoparticles of 2 nm in diameter. Notice that yields reported are referred to the total amount of azido groups available on the nanoparticle surface, whereas bracket values are referred to each individual step, taking into account the average number of azido groups present on each case.

Table 5 – Global reaction yield of click-coupling on 2 nm gold nanoparticles. Values in parenthesis are referred to the individual yield for each azido group, taking into account the total number of thiols, the proportion of azide groups and the global yield. [a]The percentage represents the amount azide thiol on the NPs surface; [b]Unless otherwise stated, values stand for H_2O:DMSO mixtures; [c]Numbers stand for the equivalents of alkyne:Cu-complex:ascorbic acid; [d]Reaction conditions: 4 days at 40 °C; [e]Cu attempted removal with chelex resin prior to thiol detachment.

			Main thiol	**1 – ZW**		**10 – TMA**	
			Azide thiol[a]	**2 AZ-4 18%**	**3 AZ-6 28%**	**2 AZ-4 21%**	**3 AZ-6 16%**
Alkyne	**Ligand**	**Solvent[b]**	**Conditions[c]**				
7	TBTA	1:1	100:10:10	54% (95.2)	—	—	—
			10:10:10	46% (94.0)	—	—	—
8	THPTA	3:1	50:5:10	—	22% (92.6)	75% (98.0)	79% (97.9)
				—	26%[d] (93.4)	—	—
		1:1	100:20:60[e]	—	11% (89.3)	—	—

Although reaction conditions were not identical and direct comparison must be taken with caution, it seems that the couplings of alkyne **7** performed better than those with **8** by almost doubling the global yield, although inclusion of more alkyne did not affect the reaction yield significantly.

Under the same conditions, substitution of zwitterionic **1** for cationic **10** improved the reaction yield from 20% to almost 80% on average, whereas longer reaction time and higher temperature had almost no impact.

Curiously, even with the inclusion of more equivalents of all reagents, the parallel higher amount of DMSO (final 1:1 instead of 3:1 H_2O:DMSO) seemed to have hindered the reaction, reducing its yield by half from 22 to 11%.

Table 6 – Reaction yield of click-coupling on 9 nm gold nanoparticles. Values in parenthesis are referred to the individual yield for each azido group, taking into account the total number of thiols, the proportion of azide groups and the global yield. [a]The percentages represent the amount azide thiol on the NPs surface; [b]Unless otherwise stated, values stand for H_2O:DMSO mixtures; [c]Numbers stand for the equivalents of alkyne:Cu-complex:ascorbic acid; [d]Reaction conditions: 4 days at 40 °C, nanoparticles precipitated; [e]Cu attempted removal with chelex resin prior to thiol detachment.

			Main thiol	**1 – ZW**		**9 – TEG**	
			Azide thiol[a]	**2 AZ-4**	**3 AZ-6**	**3 – AZ-6**	
Alkyne	**Ligand**	**Solvent[b]**	**Conditions[c]**	**20%**	**15%**	**5%**	**17%**
7	TBTA	1:1	100:10:10	21% (99.6)	—	—	—
			10:10:10	22% (99.6)	—	—	—
8	THPTA	3:1	50:5:10	—	28% (99.6)	—	—
				—	n.d.[d]	—	—
		9:1		—	—	—	45% (99.8)
		4:1		—	—	49% (99.3)	—
		1:1	100:20:60[e]	—	~ 0%	—	—

When nanoparticle diameter was increased from 2 to 9 nm, similar values below 50% global yield were obtained. Nonetheless, when the much higher multivalency of these systems is taken into account it comes clear that these similar results derive from much higher individual coupling yields, being actually above 99% and very similar among them in all cases.

Coupling with alkyne **8** onto **ZW**-functionalized nanoparticles presented very similar yields to those of the 2 nm analogues but conversion with **7** decreased by a factor of two.

Coupling with **TEG** nanoparticles presents yields higher than those of **ZW**, but still moderate compared to the 2 nm **TMA** analogues shown before. Inclusion of more equivalents of all reagents, with the subsequent increase of DMSO, decreased reaction yield to virtually no conversion.

In order to avoid the use of copper due to the inevitable contamination of the final sample, ring-strain promoted click chemistry was attempted and the results obtained are shown in Table 7**.**

Table 7 – Reaction yields corresponding to the copper-free coupling. Values in parenthesis are referred to the individual yield for each azido group, taking into account the total number of thiols, the proportion of azide groups and the global yield. [a]The percentage represents the amount azide thiol on the NPs surface; [b]Numbers stand for the equivalents of alkyne respect to the azide groups; [c]DBCO-Biot commercial reagent; [d]DBCO byproducts much more present compared to the 2 eq. sample.

			Main thiol	**1 – ZW**		**9 – TEG**
			Azide thiol[a]	**3 – AZ-6**		
Alkyne	**Solvent**	**NPs**	**Conditions[b]**	**15%**	**28%**	**5%**
DBCO[c]	H_2O	**2 nm**	5 eq	—	~ 40% (95.4)	—
		9 nm	2 eq.	—	—	93% (99.9)
			5 eq	< 1% (< 98)	—	69%[d] (99.7)

Results show very high yields for the coupling with **TEG** nanoparticles, but more curiously, the yield is significantly decreased when more equivalents of reagent were added. In addition, almost no impurities were obtained when 2 equivalents were employed but a significant amount of an insoluble precipitate as well as soluble byproducts were observed with the larger excess. With nanoparticles covered with **ZW**, both of 2 and 9 nm the reaction yields were significantly lower, specially in the latter case.

3.3 Discussion

Residual copper contamination on the samples after the click-coupling was a critical issue, since it hindered the detection and quantification of the products. The broadening and low intensity of the NMR signals could be due to enhance paramagnetic relaxation in the environment of the copper(II) ions. The broadening of the peaks close to the phosphate group led us to believe that copper might be interacting with those groups through electrostatic interactions in solution.

Although chelation ion exchange resin proved to be very efficient for copper removal once thiols were detached from gold, it had no effect when employed directly onto the nanoparticles. This suggests that copper binds to the thiols both free in solution and in the monolayer and with a relatively high binding constant (Figure 20). Similar interactions with several types of nanoparticles have already been reported in the literature.[58,59]

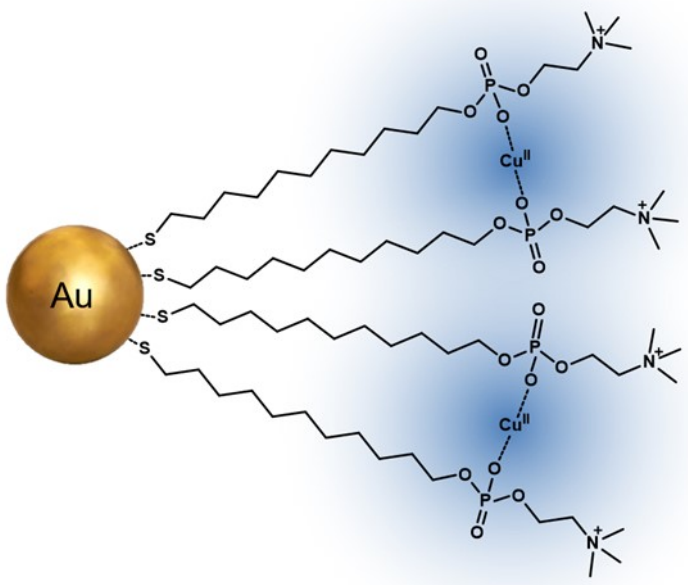

Figure 20 – Representation of Cu-phosphate interaction within the nanoparticle monolayer. Blueish shadow represent the radius of action of the enhanced paramagnetic relaxation, mainly affecting methylene signal bound to the oxygen atoms.

The increased yield when **ZW** was substituted by **TMA** is in good agreement with the arguments reported before and could be due to a higher availability of copper in solution.

Reduced yields with higher amounts of DMSO and higher yields for the non-PEGylated alkyne **7** than **8** could indicate that the reaction progress better when thiol solubility in the media is reduced. In those cases, interaction of the alkyne with the hydrophobic pocket of the monolayer could be enhanced and the proximity to the azido groups responsible of the increase of the yield.

Nanoparticle size increase from 2 to 9 nm did not modify significantly the global coupling yields, particularly with alkyne **8**. This implies much higher individual yields considering that 9 nm nanoparticles contain about 30 times more azide groups than the 2 nm analogues. This suggests that the controlling mechanism determining the final state of the system does not operate at the microscale of each coupling but is dictated by the supramolecular system.

Values for couplings with alkyne **7** present lower yields with 9 nm than with 2 nm nanoparticles whereas those for **8** remained constant. Considering the lower solubility of **7** in polar media and the fact that hydrophobic ligand TBTA was employed instead of water soluble THPTA this result supports the possibility of an interaction of either the alkyne and/or the catalyst with the hydrophobic environment inside the monolayer. The more compact disposition of the thiols when increasing nanoparticle size would impede or decrease this interaction, thus decreasing the reaction yields (see Figure 11 on page18)

Click coupling on nanoparticles covered with **TEG** derivative **9** showed higher yields than those with **ZW** but still lower than the cationic with **TMA**. This intermediate yield could be due to a smaller, non electrostatic, but still existing interaction between the PEG chains and copper ions. Similar PEGylated gold nanoparticles have already been reported to be capable of binding metal ions and complexes in solution.[59] The reaction yield will be inversely proportional to the binding constant between the copper species and the nanoparticle monolayer (Figure 21).

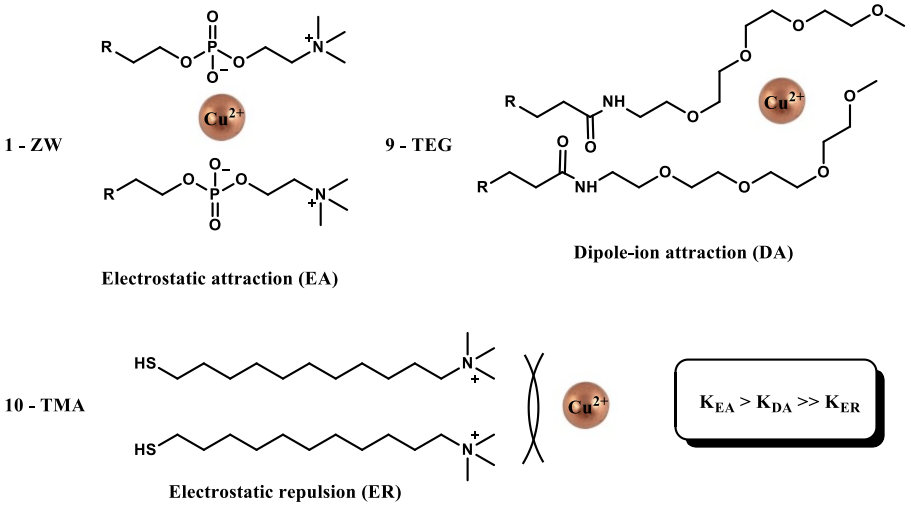

Figure 21 – Representation of interaction modes and nature between copper ion and main thiols depending on their structure. Qualitative order of the magnitude of the binding constant K is also indicated.

On the other hand, it must be also taken into account that for the uncatalyzed reaction, nanoparticles with a lower percentage of superficial azide groups typically presented higher conversion than their more substituted analogues,[60] a trend that we can also observe in our case. More experimental evidence employing nanoparticles with similar azide-coverage on the surface is required in order to exclude its influence.

Couplings in the absence of copper with DBCO proved to be successful but only when low equivalents were employed. It is particularly outstanding the large global yield for the **TEG** 9 nm nanoparticles. We believe that further diminishing the amount of equivalents could improve the results in other cases where yields were still unsatisfactory. The reason why higher equivalents induced decomposition is not clear, but a spontaneous intermolecular mechanism between two molecules of the reagent can be discarded, since the compound has been stored in solution at concentrations much higher than those employed in the reaction with no decomposition even after several weeks.

Despite the good performance with **TEG** nanoparticles, analogue experiments onto nanoparticles covered with **ZW** presented much lower or zero product formation. This could suggest that the functional group of **ZW** or some interaction of the reagent inside

the monolayer triggers or accelerate product decomposition. However, this study fell out of the scope of this thesis a no further investigations have been done.

3.4 Conclusions

Click-coupling has been done successfully onto mixed-monolayer nanoparticle bearing azide groups with low-to moderate yields similar to those reported in literature for alkyl nanoparticles.[60]

The global yield values seems to be independent on the dimension of the nanoparticles in most cases, particularly when water-soluble THPTA catalyst was employed.

Inclusion of very polar solvents such as water or water:DMSO mixtures did not improve the global yield, indicating that nanoparticle solubility and Cu^{I} stability, argued by several authors to be responsible for low click yields on alkyl-nanoparticles, might not be the cause of the low yields obtained in our case.

Increase of the reaction yield when reducing alkyne and/or catalyst solubility in the reaction media, either by chemical transformation or solvent modification, suggests that favoring interaction of the reactant species into the monolayer close to the azido groups generally lead to higher conversions.

Copper ions interacts strongly with the phosphate groups of **ZW**, both free in solution and when packed into the monolayer. This could be a key factor that prevents higher reaction yields on nanoparticles based on this molecule, as proven by the higher yields when substituted by a **TEG** or even more by **TMA** thiols.

Click-coupling in the absence of copper has been also carried out very efficiently by using a ring-strained dibenzocyclooctyne derivative onto **TEG** nanoparticles. However, the use of high amounts of reagents or nanoparticles made of **ZW** decreased reaction yields drastically and several byproducts were formed. Evidence suggests that nanoparticle presence enables or accelerates reagent decomposition.

Chapter 4 Protein Binding

4.1 Results

Monolayer availability and protein binding capabilities

In order to the test protein binding capabilities of the biotinylated nanoparticles, a commercially available kit of HABA-Avidin reagent was employed. When a biotin molecule displaces HABA from the recognition site of avidin to the solution, the UV-Visible absorption spectra is modified and measurement of ΔAbs_{500nm} allows precise quantification of the amount of ligand bound.

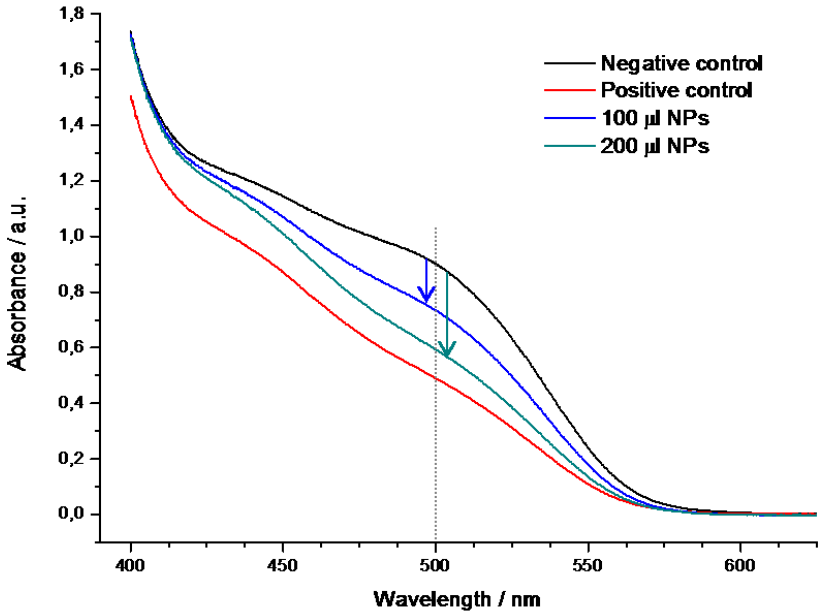

Figure 22 – UV-Visible absorption spectra of the ligand displacement experiment. ZW nanoparticles exchanged with Biot-6 were employed (89% ZW / 11% Biot-6). Negative (H_2O) an positive (biotin) controls are also shown. Nanoparticles concentration *ca* 12 mg/ml.

From the analysis of the data shown in Figure 22, about 18% of biotin present on the nanoparticle surface was actually capable to displace HABA from avidin recognition site. This corresponds to about 46 biotin molecules per nanoparticle (See Nanoparticles characterization on page 66 and Monolayer availability study on page 86).

Avidin titration and crosslinking assay

Titration of the nanoparticles with avidin presented the results shown in Figure 23.

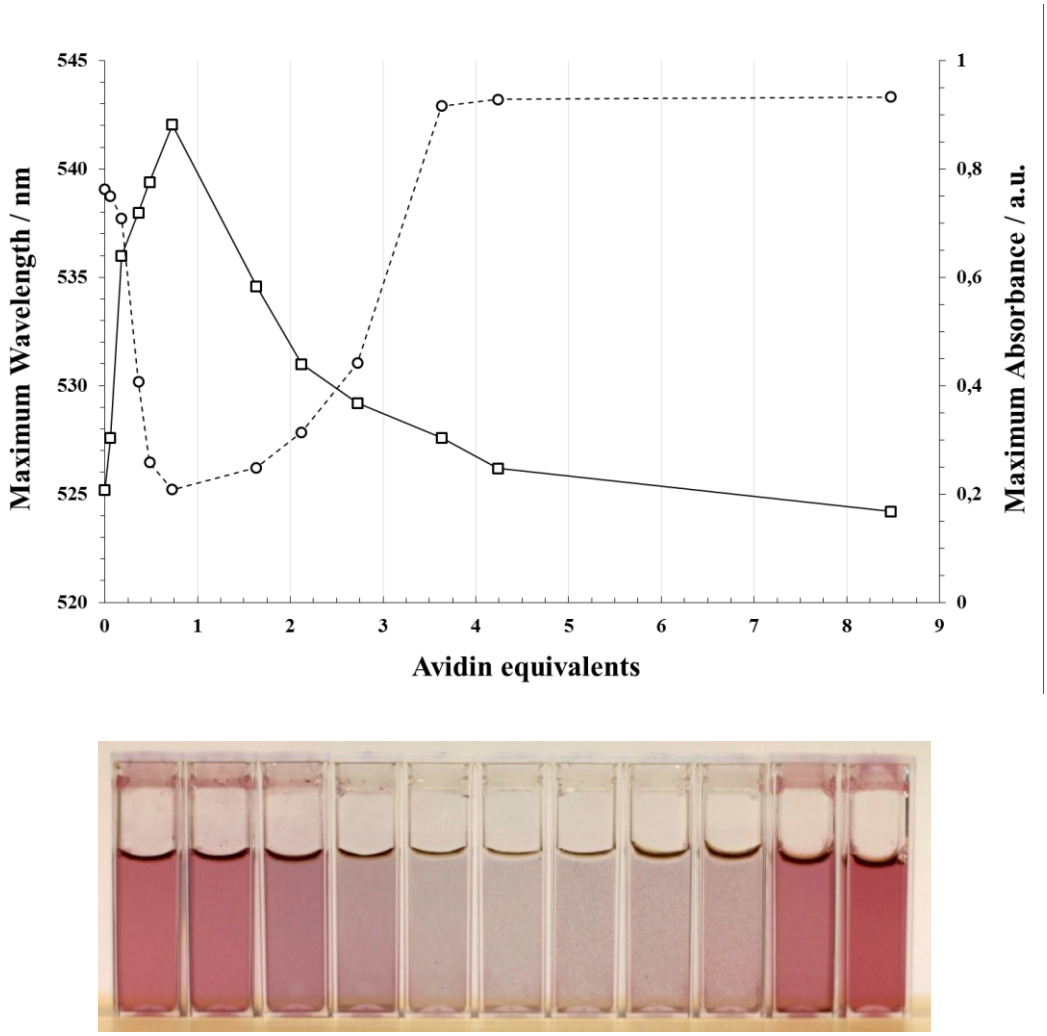

Figure 23 – Data (top) and picture of the cuvettes (bottom) from crosslinking experiment on biotinylated nanoparticles (89% ZW / 11% Biot-6). Wavelength corresponding to the plasmonic maximum (squares) and its absorbance (circles) are shown. Avidin equivalents calculated taking into account 18% biotin availability on the nanoparticle surface.

Very low amounts of avidin, between 0 and 0.1 equivalents, induced a shift of the plasmonic band greater than 10 nm with no significant change in absorbance. Bigger amount of protein produced a further shift of 8 nm coupled with an abrupt precipitation phenomena (decrease in absorbance). Past the 1-2 equivalent point, both precipitation and band shift decreased and returned to its original position when 4 or more equivalents were

added. Final absorption however was slightly higher in intensity than that of the original nanoparticle.

Figure 24 shows two different aggregates observed in the sample treated with 0.7 equivalents of avidin. Nanoparticles proximity and vertical overlapping indicates the existence of 3-dimensional aggregates, out of the observation plane.

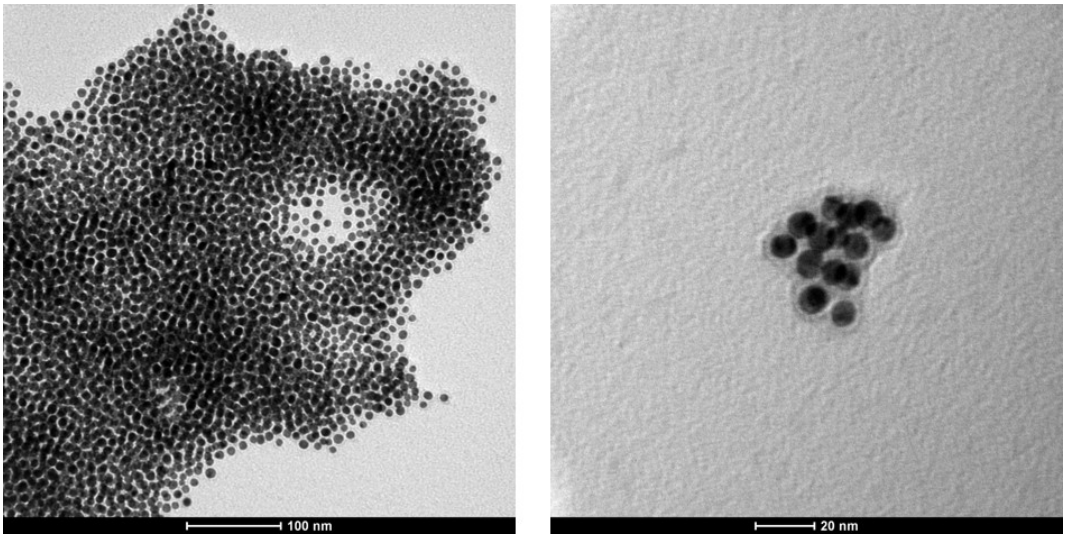

Figure 24 – TEM Images of biotinylated nanoparticles treated with 0.7 equivalents of avidin showing a big (left) and small (right) aggregates. Notice the 3-dimensional arrangement of the nanoparticles.

TEM images of the original nanoparticles and the sample treated with 25 equivalents of avidin (point not shown on Figure 23) are shown in Figure 25. It is important to notice the different packing of the nanoparticles and the bigger separation between them in the sample treated with avidin.

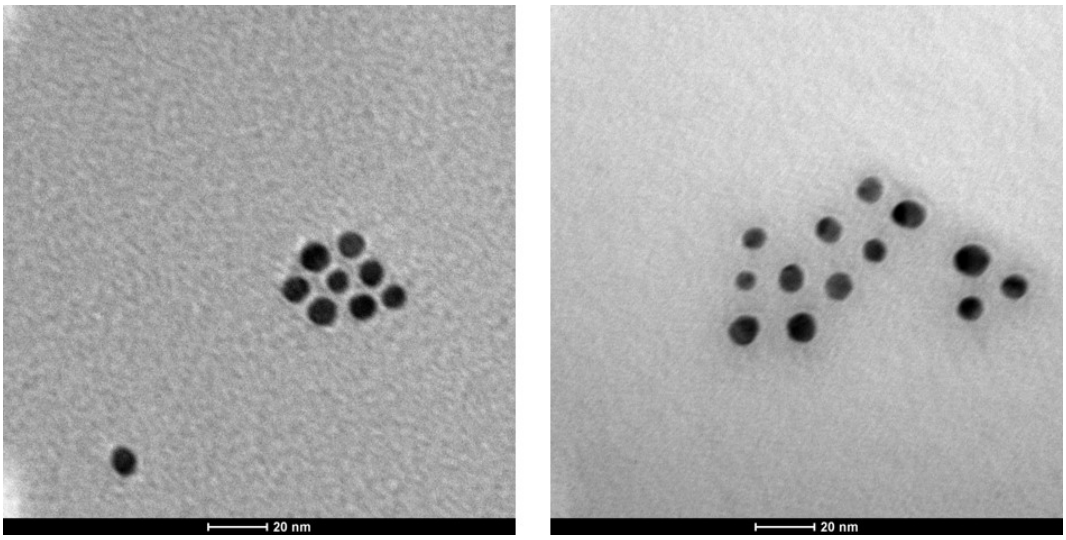

Figure 25 – TEM images of biotinylated nanoparticles before treatment (left) and after addition of 25 equivalents of avidin (right). Notice the bigger separation between the individual nanoparticles and the grey shadow around nanoparticles in the second image.

Stained samples showed a low intensity ring around nanoparticles in contrast with the dark background (Figure 26). These were observed consistently around all nanoparticles present and their dimension typically fall within the 5-10 nm interval.

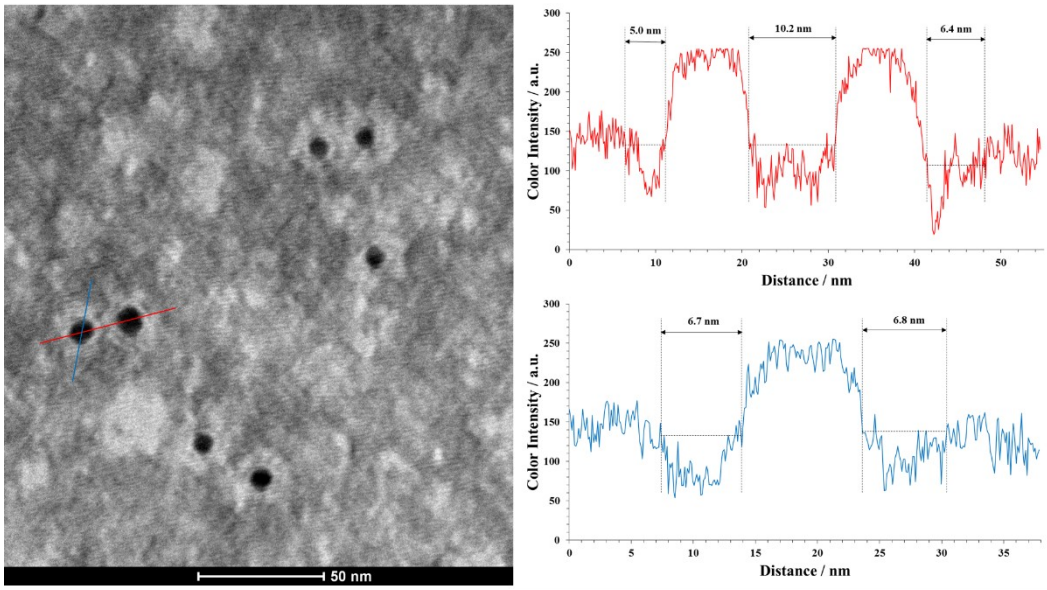

Figure 26 – Stained TEM picture (left) of biotinylated nanoparticles treated with 9 equivalents of avidin and intensity profiles (right) of two depicted directions. Indicative distances are shown.

The analogous experiment performed onto nanoparticles with only ZW showed no significant modifications of either position or value of the plasmonic maximum apart from a very small increase in absorbance (Figure 27).

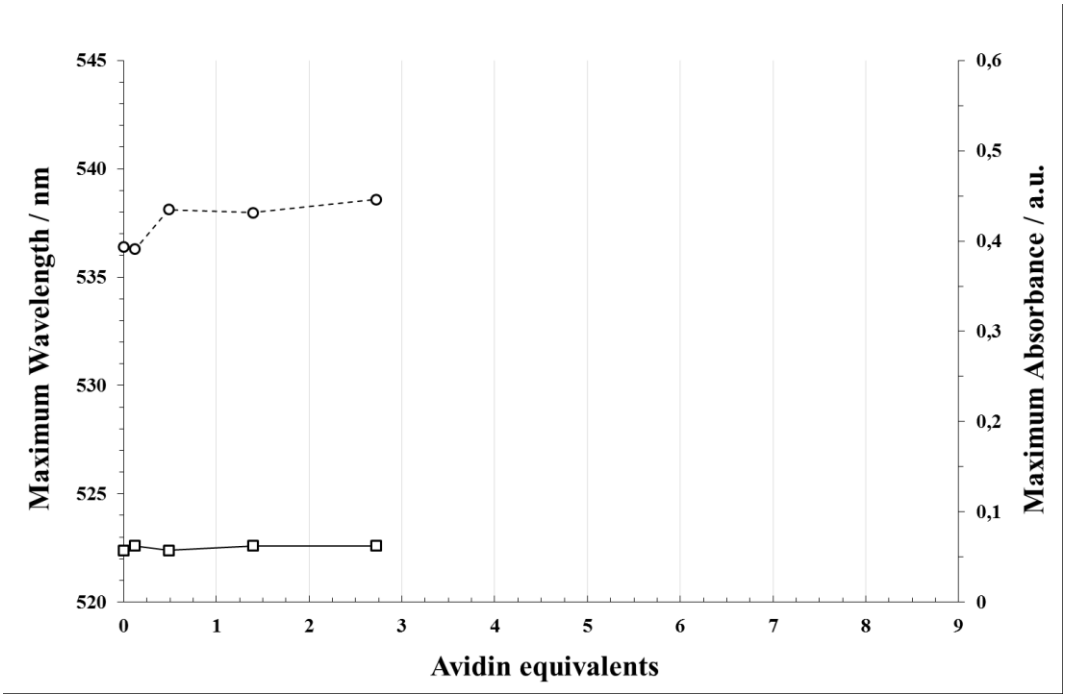

Figure 27 – Control experiment with 100% ZW nanoparticles. Notice that the same horizontal scale from Figure 23 has been employed for comparison purposes. Absorbance (circles) and position (squares) of the plasmonic maximum of the nanoparticles are shown.

Biotin/Naproxen mix-monolayer nanoparticles for combined capturing

When mix-monolayer nanoparticles with both biotin and naproxen on the surface were titrated in the same way as before (Figure 28), a very similar profile was obtained. It presented a small shift of the minimum towards smaller amounts of protein, a retardation of the plateau (existing above 5 equivalents instead of 4) and less abrupt recovery at intermediate values, being almost linear between 1 and 5 equivalents, in contrast with the trend observed before.

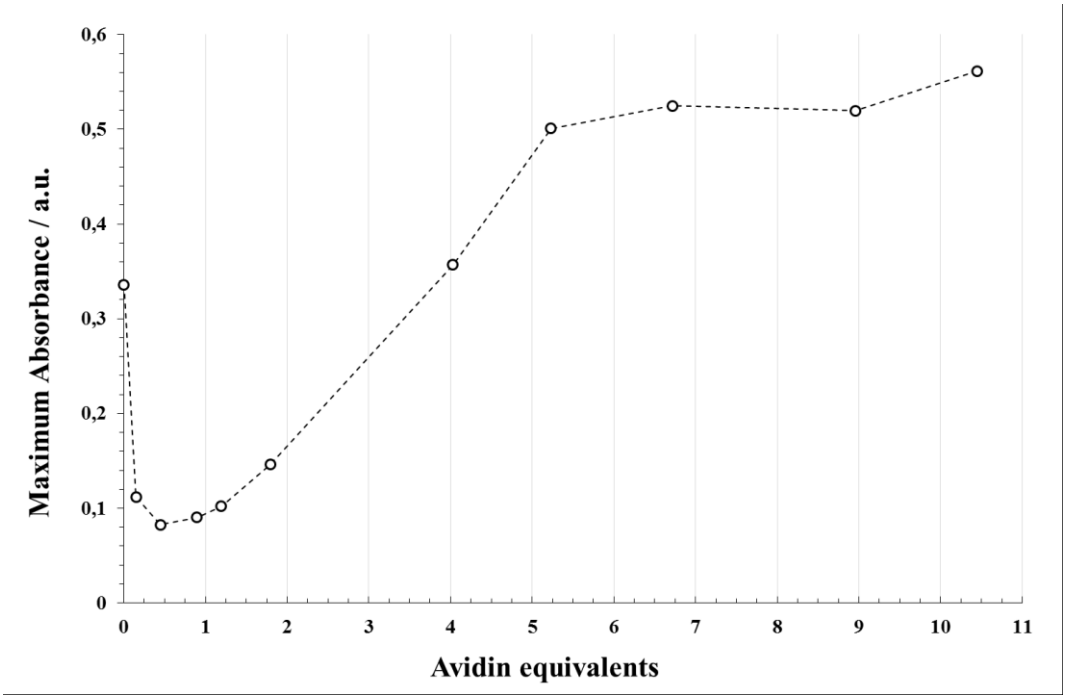

Figure 28 – Data from crosslinking titration of mixed biotin-naproxen nanoparticles (88% ZW / 6.5% Biot-6 / 5.5% Naprox). Avidin equivalents calculated estimating 18% biotin availability on the nanoparticle surface.

Bifunctional nanoparticles were also titrated with albumin, that is known to interact with the naproxen moieties (Figure 29). Aggregation of a minimal amount of albumin induced a shift of the plasmonic band position of 15 nm with no modifications upon further addition. Increasing amounts of albumin induced a slow growth in the solutions absorbance up to 0.25-0.3 protein to naproxen ratio, with no effect beyond this point; this value roughly corresponds to 21-26 proteins per nanoparticle.

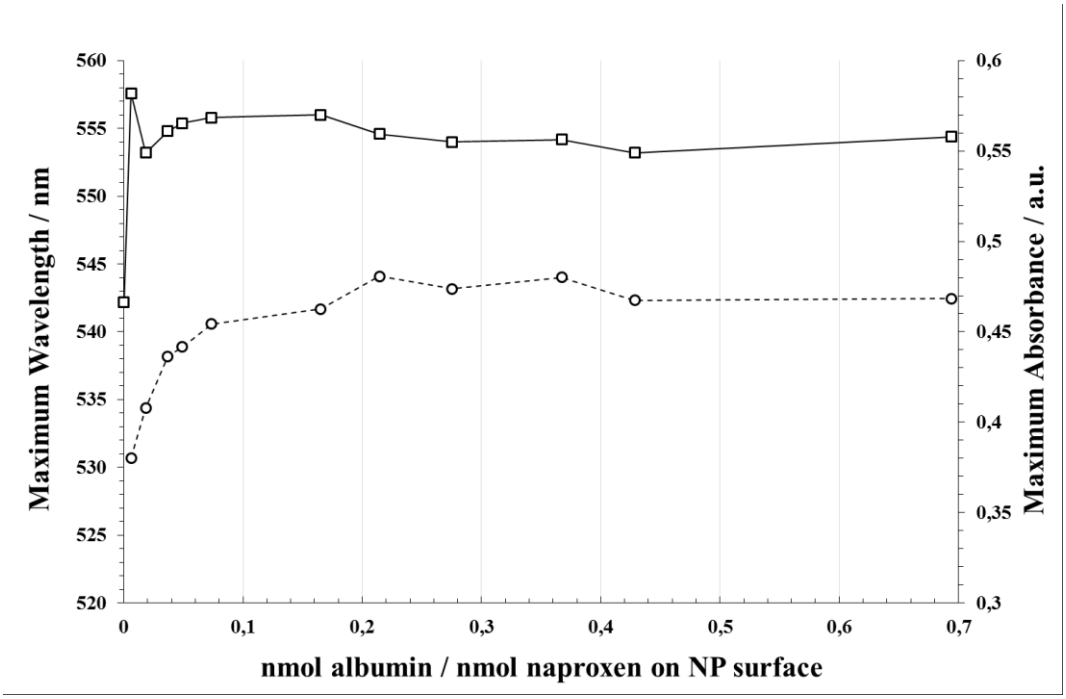

Figure 29 – Titration with albumin of mixed biotin-naproxen nanoparticles (88% ZW / 6.5% Biot-6 / 5.5% Naprox). Absorbance (circles) and position (squares) of the plasmonic maximum of the nanoparticles are shown.

4.2 Discussion

Monolayer availability and protein binding capabilities

Monolayer availability experiment showed that biotin was not only exposed on the surface of the nanoparticle but also capable of reaching and displacing HABA from the binding site of avidin in very short time, retaining a high binding constant.

However, when considering the average size of the gold nanoparticles employed (11 nm) and an approximate radius for avidin calculated from its molecular weight[25] (5 nm), it can be seen that there is no room on the nanoparticle surface to fit the value obtained of 46 proteins.

A detailed analysis of the 3-dimensional structure of avidin revealed that binding sites are distributed in two pairs, facing opposite directions, as it can be seen in Figure 30.

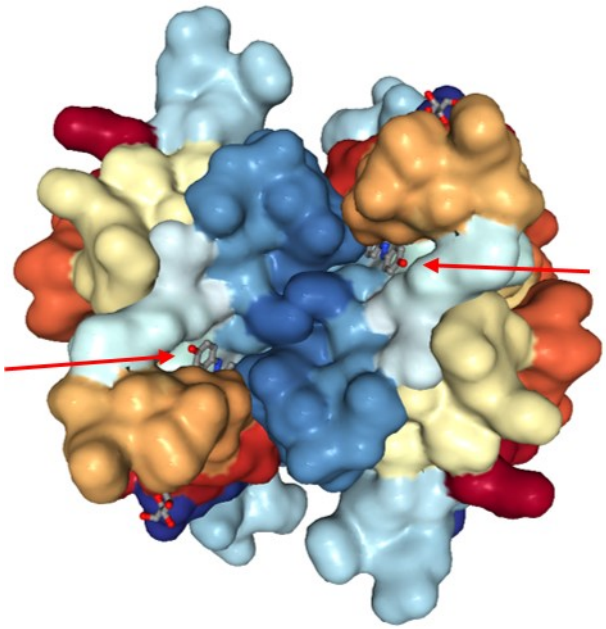

Figure 30 – 3-Dimensional structure of HABA-avidin complex (PDB code 5CHK), ligands in the active site are highlighted with red arrows. Two remaining ligands face the opposite direction. External molecules shown on the top-right and bottom-left surface of the protein are crystallization additives.

Therefore, it is possible that each active biotin moiety on the surface does not bind a single avidin but shares the protein with a second biotin molecule. This will reduce the number of proteins on the surface to be around 23. This value is in good agreement with a relatively compact packing of 5 nm spheres (a good approximation for the diameter of avidin) around a 11 nm one, which is reached with 26 binding units, as it can be seen in Figure 31.

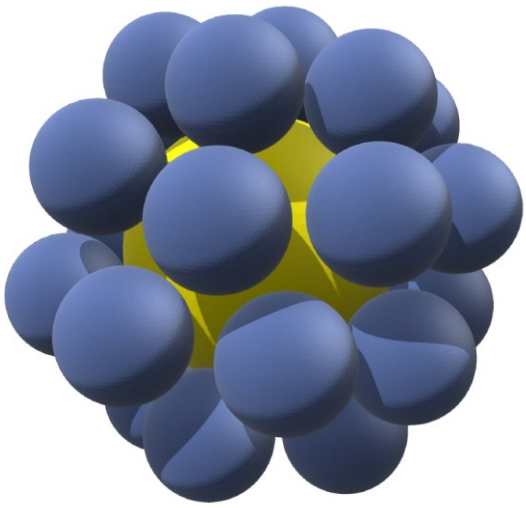

Figure 31 – Packing of 5 nm spheres around a 11 nm spherical core. 26 outer spheres are fitted around the surface.

Avidin titration and crosslinking assay

Titration data shown on Figure 23 are in good agreement with the above discussion. Double binding with a single nanoparticle would leave the remaining active sites pointing directly towards the solution, thus enabling crosslinking with another nanoparticles as observed, whereas the equivalent point around 1 equivalent of avidin also agrees with the biotin availability calculated.

Initial shift of the plasmonic band at very low concentration of protein is believed to be due to partial coverage of the nanoparticle surface by proteins themselves or by the formation of aggregates small enough to remain in solution. The anisotropic modification of the dielectric constant or the coupling between neighboring nanoparticle dipole moments could be responsible for this shift.[26,61] Further shift, coincident with absorbance decrease is believed to be due to extended crosslinking, beyond the solubility point, and precipitation of the aggregates formed.

Figure 24 shows both types of aggregates (big insoluble and small soluble). Their 3-dimensional structure supports the fact that they are generated by random isotropic crosslinking in solution and not during the deposition on the TEM grid, where three or less layers of particles are typically stacked.

When an excess of avidin is present in solution, crosslinking extension decreases and a perfectly soluble final state is recovered. Several reasons may explain why this situation is reached at 3.5 equivalents and not at 1 (Note that the term "equivalent" is employed here as the amount of protein necessary to bind precisely the number of biotin moieties on the sample). On possible explaination will be statistical; when only the exact amount of protein capable of binding all biotin is present in the sample (1 equivalent) it is very unlikely that every protein and ligand self-sorts spontaneously onto the right target avoiding any crosslinking, meaning that an excess of protein will always be required in order to avoid casual crosslinking formation. On the other hand, it could also be due to thermodynamical reasons if we consider that the binding constant decreases with nanoparticle covering, thus requiring higher amounts of protein to reach saturation.

TEM pictures of Figure 25 evidence the difference between the original and the saturated system. Although both present very similar spectral properties, the larger separation between nanoparticles when treated with avidin as well as the stained images shown in Figure 26 indicate the existence of a protein corona around the nanoparticles after the addition of avidin. In addition, interparticle distances in Figure 26 are in good agreement with protein and monolayer size. This corona is believed to be the cause of the increase in absorption of the plasmonic band upon system saturation.

Control experiment with nanoparticles covered only with **ZW** proved that the phenomena described above were not due to random aggregation and that protein binding *via* nonspecific interaction is not present. This lack of interaction was already reported in literature for this zwitterionic thiol monolayers on flat surfaces.[28]

Biotin/Naproxen mix-monolayer nanoparticles for combined capture

Nanoparticles with both biotin and naproxen presented a similar behavior when titrated with avidin, showing that the presence of naproxen does not have a significant impact on biotin binding capability. The downshift of the equivalent point could be due to the difference in biotin availability, since in order to calculate the equivalents for Figure 28, the same 18% obtained for nanoparticles without naproxen was maintained as the

initial estimate. This approximation could not be true due to the presence of naproxen on the nanoparticle and the difference in surface composition. It is interesting to remark the fact that recovery of solubility was faster at the initial stages after the equivalent point but became slower in the final section and higher amount of avidin was required in order to reach saturation. This could be correlated with two phenomena, the lower solubility of these nanoparticles and the reduced coverage of biotin on the surface. The hydrophobic naproxen moiety is little water soluble so, adsorption of avidin on the nanoparticle surface should minimize the interaction of naproxen with water, increasing the global solubility and, therefore, increasing absorbance. On the other hand, the lower biotin density on the nanoparticle could make less likely or slower for a bound avidin to find a second biotin on the surface. This could imply that available biotin will be exposed for longer times before being capped, increasing the probability of crosslinking two different nanoparticles for the same amount of protein present.

Although albumin presents two main binding sites, their spatial distribution at about 90° from one another makes crosslinking impossible, coherently with the absence of precipitation observed. However, its addition immediately induced a shift of the plasmonic band, probably due to a modification of the nanoparticle surrounding. The increase in absorbance until reaching a steady situation is compatible with a continuous increase of the adsorption on the surface until saturation is reached. Albumin size being very similar to avidin also agrees strongly with the saturation value we obtained of slightly more than 20 proteins per nanoparticle.

4.3 Conclusions

Biotinylated nanoparticles were capable to interact with avidin in solution *via* specific interactions with the recognition site, displacing weaker ligands.

The amount of biotin capable to reach avidin binding sites suggest that each protein binds two biotin units on the same nanoparticle and that the whole surface is essentially covered with protein.

The remaining recognition sites of avidin are located on the outer surface of the nanoparticle-protein complex and its activity is preserved, as confirmed by crosslinking assays. TEM Images show 3-dimensional globular structures for the crosslinked aggregates as well as the existence of a protein corona around the nanoparticles when an excess of protein was employed. Both color change and aggregation can be easily detected with the naked eye.

Nanoparticles covered with only **ZW** did not show any apparent interaction with avidin in solution, excluding the possibility non-specific interactions are responsible for the phenomena shown above.

Mix-monolayer nanoparticles bearing both biotin and naproxen presented a very similar titration profile with avidin, although differences on their monolayer structure or substitution degree may be responsible for a difference in the amount of available ligand or the protein necessary to reach surface saturation.

Nanoparticles seem to be capable to recognise and bind albumin, as shown by the shift of the plasmonic band and the profile of the absorbance when increasing amount of protein added. The saturation value obtained from the curve is in good agreement with results obtained for avidin and are compatible with a complete covering of the nanoparticles surface.

Chapter 5 Gold necklaces and nanowires

5.1 Introduction

Synthetic procedures to prepare gold nanoparticles covered with poorly water-soluble thiols initially resulted in incomplete surface functionalization and aggregation of the sample before surface coverage was complete. In an attempt to prevent this phenomena we considered to substitute the original citrate molecules on the surface of the nanoparticles with a stronger capping agent, hoping it to survive long enough to allow complete functionalization before disruption of the monolayer. Therefore, citrate-capped nanoparticles were treated with 2-glucosamine-6-phosphate (GAP) as a temporary capping agent in order to test their stability. When analysed under TEM, monodimensional chains were observed and after a few weeks in solution, a colour change was observed and it was found to correspond to gold nanorods apparently formed by aggregation of nanoparticles along the chains.

Both processes have been already reported in literature under many different experimental conditions (see below). Anisotropic metal nanoparticle systems have attracted a lot of interest in the recent years due to their properties as optical sensors. They can present additional plasmonic bands, at lower energies than usual (Visible-NIR region) and they are also more sensitive to modification on the surface, being thus capable of acting as very sensitive chemosensors.[62,63]

Nanoparticle aggregation has been studied for decades,[64] but in the last years several approaches to build organised assemblies of nanoparticles have been developed.

In order to get high-order assemblies of nanoparticles, a first approach reported in the literature was the anchoring to thiolated polymers like chitosan (Figure 32).[65–70] However, addition of many other templates or small molecules, during or after the synthesis, also lead to monodimensional aggregates, showing that some general mechanism might be operating in these cases.

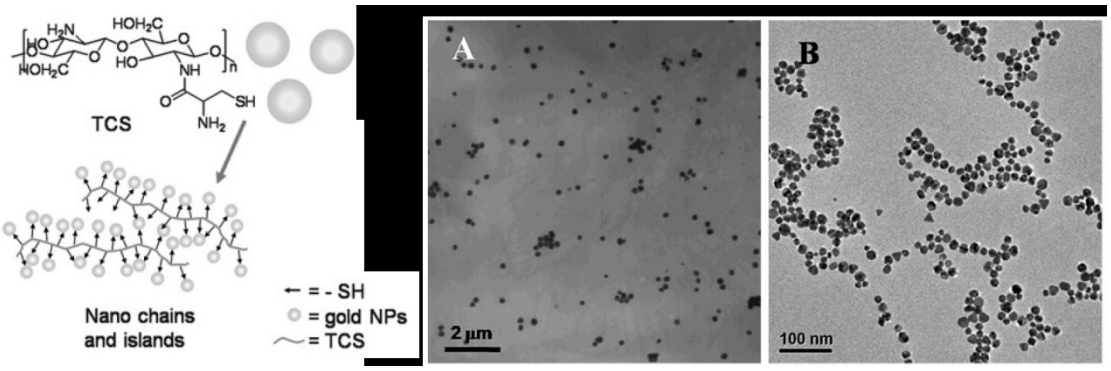

Figure 32 – Representation of the thiolated chitosan polymer (TCS) and a suspension of gold nanoparticles before (A) and after (B) its addition.[71]

All these assemblies showed, regardless the material or mechanism of formation of the nanometric chains, intense plasmonic resonance in the near infrared (NIR) region. As an example, evolution in time of gold nanoparticle synthesised by addeing linear poly(amidoamine) (PAmAm) and their corresponding absorption spectra are shown in Figure 33.

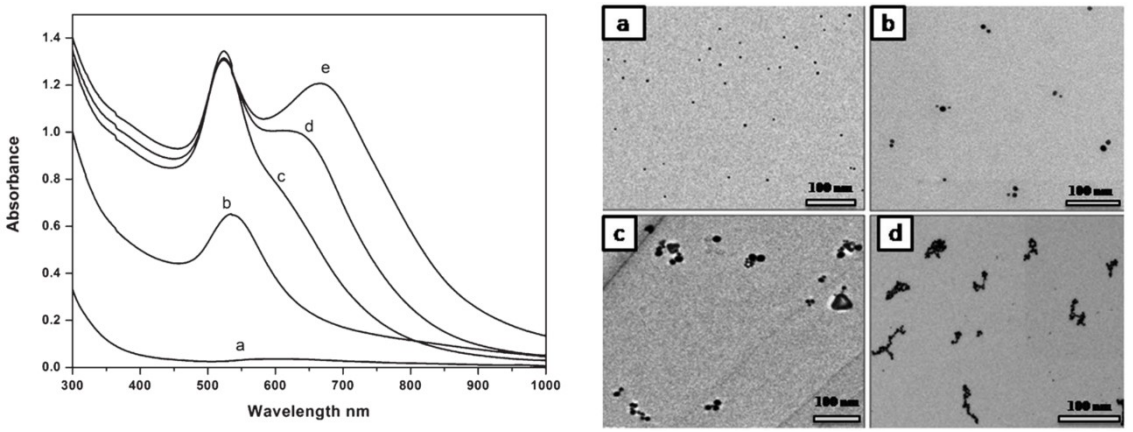

Figure 33 – Absorption spectra and TEM images of gold nanoparticle synthesised by addeing linear poly(amidoamine) (PAmAm) and their corresponding absorption spectra at increasing times (a to d).[65]

A general mechanism based on ligand-induced dipolar assembly has been proposed and studied.[72] It sustains that partial substitution of surface ligand/capping-agent on the surface induces the formation of dipoles along the nanoparticles that then tend to align forming the monodimensional chains.[73]

However, the chemistry of these systems is more complex and the chains observed above can experience additional transformation, leading to elongated wires of nanometric dimensions (Figure 34).[74,75] This has been achieved by growing gold nanoparticles inside a template, but also in its complete absence. In fact, regular synthetic procedures when carried out with a defect of the reducing/capping agent also lead to nanowires.[76–78].

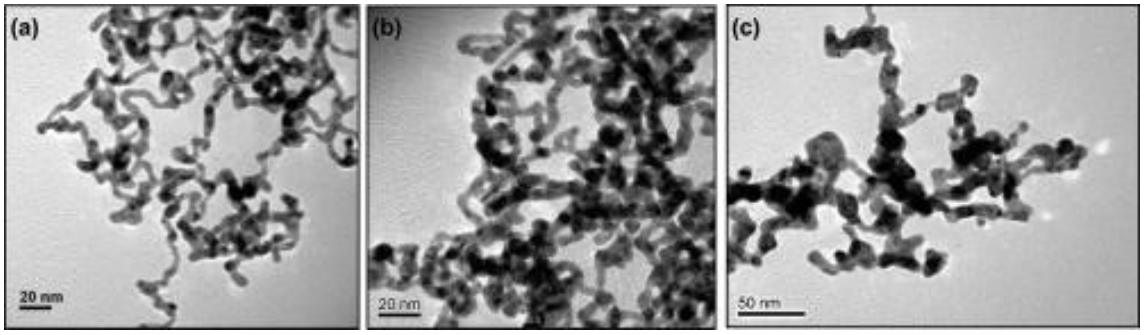

Figure 34 – TEM images of gold nanowires. Image from Pong *et al*.[79]

The formation mechanism of these wires is still poorly understood. Under conditions that favour chemical reactivity (high temperature)[80] or by partially removing the protective ligand shell,[73] spontaneous assembly of CdTe nanoparticles into linear wires have been observed. In those cases when the wires are formed directly by reducing a gold salt, a mechanism where the spherical nanoparticles that are first formed subsequently fuse, have been proposed.[76] A completely opposite alternative has arisen more recently[77,79] in which wires are first formed and then they break apart into nanoparticles In addition, it must be noticed that although gold nanorods can be nowadays prepared with a very precise control of size and aspect ratio, the mandatory use of surfactants during the synthesis and the strong interaction between these molecules and the gold surface makes that, still nowadays, there is no simple way to ensure complete functionalization of the surface of these particles due to the flater surface of the cylindrical shape.[81–84]

5.2 Results

Influence of the incubation medium

Nanoparticles preserved in an excess of citrate were mainly stable, some minor aggregation was observed but no chains or rods were found. In the case of nanoparticles incubated with water, chains were readily observed and aggregation lead to elongated assemblies of nanoparticles but without reaching a final rod-like state. In both cases, aggregation took about two weeks to occur. On the other hand, in the solution with an excess of GAP, after two days of incubation very elongated wires that resembled the structure of the initial chains were observed. An illustrative example of the three situations described above is shown in Figure 35. Notice that the nanowires keep the original shape of the necklaces.

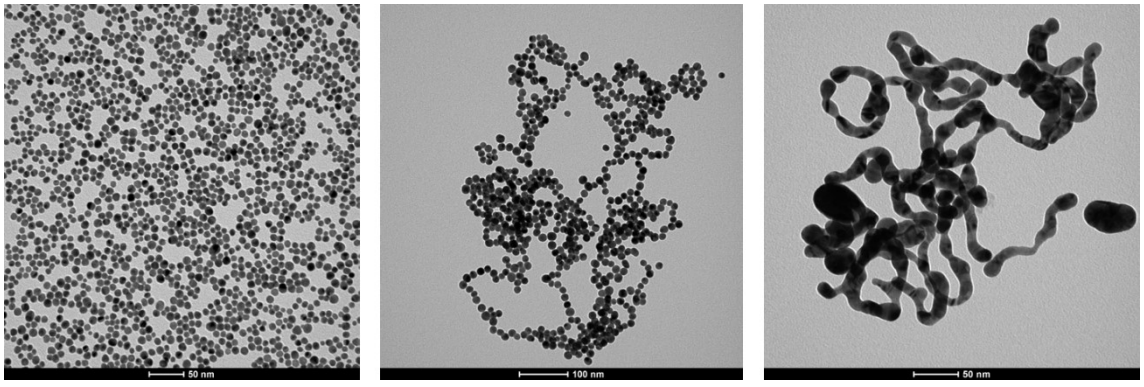

Figure 35 – TEM images of gold nanoparticles incubated with citrate (left), pure water (middle) or glucosamine phosphate (right).

Influence of GAP concentration during incubation

After one day of incubation, chains were observed in all cases, regardless the presence of GAP. The data of Fig 5 indicate that glucosamine appears to control the extent of chain formation and nanoparticle aggregation. In fact, the lower the concentration of glucosamine, more extended assemblies are observed and the lower is the aggregation (Figure 36).

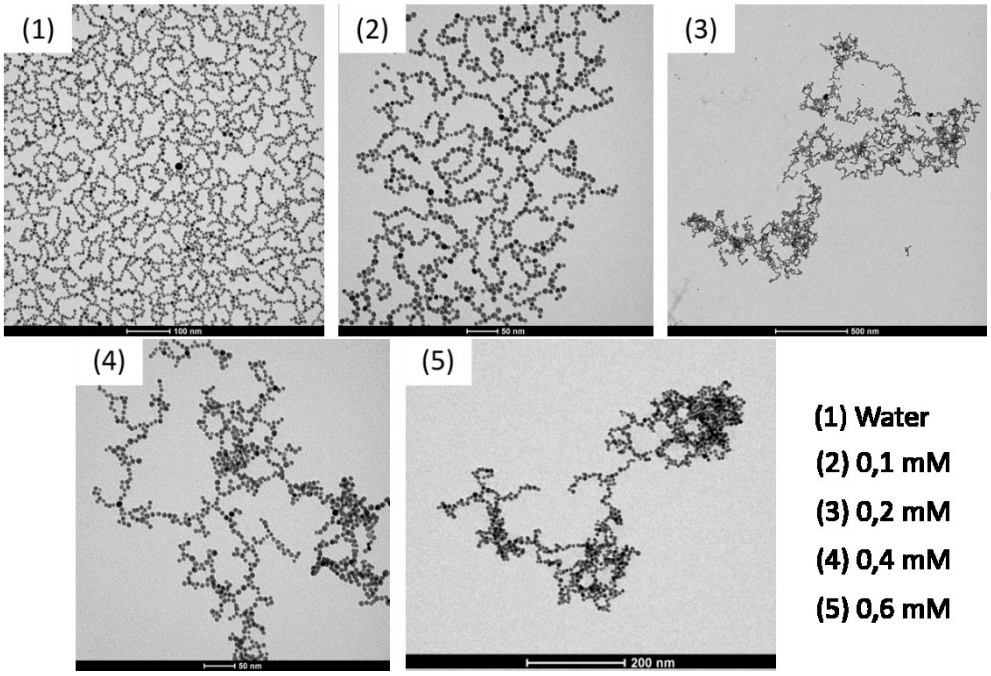

Figure 36 – TEM Image of the chain-like assemblies observed the day after the treatment.

After one week of incubation, incomplete nanoparticle fusion was observed in the cases with less GAP, including pure water, whereas above 0.4 mM precipitation occurred and large aggregates arising from the uncontrolled fusion of particles were observed.

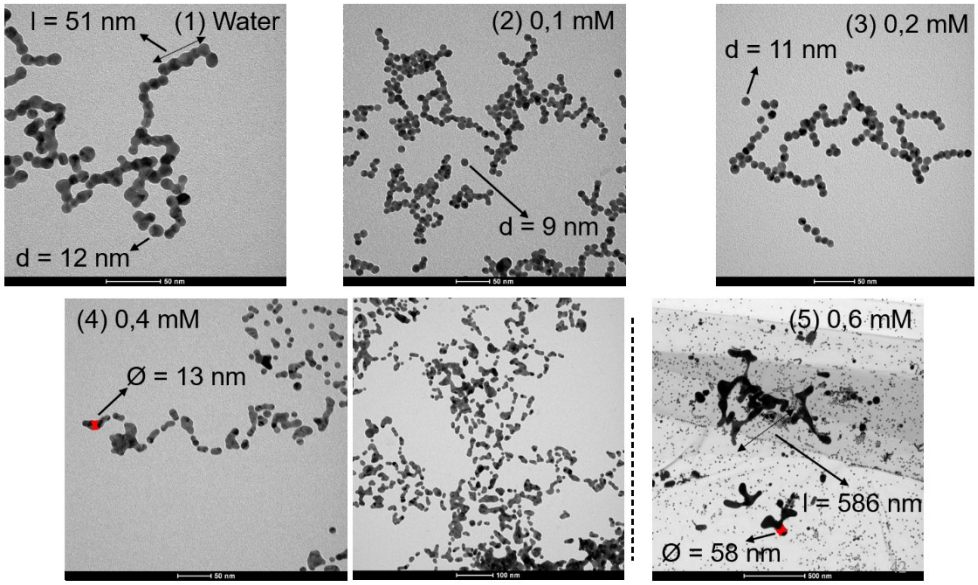

Figure 37 – TEM Images of the aggregates observed after 1 week of incubation.

Effect of exchange time

Sample incubated in citrate remained unmodified even during incubation, with no formation nor fusion of chains and preserved their spectral properties as said above (Figure 38).

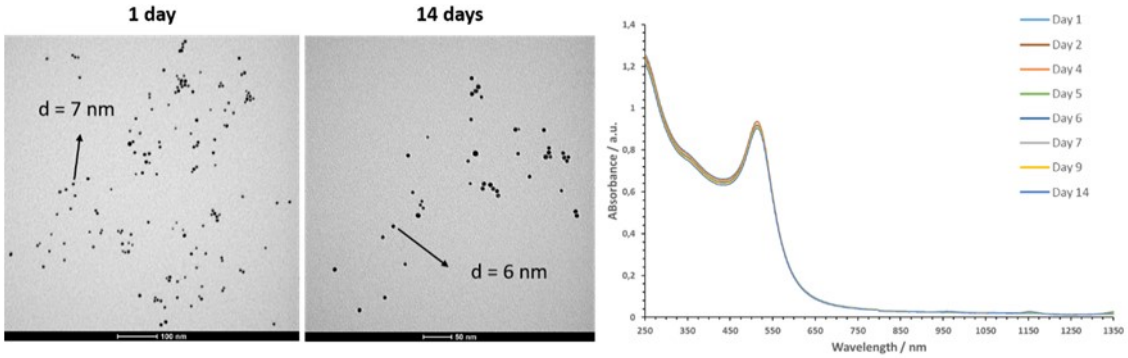

Figure 38 – TEM images of control sample incubated with 5mM citrate after 1 or 14 days of incubation and UV-Vis-NIR absorption spectra at different times.

A second control sample treated in the same way than the rest of the samples without exchanging with GAP showed minor chain formation and isotropic growth of nanoparticles, with a parallel increase of the intensity of the plasmonic band but no shift.

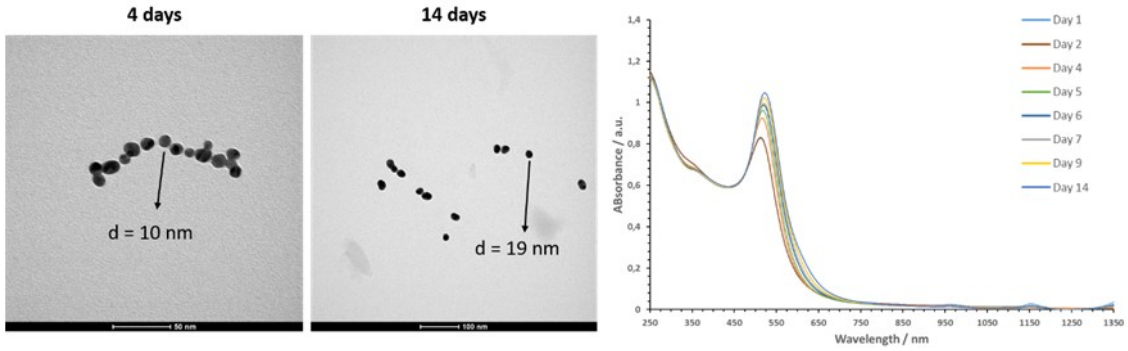

Figure 39 – TEM images of control sample not exchanged with GlcAmP after 4 or 14 days of incubation and UV-Vis-NIR spectra at different times.

On the other hand, samples exchanged with GAP and then incubated in water presented new features in the spectra, with the rise of a second plasmonic band shifting towards the NIR region and subsequent bleaching in the whole spectral window. The rate of the process was inversely proportional to the time of exchange with GAP as show the spectra taken for samples exchanged for 10 minutes, 3 hours and overnight (Figure 40).

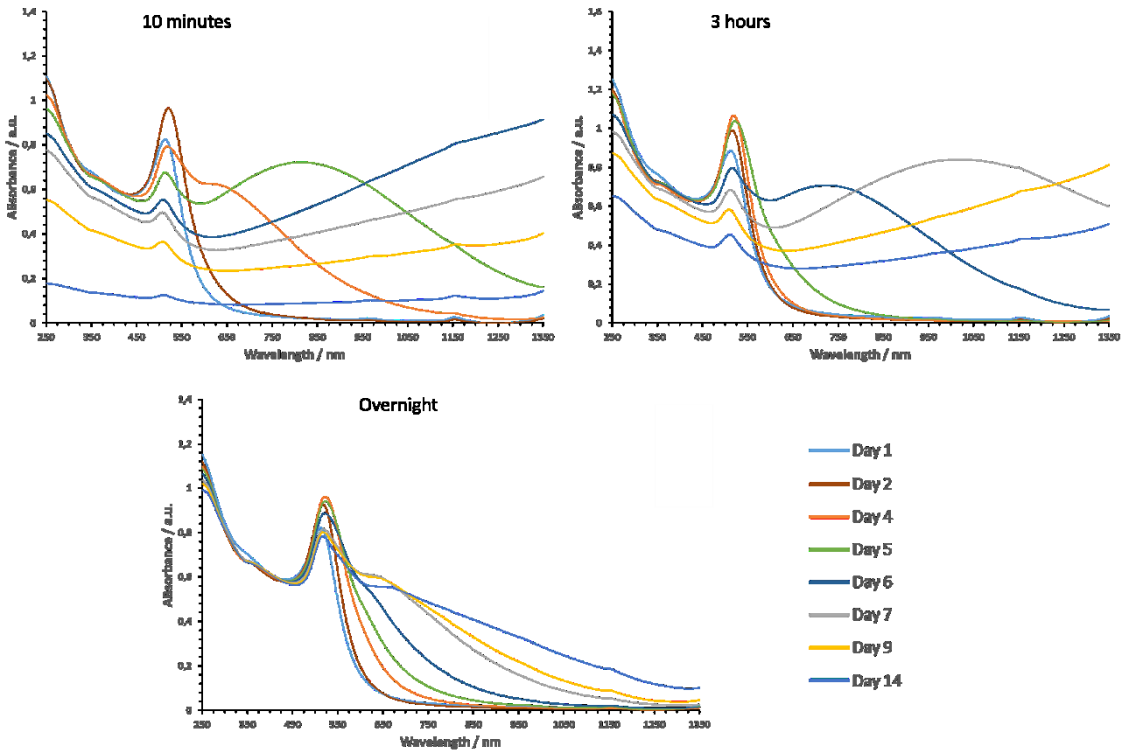

Figure 40 – Absorption spectra in time in the UV-Vis-NIR region of the samples exchanged with GAP for different times. All samples incubated in water.

TEM studies confirmed that this was due to the progressive fusion of the nanoparticle chains to form wires approximately identical in diameter but longer in the case of the shortest exchange times. After overnight exchange, the system seems to be blocked at the nanorod stage and does not evolve further to the nanowire phase.

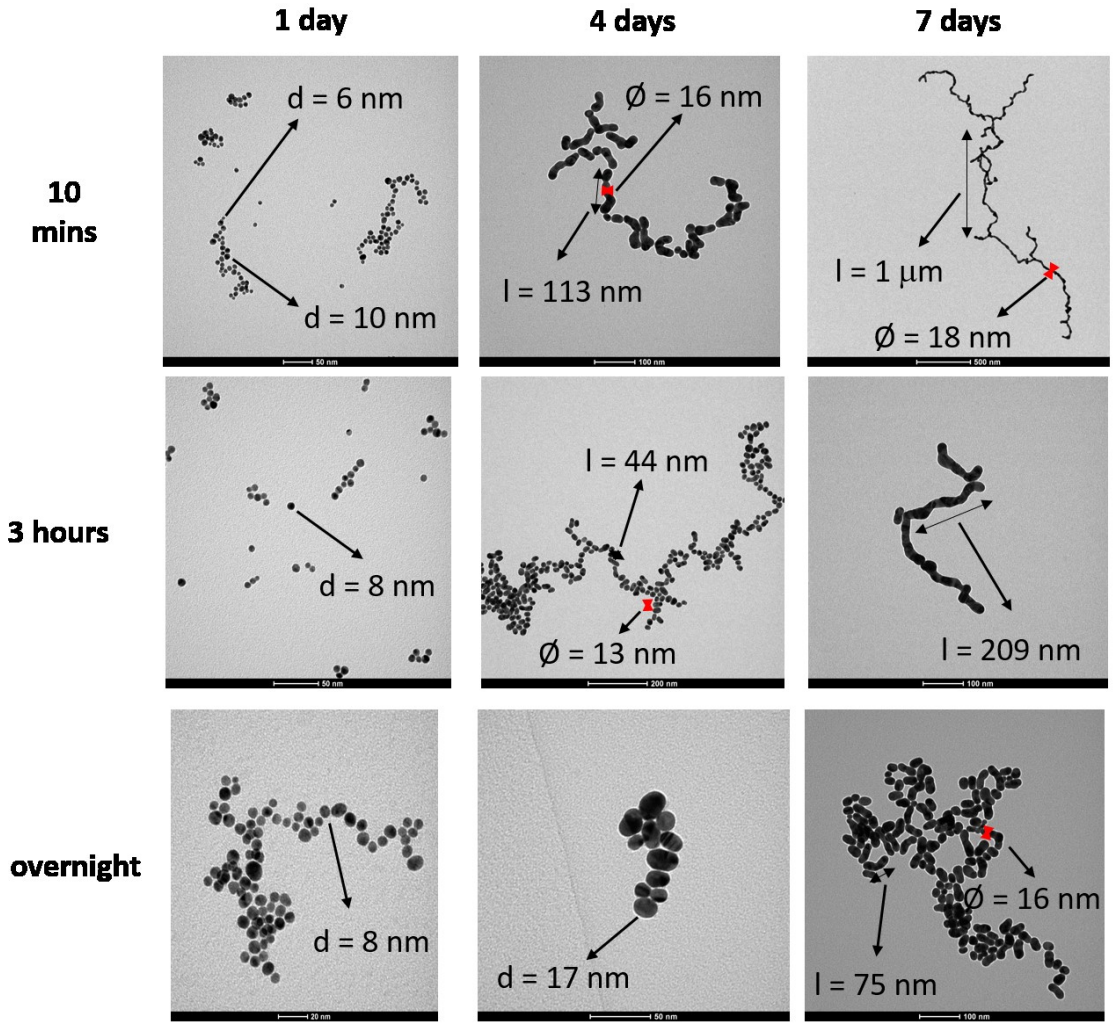

Figure 41 – Gold nanorods/nanochains formation comparison as a function of Exchange time with GAP (rows) and incubation time in water (columns)

Effects on the plasmonic resonance of the nanoparticles and precipitation phenomena can be observed with the naked eye as shown in Figure 41.

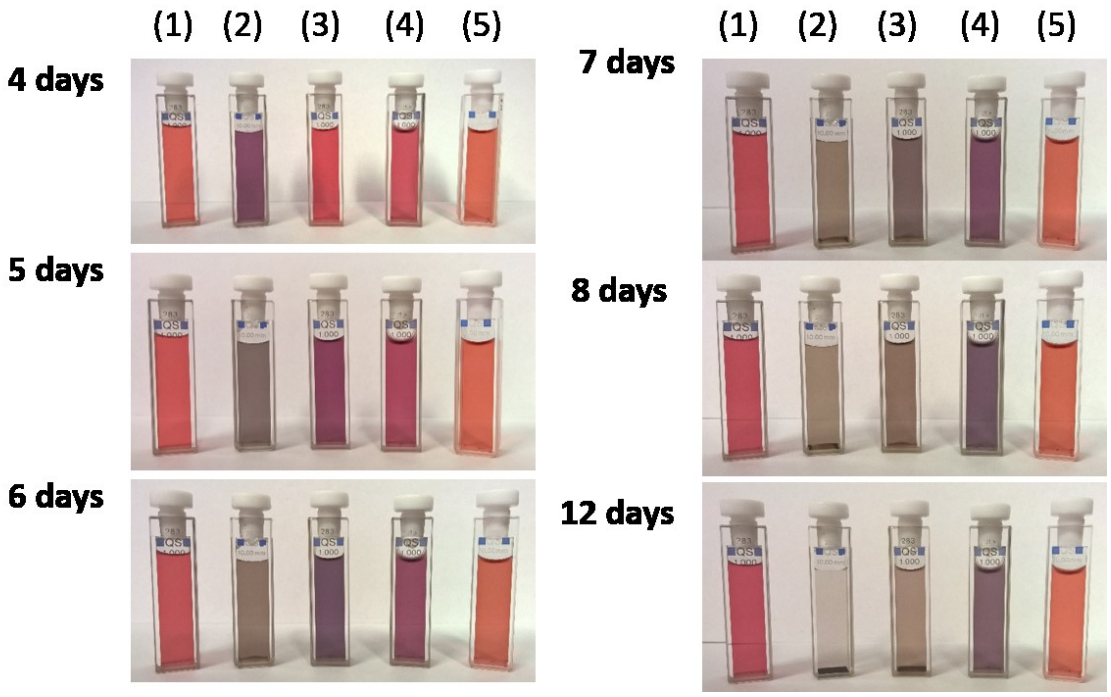

Figure 42 – Picture of the cuvettes where samples were incubated after different exchange times. (1) No exchange, (2) 10 minues, (3) 3 hours, (4) overnight, (5) 3 hours incubated in excess of sodium citrate.

Trapping and functionalizing gold nanorods by thiol addition

As mentioned before, anisotropic nanoparticles are of great interest due to their plasmonic properties. However, no one has been able yet to completely remove from the surface the surfactant employed during their synthesis by direct addition of the capping agent due to the great difficulty to detach it from the gold surface, especially the less curved regions.[81,82]

As part of the previously described experiments, after 5 days of incubation, a water solution of **ZW** was added to an aliquot of the sample and the solution then further incubated for 9 more days.

As it can be observed in Figure 43, the obtained structures are much similar to those obtained from the samples subjected to 4 days of incubation than those left to incubate for 7 days or even longer times (data not shown). It appears that the addition of thiols stops the growth of the systems and longer aggregates and wires are no longer formed (see Figure 41).

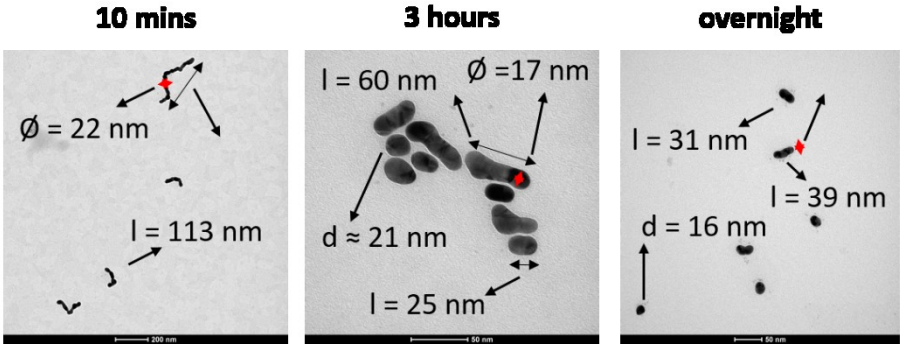

Figure 43 – TEM images of the samples at different exchange times after addition of the ZW thiol on the 5th day of incubation and incubation for another 9 days. To be compared with second and third column on Figure 41.

5.3 Discussion

The chain formation even in samples without exchange with GAP suggests that the necklaces formation mechanism arises from a depletion of capping-agent in the solution.

Influence of the incubation medium

It is important to notice that, contrary to all other experiments reported in this thesis, concentration of nanoparticles was much higher. This large excess of nanoparticles respect to the chemical reactants could have inhibited the rod formation mechanism in the water sample because of the lack of material, since they will all be present in and effective lower amounts of equivalents.

Nanoparticles exchanged with GAP were capable of self-assemble forming chains and the presence of GAP induced nanoparticle fusion. Both these processes were inhibited by addition of excess citrate after GAP treatment. The fact that nanowires retain the original shape of the necklaces strongly suggest that all the process occurs wile the system is in solution.

Influence of GAP concentration during incubation

The presence of GAP during incubation leads to shorter and less branched necklaces probably because this leads to a lower disruption of the passivating monolayer. During the exchange time, citrate molecules on the nanoparticle surface will be substituted by GAP molecules, interacting either through the amino or the phosphate groups, however, each GAP molecule displaces a trivalent citrate molecule, leaving unsaturated gold atoms on the surface that would tend to aggregate with other nanoparticles.

When concentration is increased, GAP also seems to play an active role in the necklaces fusion process, since higher concentration lead to faster and more extended nanoparticle fusion. However, process control is very poor and aggregation occurs faster than rod growth.

Effect of exchange time

Sample incubated in citrate remained unmodified as shown before and absence of GAP induced nanoparticle isotropic growth, probably to diminish surface energy as it happens during etching processes.

Modification of the GAP exchange time allowed very good control of chain fusion kinetics, although the reason behind this different behaviour remains unknown. A potential explanation would be that GAP could be responsible for bridging between different nanoparticles and, upon release of the molecule, then facilitates nanoparticle fusion (Figure 44).

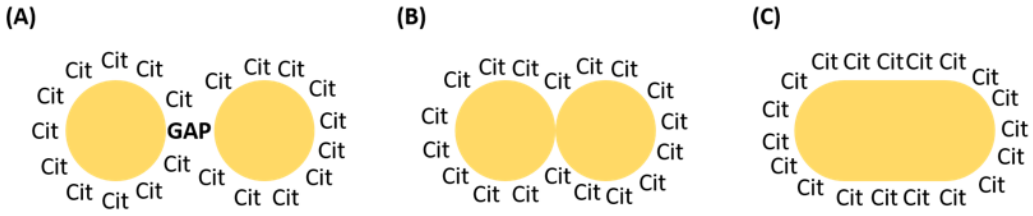

Figure 44 – Possible cascade of events leading to nanoparticle fusion. (A) GAP molecules act as bridges between nanoparticles, (B) Eventual release of GAP get nanoparticles in contact, (C) Rod formation and growth.

A possible explanation for the linear assembly of the chains would be minimisation of electrostatic repulsion. GAP molecules could induce packing by connecting two opposite poles of the nanoparticle, creating zones with a significantly lower charge density that would therefore be much more prone to get close to a similar zone onto a neighbouring nanoparticle, starting the process shown above. However, more experimental evidence is needed in order to establish a reliable mechanism.

Addition of the thiol blocks wire growth even after further incubation without any purification, showing an efficient coverage and protection of the surface that prevent further nanoparticle fusion.

5.4 Conclusions

Citrate-capped nanoparticles exchange with GAP showed the ability to form self-assembled necklaces in solution that upon incubation at room temperature fuse into nanorods and nanowires several μm in length.

These nanorods and wires present a second plasmonic band in the NIR region potentially useful for many applications, particularly in nanomedicine.

GAP seems to play a key role on nanoparticle fusion but the mechanism underneath the process remains unknown.

The ability to block nanorods growth could lead to the development of a process in which nanowires size is tuned upon incubation and both, blocking and thiol functionalization could be achieved in one step with no intermediate molecules or purification processes.

Chapter 6 Materials and methods

6.1 Solvents, Reagents and General Procedures

Chemicals, solvents and deuterated solvents for NMR were obtained from Sigma-Aldrich and used as purchased without further purification unless stated otherwise. Solid phase synthesis resin and amino acids were purchased from Iris Biotech. Hygroscopic reagents were kept inside a desiccator with the exception of tetrachloroauric acid, which was immediately dissolved upon arrival and the solution kept frozen at -20 °C.

TLC were run on 0.2 mm Macherey-Nagel Alugram Xtra SIL G/UV_{254} plates, revealed typically under 365 nm irradiation and phosphomolybdic acid ethanolic solution. Terminal alkynes were revealed employing ethanolic $KMnO_4$ and free amines with ninhydrin. Azides were revealed by *in situ* derivatization by reducing them with PPh_3 under mild heating and revealing the resulting primary amine with ninhydrin. Molecules containing polyethyleneglycol chains were revealed by employing Dragendorff's reagent.

Column chromatography was performed with silica gel employing Macherey-Nagel Keiselgel 60 with particles sizes of 0.04 – 0.063 mm (flash) or 0.063 – 0.2 mm (gravity). Flash columns were performed by applying a positive nitrogen pressure.

Glassware in contact with gold nanoparticles was washed with *aqua regia* before and after its use and rinsed with distilled water. All gold nanoparticle preparation and purification was carried out with milliQ water. Nanoparticles were purified by centrifugation on a Hettich Universal 320 R centrifuge operating with a swinging rotor ($V \leq 15$ ml, rpm ≤ 5000) or a 45° fixed angle rotor ($V \leq 5$ ml, rpm ≤ 12000) or an Eppendorf miniSpin Plus ($V \leq 1.5$ ml, rpm ≤ 14500) depending on the sample.

Molecular sieves (4 Å) were activated by heating at 300 °C for 24 hours under vacuum and stored under nitrogen before use.

6.2 Physical Measurements

UV–Visible spectra were acquired on a Varian Cary 50 or Cary 100 spectrophotometer whereas UV-Vis-NIR spectra were acquired on a Varian Cary 5000 spectrophotometer employing 10 mm path length Hellma Suprasil® quartz cuvettes; disposable PMMA cuvettes were employed for visible measurements only.

ESI mass spectra were recorded on an Agilent Technologies 1100 Series system equipped with a binary pump (G1312A) and MSD SL Trap mass spectrometer (G2445D SL) with ESI source from solutions in methanol or acetonitrile; in positive mode eluents contained 0.1% formic acid. Mass reported correspond to monocationic proton adducts.

NMR spectra were recorded on a Bruker Avance DPX 200, Avance 300 or AVIII 500 spectrometers operating at 200, 300 and 500 MHz for ^{1}H and 50.3, 75.5 and 125.7 MHz for ^{13}C, respectively. ^{1}H and ^{13}C NMR spectra were calibrated using residual solvent signals, whereas for ^{31}P calibration an automatic spectrometer reference was used. Residual solvent signals were assigned according to previously reported values.[85,86]

Thermogravimetric analyses were carried out on ~1 mg of nanoparticles with a TA Instruments Q5000 IR instrument. Solvent was removed by heating the sample at 100 °C for 10 minutes and then a 10 °C/min temperature ramp was applied from 100 to 1000 °C.

Transmission electron microscopy analysis were run on a FEI Tecnai G12 microscope operating at 100 kV and images registered with an OSIS Veleta 4K camera. Samples were typically deposited on a copper grid and the excess of solvent removed with filtering paper. Stained samples were treated by putting in contact the sample-containing grid with a drop of uranyl acetate solution for 5 minutes in the absence of light. Size distribution analysis was carried out by modelling nanoparticle intensity profiles employing PEBBLES and size distribution calculated by performing direct statistics on the previous modelled nanoparticles with PEBBLEJUGGLER.[87]

6.3 Gold Nanoparticle preparation

A modified version of a literature procedure was followed.[27] Typically, to 5.6 ml of water, sequentially and under vigorous stirring, 1.6 ml of sodium citrate (510 mM), 250 µl of silver nitrate (10 mM) and 500 µl of tetrachloroauric acid (250 mM) were added and stirred for 5 minutes. During this time, the solution changed from initial yellow color to green, grey and finally black. After the incubation time, the solution was quickly added to 117 ml of boiling water and heated under reflux for 1 hour, becoming wine-red after a few seconds. The citrate-capped nanoparticles solution obtained was then allowed to cool down to room temperature, the desired free thiol was added in 1-2 ml of isopropanol and left stirring overnight.

Nanoparticles were purified by using 15 ml Amicon® Ultra filters of 100 KDa molecular weight cutoff centrifuged for 2.5 minutes at 2000 rpm or 10 KDa at 5000 rpm for 6 minutes. Prior to use, filters were prewashed 5 times with 1:1 H_2O:MeOH, then nanoparticles washed 5 times with 1:1 H_2O:MeOH and 5 times with pure water. Typical concentrated volumes after centrifugation for 15, 4 and 0.5 ml filtering units were 1.5, 0.5 and 0.1 ml respectively. Purified nanoparticles aqueous solution were frozen with dry ice and freeze-dried overnight on a Cinquepascal 105PDGT lyophilizer equipped with and Edwards XDS 10 Pump ($P \approx 0.2$ mbar, $T = -50$ °C). Typically, an amount between 22 and 26 mg of functionalized nanoparticles was obtained, corresponding to *ca*. 75% yield.

In the case of 2 nm nanoparticle preparation, a previously reported procedure was followed.[88]

Nanoparticles were analyzed by NMR *in situ* by detaching the thiols from its surface by treating 500 µl of nanoparticles solution with 100 µl of a saturated solution of iodine in deuterated solvent.

6.4 Nanoparticles characterization

Nanoparticles core were characterized by TEM analysis. In a typical batch, a minimum of 500 nanoparticle sample was used to calculate the average size and the associated standard deviation.

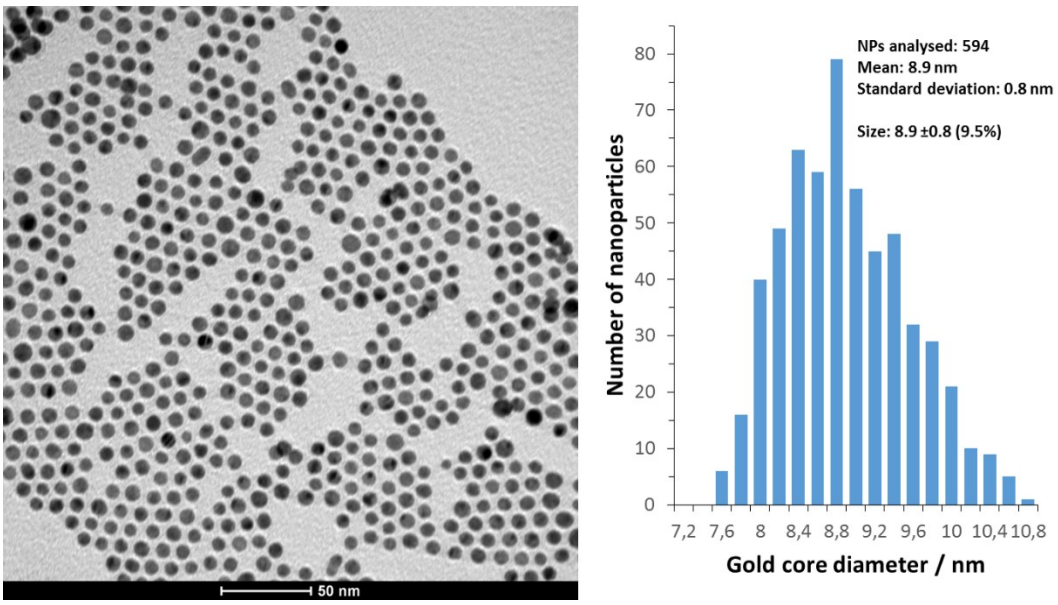

Figure 45 – TEM image and analysis of a purified batch of nanoparticles covered with a self-assembled monolayer of thiol 1.

The organic monolayer was studied by thermogravimetric analysis; a typical combustion curve of nanoparticles as the ones shown in Figure 45 is displayed in Figure 46.

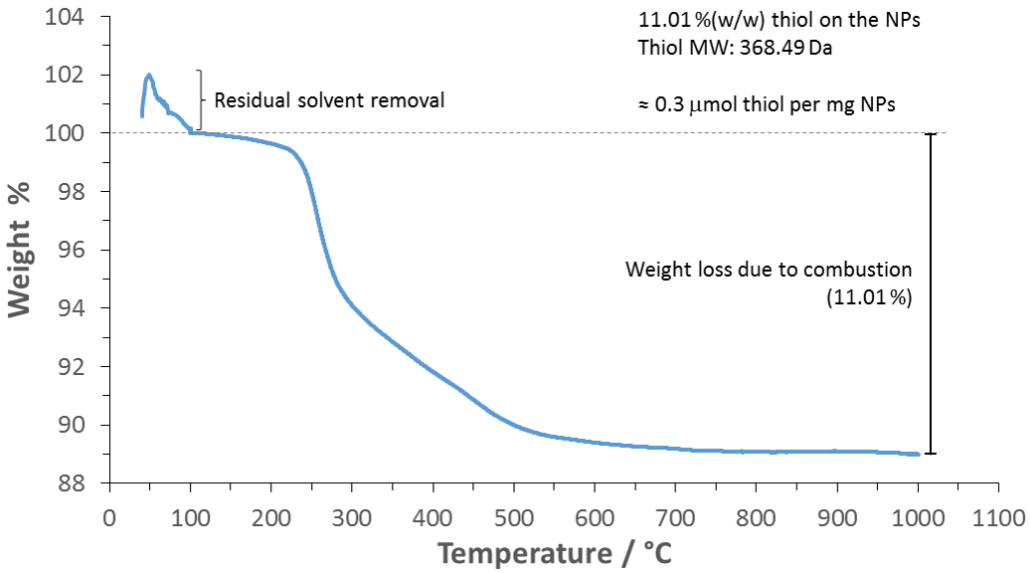

Figure 46 – Typical TGA profile of nanoparticles covered with thiol 1.

Depending on the size of the gold core, amounts of thiols on the monolayer varied in the range from 0.2 to 0.3 µmols of thiol per mg of nanoparticle.

For the estimation of the number of proteins around the nanoparticle not only the amount but the actual number of thiols around the surface of the nanoparticle in required, and therefore the formula and molecular weight of the nanoparticle need to be known. In order to retrieve those values, two parameters where employed: the gold atomic density inside gold nanoparticles (59 atoms per nm^3) and the thiol fingerprint on the nanoparticle surface. The first value has been reported in the literature[89] (as cited by[90]), whereas the second one depends significantly on the thiol chemical structure and it has to be obtained for each thiol. Based on the gold atomic density and TGA curves, we estimated it to be 0.2 nm^2 per ZW thiol, which agrees with those reported in literature for thiols of similar length.[46] With those two values, both nanoparticle approximate formula and molecular weight can be calculated from the diameter of the gold core, experimentally obtained by TEM analysis.

6.5 Chemical Synthesis

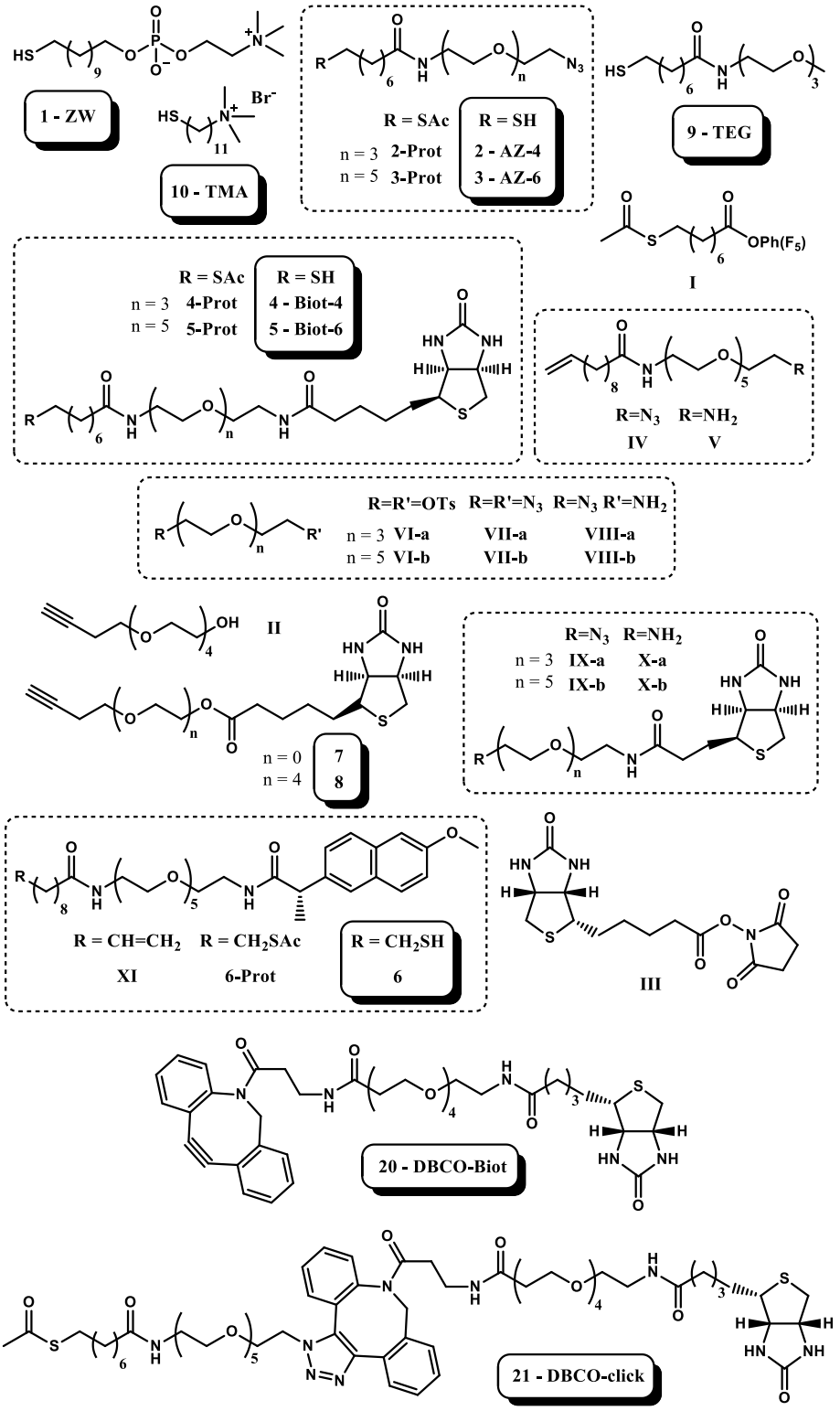

Figure 47 – List of all compounds prepared and reported in this thesis.

Final or relevant compounds are labelled with Arabic numbers and their abbreviation is shown, whereas intermediates are labelled with Roman numbers.

Compounds **1**,[28] **9**[91] and **10**[92] and intermediates **I**,[93] **III**,[94] **VI**,[95] **VII-VIII**,[96] **IX-a**,[97] **IX-b**[98] and **X-a**[99] were synthesized according to previously reported methods. PEGylated derivatives **VI-VIII** where characterized by comparing MS and ^{1}H-NMR spectra with previously reported ones.[100] Remaining compounds and intermediates are new and its synthesis and characterization is described below.

NMR labeling notation of biotin and naproxen derivatives is shown on Figure 48.

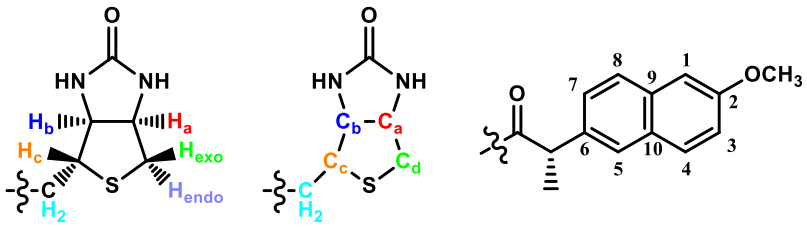

Figure 48 – Notation employed when reporting biotin and naproxen NMR signals.

Intermediates **IX** and **X-a** have been previously reported in the literature, however, since new analogous derivatives have been prepared, they are described in detail for comparison purposes. In terminal alkene ^{1}H-NMR notation, subindexes *cis* and *trans* are referred to the single hydrogen to which the terminal protons are coupled and not to the substituent.

Thioacetate deprotection was typically carried out by refluxing a solution of the protected form in a 1:1 mixture of 6 M aq. HCl and EtOH for 2-3 hours. The solvent was removed under vacuum and the product obtained in quantitative yield.

***S*-(1-azido-13-oxo-3,6,9-trioxa-12-azaicosan-20-yl) ethanethioate (2-Prot)**

I (0.5 g, 1.3 mmol, 1.0 eq) and **VIII-a** (296 mg, 1.36 mmol, 1.05 eq) were dissolved in DMF (5 ml), DIPEA (270 µl, 1.56 mmol, 1.2 eq) was added and the solution heated at 70 ºC for 3 days. Solvent was removed under vacuum and the product purified by column chromatography in AcOEt:EtOH 50:1 to yield the desired product as a colorless oil. Yield: 788 mg (39 %).

^{1}H NMR (300 MHz, Chloroform–*d*): δ_H (ppm): 6.17 (bs, 1H, NH), 3.70-3.57 (m, 10H, PEG-OCH_2), 3.57-3.50 (m, 2H, CH_2CH_2NH), 3.39-3.33 (m, 4H, $CH_2CH_2N_3$+CH_2NH), 2.83 (t, $^{3}J_{HH}$ = 7.3 Hz, 2H, CH_2S), 2.29 (s, 3H, CH_3), 2.15 (t, $^{3}J_{HH}$ = 7.4 Hz, 2H, $CH_2C(O)$), 1.68-1.46 (m, 4H, CH_2CH_2S+CH_2N_3), 1.30 (bs, 6H, $CH_2CH_2C(O)$+CH_2CH_2).

^{13}C{^{1}H} NMR (75.5 MHz, Chloroform–*d*): δ_C (ppm): 196.1 ($CO_{thioacetate}$) 176.3 (CO_{amide}), 70.8-70.0 (OCH_2+CH_2CH_2NH+$CH_2CH_2N_3$), 50.8 (CH_2N_3), 39.2 (CH_2NH), 36.7 ($CH_2C(O)$), 30.7 (CH_2CH_2S) 29.5-28.7 (CH_2CH_2), 25.7 ($CH_2CH_2C(O)$).

HR–MS: For $C_{18}H_{35}N_4O_5S$, observed mass 419.2335, calculated 419.2328, difference 0.6 mDa.

***N*-(2-(2-(2-(2-azidoethoxy)ethoxy)ethoxy)ethyl)-8-mercaptooctanamide (2 – AZ4)**

Thiol **2 (AZ4)** was obtained in its deprotected form from **2-Prot** by following the procedure described previously on page 69. Yield: quantitative.

***S*-(1-azido-19-oxo-3,6,9,12,15-pentaoxa-18-azahexacosan-26-yl) ethanethioate (3-Prot)**

The same procure described above for **2-Prot** replacing **VIII-a** for **VIII-b** (416 mg, 1.36 mmol, 1.05 eq) was employed. Yield: 443 mg (67 %).

^{1}H NMR (300 MHz, Chloroform–*d*): δ_H (ppm): 6.21 (bs, 1H, NH), 3.70-3.54 (m, 18H, PEG-OCH_2), 3.54-3.46 (m, 2H, CH_2CH_2NH), 3.44-3.30 (m, 4H, $CH_2CH_2N_3$+CH_2NH), 2.80 (t, $^{3}J_{HH}$ = 7.3 Hz, 2H, CH_2S), 2.27 (s, 3H, CH_3), 2.13 (t, $^{3}J_{HH}$ = 7.6 Hz, 2H, $CH_2C(O)$), 1.66-1.44 (m, 4H, CH_2CH_2S+CH_2N_3), 1.36-1.19 (m, 6H, $CH_2CH_2C(O)$+CH_2CH_2).

^{13}C{^{1}H} NMR (75.5 MHz, Chloroform–*d*): δ_C (ppm): 196.0 ($CO_{thioacetate}$) 173.2 (CO_{amide}), 70.7-70.0 (OCH_2+CH_2CH_2NH+$CH_2CH_2N_3$), 50.7 (CH_2N_3), 39.2 (CH_2NH), 36.6 ($CH_2C(O)$), 30.7 (CH_2CH_2S) 29.5-28.7 (CH_2CH_2), 25.6 ($CH_2CH_2C(O)$).

HR–MS: For $C_{22}H_{43}N_4O_7S$, observed mass 507.2854, calculated 507.2852, difference 0.2 mDa.

***N*-(17-azido-3,6,9,12,15-pentaoxaheptadecyl)-8-mercaptooctanamide (3 – AZ6)**

Compound **3 (AZ6)** was prepared from **3-Prot** by following the standard procedure described on page 69. Yield: quantitative.

but-3-yn-1-yl 5-((3a*S*,4*R*,6a*R*)-2-oxohexahydro-1*H*-thieno[3,4-*d*]imidazol-4-yl)pentanoate (7)

To a solution of D-biotin (134 mg, 0.55 mmol, 1 eq), EDC (157 mg, 1.1 mmol, 2 eq) and DMAP (6.7 mg, 0.055 mmol, 0.1 eq) in anydrous DMF (10 ml) cooled down to 0 °C, a 3-butyn-1-ol solution (192 mg, 2.75 mmol, 5 eq) in anydrous DMF (1 ml) was dropwise added. The solution was allowed to warm up at room temperature and was stirred overnight under N_2 atmosphere. The solvent was removed under vacuum, dissolved in CH_2Cl_2 and washed with 1M aq. NaOH once and water four times. The organic solvent was evaporated and the product purified by column chromatography in AcOEt:MeOH 5:1. Yield: 53 mg (32%).

^{1}H NMR (500 MHz, Methanol-d_4): δ_H (ppm): 4.49 (ddd, 1H, $^{3}J_{HH}$ = 7.9, 5.0, 1.0 Hz, Biotin-H_a), 4.31 (dd, 1H, $^{3}J_{HH}$ = 4.5 Hz, Biotin-H_b), 4.16 (t, 2H, $^{3}J_{HH}$ = 6.7 Hz, CH_2O), 3.21 (ddd, 1H, $^{3}J_{HH}$ = 9.0, 5.8 Hz, Biotin-H_c), 2.93 (dd, 1H, $^{1}J_{HH}$ = 12.7 Hz, $^{3}J_{HH}$ = 5.0 Hz, Biotin-H_{endo}), 2.71 (d, 1H, Biotin-H_{exo}), 2.52 (td, 2H, $^{3}J_{HH}$ = 6.7 Hz, $^{4}J_{HH}$ = 2.7 Hz, C*H*$_2$C≡CH), 2.37 (t, 2H, $^{3}J_{HH}$ = 7.4 Hz, *C*H$_2$C(O)), 2.31 (t, 1H, C≡CH), 1.79-1.55 (m, 4H, C*H*$_2$CH$_2$), 1.46 (p, 2H, $^{3}J_{HH}$ = 7.4 Hz, CH$_2$C*H*$_2$CH$_2$).

^{13}C{^{1}H} NMR (125.7 MHz, Methanol-d_4): δ_C (ppm): 175.0 (CO_{ester}), 166.1 (CO_{biotin}), 81.0 (*C*≡CH), 71.0 (C≡*C*H), 63.4 (CH_2O), 63.4 (Biotin-C_b), 61.6 (Biotin-C_a), 57.0 (Biotin-C_c), 41.0 (Biotin-C_d), 34.7 ($CH_2C(O)$), 29.6, 29.4 (*C*H$_2$CH$_2$), 25.9 (Biotin-*C*H$_2$CH$_b$), 19.6 (*C*H$_2$C≡CH).

3,6,9,12-tetraoxahexadec-15-yn-1-ol (II)

To a solution of triflic anhydride (10 ml from 1M CH_2Cl_2 solution, 10 mmol, 1.05 eq) under N_2 atmosphere and cooled at 0 ºC, a mixture of 3-butyn-1-ol (720 µl, 9.52 mmol, 1 eq.) and pyridine (800 µl, 10 mmol, 1.05 eq) in anhydrous CH_2Cl_2 (10 ml) was slowly added for 30 minutes. Then a solution of tetraethyleneglycol (4.9 ml, 28.56 mmol, 3 eq) in anhydrous CH_2Cl_2 was quickly added and the solution stirred for 30 minutes. The reaction was washed twice with sat. aq. $NaHCO_3$ and the residue purified by column chromatography in AcOEt:EtOH 9:1. Yield: 376 mg (16 %).

^{1}H NMR (500 MHz, Methanol-d_4): δ_H (ppm): 3.71-3.54 (m, 18H, PEG-OCH_2), 2.46 (td, 2H, $^{3}J_{HH}$ = 6.9 Hz, $^{4}J_{HH}$ = 2.7 Hz, C*H*$_2$C≡CH), 2.28 (t, 1H, C≡CH).

HR–MS: For $C_{12}H_{23}O_5$ observed mass 247.1550, calculated 247.1545, difference 0.5 mDa.

3,6,9,12-tetraoxahexadec-15-yn-1-yl 5-((3a*S*,4*R*,6a*R*)-2-oxohexahydro-1*H*-thieno[3,4-*d*]imidazol-4-yl)pentanoate (8)

To a solution of D-biotin (623 mg, 2.55 mmol, 2 eq), EDC (500 mg, 2.55 mmol, 2 eq) and DMAP (24 mg, 0.2 mmol, 0.15 eq) in anhydrous DMF (35 ml) at 0 ºC, a solution of **II** (320 mg, 1.3 mmol, 1 eq) in anhydrous DMF (5 ml) was added, the reaction was allowed to warm to room temperature and stirred overnight under N_2 atmosphere. The solvent was removed under vacuum and the product purified by column chromatography in AcOEt:EtOH 20:1 → 5:1. Yield: 464 mg (75 %).

^{1}H NMR (500 MHz, Methanol-d_4): δ_H (ppm): 4.49 (ddd, 1H, $^3J_{HH}$ = 7.9, 5.0, 1.0 Hz, Biotin-H_a), 4.31 (dd, 1H, $^3J_{HH}$ = 4.5 Hz, Biotin-H_b), 4.24-4.19 (m, 2H, CH_2O_{ester}), 3.73-3.68 (m, 2H, $CH_2CH_2O_{ester}$), 3.61 (2×bs, 12H, PEG-OCH_2), 3.59 (t, 2H, $^3J_{HH}$ = 6.9 Hz, $CH_2CH_2C{\equiv}CH$), 3.21 (dd, 1H, $^3J_{HH}$ = 9.0, 5.8 Hz, Biotin-H_c), 2.93 (dd, 1H, $^1J_{HH}$ = 12.7 Hz, $^3J_{HH}$ = 5.0 Hz, Biotin-H_{endo}), 2.71 (d, 1H, Biotin-H_{exo}), 2.44 (td, 2H, $^3J_{HH}$ = 6.9 Hz, $^4J_{HH}$ = 2.7 Hz, $CH_2C{\equiv}CH$), 2.38 (t, 2H, $^3J_{HH}$ = 7.3 Hz, $CH_2C(O)$), 2.23 (t, 1H, C≡CH), 1.80-1.54 (m, 4H, CH_2CH_2), 1.46 (p, 2H, $CH_2CH_2CH_2$).

^{13}C{^{1}H} NMR (125.7 MHz, Methanol-d_4): δ_C (ppm): 175.3 (CO_{ester}), 166.1 (CO_{biotin}), 82.0 ($C{\equiv}CH$), 71.6-70.5 (OCH_2), 70.1 ($C{\equiv}CH$), 64.6 (CH_2O_{ester}), 63.4 (Biotin-C_b), 61.6 (Biotin-C_a), 57.0 (Biotin-C_c), 41.0 (Biotin-C_d), 29.7, 29.5 (CH_2CH_2), 25.9 (Biotin-CH_2CH_b), 20.5 ($CH_2C{\equiv}CH$).

HR–MS: For $C_{22}H_{37}N_2O_7S$, observed mass 473.2355, calculated 473.2321, difference 3.4 mDa.

_N_-(2-(2-(2-(2-azidoethoxy)ethoxy)ethoxy)ethyl)-5-((3a_S_,4_S_,6a_R_)-2-oxohexahydro-1_H_-thieno[3,4-_d_]imidazol-4-yl)pentanamide (IX-a)

To a solution of D-biotin (195 mg, 0.8 mmol, 1 eq), EDC (306 mg, 1.6 mmol, 2 eq) and DMAP (10 mg, 0.08 mmol, 0.1 eq) in anhydrous DMF (5 ml) at 0 ºC, a solution of **VIII-a** (175 mg, 0.8 mmol, 1 eq) in anhydrous DMF (5 ml) was added dropwise. The reaction was allowed to warm to room temperature and stirred overnight under N_2 atmosphere. The solvent was removed under vacuum and the product purified by column chromatography in CH_2Cl_2:MeOH 8:1. Yield: 224 mg (63 %).

^{1}H NMR (500 MHz, Methanol-d_4): δ_H (ppm): 4.49 (ddd, 1H, $^3J_{HH}$ = 7.9, 5.0, 0.9 Hz, Biotin-H_a), 4.31 (dd, 1H, $^3J_{HH}$ = 4.5 Hz, Biotin-H_b), 3.69-3.59 (m, 10H, PEG-OCH_2), 3.55 (t, 2H, $^3J_{HH}$ = 5.5 Hz, OCH_2CH_2NH), 3.40-3.35 (m, 4H, $CH_2CH_2N_3$+CH_2NH), 3.24-3.18 (m, 1H, Biotin-H_c), 2.95-2.90 (m, 1H, Biotin-H_{endo}), 2.71 (d, 1H, , $^1J_{HH}$ = 12.6 Hz, Biotin-H_{exo}), 2.22 (t, 2H, $^3J_{HH}$ = 7.3 Hz, CH_2C(O)), 1.80-1.55 (m, 4H, CH_2N_3+CH_2CH_2), 1.50-1.40 (m, 2H, CH_2CH_2).

ESI–MS: For $C_{18}H_{33}N_6O_5S$, observed mass 445.40, calculated 445.22.

_N_-(2-(2-(2-(2-aminoethoxy)ethoxy)ethoxy)ethyl)-5-((3a_S_,4_S_,6a_R_)-2-oxohexahydro-1_H_-thieno[3,4-_d_]imidazol-4-yl)pentanamide (X-a)

To a flask containing **IX-a** (168 mg, 0.38 mmol, 1 eq) a THF (4 ml) solution of triphenylphosphine (109 mg, 0.42 mmol, 1.1 eq) and then water (2 ml) were added and the solution vigorously stirred overnight. The organic solvent was removed under vacuum and the aqueous phase washed twice with CH_2Cl_2 and one with Et_2O. The desired product was obtained as a white solid upon freeze-drying. Yield: 132 mg (83 %).

^{1}H NMR (500 MHz, Methanol-d_4): δ_H (ppm): 4.49 (ddd, 1H, $^3J_{HH}$ = 7.9, 5.0, 0.9 Hz, Biotin-H_a), 4.30 (dd, 1H, $^3J_{HH}$ = 4.5 Hz, Biotin-H_b), 3.68-3.60 (m, 8H, PEG-OCH_2), 3.57-3.52 (m, 4H, 2×C$H_2$$CH_2NH$), 3.36 (t, 2H, $^3J_{HH}$ = 5.5 Hz, CH_2NH), 3.21 (ddd, 1H, $^3J_{HH}$ = 9.0, 5.8 Hz, Biotin-H_c), 2.95-2.90 (m, 1H, Biotin-H_{endo}), 2.85 (t, 2H, $^3J_{HH}$ = 7.4 Hz, C$H_2$$CH_2NH_2$), 2.71 (d, 1H, , $^1J_{HH}$ = 12.7 Hz, Biotin-H_{exo}), 2.22 (t, 2H, $^3J_{HH}$ = 7.4 Hz, *C*H_2C(O)), 1.80-1.54 (m, 4H, C$H_2$$CH_2$), 1.50-1.40 (m, 2H, CH_2CH_2).

ESI–MS: For $C_{18}H_{35}N_4O_5S$, observed mass 419.37, calculated 419.23.

***S*-(5,19-dioxo-1-((3a*S*,4*S*,6a*R*)-2-oxohexahydro-1*H*-thieno[3,4-*d*]imidazol-4-yl)-9,12,15-trioxa-6,18-diazahexacosan-26-yl) ethanethioate (4-Prot)**

A solution of **X-a** (150 mg, 0.36 mmol, 1 eq) was stirred in the presence of activated molecular sieves in anhydrous DMF (8 ml) for 30 minutes, then a solution of **I** (206 mg, 0.54 mmol, 1.5 eq) in anhydrous DMF (3 ml) was added, followed by DIPEA (75 µl, 0.43 mmol, 1.2 eq) and the reaction was heated at 70 ºC for 2 days. The mixture was filtered, the solvent removed under vacuum and the product purified by column chromatography in CH_2Cl_2:MeOH 10:1 → 6:1. Yield: 112 mg (51 %).

^{1}H NMR (500 MHz, Methanol-d_4): δ_H (ppm): 4.49 (ddd, 1H, $^3J_{HH}$ = 7.9, 5.0, 0.9 Hz, Biotin-H_a), 4.31 (dd, 1H, $^3J_{HH}$ = 4.4 Hz, Biotin-H_b), 3.67-3.60 (m, 8H, PEG-OCH_2), 3.54 (m, 4H, 2×OC$H_2$$CH_2NH$), 3.36 (m, 4H, C$H_2$NH), 3.21 (ddd, 1H, $^3J_{HH}$ = 8.9, 5.8 Hz, Biotin-H_c), 2.93 (dd, 1H, $^1J_{HH}$ = 12.7 Hz, Biotin-H_{endo}), 2.86 (t, 2H, $^3J_{HH}$ = 7.3 Hz, CH_2S), 2.71 (d, 1H, Biotin-H_{exo}), 2.30 (s, 3H, CH_3), 2.25-2.17 (m, 4H, CH_2C(O)), 1.79-1.52 (m, 8H, C$H_2$$CH_2$), 1.49-1.41 (m, 2H, CH_2CH_2), 1.40-1.30 (m, 6H, CH_2).

^{13}C{^{1}H} NMR (125.7 MHz, Methanol-d_4): δ_C (ppm): 197.6 ($CO_{thioacetate}$), 176.3, 176.1 (2×CO_{amide}), 166.1 (CO_{biotin}), 71.6 (OCH_2), 71.2, 70.6 (2×*C*$H_2$$CH_2NH$), 63.4 (Biotin-$C_b$), 61.6 (Biotin-$C_a$), 57.0 (Biotin-$C_c$), 41.0 (Biotin-$C_d$), 40.3 (2×$CH_2NH$), 37.0, 36.8 (2×*C*$H_2$C(O)), 30.7 (*C*$H_2$$CH_2S$), 30.5 ($CH_3$), 30.0-29.6 (*C*$H_2$$CH_2$), 29.5 ($CH_2S$), 26.9, 26.8 (2×*C*$H_2$$CH_2$C(O)).

HR–MS: For $C_{28}H_{51}N_4O_7S_2$, observed mass 619.3217, calculated 619.3199, difference 1.8 mDa.

8-mercapto-*N*-(13-oxo-17-((3a*S*,4*S*,6a*R*)-2-oxohexahydro-1*H*-thieno[3,4-*d*]imidazol-4-yl)-3,6,9-trioxa-12-azaheptadecyl)octanamide (4 – Biot-4)

The protecting thioacetate group of **4-Prot** was removed by following the general procedure described on page 69, obtaining **4** (**Biot-4**) in quantitative yield.

^{1}H NMR (500 MHz, Methanol-d_4): δ_H (ppm): 4.63 (dd, 1H, $^3J_{HH}$ = 8.1, 4.8 Hz, Biotin-H_a), 4.43 (dd, 1H, $^3J_{HH}$ = 4.4 Hz, Biotin-H_b), 3.74-3.60 (m, 8H, PEG-OCH_2), 3.56 (td, 4H, $^3J_{HH}$ = 5.5 Hz, $^4J_{HH}$ = 1.6 Hz, 2×OCH_2CH_2NH), 3.42-3.36 (m, 4H, CH_2NH), 3.29-3.25 (m, 1H, Biotin-H_c), 2.99 (dd, 1H, $^1J_{HH}$ = 13.0 Hz, Biotin-H_{endo}), 2.77 (d, 1H, Biotin-H_{exo}), 2.50 (t, 2H, $^3J_{HH}$ = 7.1 Hz, CH_2S), 2.29-2.22 (m, 4H, $CH_2C(O)$), 1.82-1.55 (m, 8H, CH_2CH_2), 1.50-1.28 (m, 8H, CH_2CH_2).

^{13}C{^{1}H} NMR (125.7 MHz, Methanol-d_4): δ_C (ppm): 176.9, 176.4 (2×CO_{amide}), 165.8 (CO_{biotin}), 71.6, 71.2 (OCH_2), 70.4, 70.3 (2×CH_2CH_2NH), 64.3 (Biotin-C_b), 62.7 (Biotin-C_a), 56.8 (Biotin-C_c), 40.7 (Biotin-C_d), 40.7, 40.6 (2×CH_2NH), 36.7, 36.5 (2×$CH_2C(O)$), 35.1 (CH_2CH_2S), 30.1 (CH_3), 29.8-29.2 (CH_2CH_2), 27.0, 26.8 (2×$CH_2CH_2C(O)$), 24.9 (CH_2S).

HR–MS: For $C_{26}H_{49}N_4O_6S_2$, observed mass 577.3113, calculated 577.3094, difference 1.9 mDa.

_N_-(17-azido-3,6,9,12,15-pentaoxaheptadecyl)-5-((3a_S_,4_S_,6a_R_)-2-oxohexahydro-1_H_-thieno[3,4-_d_]imidazol-4-yl)pentanamide (IX-b)

The same procedure for **IX-a** was followed replacing **VIII-a** by **VIII-b** (174 mg, 0.57 mmol, 1 eq). Yield: 170 mg (56 %).

^{1}H NMR (500 MHz, Methanol-d_4): δ_H (ppm): 4.49 (ddd, 1H, $^3J_{HH}$ = 7.9, 5.0, 0.9 Hz, Biotin-H_a), 4.31 (dd, 1H, $^3J_{HH}$ = 4.5 Hz, Biotin-H_b), 3.70-3.54 (m, 18H, PEG-OCH_2), 3.55 (t, 2H, $^3J_{HH}$ = 5.4 Hz, OCH_2CH_2NH), 3.40-3.34 (m, 4H, $CH_2CH_2N_3$+CH_2NH), 3.21 (ddd, 1H, $^3J_{HH}$ = 8.9, 5.9 Hz, Biotin-H_c), 2.96-2.89 (m, 1H, Biotin-H_{endo}), 2.71 (d, 1H, , $^1J_{HH}$ = 12.7 Hz, Biotin-H_{exo}), 2.22 (t, 2H, $^3J_{HH}$ = 7.5 Hz, CH_2C(O)), 1.79-1.56 (m, 4H, CH_2N_3+ CH_2CH_2C(O)), 1.50-1.40 (m, 4H, CH_2CH_2).

ESI–MS: For $C_{22}H_{41}N_6O_7S$, observed mass 533.43, calculated 533.28.

_N_-(17-amino-3,6,9,12,15-pentaoxaheptadecyl)-5-((3a_S_,4_S_,6a_R_)-2-oxohexahydro-1_H_-thieno[3,4-_d_]imidazol-4-yl)pentanamide (X-b)

Intermediate **X-b** was obtained from **IX-b** (300 mg, 0.56 mmol, 1 eq) following the same procedure described for **X-a**. Yield: 240 mg (84 %).

^{1}H NMR (500 MHz, Methanol-d_4): δ_H (ppm): 4.49 (ddd, 1H, $^3J_{HH}$ = 8.0, 5.0, 0.9 Hz, Biotin-H_a), 4.31 (dd, 1H, $^3J_{HH}$ = 4.5 Hz, Biotin-H_b), 3.68-3.60 (m, 16H, PEG-OCH_2), 3.60-3.50 (m, 4H, 2×OCH_2CH_2N), 3.36 (t, 2H, $^3J_{HH}$ = 5.5 Hz, CH_2NH), 3.21 (ddd, 1H, $^3J_{HH}$ = 9.0, 5.8 Hz, Biotin-H_c), 2.97-2.90 (m, 1H, Biotin-H_{endo}), 2.87 (t, 2H, $^3J_{HH}$ = 5.3 Hz, $CH_2CH_2NH_2$), 2.71 (d, 1H, , $^1J_{HH}$ = 12.7 Hz, Biotin-H_{exo}), 2.22 (t, 2H, $^3J_{HH}$ = 7.4 Hz, CH_2C(O), 1.81-1.54 (m, 4H, CH_2CH_2), 1.50-1.40 (m, 2H, CH_2CH_2).

^{13}C{^{1}H} NMR (125.7 MHz, Methanol-d_4): δ_C (ppm): 176.2 (2×CO_{amide}), 166.1 (CO_{biotin}), 72.2, 71.6, 71.5, 71.2 (OCH_2), 70.6 (CH_2CH_2NH), 63.4 (Biotin-C_b), 61.6 (Biotin-C_a), 57.0 (Biotin-C_c), 41.8 (CH_2NH_2) 41.0 (Biotin-C_d), 40.3 (CH_2NH), 36.7 (CH_2C(O)), 29.8, 29.5 (CH_2CH_2), 26.8 (CH_2CH_2C(O)).

ESI–MS: For $C_{22}H_{43}N_4O_7S$, observed mass 507.44, calculated 507.29.

_S_-(5,25-dioxo-1-((3a_S_,4_S_,6a_R_)-2-oxohexahydro-1_H_-thieno[3,4-_d_]imidazol-4-yl)-9,12,15,18,21-pentaoxa-6,24-diazadotriacontan-32-yl) ethanethioate (5-Prot)

The same procedure described for **4-Prot** was employed on **X-b** (240 mg, 0.47 mmol, 1 eq) instead of **X-a**. Yield: 190 mg (57%).

^{1}H NMR (500 MHz, Methanol-d_4): δ_H (ppm): 4.50 (ddd, 1H, $^3J_{HH}$ = 7.9, 5.0, 0.9 Hz, Biotin-H_a), 4.31 (dd, 1H, $^3J_{HH}$ = 4.5 Hz, Biotin-H_b), 3.68-3.59 (m, 16H, PEG-OCH_2), 3.54 (m, 4H, 2×OCH_2CH_2NH), 3.36 (m, 4H, CH_2NH), 3.21 (ddd, 1H, $^3J_{HH}$ = 8.9, 5.8 Hz, Biotin-H_c), 2.93 (dd, 1H, $^1J_{HH}$ = 12.8 Hz, Biotin-H_{endo}), 2.86 (t, 2H, $^3J_{HH}$ = 7.3 Hz, CH_2S), 2.71 (d, 1H, Biotin-H_{exo}), 2.30 (s, 3H, CH_3), 2.25-2.16 (m, 4H, CH_2C(O)), 1.80-1.51 (m, 8H, CH_2CH_2), 1.49-1.28 (m, 8H, CH_2CH_2).

^{13}C{^{1}H} NMR (125.7 MHz, Methanol-d_4): δ_C (ppm): 197.6 ($CO_{thioacetate}$), 176.3, 176.1 (2×CO_{amide}), 166.1 (CO_{biotin}), 71.6, 71.5 (OCH_2), 71.3, 70.6 (2×CH_2CH_2NH), 63.4 (Biotin-C_b), 61.6 (Biotin-C_a), 57.0 (Biotin-C_c), 41.0 (Biotin-C_d), 40.3 (2×CH_2NH), 37.0, 36.7 (2×CH_2C(O)), 30.7 (CH_2CH_2S), 30.5 (CH_3), 30.1-29.6 (CH_2CH_2), 29.5 (CH_2S), 26.9, 26.8 (2×CH_2CH_2C(O)).

ESI–MS: For $C_{32}H_{59}N_4O_9S_2$, observed mass 707.29, calculated 707.37.

8-mercapto-*N*-(19-oxo-23-((3a*S*,4*S*,6a*R*)-2-oxohexahydro-1*H*-thieno[3,4-*d*]imidazol-4-yl)-3,6,9,12,15-pentaoxa-18-azatricosyl)octanamide (5 – Biot-6)

5-Prot was deprotected following the standard protocol described earlier on page 69 to yield **5** (**Biot-6**) quantitatively.

^{1}H NMR (500 MHz, Methanol-d_4): δ_H (ppm): 4.59 (ddd, 1H, $^{3}J_{HH}$ = 7.9, 5.0, 0.8 Hz, Biotin-H_a), 4.40 (dd, 1H, $^{3}J_{HH}$ = 4.4 Hz, Biotin-H_b), 3.77-3.61 (m, 16H, PEG-OCH_2), 3.55 (t, 4H, $^{3}J_{HH}$ = 5.5 Hz, 2×OCH_2CH_2NH), 3.38 (m, 4H, CH_2NH), 3.29-3.22 (m, 1H, Biotin-H_c), 2.97 (dd, 1H, $^{1}J_{HH}$ = 12.9 Hz, Biotin-H_{endo}), 2.76 (d, 1H, Biotin-H_{exo}), 2.50 (t, 2H, $^{3}J_{HH}$ = 7.3 Hz, CH_2S), 2.28-2.19 (m, 4H, CH_2C(O)), 1.80-1.55 (m, 8H, CH_2CH_2), 1.51-1.28 (m, 8H, CH_2CH_2).

^{13}C{^{1}H} NMR (125.7 MHz, Methanol-d_4): δ_C (ppm): 176.7, 176.3 (2×CO_{amide}), 165.9 (CO_{biotin}), 71.6, 71.5 (OCH_2), 71.3, 70.4 (2×CH_2CH_2NH), 64.0 (Biotin-C_b), 62.4 (Biotin-C_a), 56.9 (Biotin-C_c), 40.8 (Biotin-C_d), 40.6 (2×CH_2NH), 36.8, 36.5 (2×CH_2C(O)), 35.1 (CH_2CH_2S), 30.1 (CH_3), 30.1-29.2 (CH_2CH_2), 27.0, 26.8 (2×CH_2CH_2C(O)), 24.9 (CH_2S).

HR–MS: For $C_{30}H_{57}N_4O_8S_2$, observed mass 665.3625, calculated 665.3618, difference 0.7 mDa.

***N*-(17-azido-3,6,9,12,15-pentaoxaheptadecyl)undec-10-enamide (IV)**

A solution of **VIII-b** (0.5 g, 1.6 mmol, 1 eq) in anhydrous DMF (7 ml) was stirred in the presence of activated molecular sieves for 1 hour. After the treatment, the former solution was dropwise added to a DMF solution (anhydrous, 20 ml) of 10-undenoic acid (300 mg, 1.6 mmol, 1 eq), EDC (625 mg, 3.2 mmol, 2 eq) and DMAP (20 mg, 0.16 eq, 0.1 eq) previously cooled down at 0 ºC. The solution was then allowed to warm to room temperature and stirred overnight. The solvent was removed under vacuum and the product purified by column chromatography in CH_2Cl_2:MeOH 8:1. Yield: 507 mg (66%).

^{1}H NMR (500 MHz, Methanol-d_4): δ_H (ppm): 5.81 (ddt, 1H, $^3J_{HH trans}$ = 17.0 Hz, $^3J_{HH cis}$ = 10.2 Hz, $^3J_{HH}$ = 6.7 Hz, CH_2=C*H*CH_2), 5.01-4.95 (m, 1H, C*H*$_2$=CH_{trans}), 4.91 (ddt, 1H, $^2J_{HH}$ = 2.3 Hz, $^4J_{HH}$ = 1.2 Hz, C*H*$_2$=CH_{cis}), 3.69-3.59 (m, 18H, PEG-OCH_2), 3.53 (t, 2H, $^3J_{HH}$ = 5.5 Hz, OC*H*$_2$$CH_2N_3$), 3.39-3.33 (m, 4H, CH_2N_3+C*H*$_2$NH), 2.19 (t, 2H, CH_2C(O)), 2.08-2.01 (m, 2H, CH_2=CHC*H*$_2$), 1.60 (p, 2H, $^3J_{HH}$ = 6.7 Hz, C*H*$_2$$CH_2$C(O)), 1.43-1.35 (m, 2H, CH_2=$CHCH_2$C*H*$_2$), 1.32 (bs, 8H, CH_2C*H*$_2$).

^{13}C{^{1}H} NMR (125.7 MHz, Methanol-d_4): δ_C (ppm): 176.3 (CO_{amide}), 140.1 (CH_2=*C*H), 114.7 (*C*H_2=CH), 71.6, 71.5, 70.3, 70.1 (OCH_2+*C*$H_2$$CH_2$NH), 70.6 (*C*$H_2$$CH_2N_3$), 51.8 ($CH_2N_3$), 40.4 ($CH_2$NH), 37.0 (*C*$H_2$C(O)), 34.9 ($CH_2$=CH*C*$H_2$), 30.5-30.1 (*C*$H_2$$CH_2$), 27.0 (*C*$H_2$$CH_2$C(O)).

ESI–MS: For $C_{23}H_{45}N_4O_6$, observed mass 473.31, calculated 473.33.

***N*-(17-amino-3,6,9,12,15-pentaoxaheptadecyl)undec-10-enamide (V)**

The same procedure described for the preparation of **X-a** was followed in this case and used in the following step without further purification.

^{1}H NMR (500 MHz, DIMSO-d_6): δ_H (ppm): 5.79 (ddt, 1H, $^3J_{HH trans}$ = 17.0 Hz, $^3J_{HH cis}$ = 10.2 Hz, $^3J_{HH}$ = 6.7 Hz, CH_2=C*H*CH_2), 4.99 (dq, $^2J_{HH}$ = 1.7 Hz, 1H, C*H*$_2$=CH_{trans}), 4.91 (ddt, 1H, $^4J_{HH}$ = 1.2 Hz, C*H*$_2$=CH_{cis}), 3.56-3.44 (m, 16H, PEG-OCH_2), 3.38 (t, 2H, $^3J_{HH}$ = 5.9 Hz, C*H*$_2$NH), 2.63 (t, 2H, $^3J_{HH}$ = 5.8 Hz, C*H*$_2$$NH_2$), 2.07-1.97 (m, 4H, CH_2C(O)+CH_2=CHC*H*$_2$), 1.46 (q, 2H, $^3J_{HH}$ = 7.4 Hz, C*H*$_2$$CH_2$C(O)), 1.34 (p, $^3J_{HH}$ = 6.8 Hz, 2H, CH_2=$CHCH_2$C*H*$_2$), 1.23 (bs, 8H, CH_2C*H*$_2$).

(*S*)-*N*-(20-(6-methoxynaphthalen-2-yl)-19-oxo-3,6,9,12,15-pentaoxa-18-azahenicosyl)undec-10-enamide (XI)

A variation of the procedure described for the preparation of **IX-a** was followed, employing 2 equivalents of Naproxen. The product was purified by column chromatography in CH_2Cl_2:MeOH 50:1 → 20:1. Yield: 195 mg (33% 2-steps from **IV**).

^{1}H NMR (500 MHz, Methanol-d_4): δ_H (ppm): 7.75-7.71 (m, 1H, Naproxen-$H_{4,5,8}$), 7.45 (dd, 1H, $^{3}J_{HH}$ = 8.5 Hz, $^{4}J_{HH}$ = 1.9 Hz, Naproxen-H_7), 7.21 (d, 1H, $^{4}J_{HH}$ = 2.6 Hz, Naproxen-H_1), 7.12 (dd, 1H, $^{3}J_{HH}$ = 9.0 Hz, Naproxen-H_3), 5.80 (ddt, 1H, $^{3}J_{HH\mathit{trans}}$ = 17.0 Hz, $^{3}J_{HH\mathit{cis}}$ = 10.2 Hz, $^{3}J_{HH}$ = 6.7 Hz, CH_2=C*H*CH_2), 4.94-4.79 (m, 1H, CH_2=CH_{trans}), 4.93-4.89 (m, 1H, CH_2=CH_{cis}), 3.90 (s, 3H, OCH_3), 3.79 (q, 1H, $^{3}J_{HH}$ = 7.1 Hz, C*H*CH_3), 3.69-3.45 (m, 18H, PEG-OCH_2+2×OCH_2CH_2NH), 3.38-3.32 (m, 4H, 2×CH_2NH), 2.18 (t, 2H, $^{3}J_{HH}$ = 7.5 Hz $CH_2C(O)$), 2.06-2.00 (m, 2H, CH_2=CHCH_2), 1.59 (p, 2H, $^{3}J_{HH}$ = 7.2 Hz, C$H_2CH_2C(O)$), 1.53 (d, 3H, CHCH_3) 1.41-1.33 (m, 2H, CH_2=$CHCH_2CH_2$), 1.30 (bs, 8H, CH_2CH_2).

^{13}C{^{1}H} NMR (125.7 MHz, Methanol-d_4): δ_C (ppm): 177.2, 176.3 (2×CO_{amide}), 159.0 (Naproxen-C_2), 140.1 (CH_2=*C*H), 138.2 (Naproxen-C_6), 135.2 (Naproxen-C_9), 130.4 (Naproxen-C_{10}), 130.2 (Naproxen-C_4), 128.2 (Naproxen-C_8), 127.2 (Naproxen-C_7), 126.8 (Naproxen-C_5), 119.9 (Naproxen-C_3), 114.7 (*C*H_2=CH), 106.6 (Naproxen-C_1), 71.5, 71.4, 70.2 (OCH_2), 70.6, 70.5 (2×*C*H_2CH_2NH), 55.8 (OCH_3), 47.4 (*C*HCH_3), 40.5, 40.3 (2×*C*H_2NH), 37.0 (*C*$H_2C(O)$), 34.9 (CH_2=CH*C*H_2), 30.5-30.1 (*C*H_2CH_2), 27.0 (*C*$H_2CH_2C(O)$), 18.9 (CH*C*H_3).

ESI–MS: For $C_{37}H_{59}N_2O_8$, observed mass 659.36, calculated 659.43.

(*S*)-*S*-(2-(6-methoxynaphthalen-2-yl)-3,23-dioxo-7,10,13,16,19-pentaoxa-4,22-diazatritriacontan-33-yl) ethanethioate (6-Prot)

A degassed solution of **XI** (175 mg, 0.27 mmo, 1 eq), thioacetic acid (76 µl, 1.06 mmol, 4 eq) and 2,2-dimethoxy-2-phenyl-acetophenone (6.8 mg, 0.026 mmol, 0.1 eq) in MeOH (3 ml) was irradiated with 395 nm wavelength light from a LED black lamp overnight. The solvent was removed under vacuum and the product purified by column chromatography in CH_2Cl_2:MeOH 50:1 → 30:1. Yield: 185 mg (95%).

^{1}H NMR (500 MHz, Methanol-d_4): δ_H (ppm): 7.75-7.71 (m, 3H, Naproxen-$H_{4,5,8}$), 7.45 (dd, 1H, $^{3}J_{HH}$ = 8.4 Hz, $^{4}J_{HH}$ = 1.9 Hz, Naproxen-H_7), 7.22 (d, 1H, $^{4}J_{HH}$ = 2.5 Hz, Naproxen-H_1), 7.13 (dd, 1H, $^{3}J_{HH}$ = 9.0 Hz, Naproxen-H_3), 3.91 (s, 3H, OCH_3), 3.80 (q, 1H, $^{3}J_{HH}$ = 7.1 Hz, C*H*CH_3), 3.64-3.45 (m, 18H, PEG-OCH_2+2×O*C*H_2CH_2NH), 3.42-3.33 (m, 4H, 2×CH_2NH), 2.85 (t, 2H, $^{3}J_{HH}$ = 7.3 Hz, CH_2S), 2.30 (s, 3H, $CH_3C(O)$), 2.18 (t, 2H, $^{3}J_{HH}$ = 7.5 Hz $CH_2C(O)$), 1.59 (p, 2H, $^{3}J_{HH}$ = 7.1 Hz, C$H_2CH_2C(O)$), 1.53 (d, 3H, CHCH_3), 1.39-1.25 (m, 14H, CH_2CH_2).

^{13}C{^{1}H} NMR (125.7 MHz, Methanol-d_4): δ_C (ppm): 197.6 ($CO_{thioacetate}$), 177.2, 176.3 (2×CO_{amide}), 159.1 (Naproxen-C_2), 138.2 (Naproxen-C_6), 135.2 (Naproxen-C_9), 130.4 (Naproxen-C_{10}), 130.2 (Naproxen-C_4), 128.2 (Naproxen-C_8), 127.2 (Naproxen-C_7), 126.8 (Naproxen-C_5), 119.9 (Naproxen-C_3), 106.6 (Naproxen-C_1), 71.5, 71.4, 70.2 (OCH_2), 70.6, 70.5 (2×*C*H_2CH_2NH), 55.8 (OCH_3), 47.4 (*C*HCH_3), 40.6, 40.3 (2×*C*H_2NH), 37.0 (*C*$H_2C(O)$), 30.8 (*C*$H_3C(O)$) 30.5-29.8 (*C*H_2CH_2), 29.8 (CH_2S) 27.8 (2×*C*$H_2CH_2C(O)$), 18.9 (CH*C*H_3).

ESI–MS: For $C_{39}H_{62}N_2O_9S$, observed mass 735.39, calculated 735.43.

(*S*)-11-mercapto-N-(20-(6-methoxynaphthalen-2-yl)-19-oxo-3,6,9,12,15-pentaoxa-18-azahenicosyl)undecanamide (6)

The standard procedure reported before (see page 69) was employed on the thioacetate precursor **6-Prot** to obtain the free thiol **6** in quantitative yield.

^{1}H NMR (500 MHz, Methanol-d_4): δ_H (ppm): 7.75-7.71 (m, 3H, Naproxen-$H_{4,5,8}$), 7.44 (dd, 1H, $^{3}J_{HH}$ = 8.5 Hz, $^{4}J_{HH}$ = 1.9 Hz, Naproxen-H_7), 7.21 (d, 1H, $^{4}J_{HH}$ = 2.6 Hz, Naproxen-H_1), 7.11 (dd, 1H, $^{3}J_{HH}$ = 9.0 Hz, Naproxen-H_3), 3.90 (s, 3H, OCH_3), 3.79 (q, 1H, $^{3}J_{HH}$ = 7.1 Hz, C*H*CH_3), 3.68-3.43 (m, 18H, PEG-OCH_2+2×O*C*H_2CH_2NH), 3.41-3.32 (m, 4H, 2×CH_2NH), 2.47 (t, 2H, $^{3}J_{HH}$ = 7.1 Hz, CH_2S), 2.17 (t, 2H, $^{3}J_{HH}$ = 7.5 Hz $CH_2C(O)$), 1.62-1.54 (m, 2H, C$H_2CH_2C(O)$), 1.52 (d, 3H, CHCH_3), 1.42-1.25 (m, 14H, CH_2CH_2).

$^{13}C\{^{1}H\}$ NMR (125.7 MHz, Methanol-d_4): δ_C (ppm): 177.2, 176.3 (2×CO_{amide}), 159.1 (Naproxen-C_2), 138.2 (Naproxen-C_6), 135.2 (Naproxen-C_9), 130.4 (Naproxen-C_{10}), 130.2 (Naproxen-C_4), 128.2 (Naproxen-C_8), 127.2 (Naproxen-C_7), 126.8 (Naproxen-C_5), 119.9 (Naproxen-C_3), 106.6 (Naproxen-C_1), 71.6, 71.5, 71.2 (OCH_2), 70.6, 70.5 (2×CH_2CH_2NH), 55.8 (OCH_3), 47.4 ($CHCH_3$), 40.6, 40.3 (2×CH_2NH), 37.0 ($CH_2C(O)$), 35.2 (CH_2CH_2S) 30.6-29.4 (CH_2CH_2), 27.0 (2×$CH_2CH_2C(O)$), 25.0 (CH_2S), 18.9 ($CHCH_3$).

HR–MS: For $[M+NH_4]^+$ $C_{37}H_{64}N_3O_8S$, observed mass 710.4432, calculated 710.4414, difference 1.8 mDa.

_S_-(1-(8-(5,21-dioxo-25-((3a_S_,4_S_,6a_R_)-2-oxohexahydro-1_H_-thieno[3,4-_d_]imidazol-4-yl)-8,11,14,17-tetraoxa-4,20-diazapentacosan-1-oyl)-8,9-dihydro-3_H_-dibenzo[_b_,_f_][1,2,3]triazolo[4,5-_d_]azocin-3-yl)-19-oxo-3,6,9,12,15-pentaoxa-18-azahexacosan-26-yl) ethanethioate and triazole regioisomer (1_H_-1_H_) (DBCO-click)

10 μl of 10 mM solutions of **3-Prot** and **DBCO-Biot** in methanol-d_4 were mixed inside an NMR tube containing 480 μl of D_2O and allowed to react for 24 hours. Based on the NMR spectrum, reaction yield was virtually quantitative.

ESI–MS: For $[M+Na]^+$, observed mass 1278.62, calculated 1278.61; $[M+2Na]^{2+}$, observed mass 650.80, calculated 650.80

6.6 Thiol exchange

Nanoparticles were dissolved in methanol and the desired thiol was added in methanol after deprotection. Final solution was typically 1.5 mM in thiol (considering nanoparticle-bound thiol) and was allowed to exchange at 30 °C for 18 hours. In the case of multiple thiol exchange, both thiols were premixed prior to be added to the nanoparticles solution and then allowed to exchange under identical conditions.

Quantification of the different components of the monolayer was carried out by comparing the integration of isolated ^{1}H-NMR signals from the different thiols or by integration of the multiplet corresponding the the PEG methylene groups with respect to the methylene bound to the sulfur in the case of nanoparticles made with **8** instead of **1**. In particular, the multiplet at 4.2 ppm or quartet at 3.9 (when overlapping of the other signal with biotin proton) was employed for **1**, the triplet around 3.6 ppm was employed for azido compounds **2** and **3**, the biotin signal at 4.6 ppm was employed for **4**, **5**, **7** and **DBCO-Biot**, the methoxy 3.9 ppm singlet for **6**, the methyl singlet at 3.2 ppm for **10** and, in the case of **2** and **3** exchanging with **9**, the integral ranging from 3.7 to 3.5 ppm was compared to that from 2.9 to 2.7 ppm.

6.7 Click-coupling on gold nanoparticles

Click coupling attempts between azido-covered nanoparticles and alkynes was typically carried out in H_2O:DMSO mixtures in the presence of either copper sulfate or a 1:1 copper complex with THPTA or TBTA and sodium ascorbate. In all cases, excess of all reagents were employed. Reaction was normally carried out in solution 1.5 mM in thiol at 30 °C for 18 hours. Typically, the desired alkyne was added to the nanoparticle solution, followed by the copper reagent and finally sodium ascorbate from a freshly prepared solution.

Couplings with **DBCO-Biot** were carried out in water solution, 1.5 mM in thiol to which the required amount of reagent was added from a methanol stock solution. Reactions were incubated at 30 °C for 18 hours.

Success of the coupling reaction was evaluated by ^{1}H-NMR on the basis of the presence of the peaks corresponding to the biotin moiety and the triazole proton (around 8 ppm). Quantification of the reaction yield was carried out directly when possible by comparing the integral of a the triplet at 2.4 ppm, corresponding to the biotinylated alkyne fragment, with the triplet at 2.2 ppm, present in the azide derivatives **2** and **3.** When this approach was not possible due to signal overlapping, the amount of biotin present relative to the most abundant thiol (**1**, **9** or **10**) was measured as described above for thiol exchange experiments and that value was compared to the known amount of azido groups present before the reaction.

Copper contamination of the NMR samples was removed by eluting the content of the NMR tube through a column filled with Chelex-100 resin, previously washed with methanol and then the solvent was removed.

Attempted removal of cooper from the nanoparticles after the coupling was performed by treating the resulting methanol solution overnight under gentle agitation with washed Chelex-100 resin. In order to ensure all copper was on its (II) oxidation state, air was

bubbled through the solution during the treatment. The resulting solution was then filtered over cotton to separate the resin and then purified as usual.

6.8 Nanoparticles and protein solutions

For accurate determination of monolayer properties or protein interaction, nanoparticles and protein solutions were prepared by approximately weighting the desired amount of material and the accurate concentration determined by weighting the content of 50 μl in the high-precision balance of the TGA instrument after heating the sample 30 minutes at 100 ºC to remove residual water.

6.9 Monolayer availability study

A commercially available (Sigma-Aldrich) kit for the study of biotinylated materials based on the HABA-Avidin reagent was employed. To 900 μl of the commercial reagent 100 or and 200 μl of nanoparticles solution (approx.12 mg/ml) were added, stirred and incubated at 25 ºC for 1 hour. Afterwards, the resulting solution was centrifuged at 14.5k rpm for 2 hours to separate the nanoparticles from the rest of the solution and the supernatant transferred to a cuvette. Control experiments showed that centrifugation did not affect the reagent mixture spectrum.

In order to correct residual nanoparticles that could mask the effect of the biotin, a nanoparticles spectrum scaled to match the sample absorbance at 600 nm (where the reagent shows no absorption) was subtracted.

The amount of biotin bound to the avidin can be calculated from the difference in absorbance at 500 nm between the control (to which milliQ water was added) and the sample by following the technical document of the reagent, considering the difference in the extinction coefficient of HABA on its free and bound form. In the case of the 200 ml experiment, a volume correction factor of 1.1 had to be included to correct the dilution of the sample.

6.10 Protein binding experiments

Nanoparticles solution in milliQ water (100 µl, approx. 2 mg/ml) was added to 800 µl of buffer solution (HEPES 10 mM pH 7.3, 150 mM NaCl, 10 mM $MgCl_2$) and then different amount of protein were added in the adequate dilution to employ 100 µl of solution. The solution was vigorously agitated for 10 minutes and then the UV-Visible spectrum acquired.

In the case of albumin binding, this was added in different amounts and incubated for 10 minutes, followed by the addition of the amount of avidin that induced the maximum crosslinking and left incubating 10 additional minutes before acquiring the spectra.

Aggregation kinetics studies were carried out by incubating the nanoparticle solution with albumin for ten minutes followed by monitoring the spectral changes immediately after the addition of avidin with direct stirring inside the spectrophotometer.

6.11 Nanoparticle necklaces and nanowires formation

Influence of GAP presence and concentration on nanoparticles fusion

Nanoparticles were prepared as in the standard protocol described on page 65 with the exception that no thiol but D-glucosamine-6-phosphate (GAP) was added to the solution. Accordingly, after cooling down 8 mg GAP were added in 1 ml of water and the solution stirred for 1.5 hours prior to purification *via* size exclusion filtration by washing with water five times. Remaining nanoparticles were then incubated, in high concentration (400 µl of filtered concentrated solution diluted up to 1 ml), in water, 2.5 mM GAP or 10 mM sodium citrate. In order to study the impact of GAP concentration, additional experiments were carried out with solutions in the range from 0.1 to 0.6 mM. Solutions were incubated at room temperature.

Effect of GAP exchange time on nanowires growth

Nanoparticles were prepared as indicated above but aliquots were separated and filtrated 10 minutes, 3 hours and overnight after the addition of GAP to the solution. After filtration and washing with water, 100 µl of the concentrated solution were diluted up to 3 ml with pure water and the evolution monitored via UV-Visibile-NIR spectroscopy and TEM for two weeks. Two control samples were made, one in which the same treatment was applied before addition of GAP and a second one in which nanoparticles exchanged for 3 hours were washed with 5 mM sodium citrate solution instead of pure water.

Trapping and functionalizing gold nanowires by thiol addition

As part of the previously described experiments, after 5 days of incubation, an aqueous solution of **1** in large excess respect to the nanoparticles was added to an aliquot of the samples and the solution further incubated for another 9 days (as the rest of the cuvettes).

References

[1] A. J. Atkinson Jr., W. G. Magnuson, W. A. Colburn, V. G. DeGruttola, D. L. DeMets, G. J. Downing, D. F. Hoth, J. A. Oates, C. C. Peck, R. T. Schooley, et al., *Clin. Pharmacol. Ther.* **2001**, *69*, 89–95.

[2] World Health Organization - International Programme on Chemical Safety, "Biomarkers and risk assessment: concepts and principles," can be found under http://www.inchem.org/documents/ehc/ehc/ehc155.htm, **1993**.

[3] K. Strimbu, J. A. Tavel, *Curr. Opin. HIV AIDS* **2011**, *5*, 463–466.

[4] World Health Organization, "Knowledge into Action Early Detection Cancer Control Knowledge into Action Early Detection," can be found under http://whqlibdoc.who.int/publications/2007/9241547338_eng.pdf, **2007**.

[5] M. Prince, R. Bryce, C. Ferri, "The benefits of early diagnosis and intervention. World Alzheimer Report 2011," can be found under http://www.alz.co.uk/research/WorldAlzheimerReport2011.pdf, **2011**.

[6] T. Ninomiya, M. Nagata, J. Hata, Y. Hirakawa, M. Ozawa, D. Yoshida, T. Ohara, H. Kishimoto, N. Mukai, M. Fukuhara, et al., *Atherosclerosis* **2013**, *231*, 261–267.

[7] R. R. Shivkar, S. A. Abhang, *J. Clin. Diagn. Res.* **2014**, *8*, C004–C006.

[8] National Cancer Institute - National Institute of Health, "What is Cancer Proteomics?," can be found under http://proteomics.cancer.gov/whatisproteomics, **2011**.

[9] G. C. Adam, E. J. Sorensen, B. F. Cravatt, *Mol. Cell. Proteomics* **2002**, *1*, 781–790.

[10] D. K. Nomura, M. M. Dix, B. F. Cravatt, *Nat. Rev. Cancer* **2010**, *10*, 630–638.

[11] D. Leung, C. Hardouin, D. L. Boger, B. F. Cravatt, *Nat. Biotechnol.* **2003**, *21*, 687–691.

[12] R. E. Moellering, B. F. Cravatt, *Chem. Biol.* **2012**, *19*, 11–22.

[13] D. A. Bachovchin, S. J. Brown, H. Rosen, B. F. Cravatt, *Nat. Biotechnol.* **2009**, *27*, 387–394.

[14] E. C. Dreaden, A. M. Alkilany, X. Huang, C. J. Murphy, M. A. El-Sayed, *Chem. Soc. Rev.* **2012**, *41*, 2740–2779.

[15] T. L. Doane, C. Burda, *Chem. Soc. Rev.* **2012**, *41*, 2885–2911.

[16] Y. Wang, K. Lee, J. Irudayaraj, *Chem. Commun. (Camb).* **2010**, *46*, 613–615.

[17] B. Lutz, C. Dentinger, L. Sun, L. Nguyen, J. Zhang, A. Chmura, A. Allen, S. Chan, B. Knudsen, *J. Histochem. Cytochem.* **2008**, *56*, 371–379.

[18] D. S. Grubisha, R. J. Lipert, H.-Y. Park, J. Driskell, M. D. Porter, *Anal. Chem.* **2003**, *75*, 5936–5943.

[19] J. Conde, C. Bao, D. Cui, P. V Baptista, F. Tian, *J. Control. Release* **2014**, *183*, 87–93.

[20] A. M. Vera, J. J. Cárcamo, A. E. Aliaga, J. S. Gómez-Jeria, M. J. Kogan, M. M. Campos-Vallette, *Spectrochim. Acta. A. Mol. Biomol. Spectrosc.* **2015**, *134*, 251–256.

[21] N. Thioune, N. Lidgi-Guigui, M. Cottat, A.-M. Gabudean, M. Focsan, H.-M. Benoist, S. Astilean, M. L. de la Chapelle, *Gold Bull.* **2013**, *46*, 275–281.

[22] I. H. El-Sayed, X. Huang, M. A. El-Sayed, *Nano Lett.* **2005**, *5*, 829–834.

[23] A. Lesniewski, M. Los, M. Jonsson-Niedziółka, A. Krajewska, K. Szot, J. M. Los, J. Niedziolka-Jonsson, *Bioconjug. Chem.* **2014**, *25*, 644–648.

[24] Y.-J. Guo, G.-M. Sun, L. Zhang, Y.-J. Tang, J.-J. Luo, P.-H. Yang, *Sensors Actuators B Chem.* **2014**, *191*, 741–749.

[25] H. P. Erickson, *Biol. Proced. Online* **2009**, *11*, 32–51.

[26] U. Kreibig, L. Genzel, *Surf. Sci.* **1985**, *156*, *Part*, 678–700.

[27] H. Xia, S. Bai, J. Hartmann, D. Wang, *Langmuir* **2010**, *26*, 3585–3589.

[28] R. E. Holmlin, X. Chen, R. G. Chapman, S. Takayama, G. M. Whitesides, *Langmuir* **2001**, *17*, 2841–2850.

[29] H. Häkkinen, *Nat. Chem.* **2012**, *4*, 443–455.

[30] T. Bürgi, *Nanoscale* **2015**, *7*, 15553–15567.

[31] G. G. Baralia, A.-S. Duwez, B. Nysten, A. M. Jonas, *Langmuir* **2005**, *21*, 6825–6829.

[32] R. Dinkel, B. Braunschweig, W. Peukert, *J. Phys. Chem. C* **2016**, *120*, 1673–1682.

[33] R. Guo, Y. Song, G. Wang, R. W. Murray, *J. Am. Chem. Soc.* **2005**, *127*, 2752–2757.

[34] Q. Dai, J. Coutts, J. Zou, Q. Huo, *Chem. Commun.* **2008**, 2858–2860.

[35] C. Kinnear, H. Dietsch, M. J. D. Clift, C. Endes, B. Rothen-Rutishauser, A. Petri-Fink, *Angew. Chem. Int. Ed. Engl.* **2013**, *52*, 1934–1938.

[36] A. Fernando, C. M. Aikens, *J. Phys. Chem. C* **2015**, *119*, 20179–20187.

[37] A. Fernando, C. M. Aikens, *J. Phys. Chem. C* **2016**, *120*, 14948–14961.

[38] C. L. Heinecke, T. W. Ni, S. Malola, V. Mäkinen, O. A. Wong, H. Häkkinen, C. J. Ackerson, *J. Am. Chem. Soc.* **2012**, *134*, 13316–13322.

[39] T. W. Ni, M. A. Tofanelli, B. D. Phillips, C. J. Ackerson, *Inorg. Chem.* **2014**, *53*, 6500–6502.

[40] P. Ionita, A. Caragheorgheopol, B. C. Gilbert, V. Chechik, *Langmuir* **2010**, *20*, 11536–11544.

[41] P. Ionita, B. C. Gilbert, V. Chechik, *Angew. Chemie - Int. Ed.* **2005**, *44*, 3720–3722.

[42] P. Ionita, A. Caragheorgheopol, B. C. Gilbert, V. Chechik, *J. Am. Chem. Soc.* **2002**, *124*, 9048–9049.

[43] M. Zachary, V. Chechik, *Angew. Chemie - Int. Ed.* **2007**, *46*, 3304–3307.

[44] Y.-S. Shon, C. Mazzitelli, R. W. Murray, *Langmuir* **2001**, *17*, 7735–7741.

[45] R. S. Ingram, M. J. Hostetler, R. W. Murray, *J. Am. Chem. Soc.* **1997**, *119*, 9175–9178.

[46] H. Hinterwirth, S. Kappel, T. Waitz, T. Prohaska, W. Lindner, M. Lämmerhofer, *ACS Nano* **2013**, *7*, 1129–1136.

[47] S. Perumal, A. Hofmann, N. Scholz, E. Rühl, C. Graf, *Langmuir* **2011**, *27*, 4456–4464.

[48] S. Antonello, G. Arrigoni, T. Dainese, M. De Nardi, G. Parisio, L. Perotti, A.

René, A. Venzo, F. Maran, *ACS Nano* **2014**, *8*, 2788–2795.

[49] M. Montalti, L. Prodi, N. Zaccheroni, R. Baxter, G. Teobaldi, F. Zerbetto, *Langmuir* **2003**, *19*, 5172–5174.

[50] K. M. Harkness, A. Balinski, J. A. Mclean, D. E. Cliffel, *Angew. Chemie - Int. Ed.* **2011**, *50*, 10554–10559.

[51] H. C. Kolb, M. G. Finn, K. B. Sharpless, *Angew. Chemie - Int. Ed.* **2001**, *40*, 2004–2021.

[52] D. A. Fleming, C. J. Thode, M. E. Williams, *Chem. Mater.* **2006**, *18*, 2327–2334.

[53] A. Kimoto, K. Iwasaki, J. Abe, *Photochem. Photobiol. Sci.* **2010**, *9*, 152–156.

[54] L. Na, L. Salmon, J. Ruiz, M. Zabawa, N. S. Hosmane, D. Astruc, *Inorg. Chem.* **2013**, *52*, 11146–11155.

[55] A. Rapakousiou, R. Djeda, M. Grillaud, N. Li, J. Ruiz, D. Astruc, *Organometallics* **2014**, *33*, 6953–6962.

[56] E. Boisselier, L. Salmon, J. Ruiz, D. Astruc, *Chem. Commun.* **2008**, 5788–5790.

[57] E. M. Sletten, C. R. Bertozzi, *Angew. Chem. Int. Ed. Engl.* **2009**, *48*, 6974–6998.

[58] H. Li, Q. Zheng, C. Han, *Analyst* **2010**, *135*, 1360–1364.

[59] S. Z. Pan, L. X. Song, J. Chen, F. Y. Du, J. Yang, J. Xia, *Dalt. Trans.* **2011**, *40*, 10117–10124.

[60] C. J. Thode, M. E. Williams, *J. Colloid Interface Sci.* **2008**, *320*, 346–352.

[61] G. C. Papavassiliou, *Prog. Solid State Chem.* **1979**, *12*, 185–271.

[62] J. Cao, T. Sun, K. T. V. Grattan, *Sensors Actuators B Chem.* **2014**, *195*, 332–351.

[63] H. Chen, L. Shao, Q. Li, J. Wang, *Chem. Soc. Rev.* **2013**, *42*, 2679–2724.

[64] M. Y. Lin, H. M. Lindsay, D. A. Weitz, R. V Ball, R. Klein, P. Meakin, *Nature* **1989**, *339*, 360–362.

[65] S. C. Biradar, M. G. Kulkarni, *RSC Adv.* **2013**, *3*, 4261–4270.

[66] A. Fernández-Lodeiro, J. Fernández-Lodeiro, C. Núñez, R. Bastida, J. L. Capelo, C. Lodeiro, *ChemistryOpen* **2013**, *2*, 200–207.

[67] E. Filippo, a. Serra, a. Buccolieri, D. Manno, *Colloids Surfaces A Physicochem. Eng. Asp.* **2013**, *417*, 10–17.

[68] H. Jia, X. Bai, N. Li, L. Yu, L. Zheng, *CrystEngComm* **2011**, *13*, 6179–6184.

[69] K. Silambarasan, A. V. Narendra Kumar, C. Sivakumar, J. Joseph, *RSC Adv.* **2014**, *4*, 40003–40007.

[70] H. Wang, L. Chen, X. Shen, L. Zhu, J. He, H. Chen, *Angew. Chemie Int. Ed.* **2012**, *51*, 8021–8025.

[71] Y. Ding, G. Gu, X.-H. Xia, Q. Huo, *J. Mater. Chem.* **2009**, *17*, 795–799.

[72] M. Li, S. Johnson, H. Guo, E. Dujardin, S. Mann, *Adv. Funct. Mater.* **2011**, *21*, 851–859.

[73] Z. Tang, N. a Kotov, M. Giersig, *Science (80-.).* **2002**, *297*, 237–240.

[74] C. Morita, H. Tanuma, C. Kawai, Y. Ito, Y. Imura, T. Kawai, *Langmuir* **2013**, *29*, 1669–1675.

[75] P. R. Sajanlal, T. S. Sreeprasad, A. S. Nair, T. Pradeep, *Langmuir* **2008**, *24*, 4607–4614.

[76] L. Pei, K. Mori, M. Adachi, *Langmuir* **2004**, *20*, 7837–7843.

[77] P. Qiu, C. Mao, *J. Nanoparticle Res.* **2009**, *11*, 885–894.

[78] Y. N. Tan, J. T. Lee, D. I. C. Wang, *J. Phys. Chem. C* **2008**, *112*, 5463–5470.

[79] B.-K. Pong, H. I. Elim, J.-X. Chong, W. Ji, B. L. Trout, J. Y. Lee, *J. Phys. Chem. C* **2007**, *111*, 6281–6287.

[80] M. Giersig, I. Pastoriza-Santos, L. M. Liz-Marzán, *J. Mater. Chem.* **2004**, *14*, 607–610.

[81] K. Liu, Y. Zheng, X. Lu, T. Thai, N. A. Lee, U. Bach, J. J. Gooding, *Langmuir* **2015**, *31*, 4973–4980.

[82] A. Z. Mirza, H. Shamshad, *J. Nanoparticle Res.* **2013**, *15*, 1404.

[83] W. M. Park, B. G. Choi, Y. S. Huh, W. H. Hong, S. Y. Lee, T. J. Park, *Chempluschem* **2013**, *78*, 48–51.

[84] B. Thierry, J. Ng, T. Krieg, H. J. Griesser, *Chem. Commun.* **2009**, *1*, 1724–1726.

[85] H. E. Gottlieb, V. Kotlyar, A. Nudelman, *J. Org. Chem.* **1997**, *62*, 7512–7515.

[86] G. R. Fulmer, A. J. M. Miller, N. H. Sherden, H. E. Gottlieb, A. Nudelman, B. M. Stoltz, J. E. Bercaw, K. I. Goldberg, *Organometallics* **2010**, *29*, 2176–2179.

[87] S. Mondini, A. M. Ferretti, A. Puglisi, A. Ponti, *Nanoscale* **2012**, *4*, 5356–5372.

[88] F. Manea, C. Bindoli, S. Polizzi, L. Lay, P. Scrimin, *Langmuir* **2008**, *24*, 4120–

4124.

[89] C. Kittle, *Introduction to Solid-States Physics*, Wiley, New York, **1996**.

[90] M. Gilles, E. Brun, C. Sicard-roselli, *Colloids Surfaces B Biointerfaces* **2014**, *123*, 770–777.

[91] P. Pengo, S. Polizzi, M. Battagliarin, L. Pasquato, P. Scrimin, *J. Mater. Chem.* **2003**, *13*, 2471–2478.

[92] P. Thebault, E. Taffin de Givenchy, R. Levy, Y. Vandenberghe, F. Guittard, S. Géribaldi, *Eur. J. Med. Chem.* **2009**, *44*, 717–724.

[93] G. Guarino, F. Rastrelli, P. Scrimin, F. Mancin, *J. Am. Chem. Soc.* **2012**, *134*, 7200–7203.

[94] K. Susumu, H. T. Uyeda, I. L. Medintz, T. Pons, J. B. Delehanty, H. Mattoussi, *J. Am. Chem. Soc.* **2007**, *129*, 13987–13996.

[95] P. Bandyopadhyay, P. Bandyopadhyay, S. L. Regen, *J. Am. Chem. Soc.* **2002**, *124*, 11254–11255.

[96] L. N. Goswami, Z. H. Houston, S. J. Sarma, S. S. Jalisatgi, M. F. Hawthorne, *Org. Biomol. Chem.* **2013**, *11*, 1116–1126.

[97] M. Tantama, W. Lin, S. Licht, *J. Am. Chem. Soc.* **2008**, *5*, 15766–15767.

[98] S. Fusz, S. G. Srivatsan, D. Ackermann, M. Famulok, *J. Org. Chem.* **2008**, *73*, 5069–5077.

[99] M. Kitamura, F. Kawasaki, K. Ogawa, S. Nakanishi, H. Tanaka, K. Yamada, M. Kunishima, *J. Org. Chem.* **2014**, *79*, 3709–3714.

[100] S. S. Iyer, A. S. Anderson, S. Reed, B. Swanson, J. G. Schmidt, *Tetrahedron Lett.* **2004**, *45*, 4285–4288.

Appendix I – NMR Spectra of Thiol Exchanges

Legend includes NP size, leaving thiol, entering thiols and reaction ratio.

2 nm ZW – AZ-4 1:1

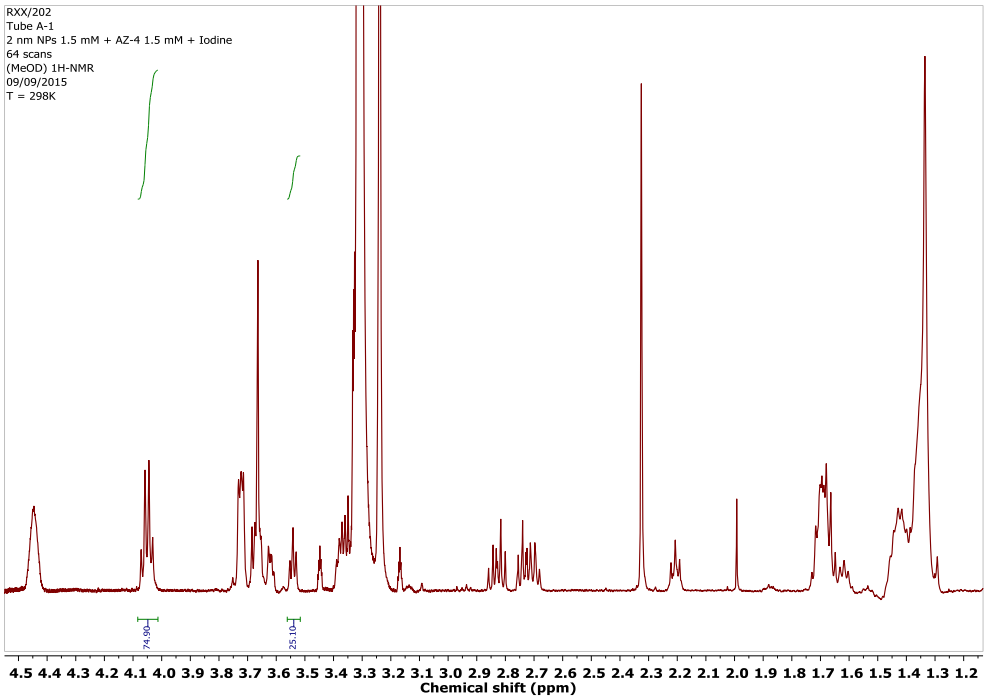

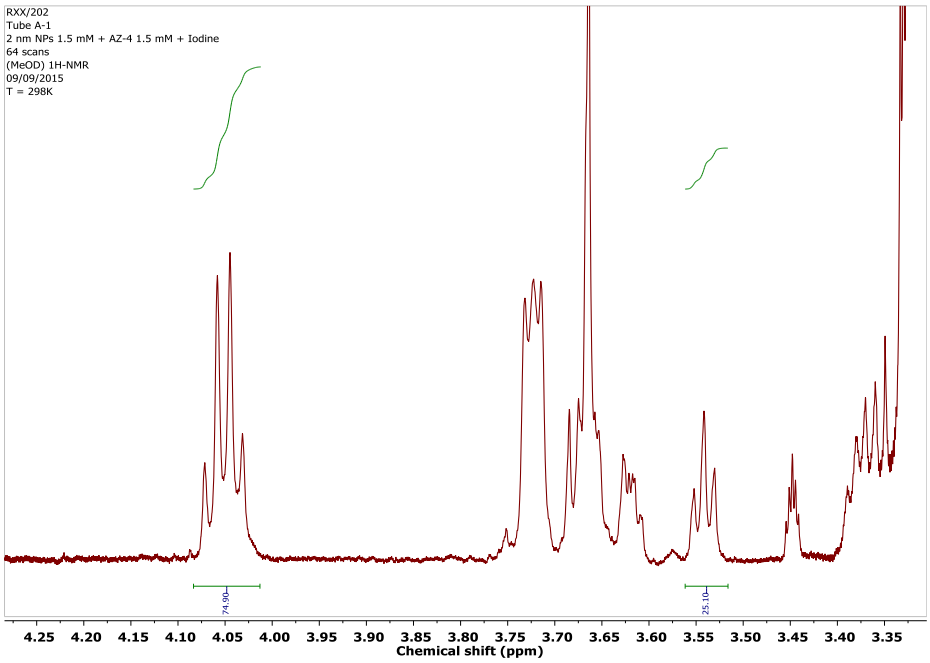
RXX/202
Tube A-1
2 nm NPs 1.5 mM + AZ-4 1.5 mM + Iodine
64 scans
(MeOD) 1H-NMR
09/09/2015
T = 298K
74.90
25.10
4.25 4.20 4.15 4.10 4.05 4.00 3.95 3.90 3.85 3.80 3.75 3.70 3.65 3.60 3.55 3.50 3.45 3.40 3.35
Chemical shift (ppm)

2 nm ZW – AZ-4 1:4

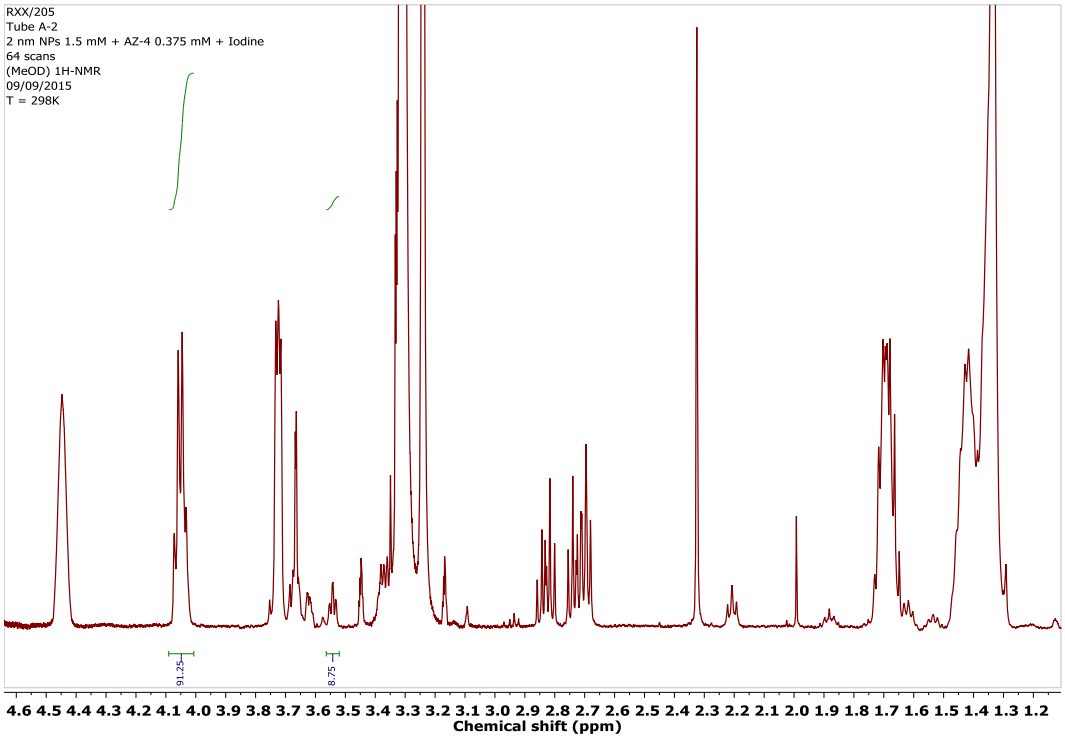
RXX/205
Tube A-2
2 nm NPs 1.5 mM + AZ-4 0.375 mM + Iodine
64 scans
(MeOD) 1H-NMR
09/09/2015
T = 298K
91.25
8.75
4.6 4.5 4.4 4.3 4.2 4.1 4.0 3.9 3.8 3.7 3.6 3.5 3.4 3.3 3.2 3.1 3.0 2.9 2.8 2.7 2.6 2.5 2.4 2.3 2.2 2.1 2.0 1.9 1.8 1.7 1.6 1.5 1.4 1.3 1.2
Chemical shift (ppm)

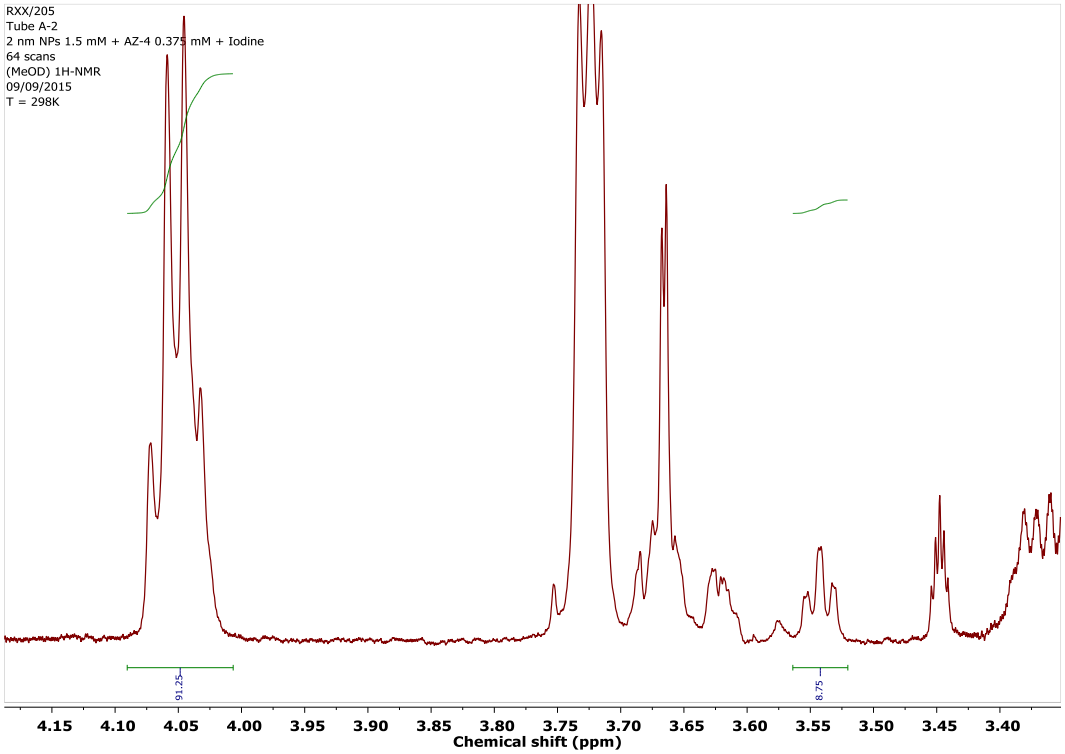

2 nm ZW – AZ-4 1:20

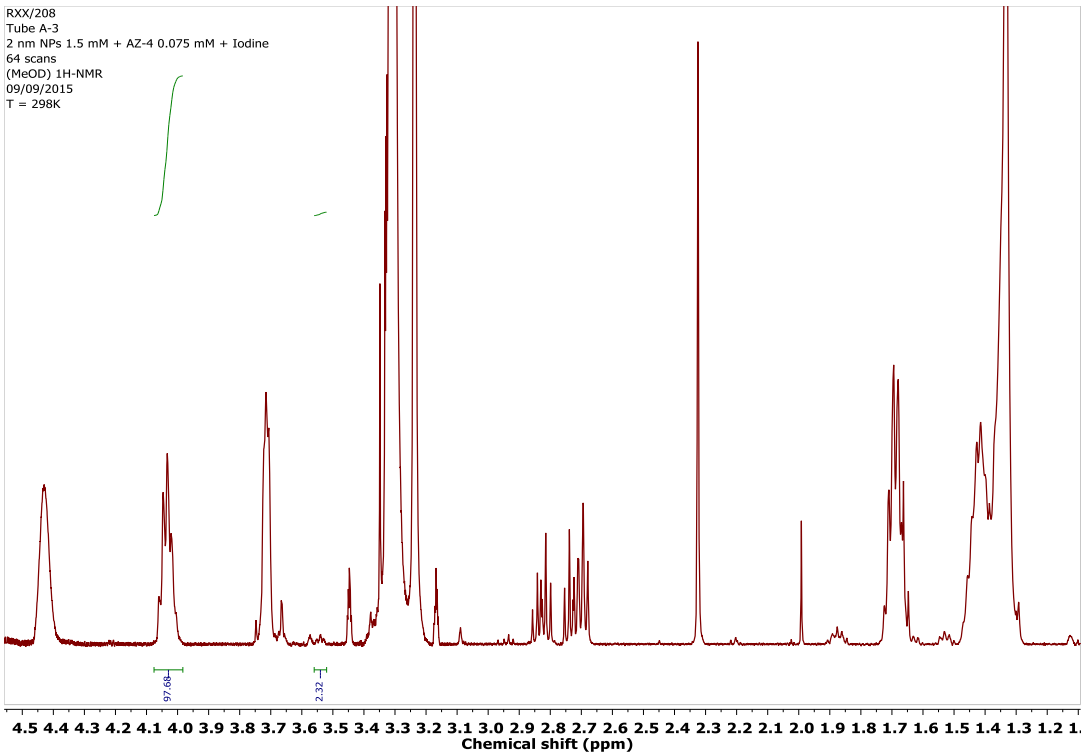

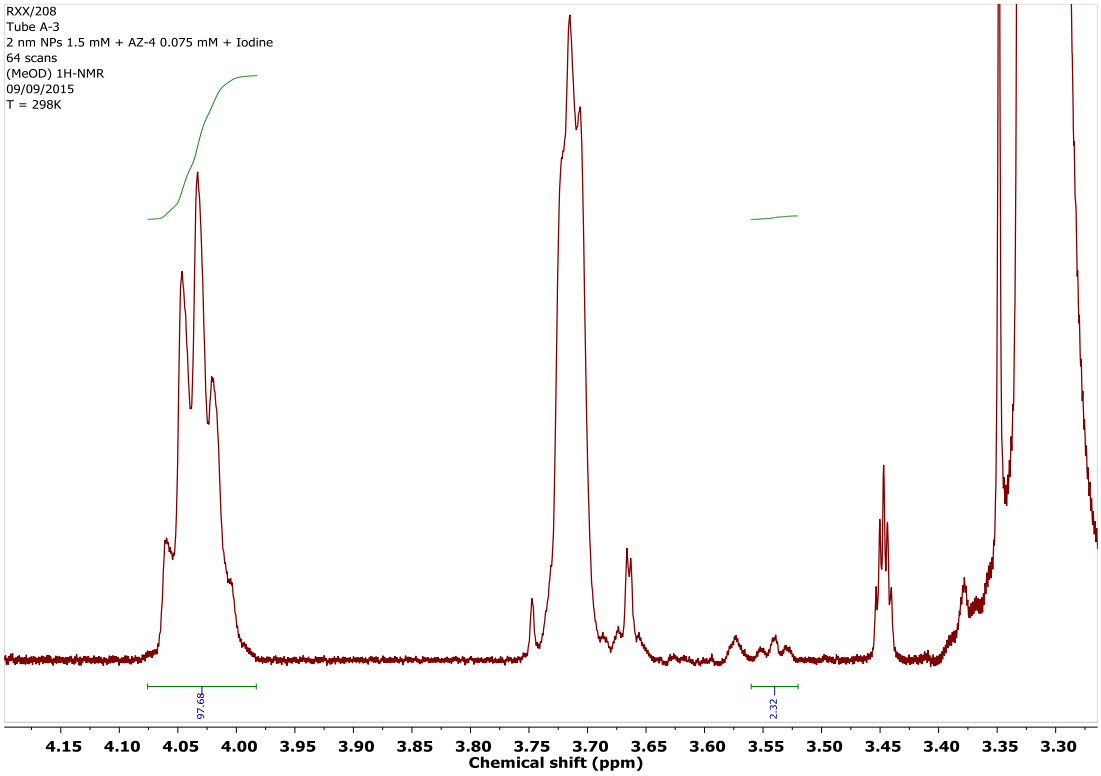
RXX/208
Tube A-3
2 nm NPs 1.5 mM + AZ-4 0.075 mM + Iodine
64 scans
(MeOD) 1H-NMR
09/09/2015
T = 298K
97.68
2.32
4.15 4.10 4.05 4.00 3.95 3.90 3.85 3.80 3.75 3.70 3.65 3.60 3.55 3.50 3.45 3.40 3.35 3.30
Chemical shift (ppm)

2 nm ZW – AZ-6 1:1

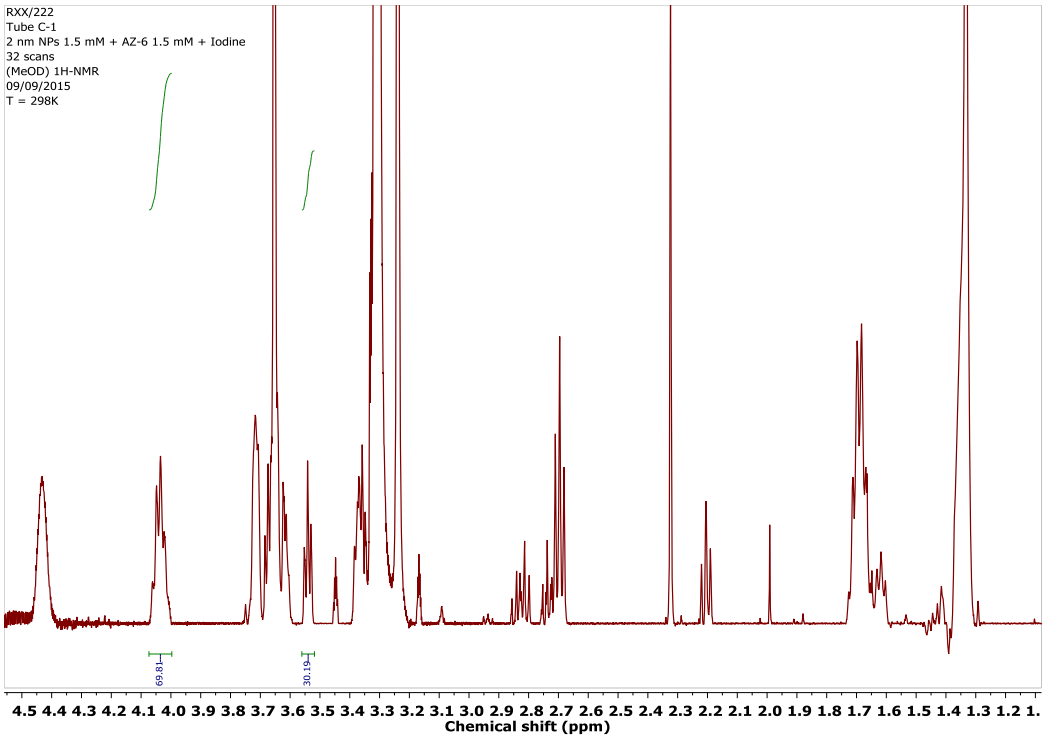
RXX/222
Tube C-1
2 nm NPs 1.5 mM + AZ-6 1.5 mM + Iodine
32 scans
(MeOD) 1H-NMR
09/09/2015
T = 298K
69.81
30.19
4.5 4.4 4.3 4.2 4.1 4.0 3.9 3.8 3.7 3.6 3.5 3.4 3.3 3.2 3.1 3.0 2.9 2.8 2.7 2.6 2.5 2.4 2.3 2.2 2.1 2.0 1.9 1.8 1.7 1.6 1.5 1.4 1.3 1.2 1.
Chemical shift (ppm)

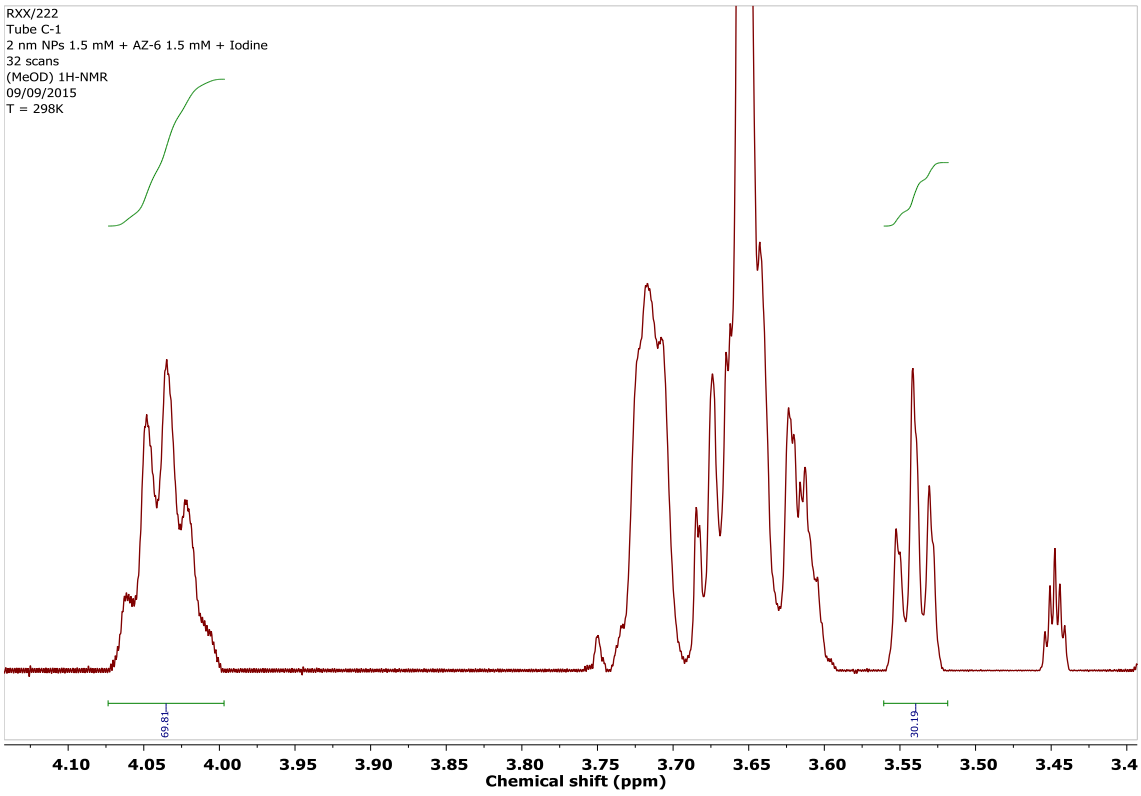
RXX/222
Tube C-1
2 nm NPs 1.5 mM + AZ-6 1.5 mM + Iodine
32 scans
(MeOD) 1H-NMR
09/09/2015
T = 298K
69.81
30.19
4.10 4.05 4.00 3.95 3.90 3.85 3.80 3.75 3.70 3.65 3.60 3.55 3.50 3.45 3.4
Chemical shift (ppm)

2 nm ZW – AZ-6 1:4

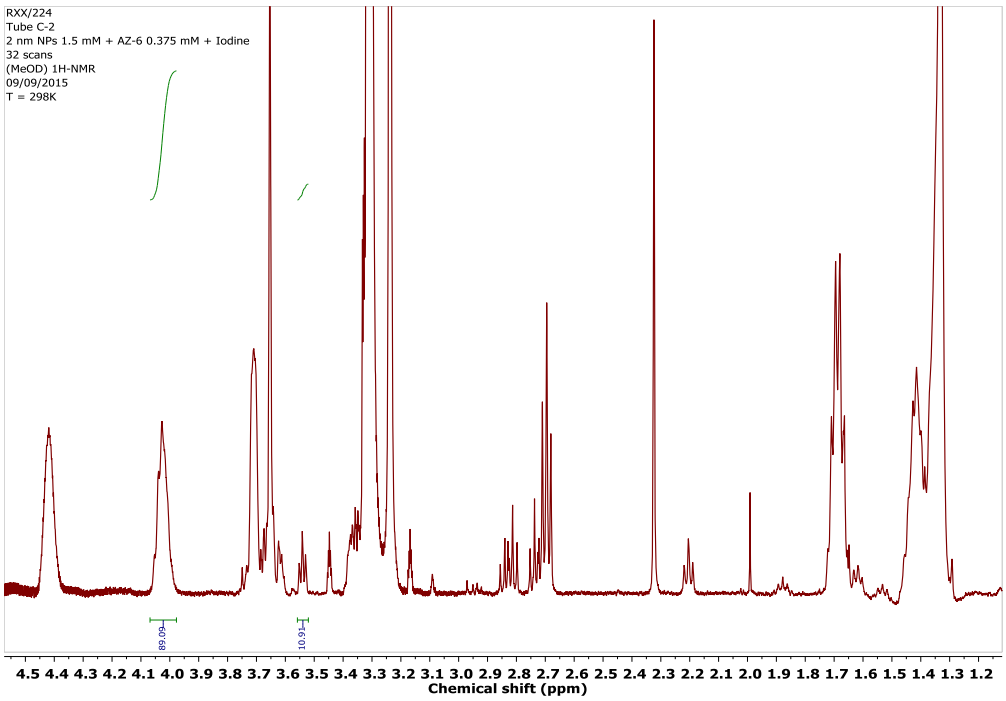
RXX/224
Tube C-2
2 nm NPs 1.5 mM + AZ-6 0.375 mM + Iodine
32 scans
(MeOD) 1H-NMR
09/09/2015
T = 298K
89.09
10.91
4.5 4.4 4.3 4.2 4.1 4.0 3.9 3.8 3.7 3.6 3.5 3.4 3.3 3.2 3.1 3.0 2.9 2.8 2.7 2.6 2.5 2.4 2.3 2.2 2.1 2.0 1.9 1.8 1.7 1.6 1.5 1.4 1.3 1.2
Chemical shift (ppm)

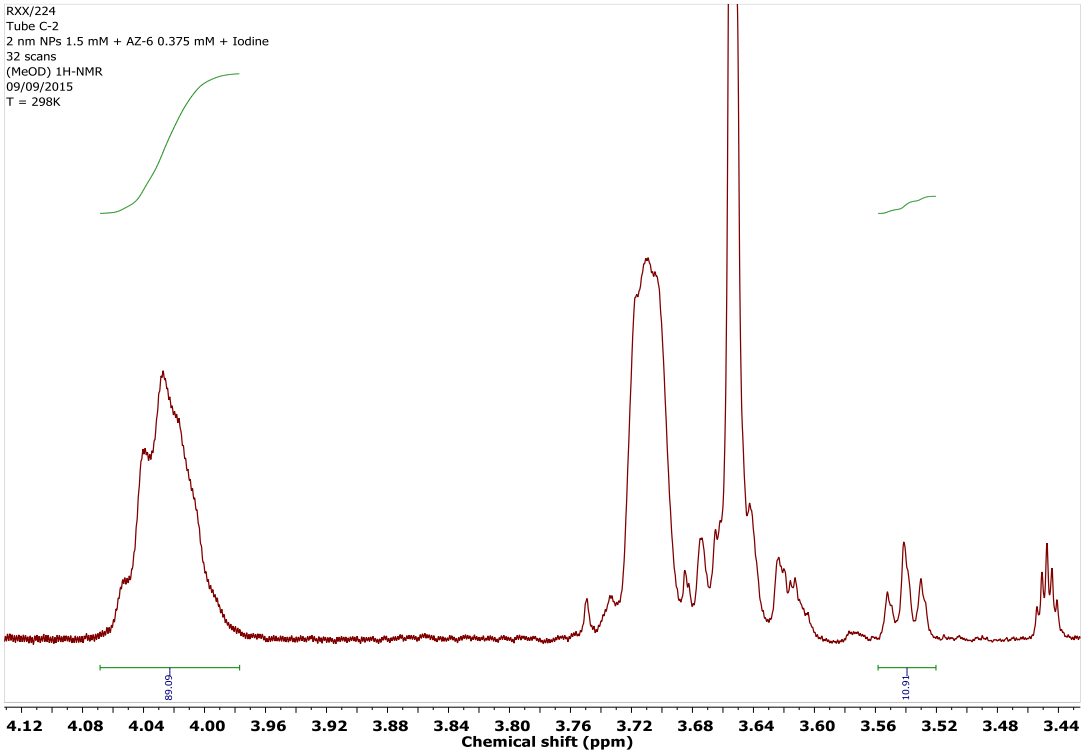

2 nm ZW – AZ-6 1:20

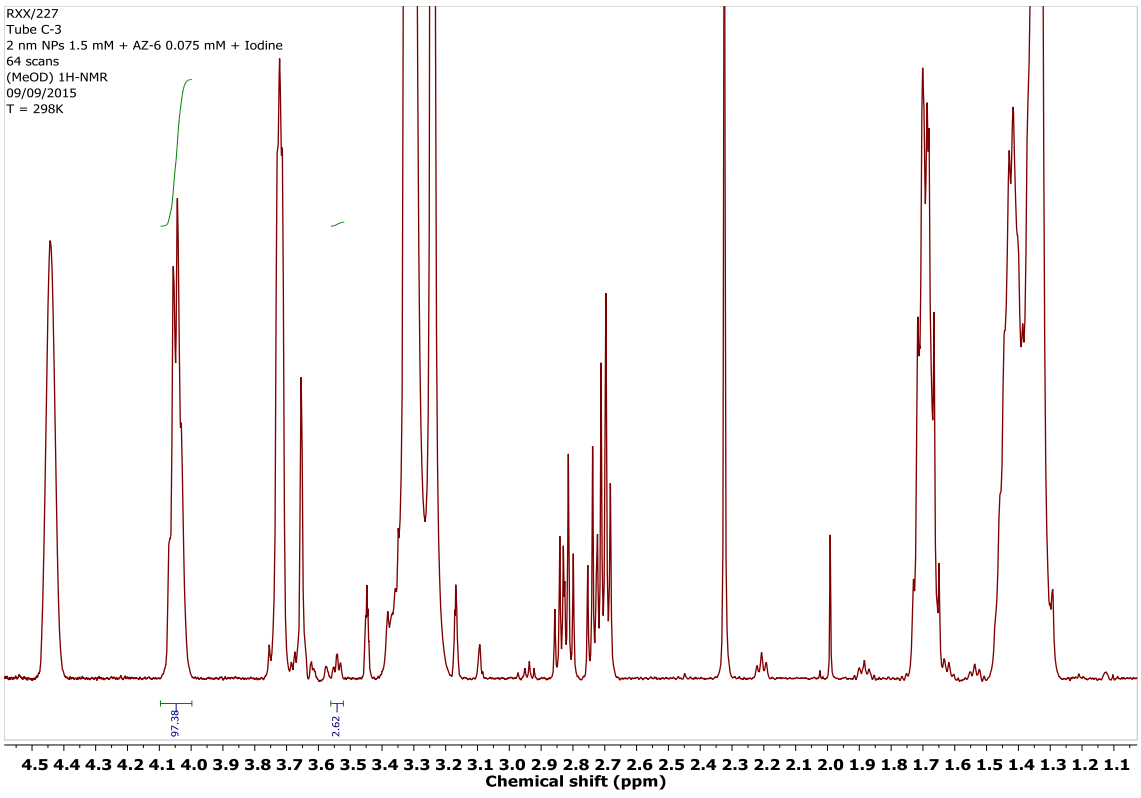

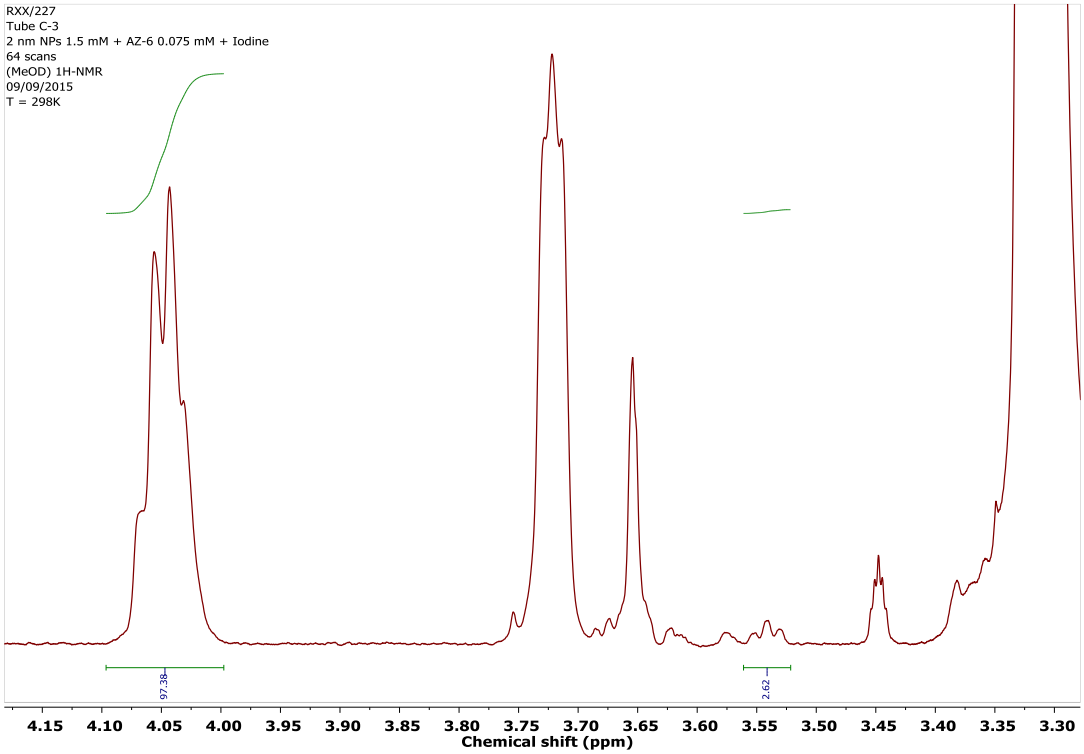
RXX/227
Tube C-3
2 nm NPs 1.5 mM + AZ-6 0.075 mM + Iodine
64 scans
(MeOD) 1H-NMR
09/09/2015
T = 298K
97.38
2.62
4.15 4.10 4.05 4.00 3.95 3.90 3.85 3.80 3.75 3.70 3.65 3.60 3.55 3.50 3.45 3.40 3.35 3.30
Chemical shift (ppm)

9 nm ZW – AZ-4 1:1

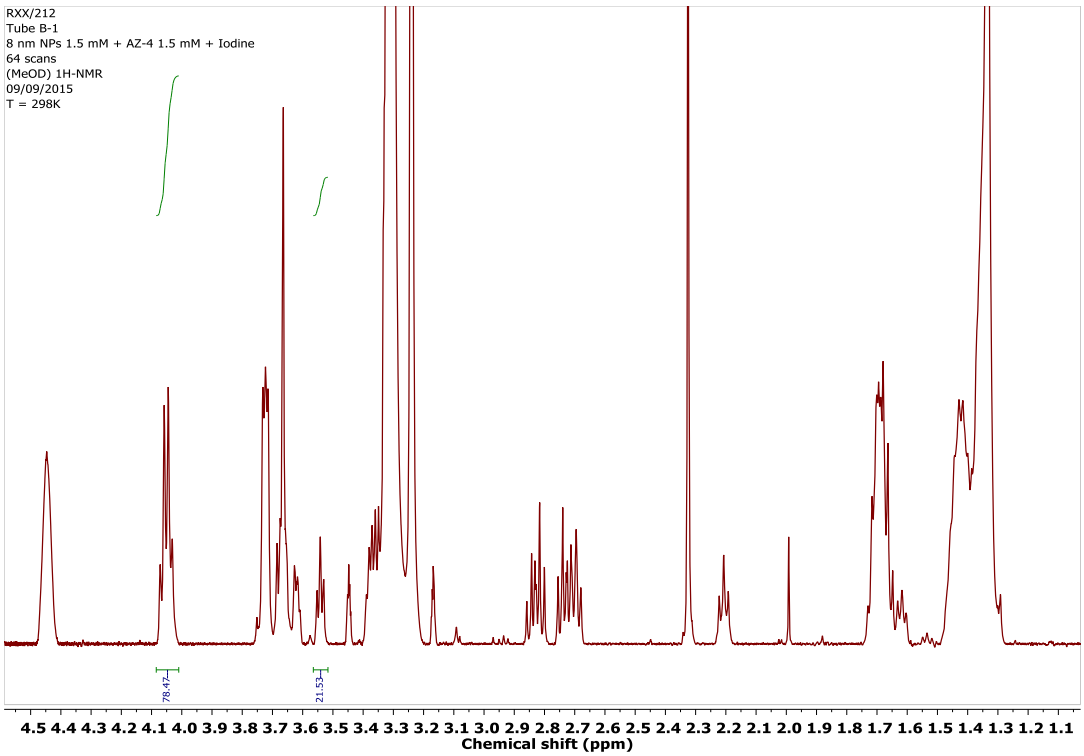
RXX/212
Tube B-1
8 nm NPs 1.5 mM + AZ-4 1.5 mM + Iodine
64 scans
(MeOD) 1H-NMR
09/09/2015
T = 298K
78.47
21.53
4.5 4.4 4.3 4.2 4.1 4.0 3.9 3.8 3.7 3.6 3.5 3.4 3.3 3.2 3.1 3.0 2.9 2.8 2.7 2.6 2.5 2.4 2.3 2.2 2.1 2.0 1.9 1.8 1.7 1.6 1.5 1.4 1.3 1.2 1.1
Chemical shift (ppm)

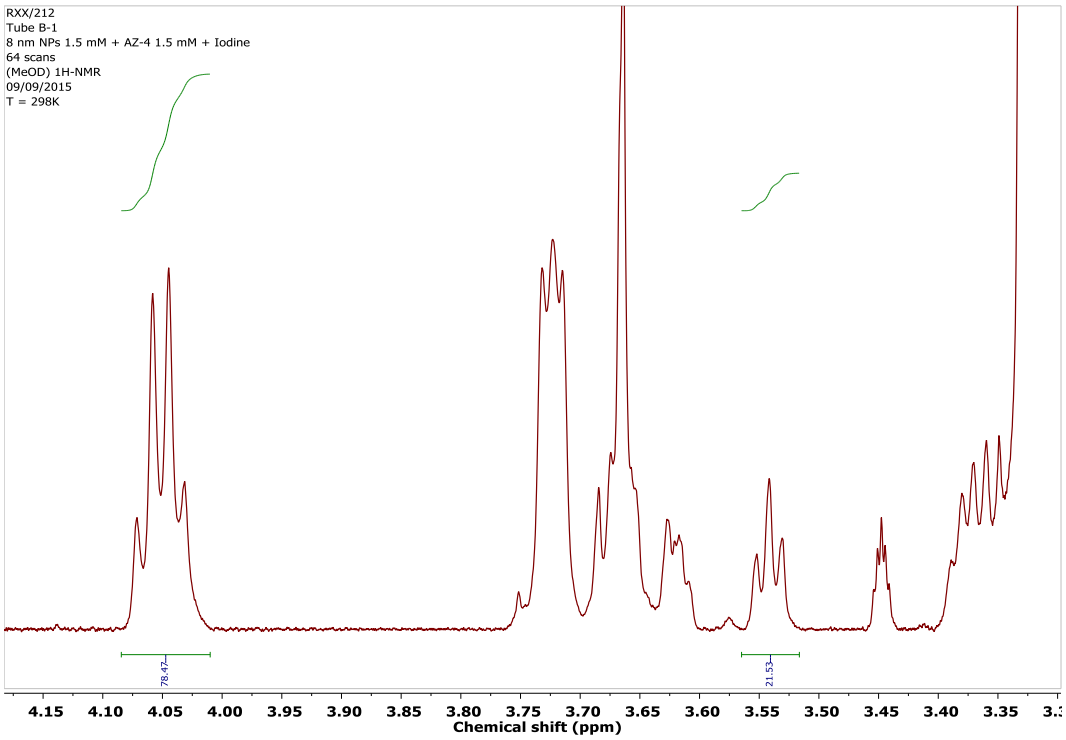
RXX/212
Tube B-1
8 nm NPs 1.5 mM + AZ-4 1.5 mM + Iodine
64 scans
(MeOD) 1H-NMR
09/09/2015
T = 298K
78.47
21.53
4.15 4.10 4.05 4.00 3.95 3.90 3.85 3.80 3.75 3.70 3.65 3.60 3.55 3.50 3.45 3.40 3.35
Chemical shift (ppm)

9 nm ZW – AZ-4 1:4

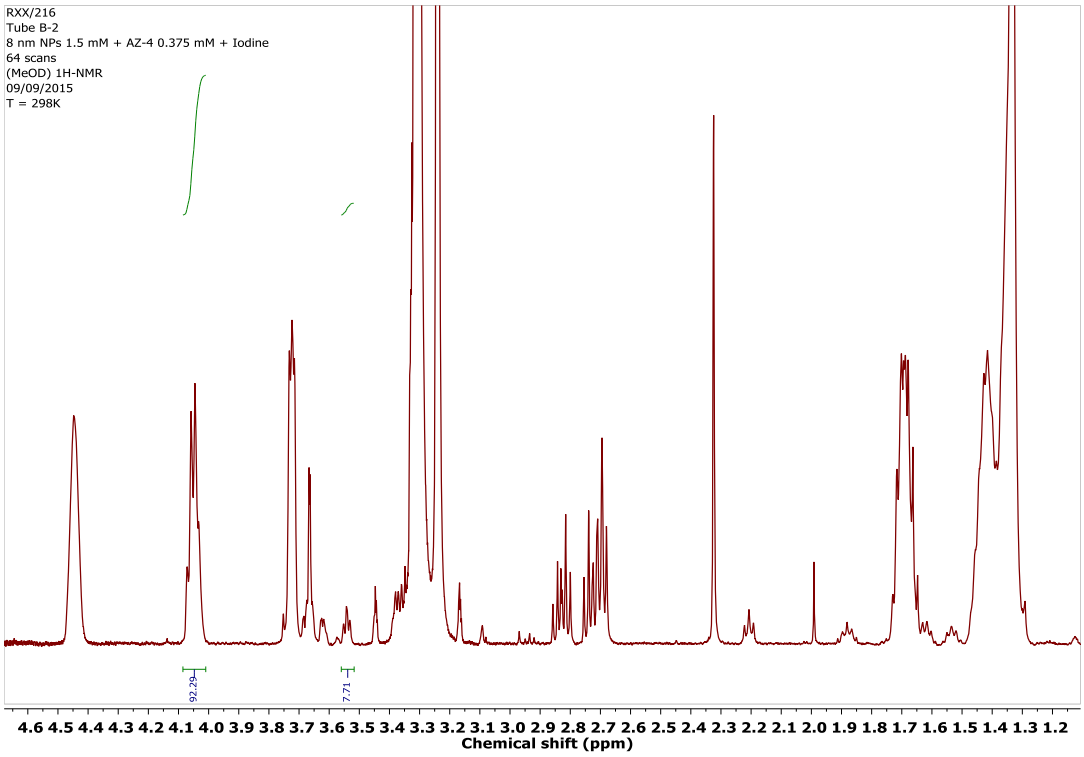
RXX/216
Tube B-2
8 nm NPs 1.5 mM + AZ-4 0.375 mM + Iodine
64 scans
(MeOD) 1H-NMR
09/09/2015
T = 298K
92.29
7.71
4.6 4.5 4.4 4.3 4.2 4.1 4.0 3.9 3.8 3.7 3.6 3.5 3.4 3.3 3.2 3.1 3.0 2.9 2.8 2.7 2.6 2.5 2.4 2.3 2.2 2.1 2.0 1.9 1.8 1.7 1.6 1.5 1.4 1.3 1.2
Chemical shift (ppm)

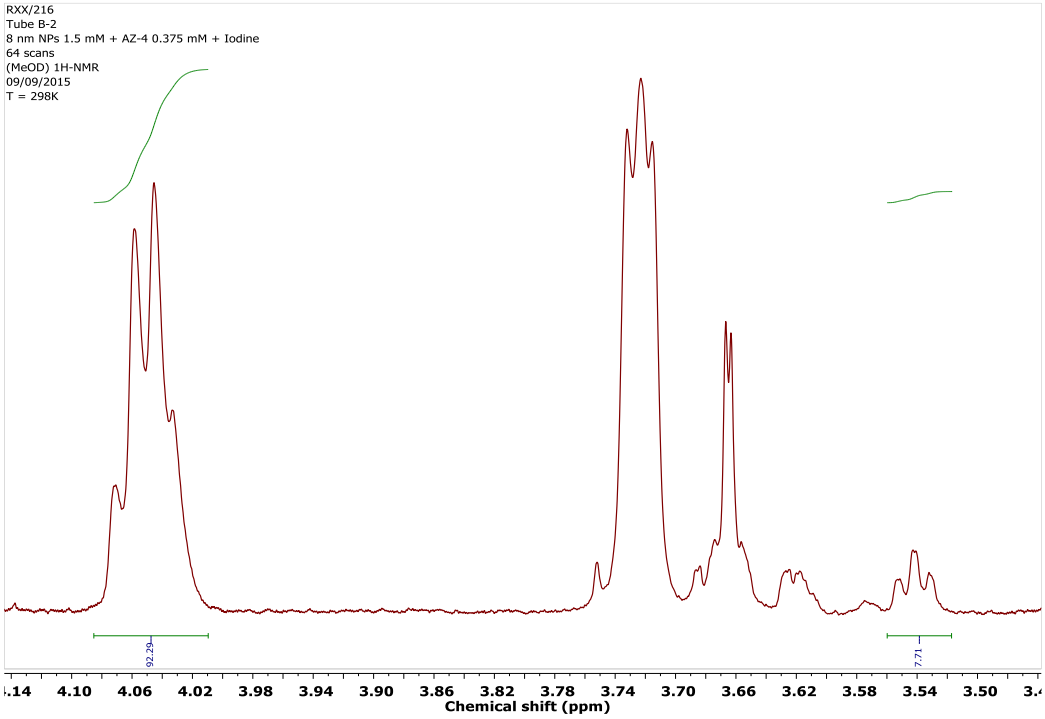

9 nm ZW – AZ-4 1:20

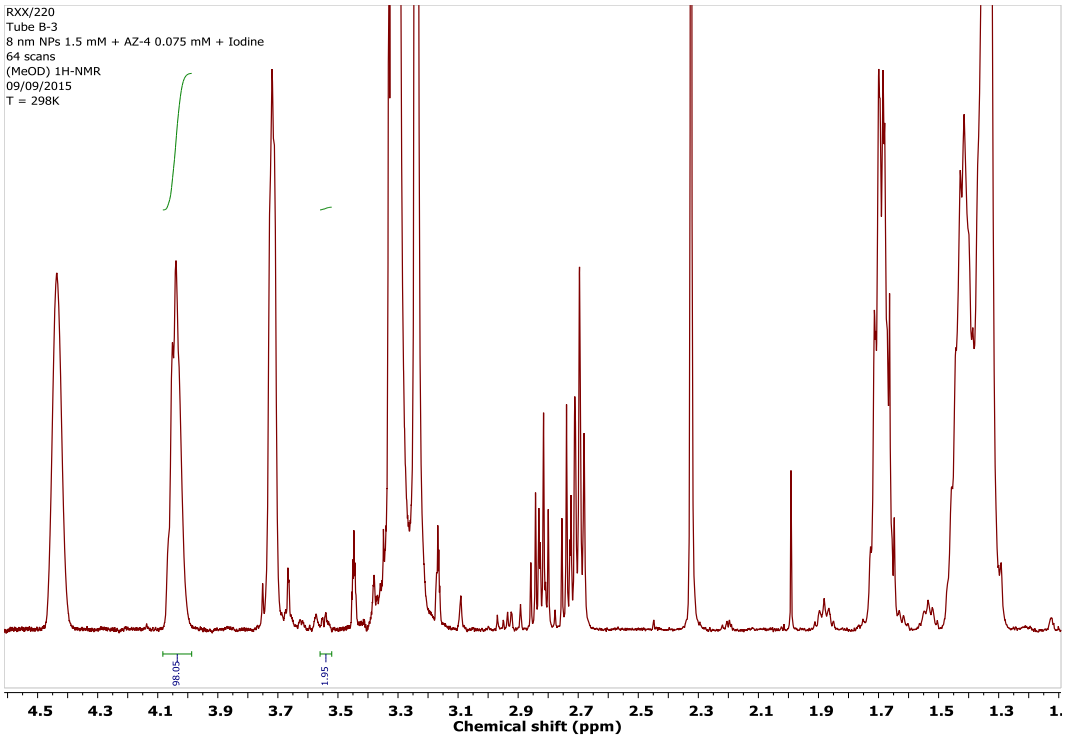

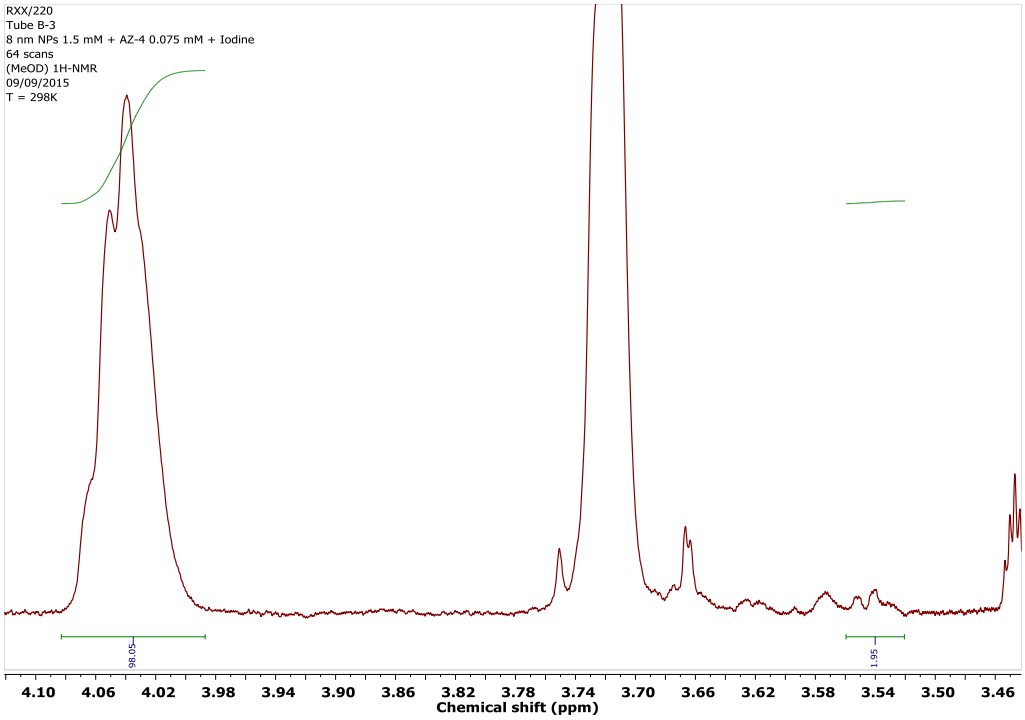
RXX/220
Tube B-3
8 nm NPs 1.5 mM + AZ-4 0.075 mM + Iodine
64 scans
(MeOD) 1H-NMR
09/09/2015
T = 298K
98.05
1.95
4.10 4.06 4.02 3.98 3.94 3.90 3.86 3.82 3.78 3.74 3.70 3.66 3.62 3.58 3.54 3.50 3.46
Chemical shift (ppm)

9 nm ZW – AZ-6 1:1

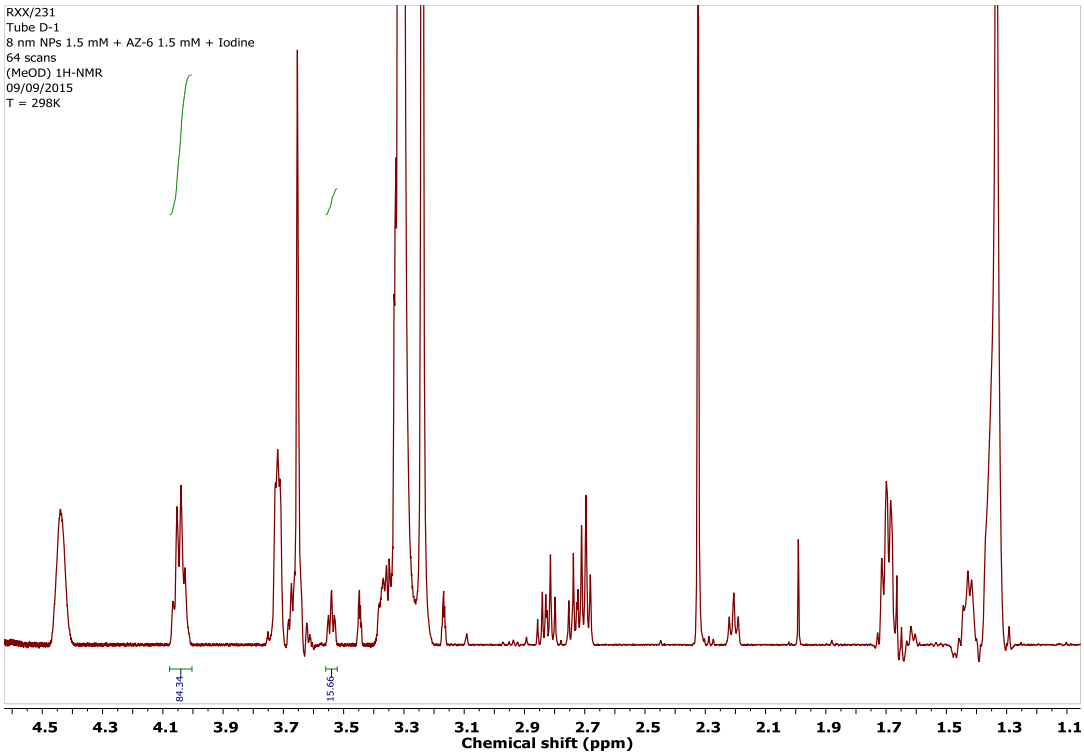
RXX/231
Tube D-1
8 nm NPs 1.5 mM + AZ-6 1.5 mM + Iodine
64 scans
(MeOD) 1H-NMR
09/09/2015
T = 298K
84.34
15.66
4.5 4.3 4.1 3.9 3.7 3.5 3.3 3.1 2.9 2.7 2.5 2.3 2.1 1.9 1.7 1.5 1.3 1.1
Chemical shift (ppm)

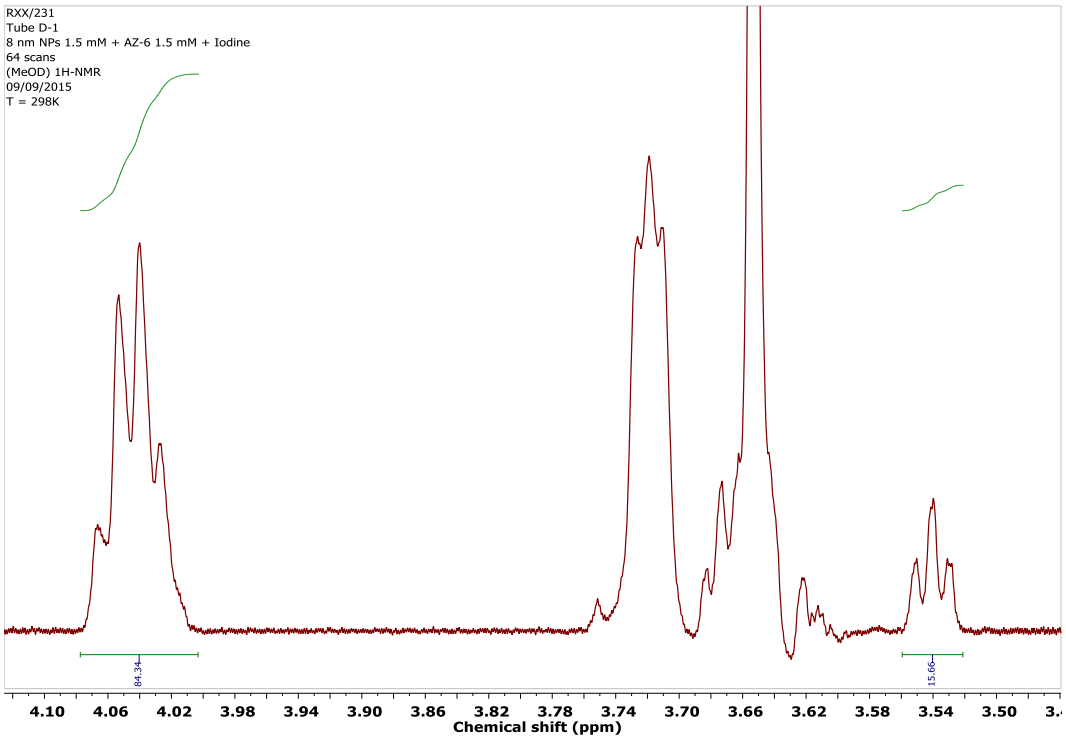
RXX/231
Tube D-1
8 nm NPs 1.5 mM + AZ-6 1.5 mM + Iodine
64 scans
(MeOD) 1H-NMR
09/09/2015
T = 298K
84.34
15.66
4.10 4.06 4.02 3.98 3.94 3.90 3.86 3.82 3.78 3.74 3.70 3.66 3.62 3.58 3.54 3.50
Chemical shift (ppm)

9 nm ZW – AZ-6 1:4

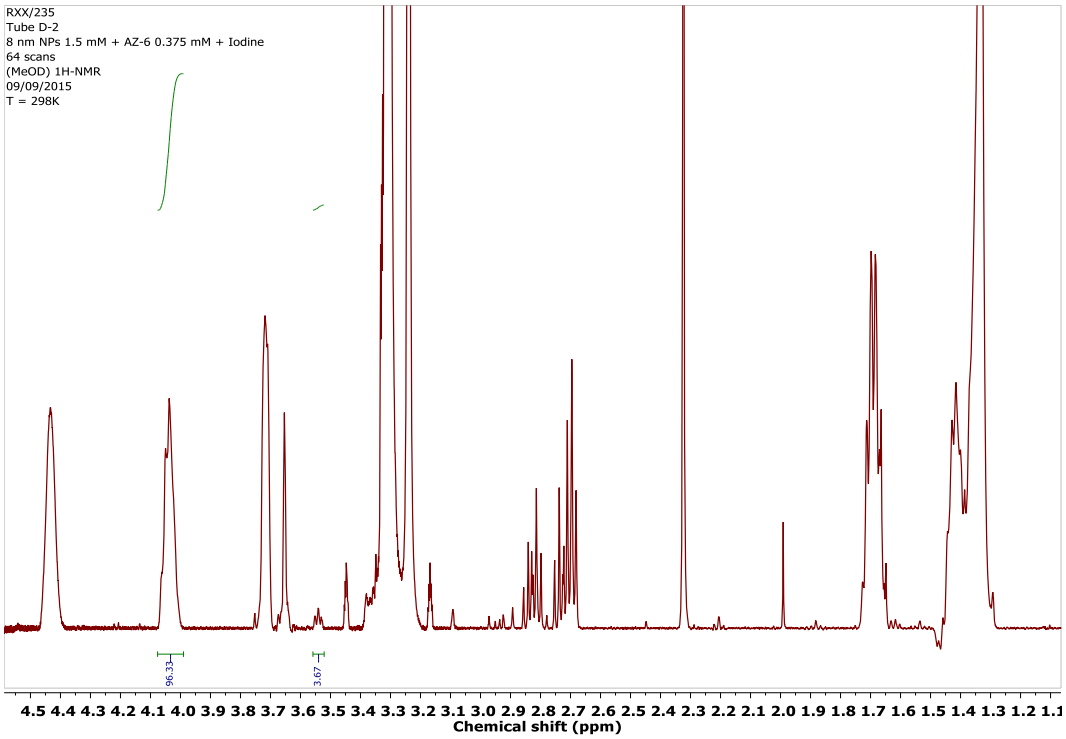
RXX/235
Tube D-2
8 nm NPs 1.5 mM + AZ-6 0.375 mM + Iodine
64 scans
(MeOD) 1H-NMR
09/09/2015
T = 298K
96.33
3.67
4.5 4.4 4.3 4.2 4.1 4.0 3.9 3.8 3.7 3.6 3.5 3.4 3.3 3.2 3.1 3.0 2.9 2.8 2.7 2.6 2.5 2.4 2.3 2.2 2.1 2.0 1.9 1.8 1.7 1.6 1.5 1.4 1.3 1.2
Chemical shift (ppm)

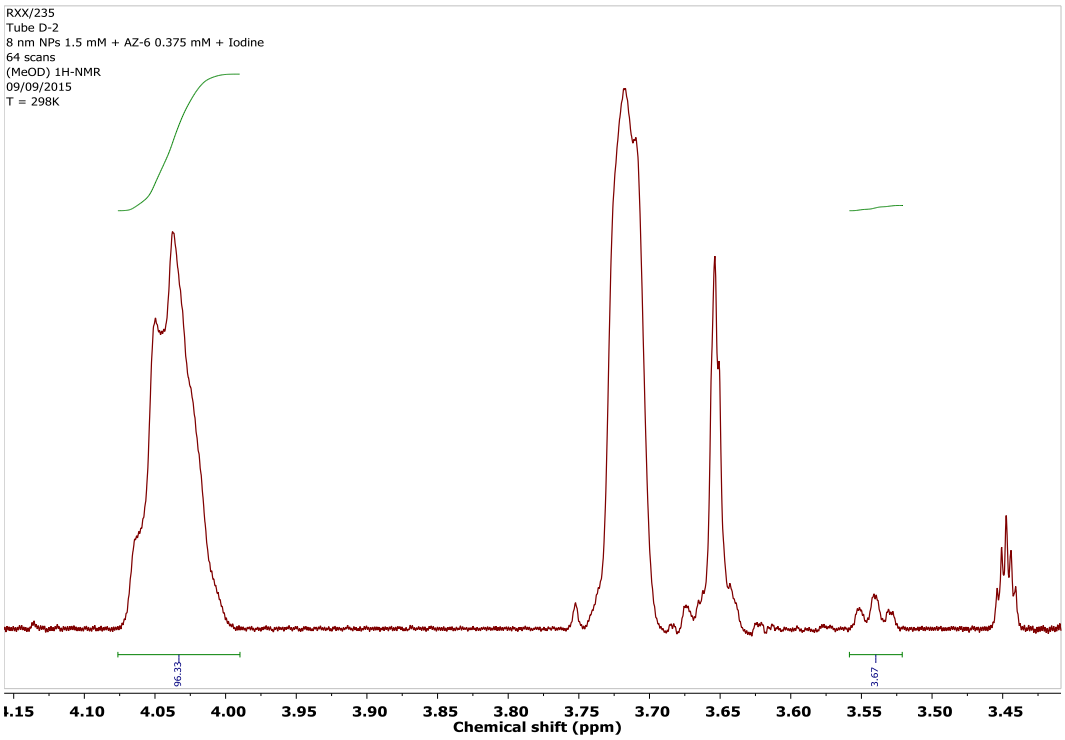

9 nm ZW – AZ-6 1:20

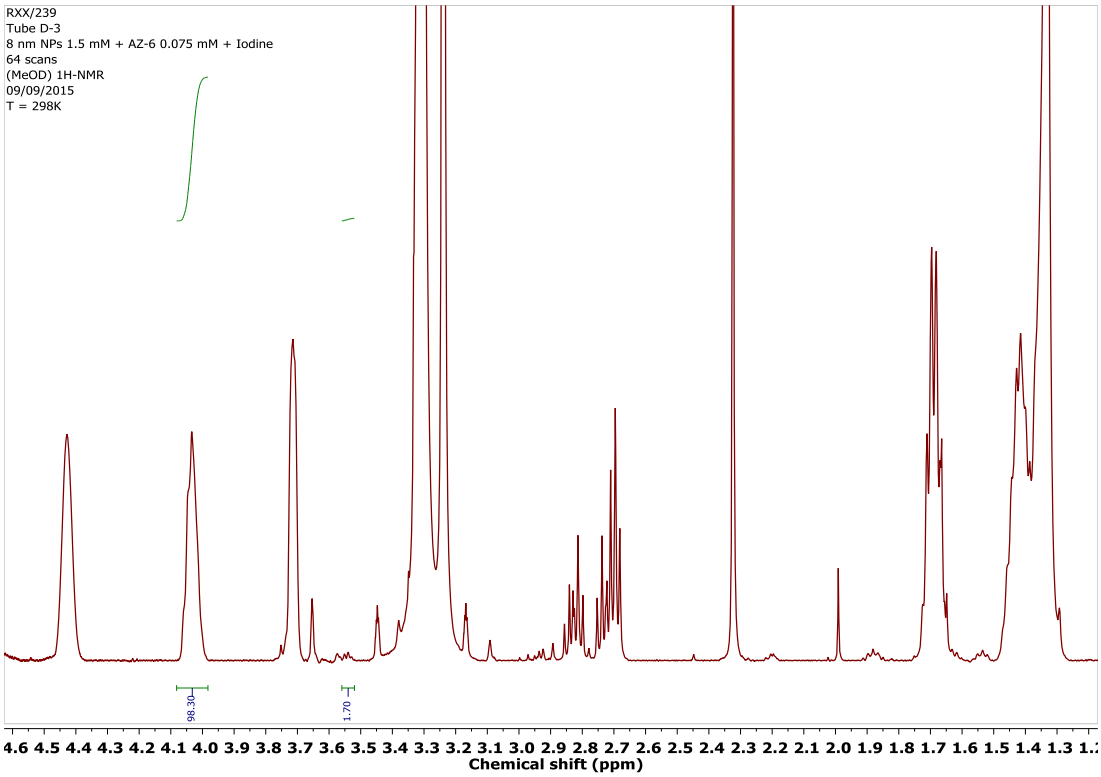

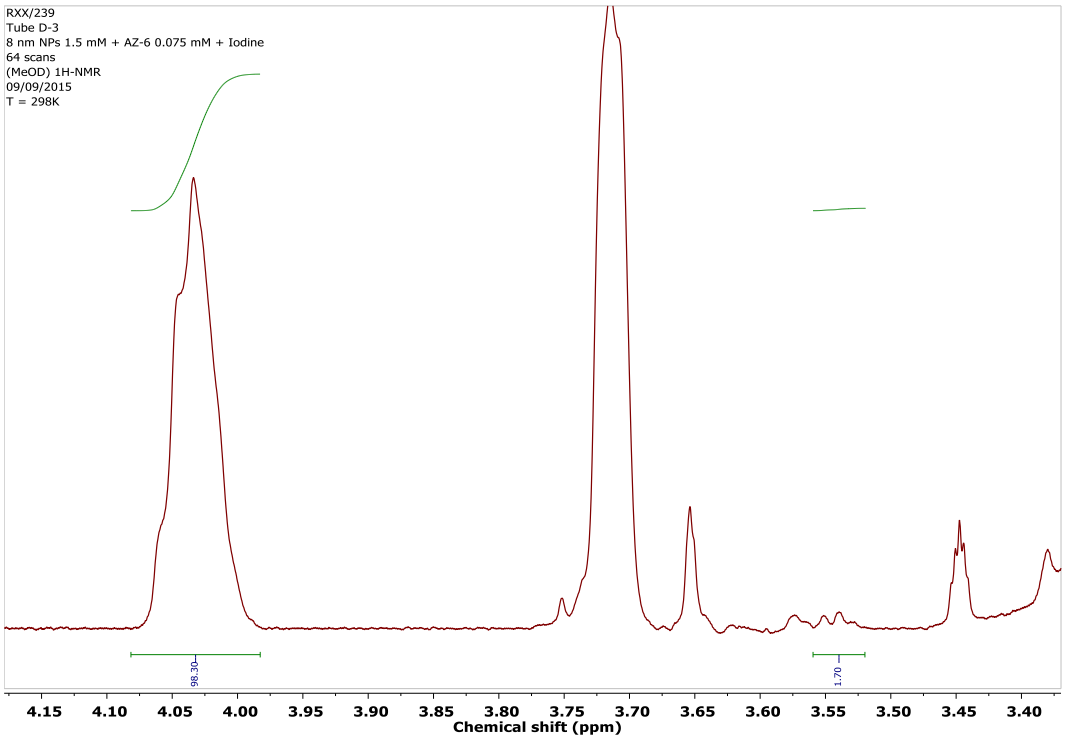

2 nm TMA – AZ-4 1:1

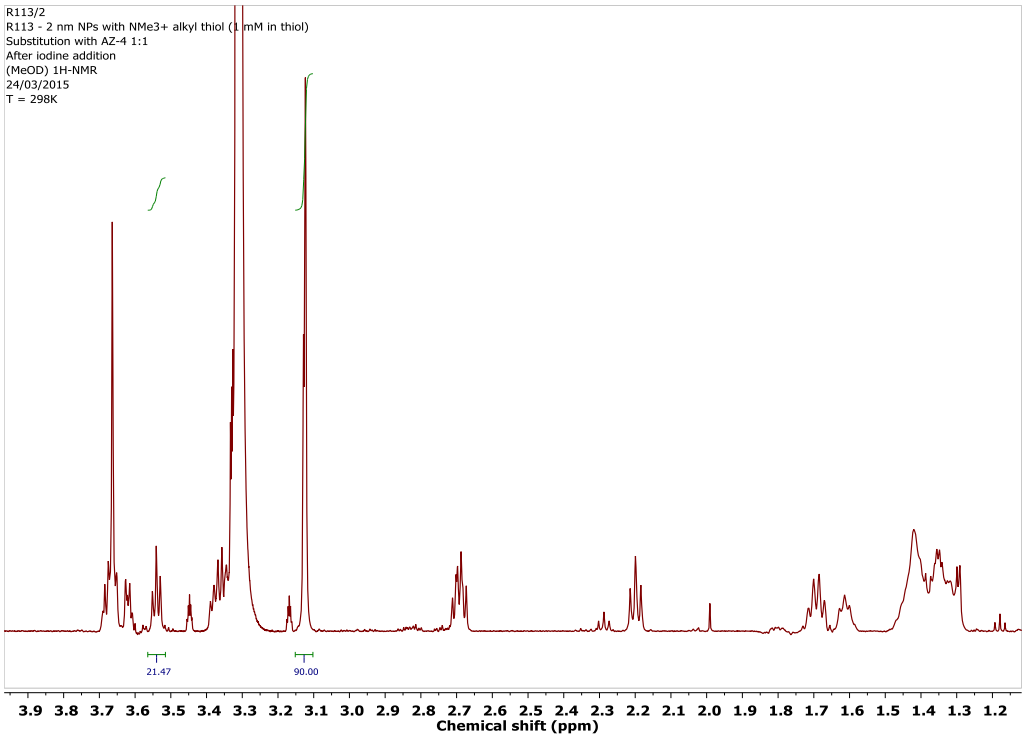

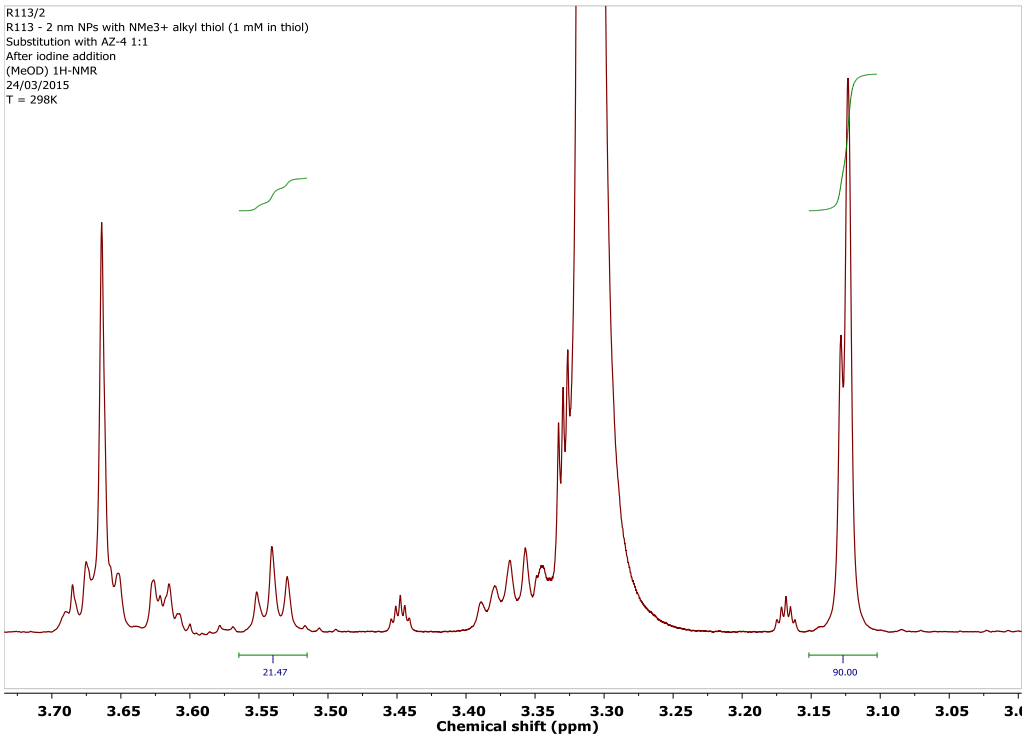

2 nm TMA – AZ-4 1:4

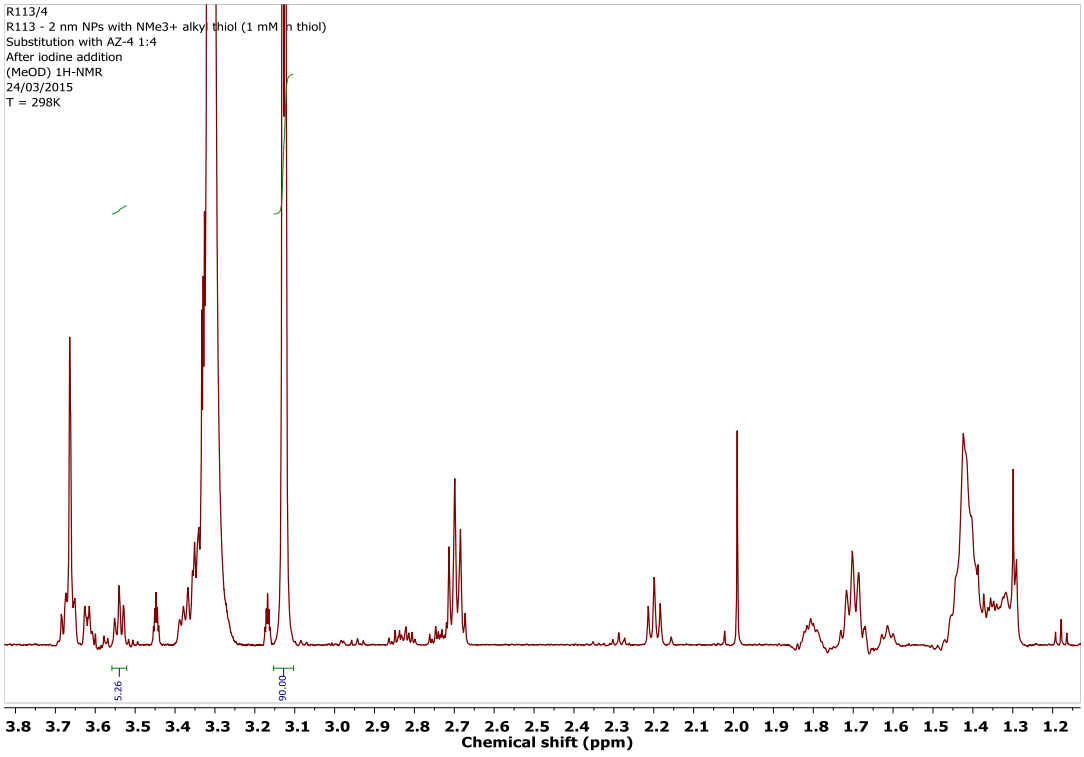

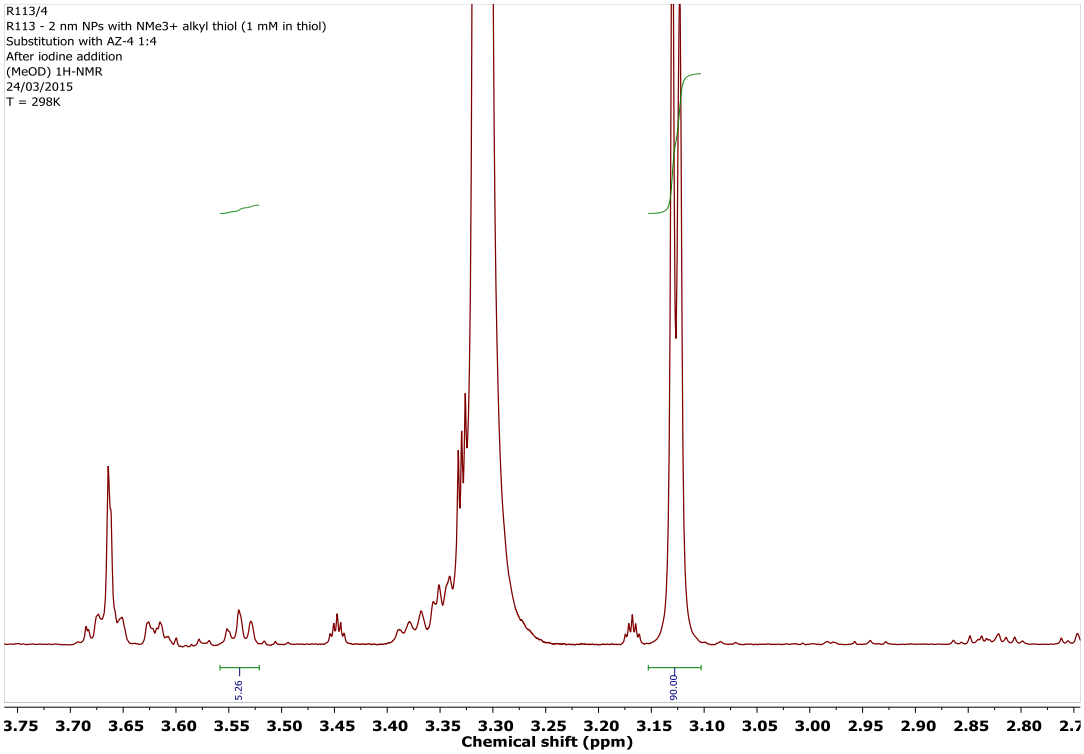

2 nm TMA – AZ-4 1:20

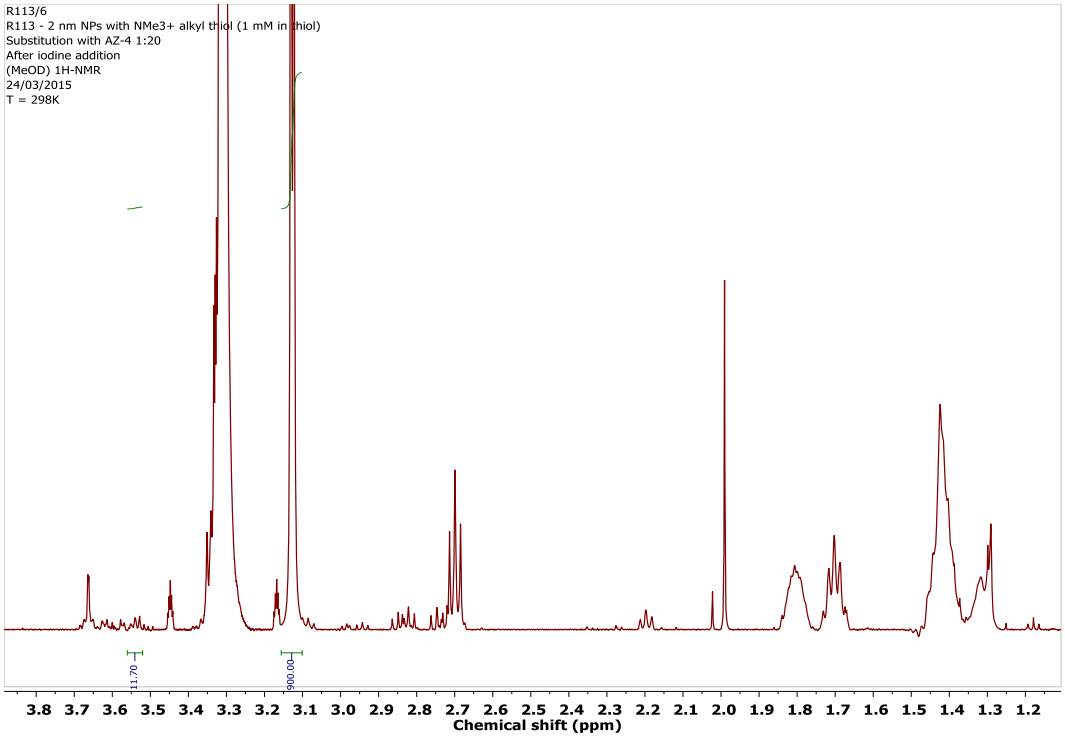

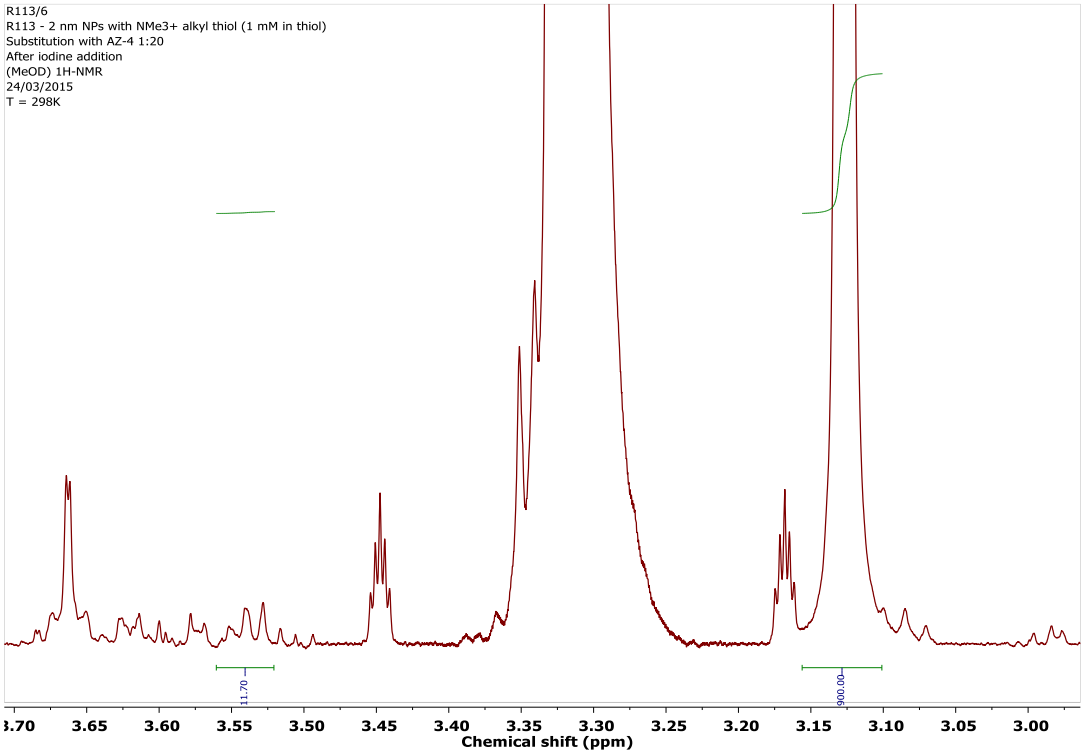

2 nm TMA – AZ-6 1:1

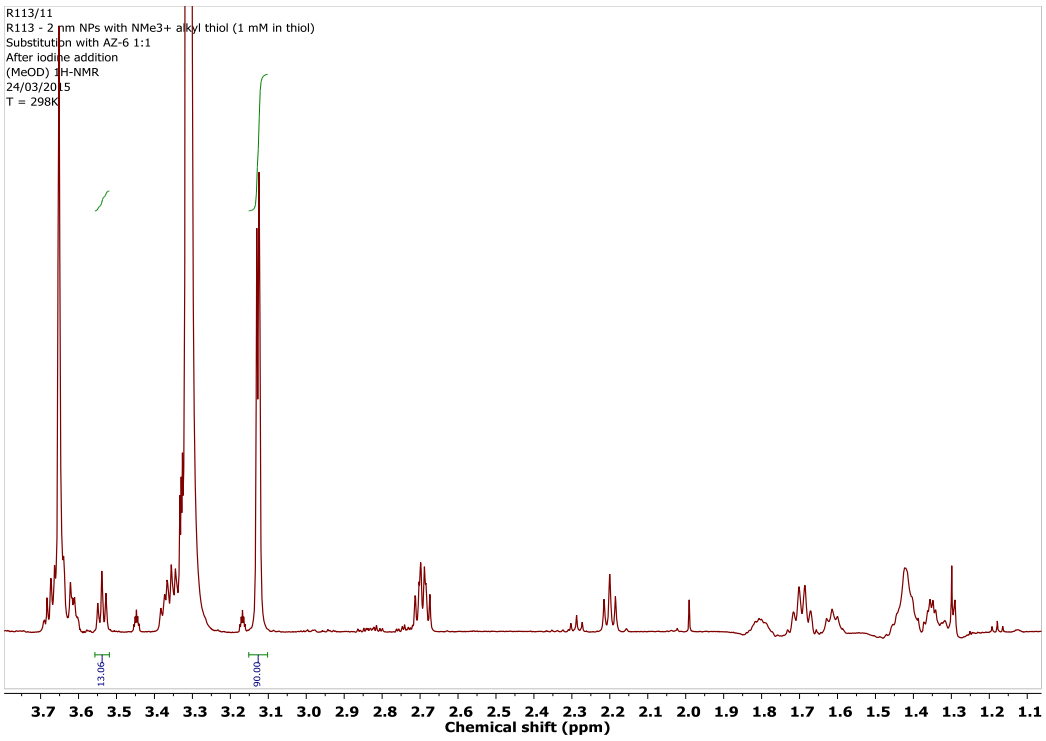

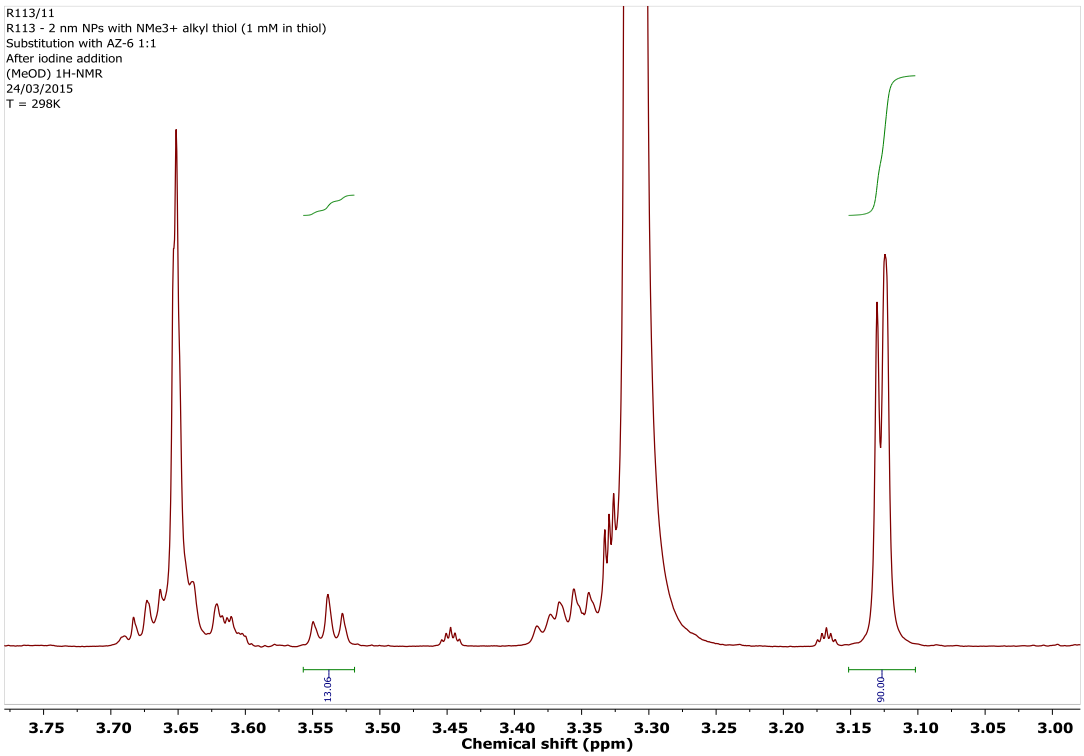

2 nm TMA – AZ-6 1:4

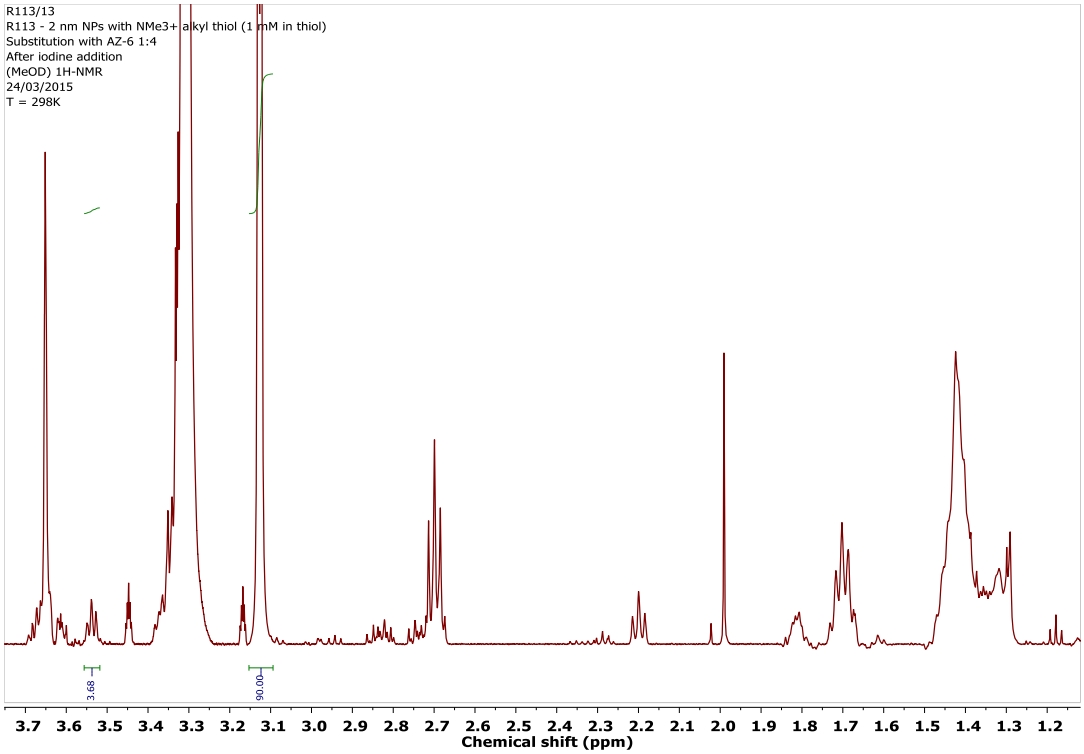

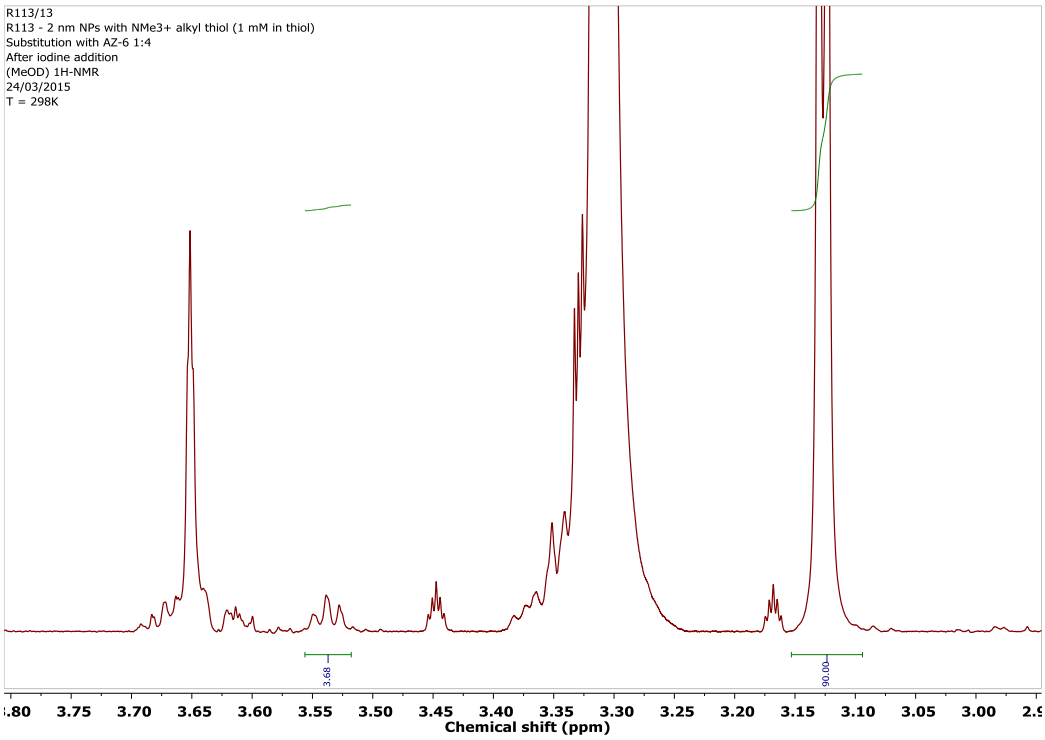

2 nm TMA – AZ-6 1:20

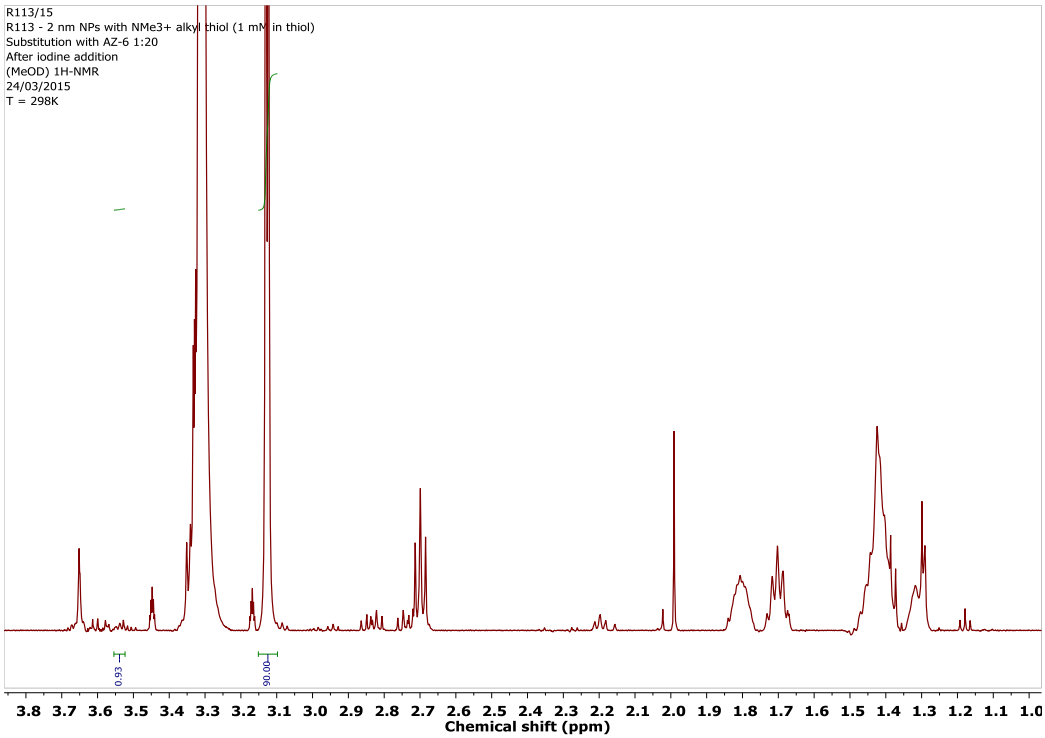

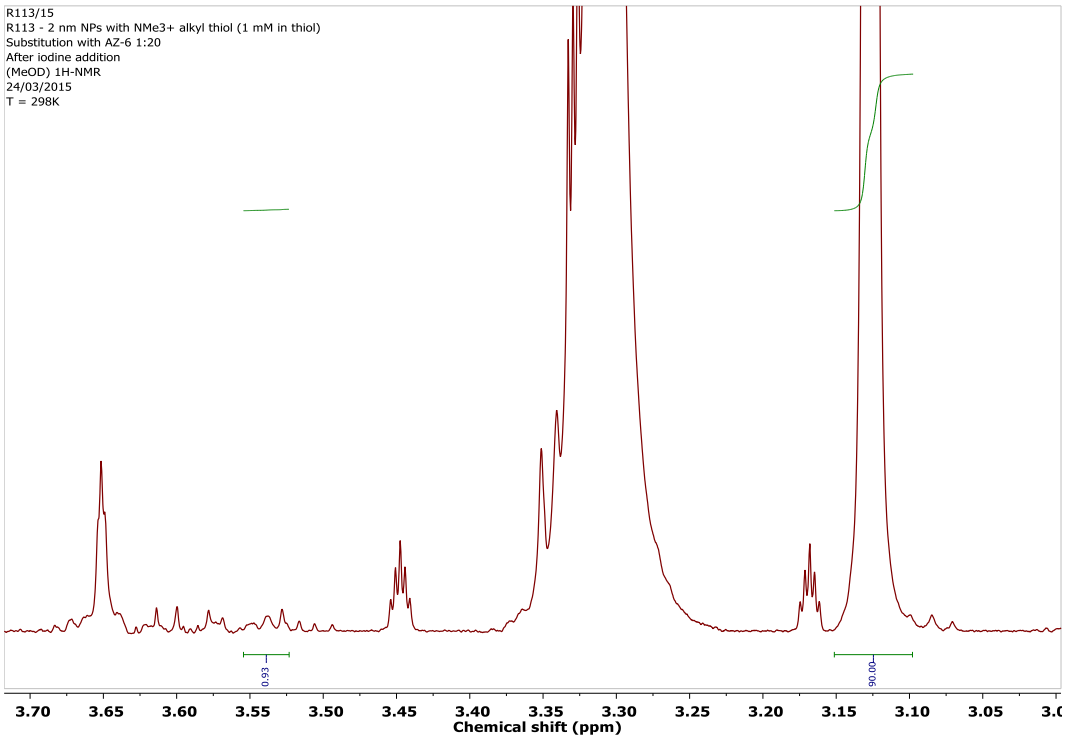

9 nm TEG nanoparticles (only TEG thiol, for integral reference)

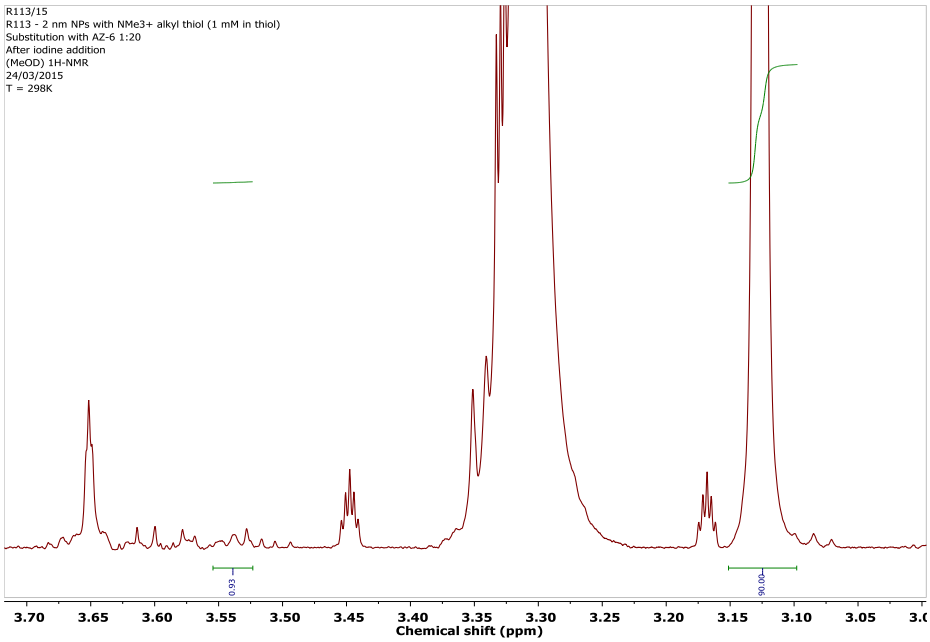

AZ-6 (for integral reference when integrating exchanges with TEG NPs)

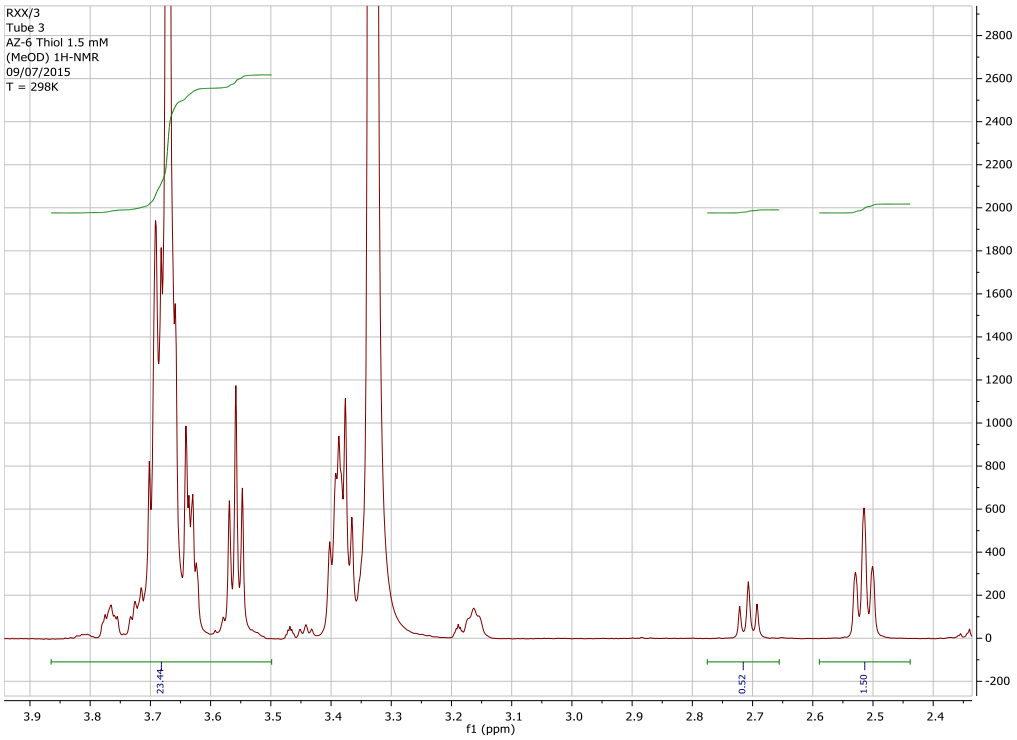

9 nm TEG – AZ-6 1:1

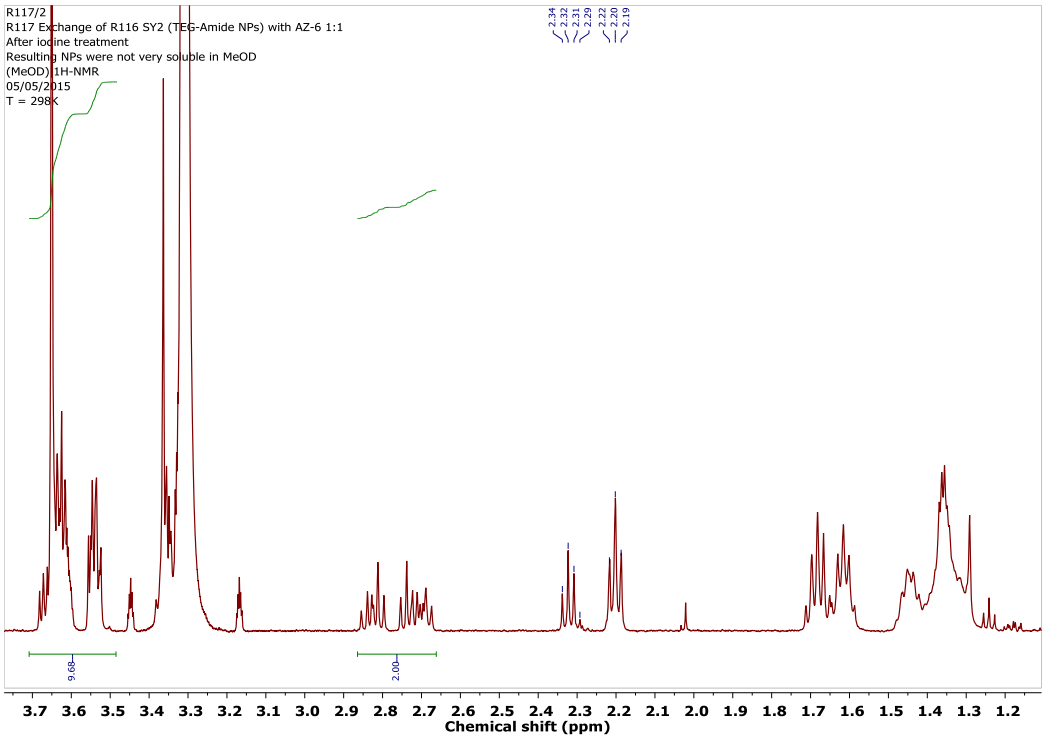

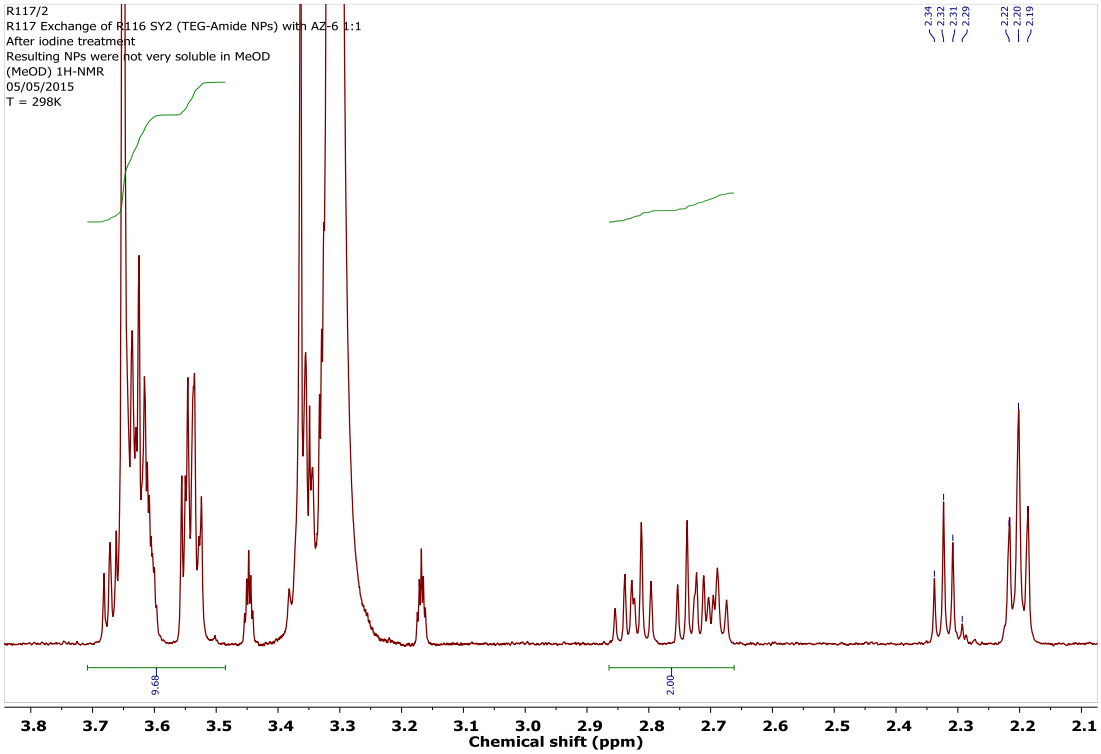

9 nm TEG – AZ-6 1:4

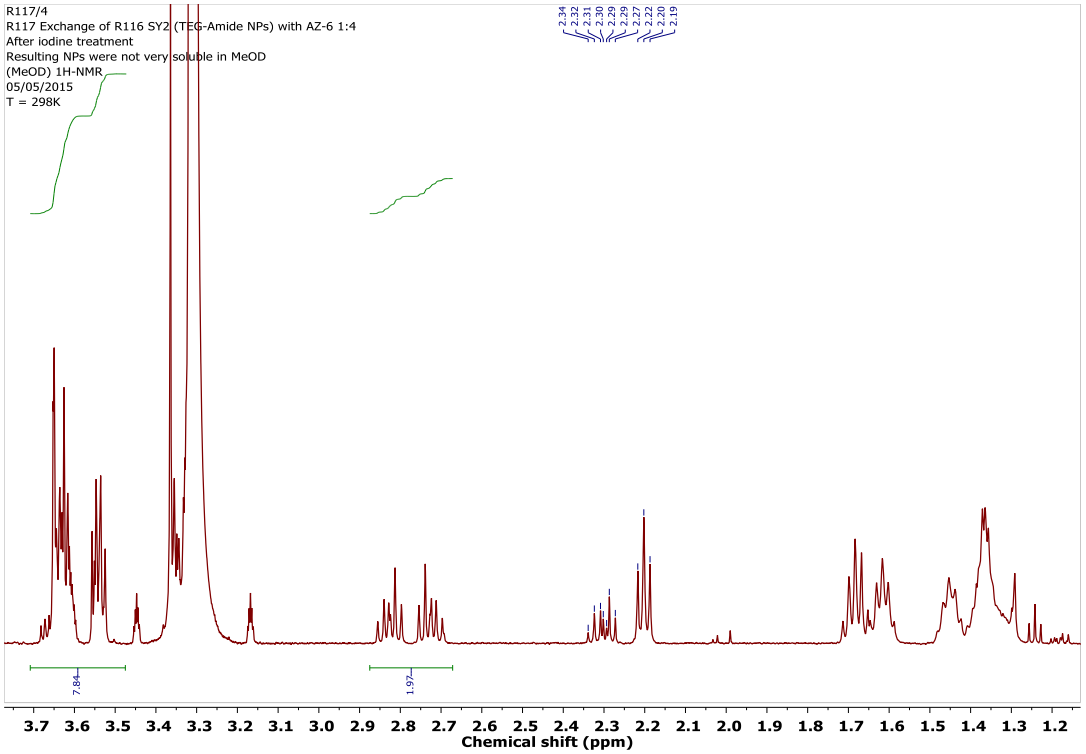

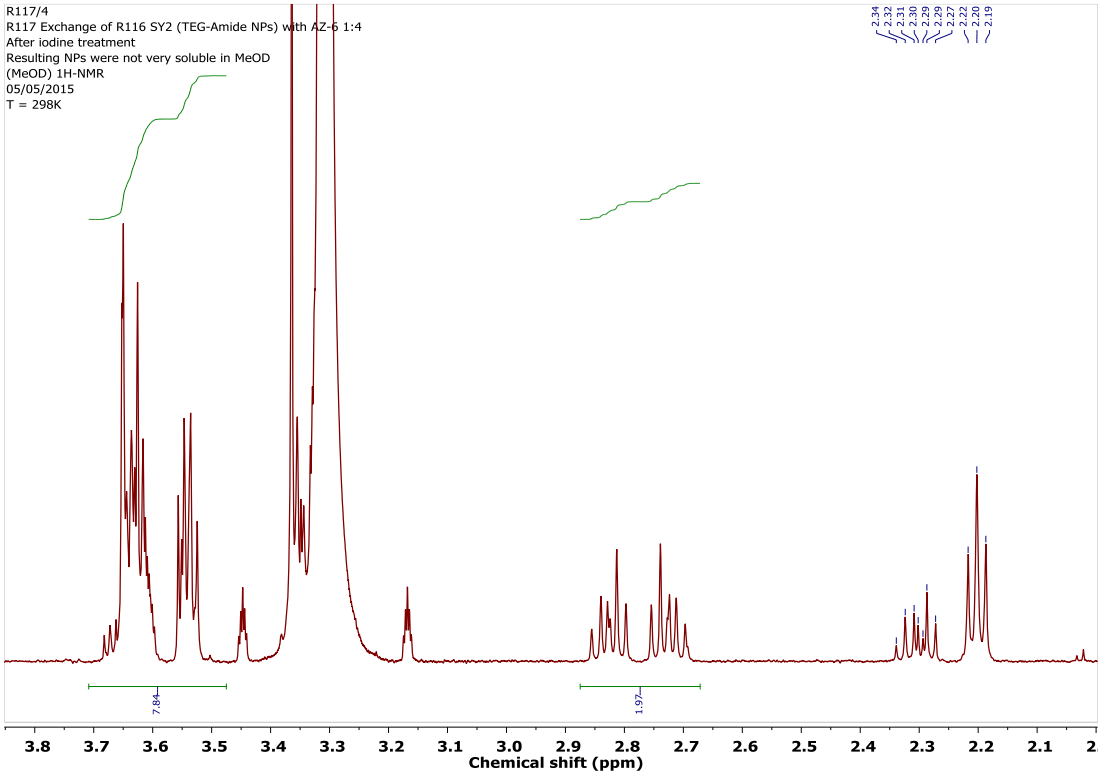

9 nm ZW – Biot-4 1:1

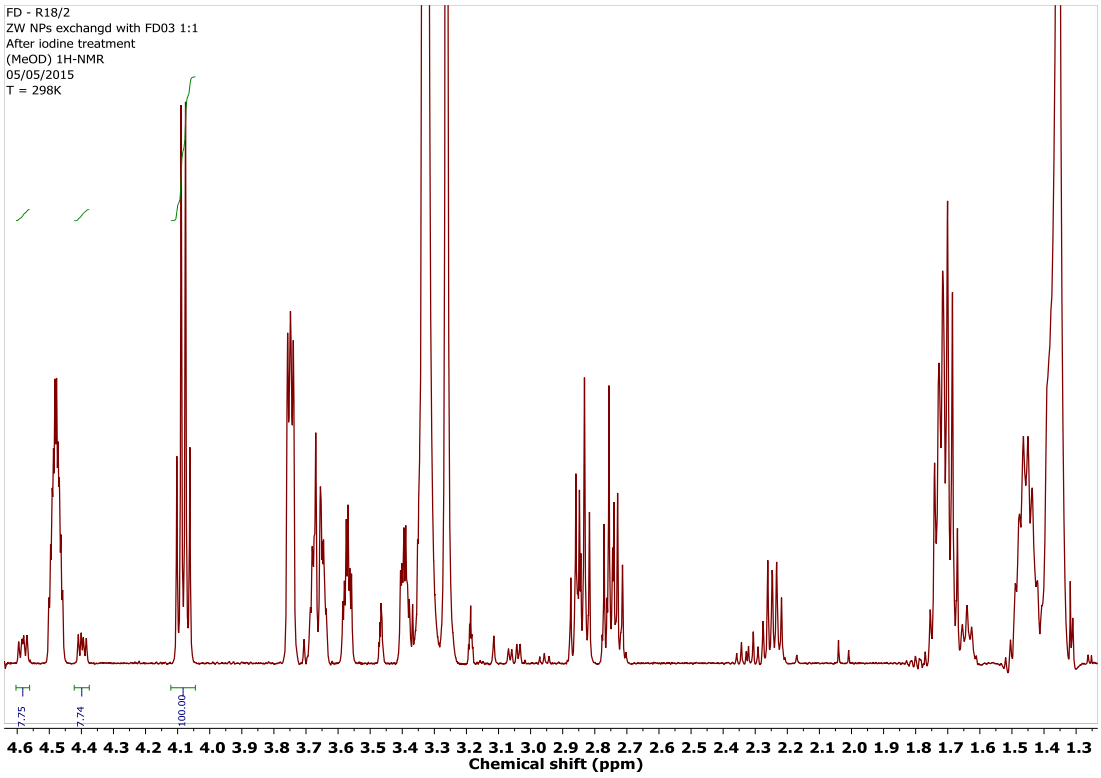

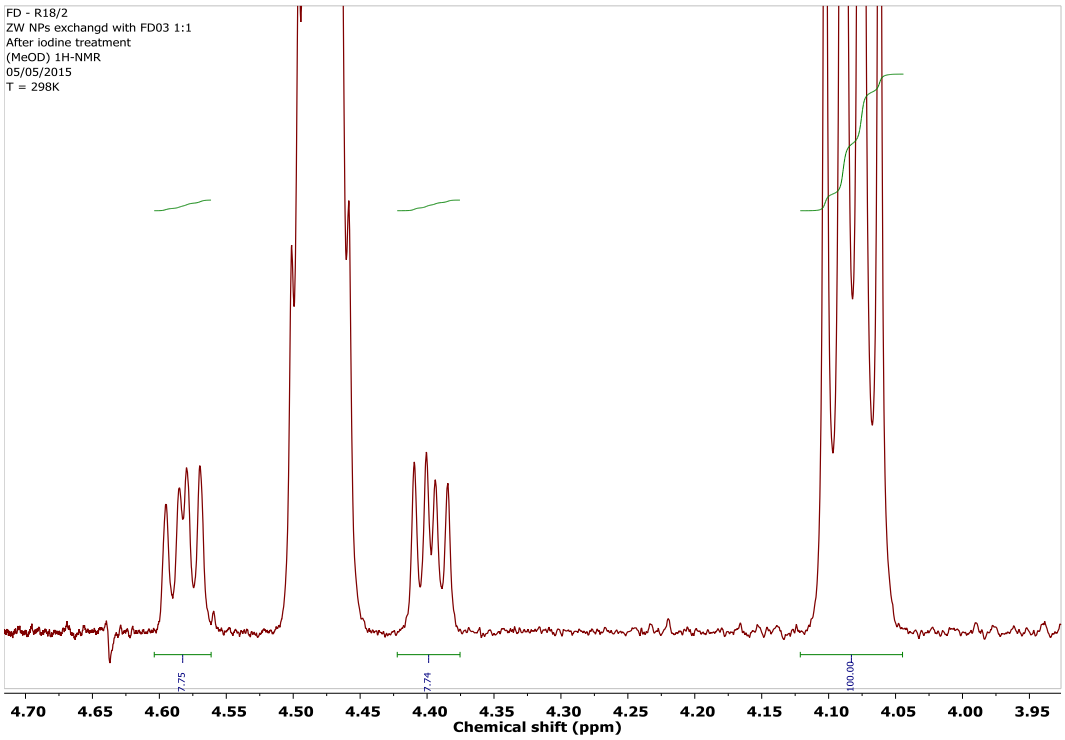

9 nm TEG – Biot-4 1:1

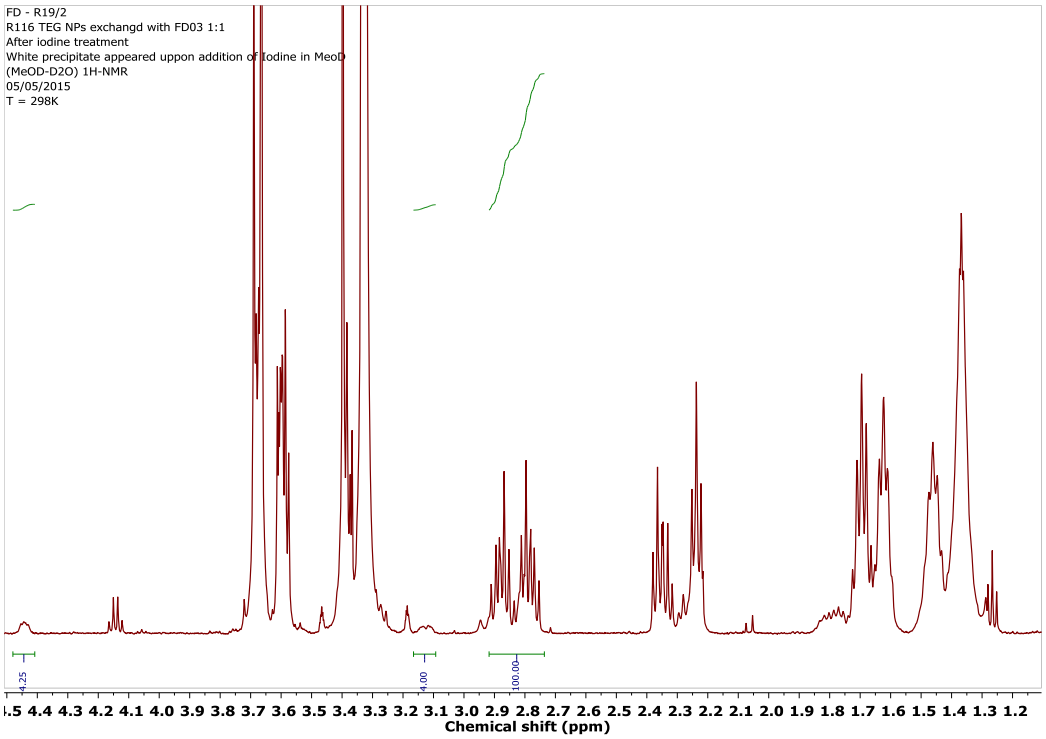

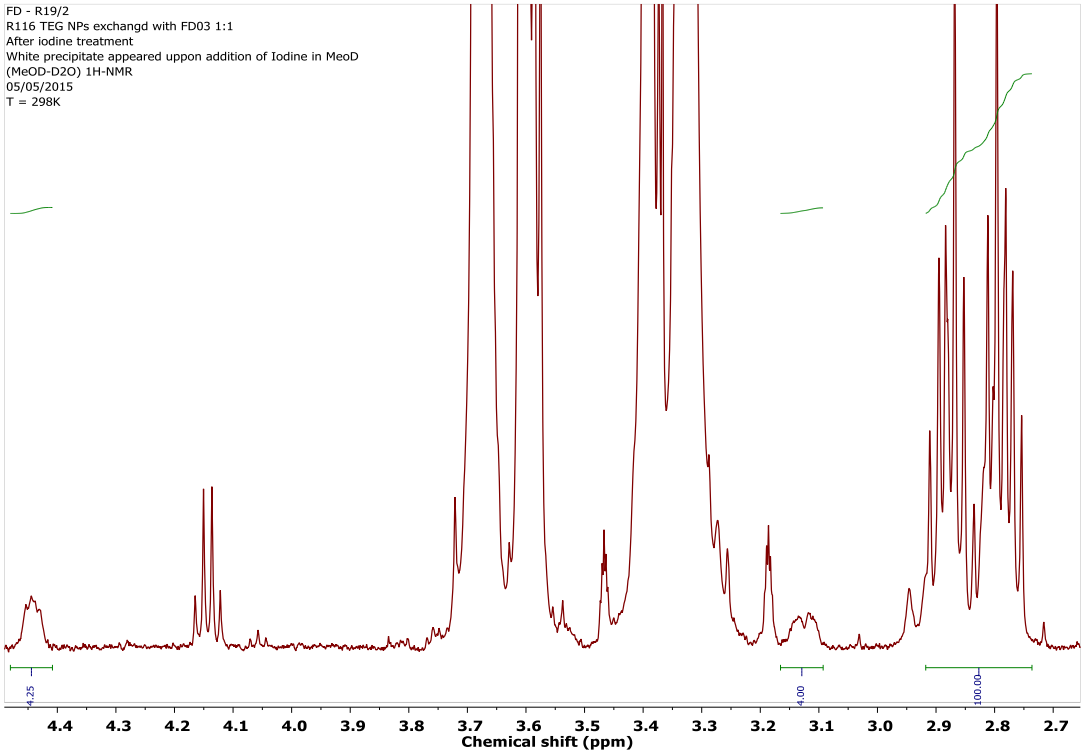

9 nm ZW – Biot-6 1:1

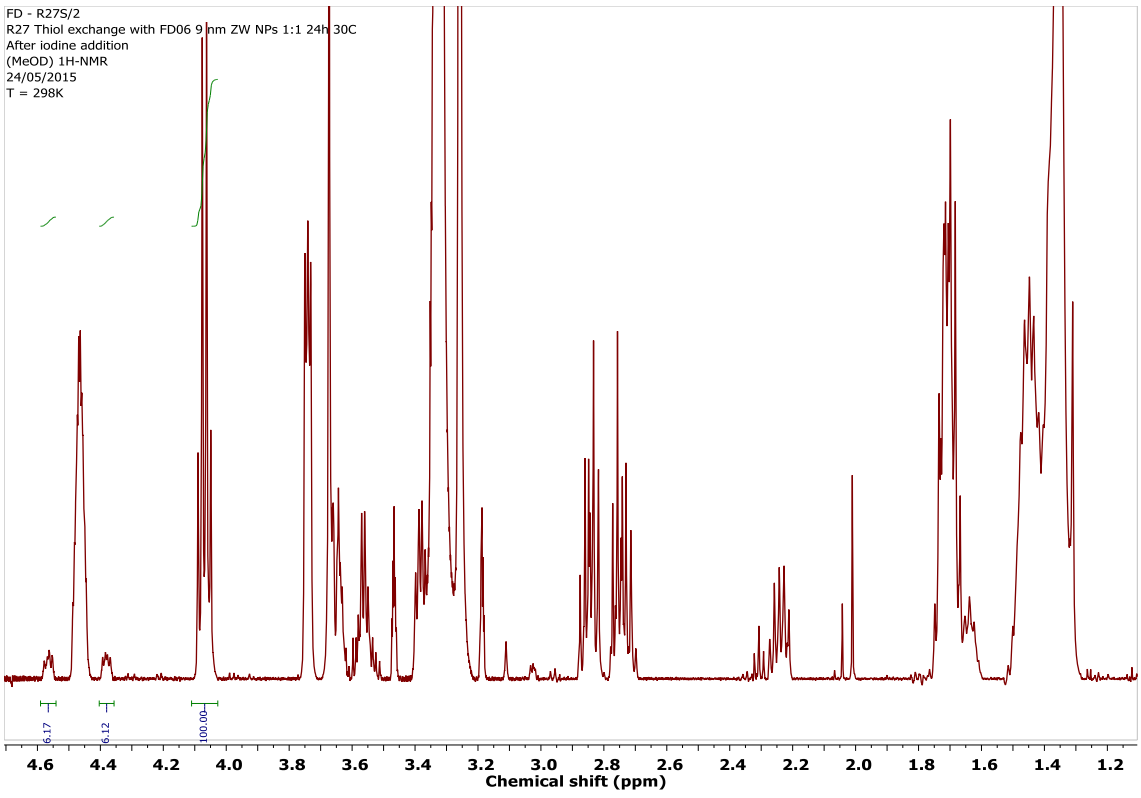

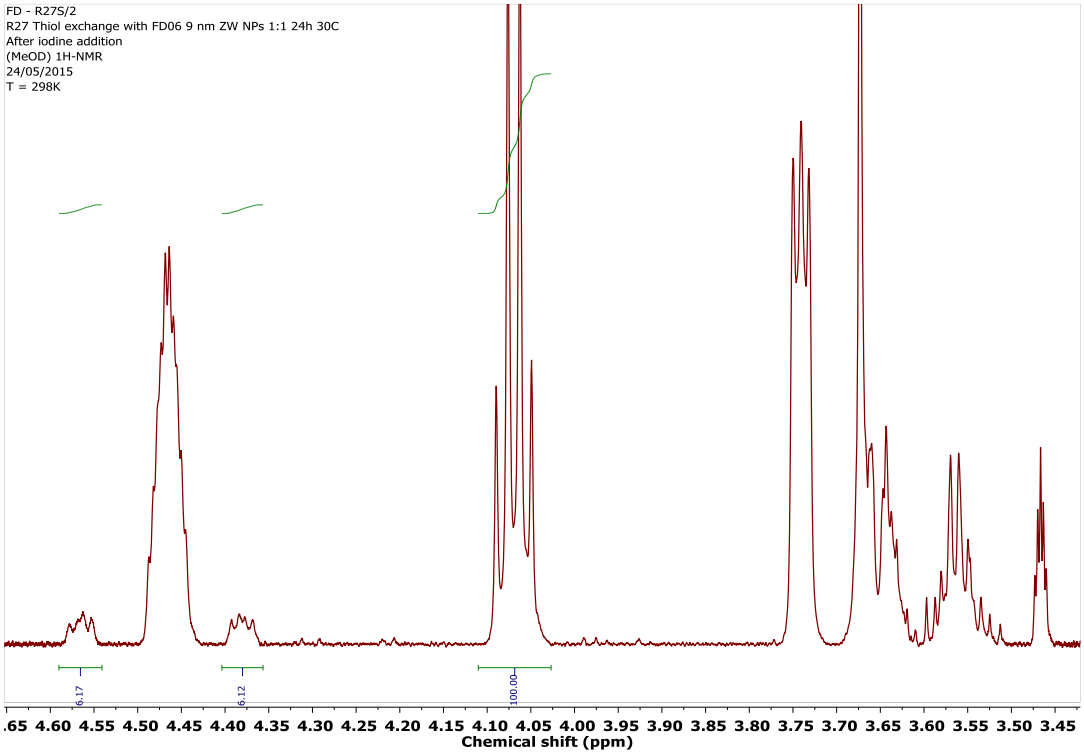

9 nm ZW – Naprox (6) 1:4

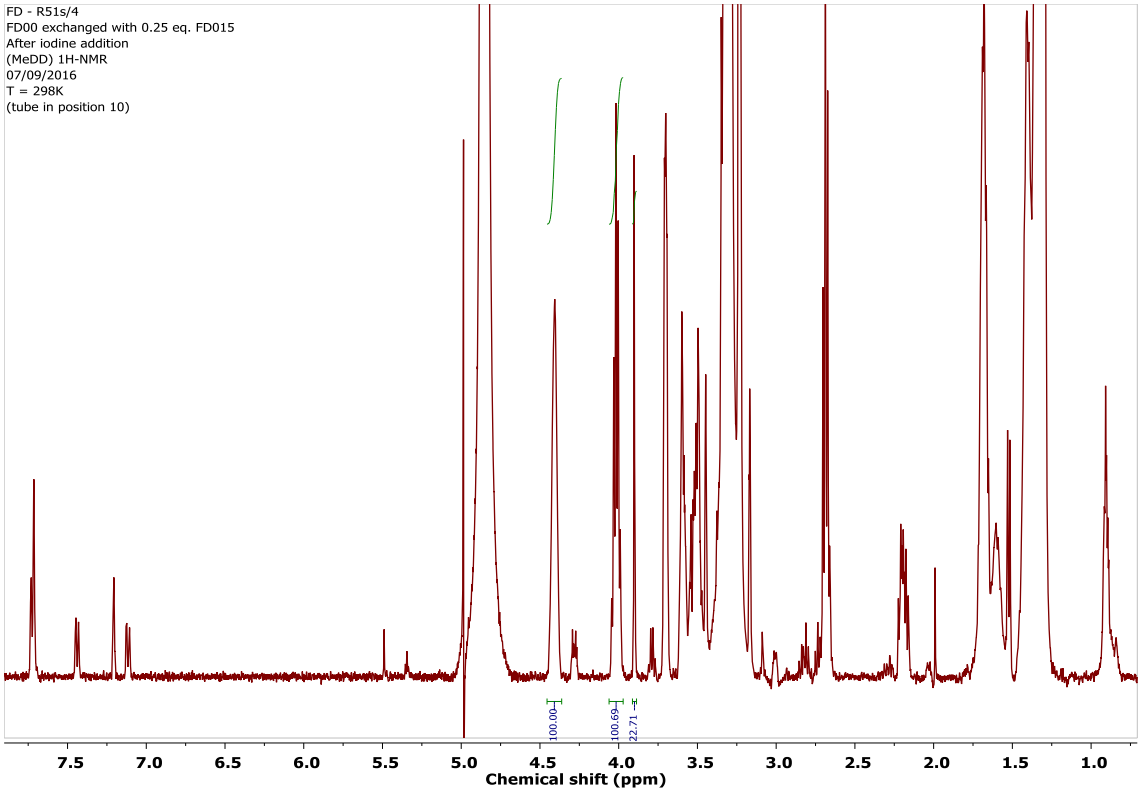

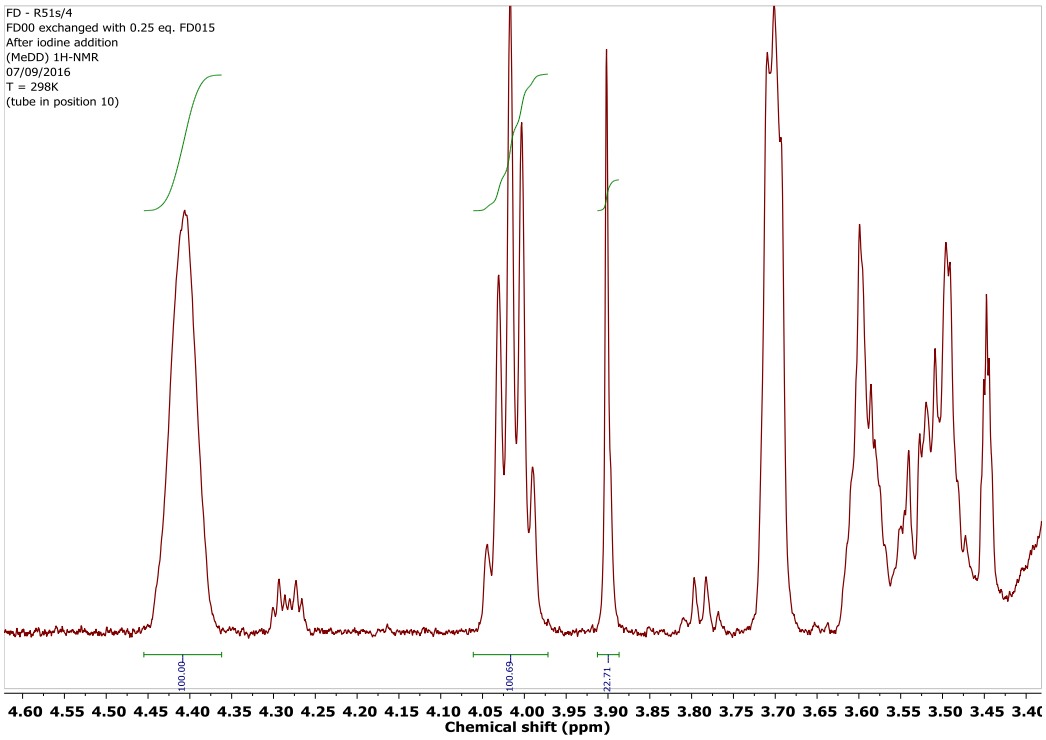

9 nm ZW – Naprox (6) 1:20

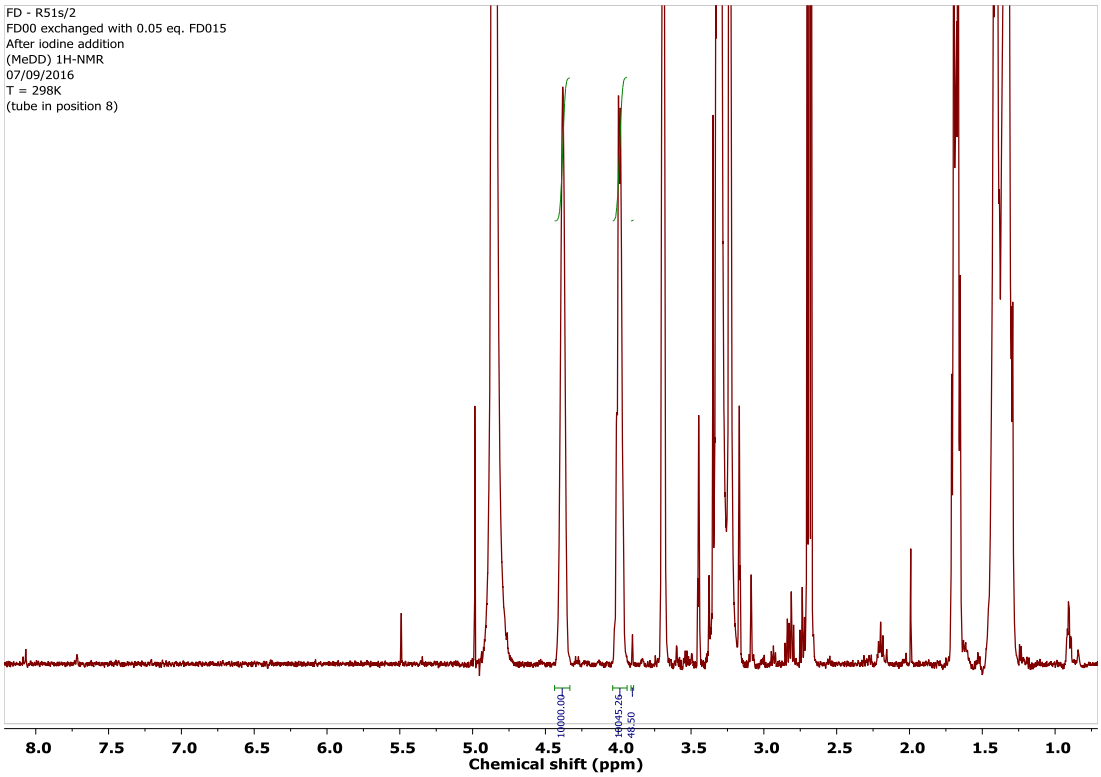

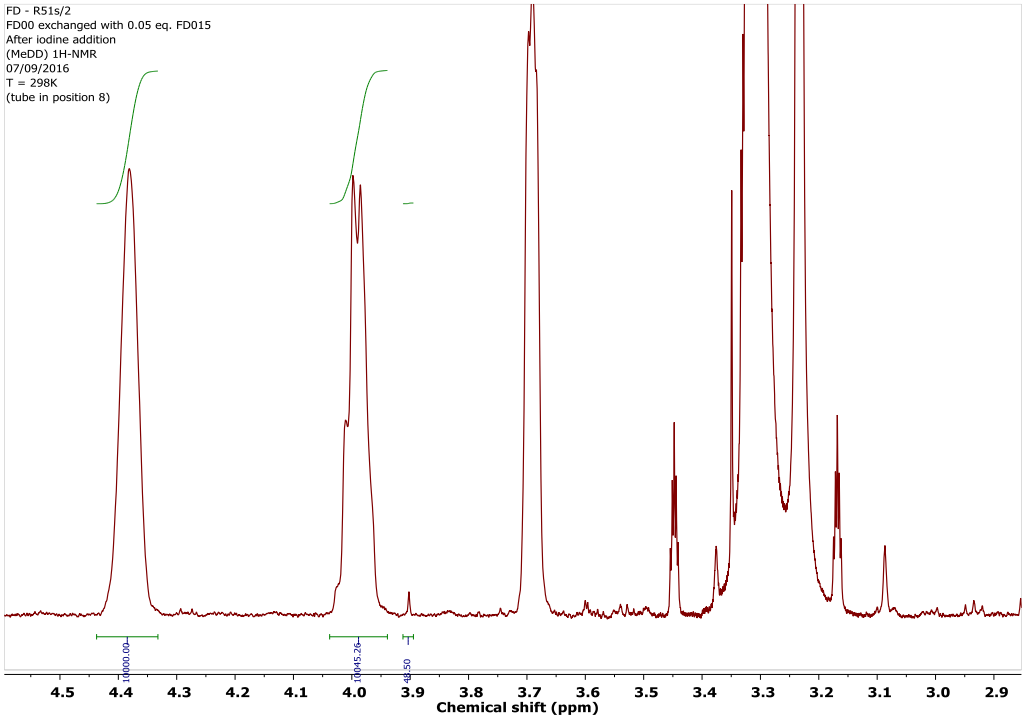

9 nm ZW Mixed exchange– Naprox 1:2 + Biot-6 1:2 (Water soluble fraction)

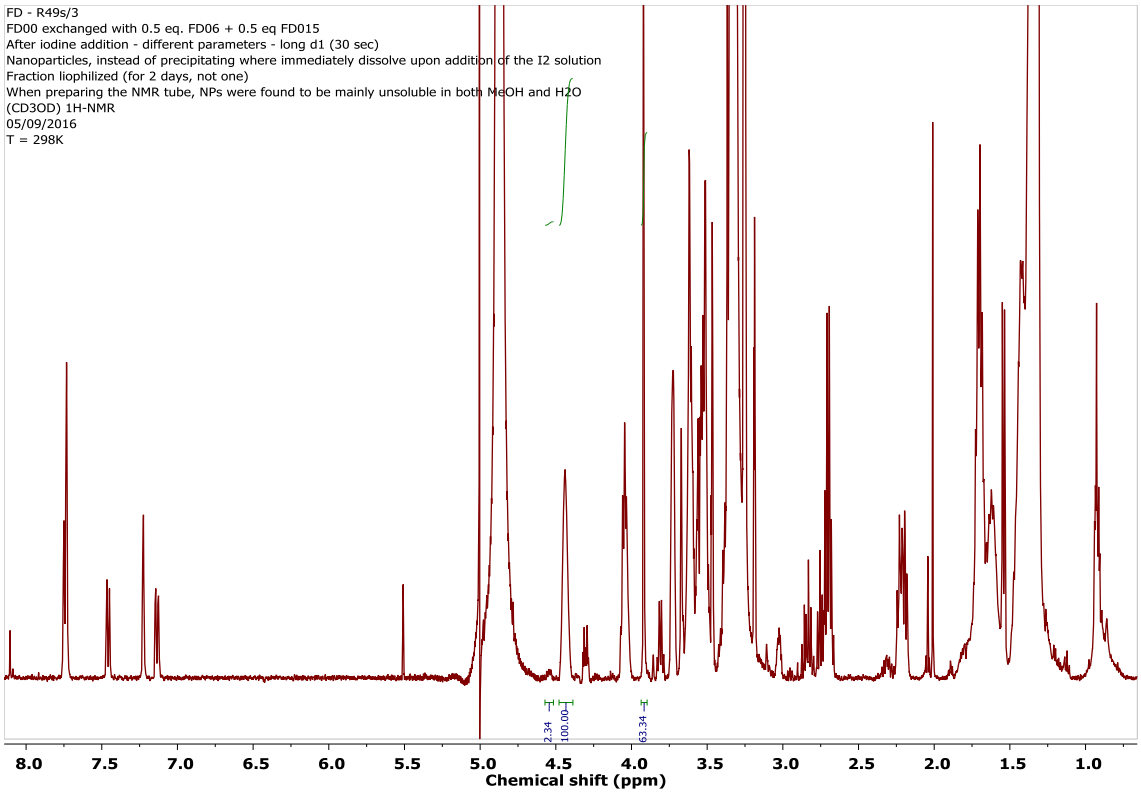

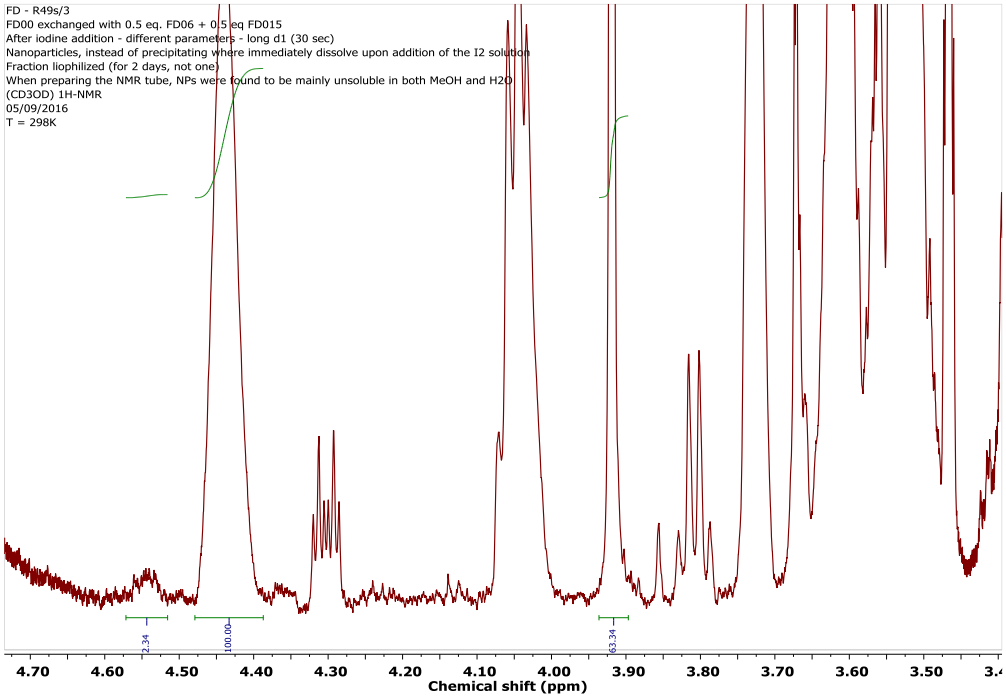

9 nm ZW Mixed exchange– Naprox 1:2 + Biot-6 1:2 (Methanol soluble fraction)

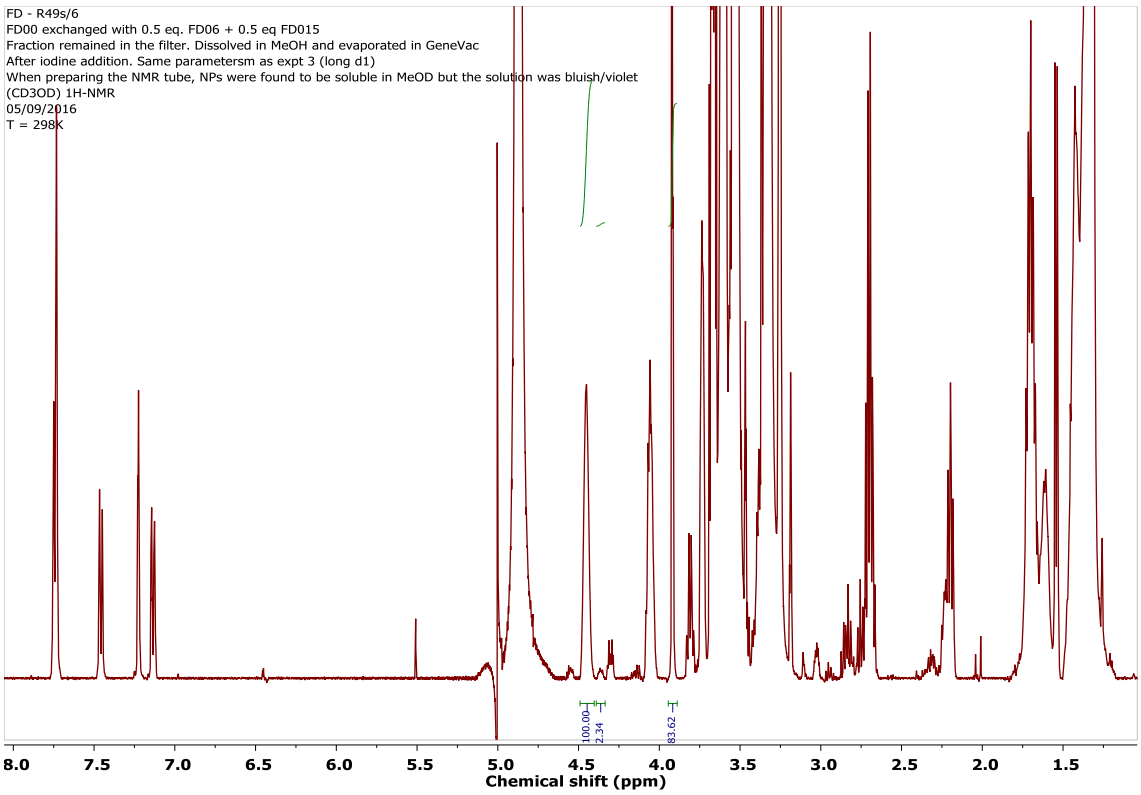

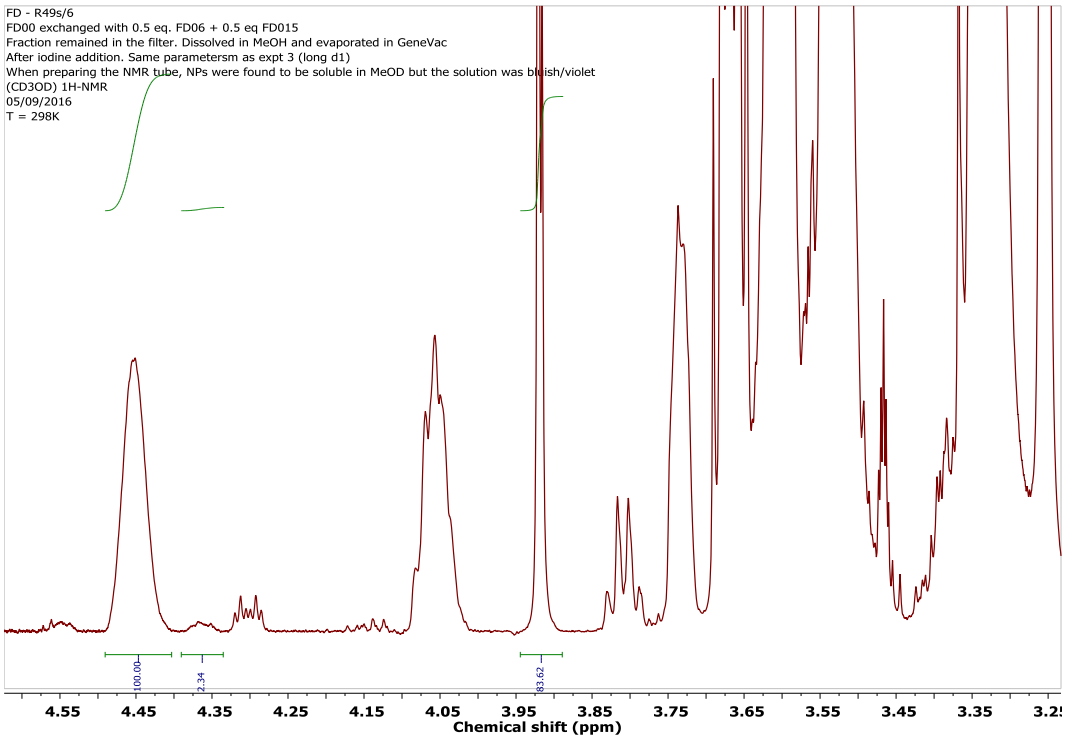

9 nm ZW Mixed exchange– Naprox 1:7 + Biot-6 1:1.25

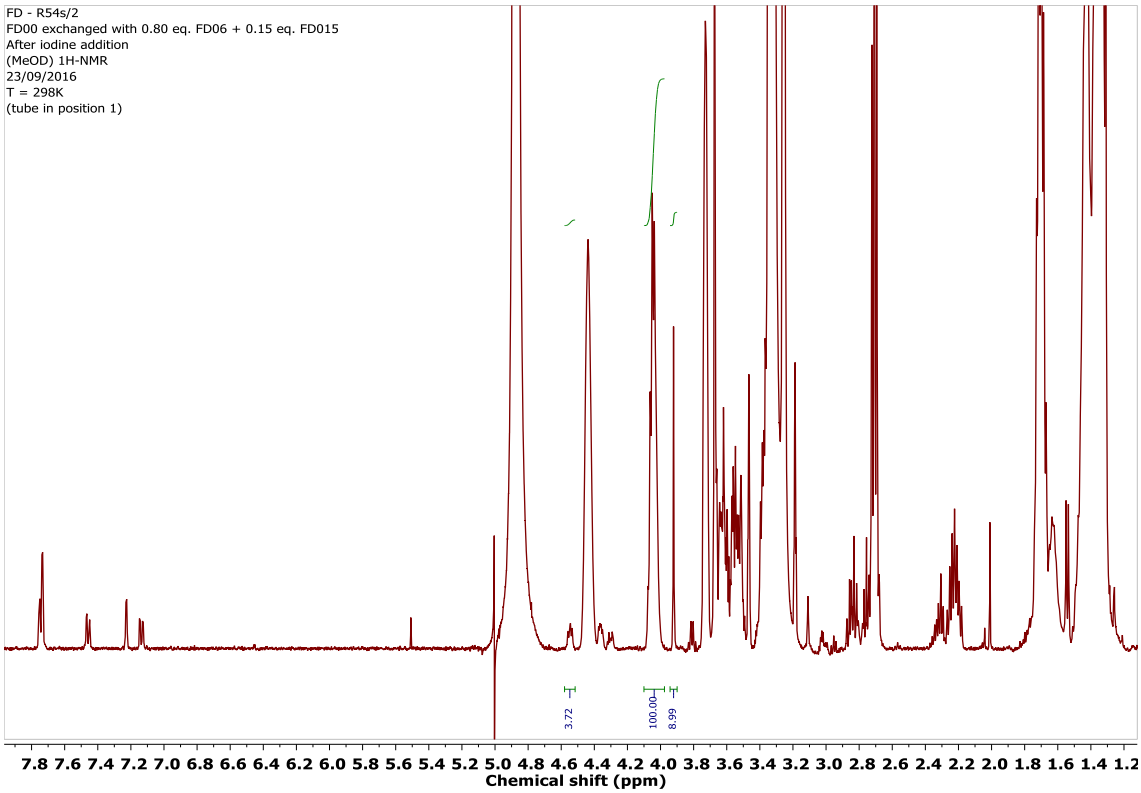

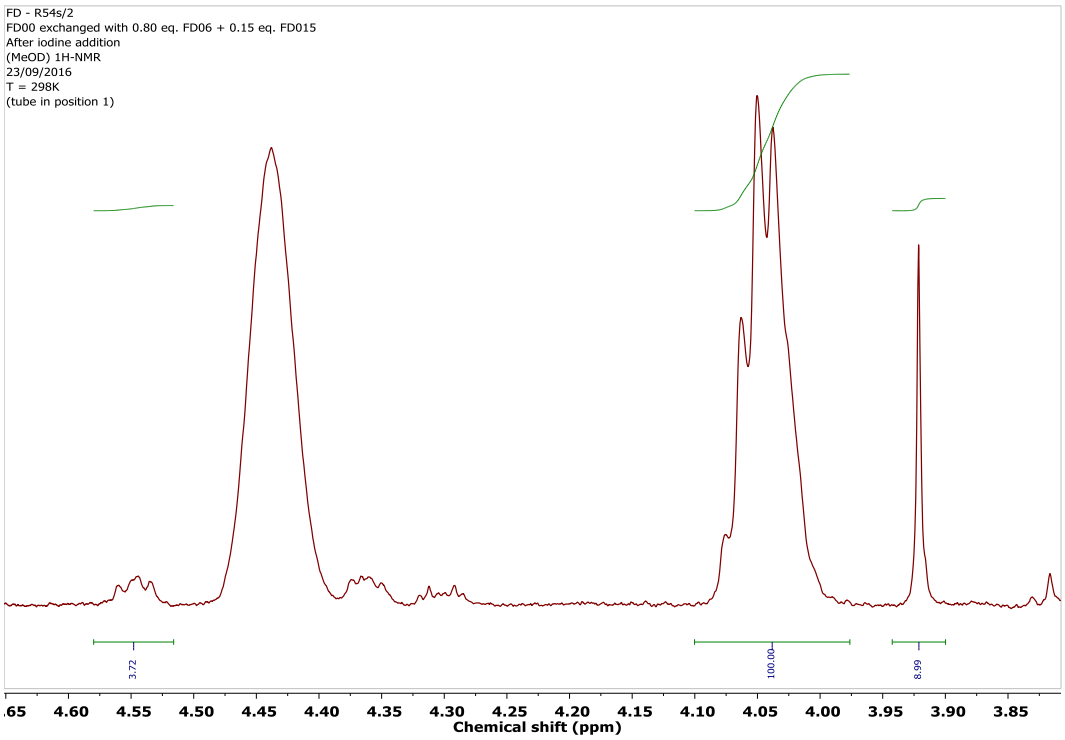
FD - R54s/2
FD00 exchanged with 0.80 eq. FD06 + 0.15 eq. FD015
After iodine addition
(MeOD) 1H-NMR
23/09/2016
T = 298K
(tube in position 1)
3.72
100.00
8.99
.65 4.60 4.55 4.50 4.45 4.40 4.35 4.30 4.25 4.20 4.15 4.10 4.05 4.00 3.95 3.90 3.85
Chemical shift (ppm)

Appendix II – NMR Spectra of Click-couplings

2 nm NPs – TBTA (ZW + AZ-4 18%)– 10:10:10

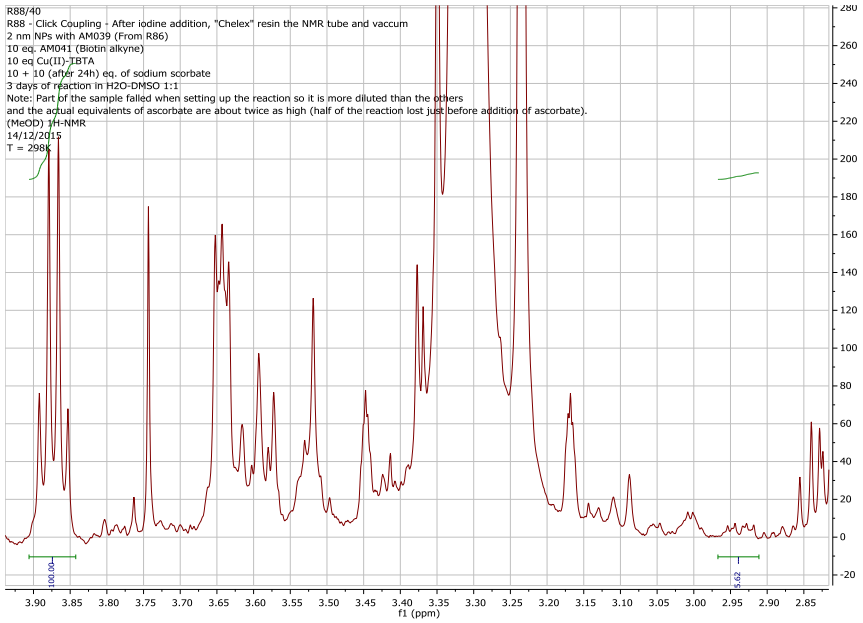

2 nm NPs – TBTA (ZW + AZ-4 1%)– 100:10:10

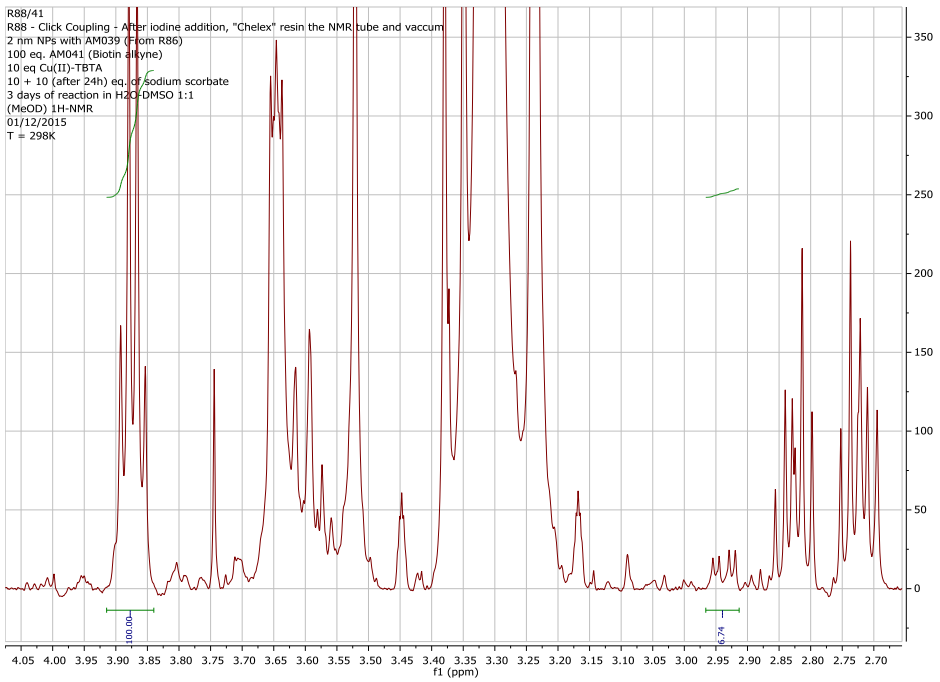

9 nm NPs – TBTA (ZW + AZ-4 20%)– 10:10:10

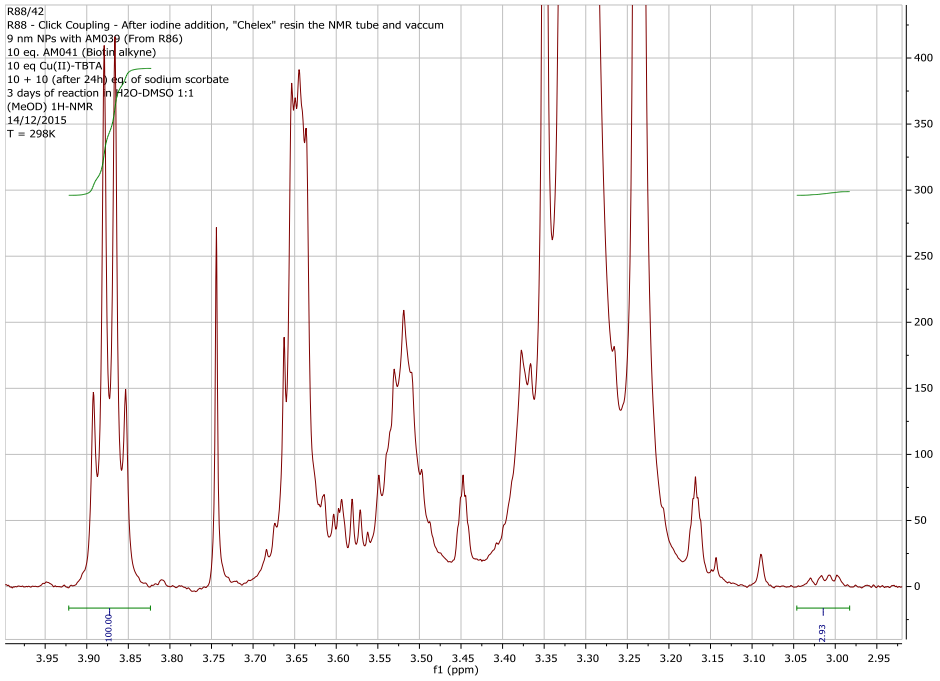

9 nm NPs – TBTA (ZW + AZ-4 20%)– 100:10:10

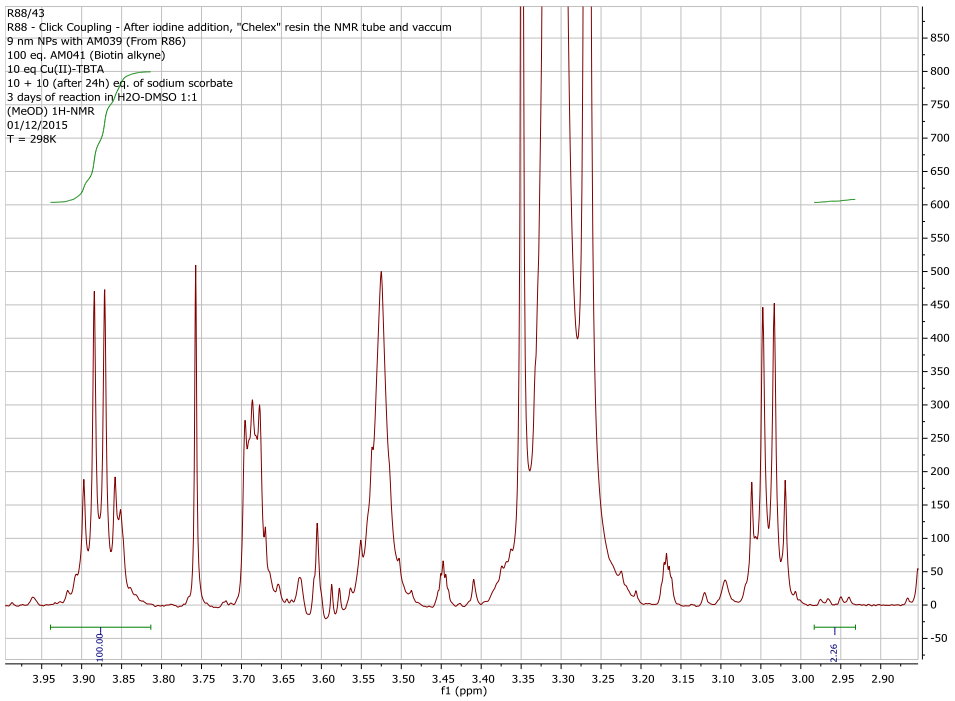

2 nm NPs – THPTA (ZW + AZ-6 28%) – 50:5:10

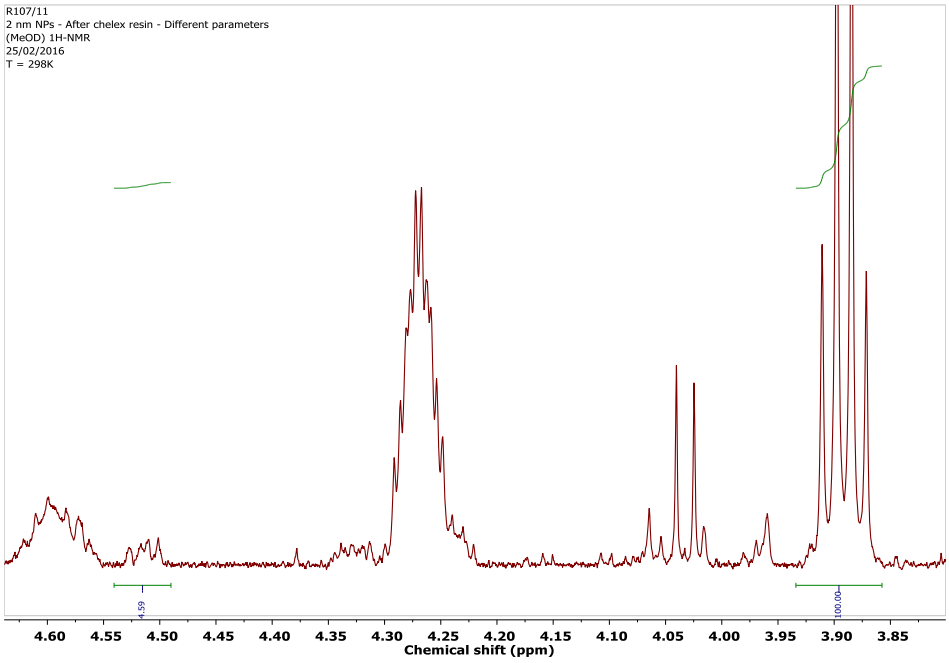

9 nm NPs – THPTA (ZW + AZ-6 15%) – 50:5:10

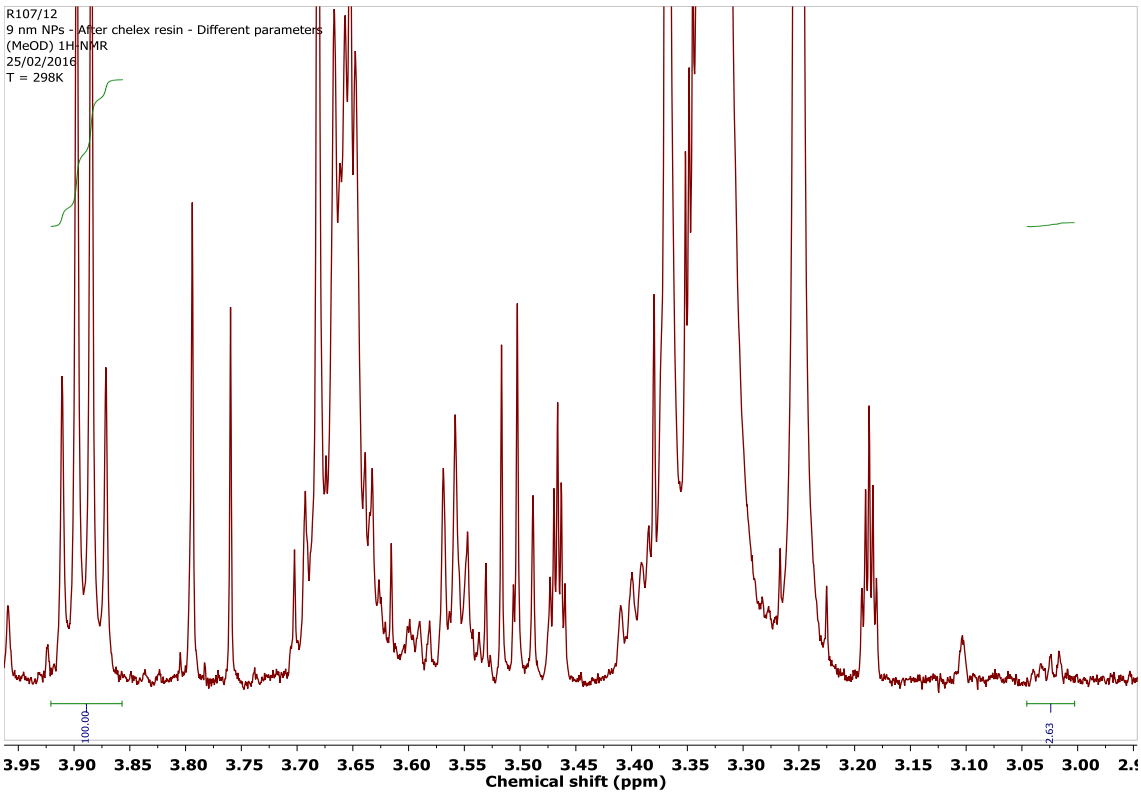

2 nm NPs – THPTA (ZW + AZ-6 28%) – 50:5:10 / 40C 4 days

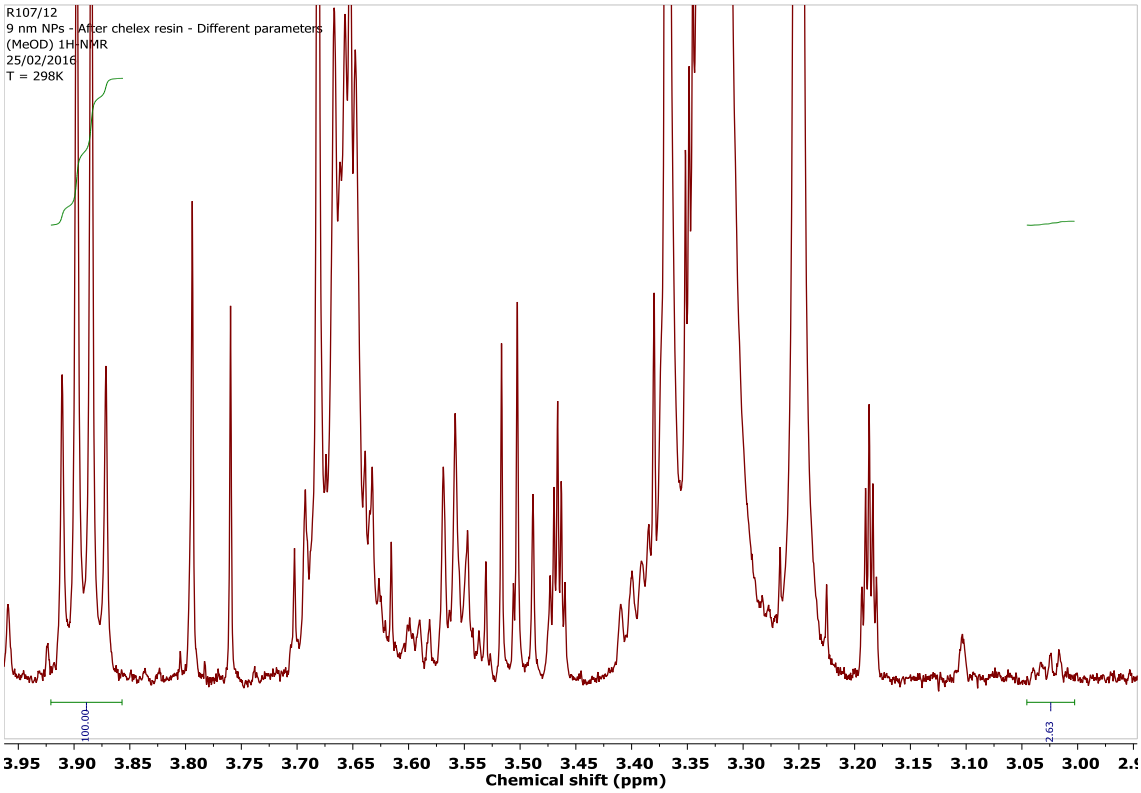

2 nm NPs – THPTA (ZW + AZ-6 28%) – 100:20:60

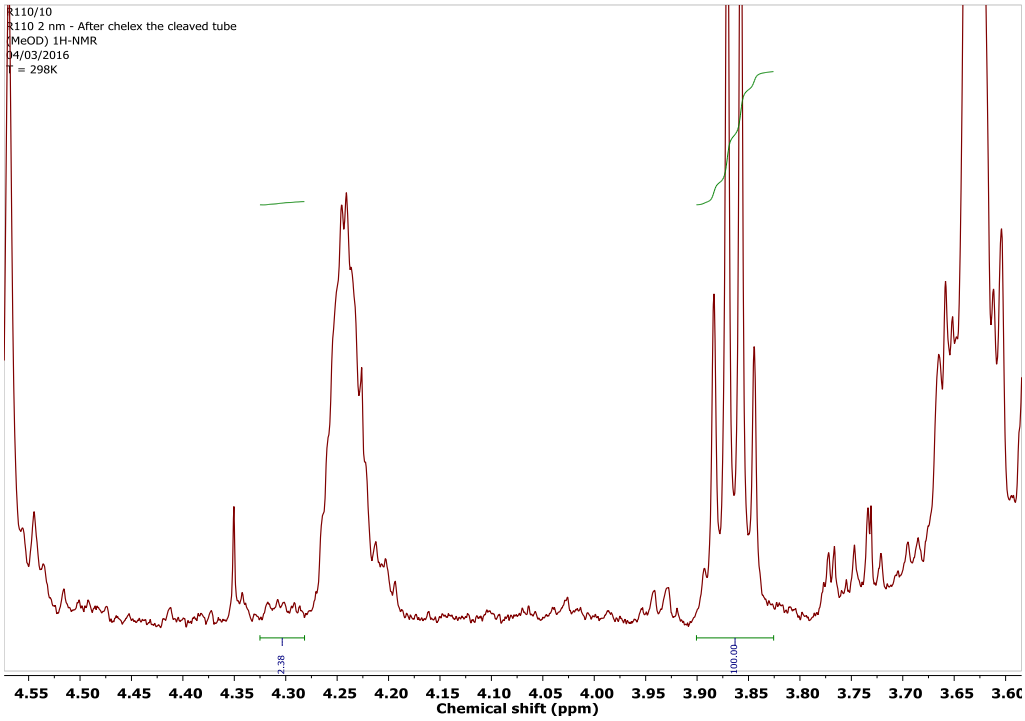

9 nm NPs – THPTA (ZW + AZ-6 15%) – 100:20:60

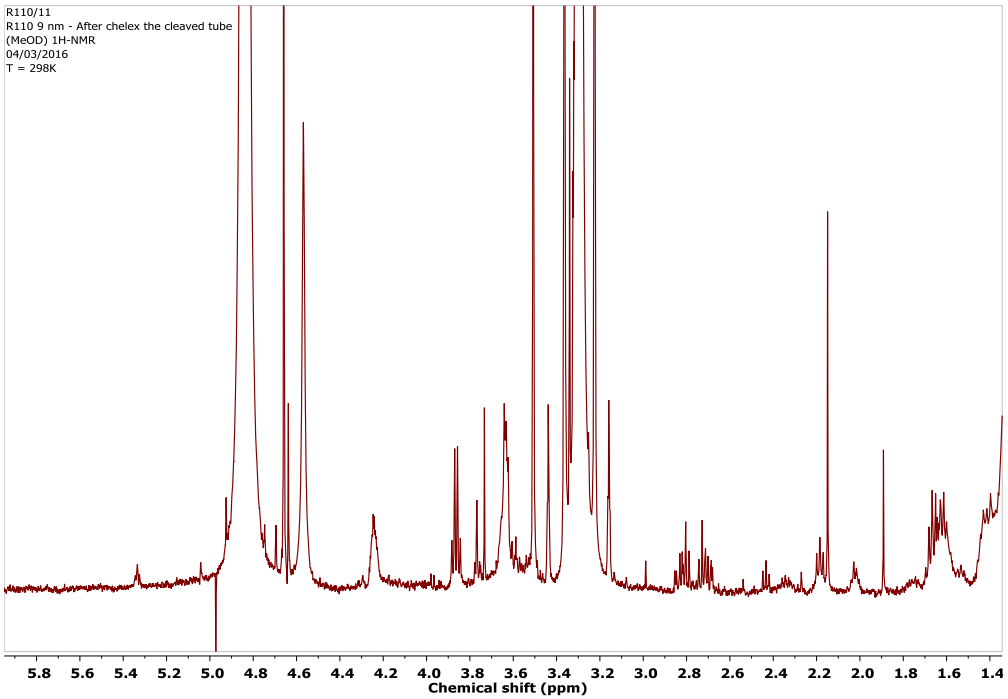

2 nm NPs – THPTA (TMA + AZ-4 21%) – 50:5:10

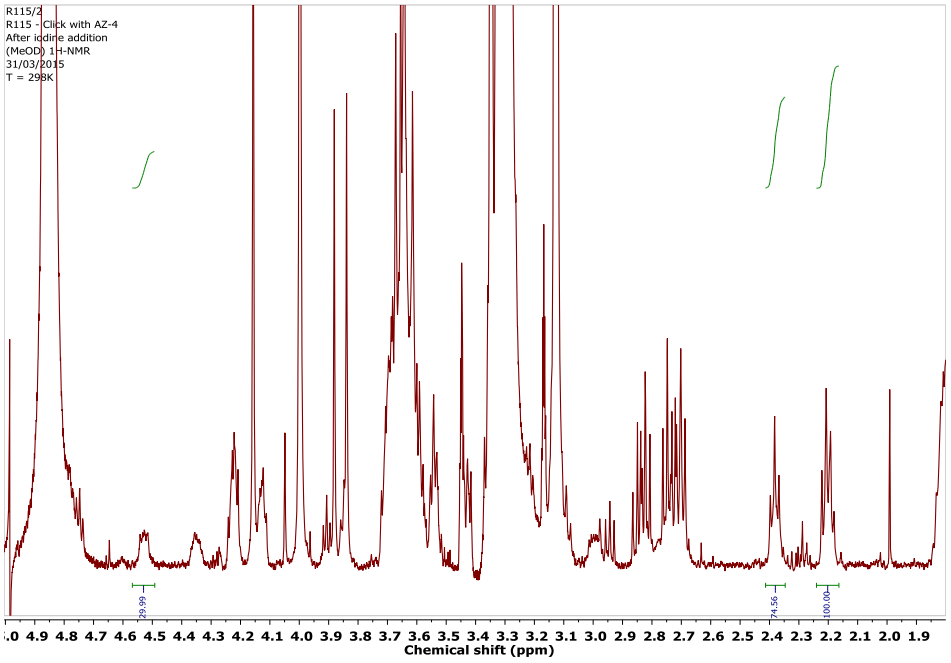

2 nm NPs – THPTA (TMA + AZ-6 16%) – 50:5:10

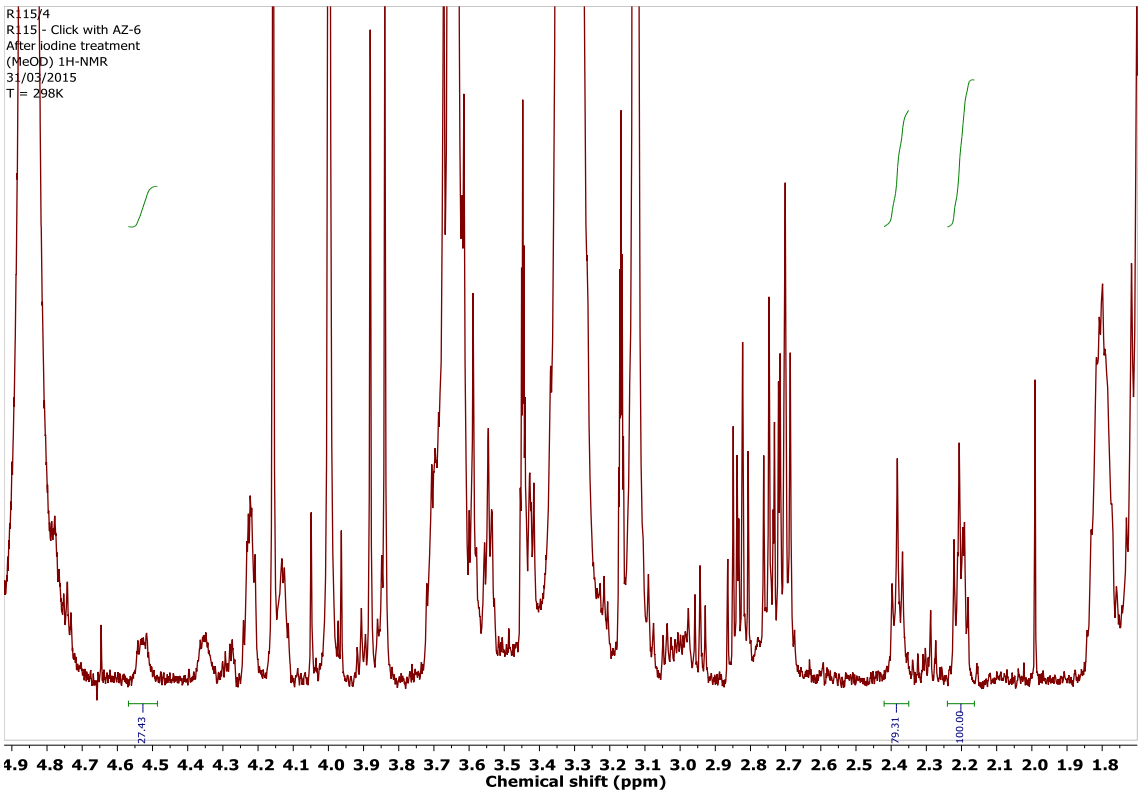

9 nm NPs – THPTA (TEG + AZ-6 17%) – 50:5:10

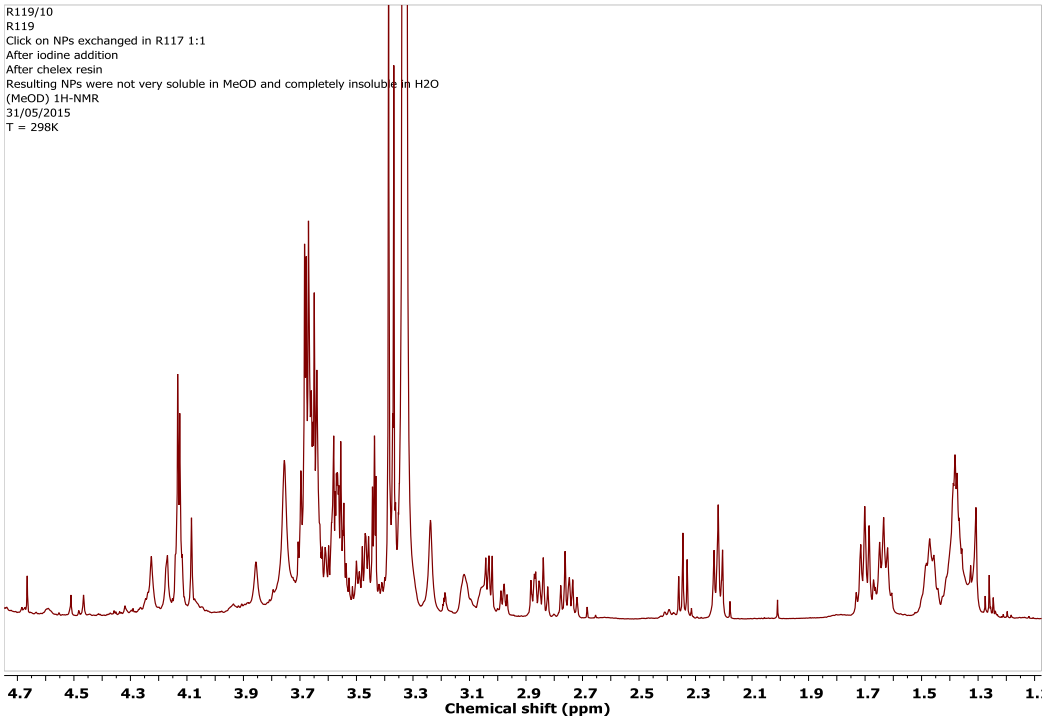

9 nm NPs – THPTA (TEG + AZ-6 5%) – 50:5:10

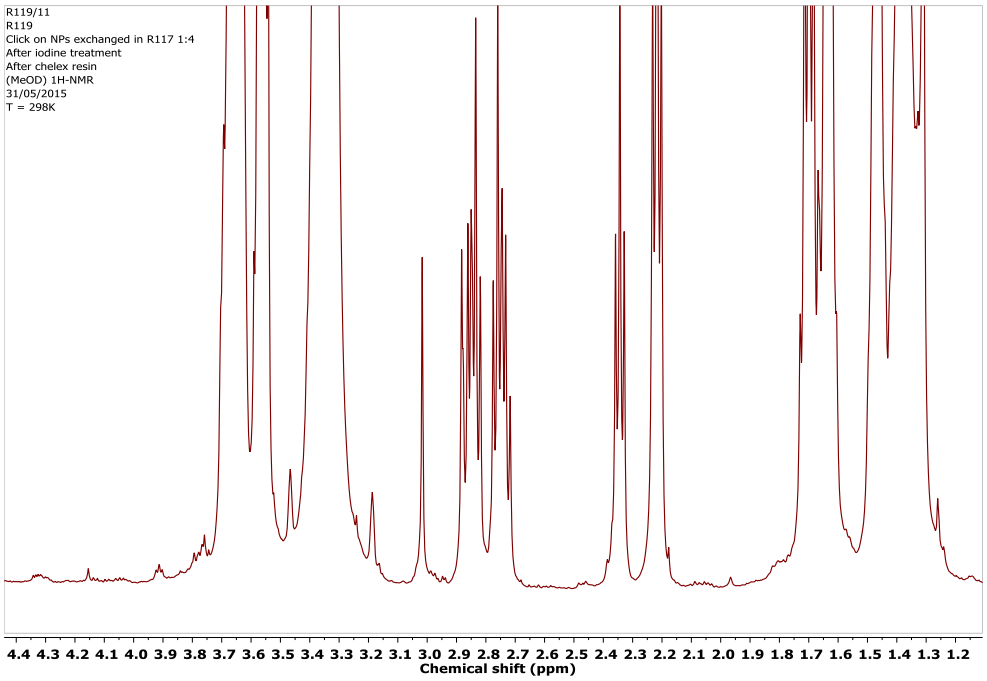

2 nm NPs – DBCO (ZW + AZ-6 28%) – 5 eq

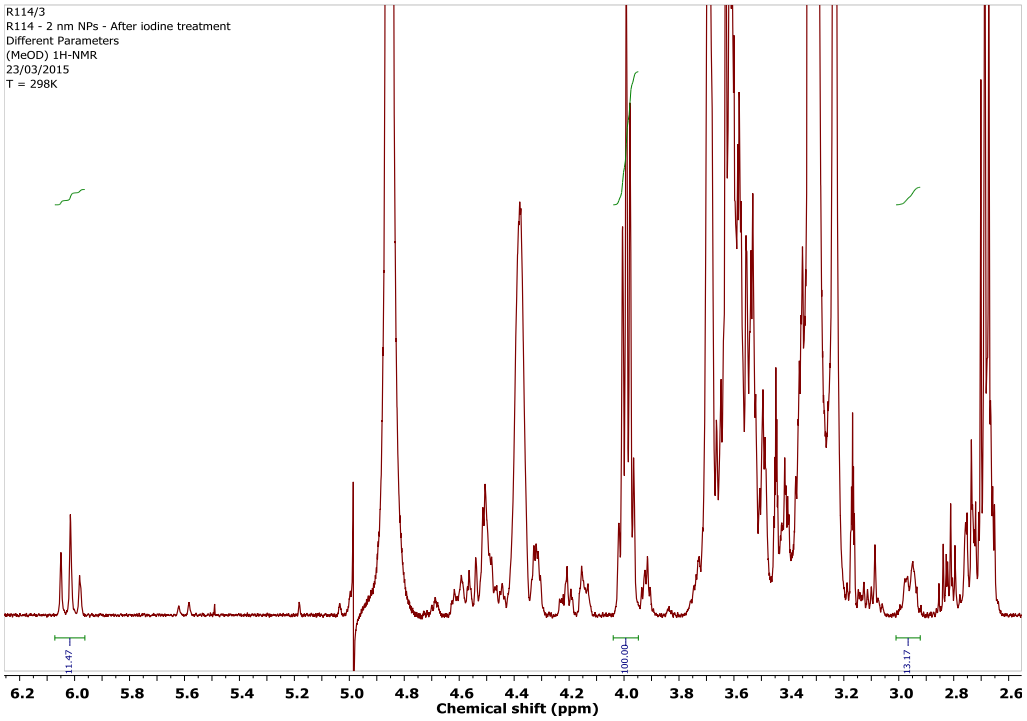

9 nm NPs – DBCO (ZW + AZ-6 15%) – 5 eq

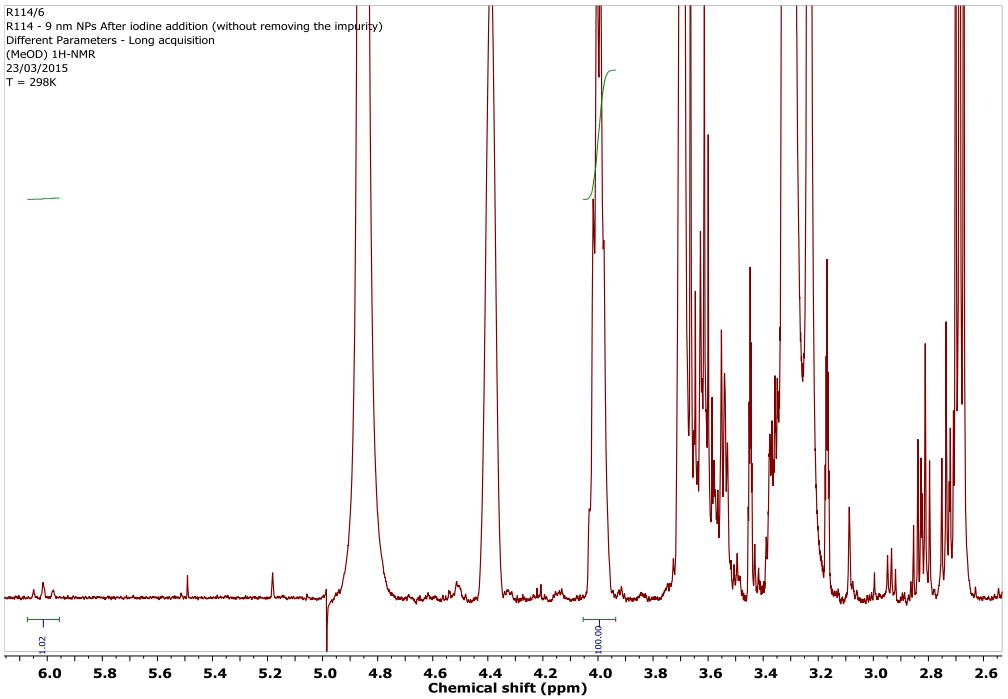

9 nm NPs – DBCO (TEG + AZ-6 5%) – 2 eq

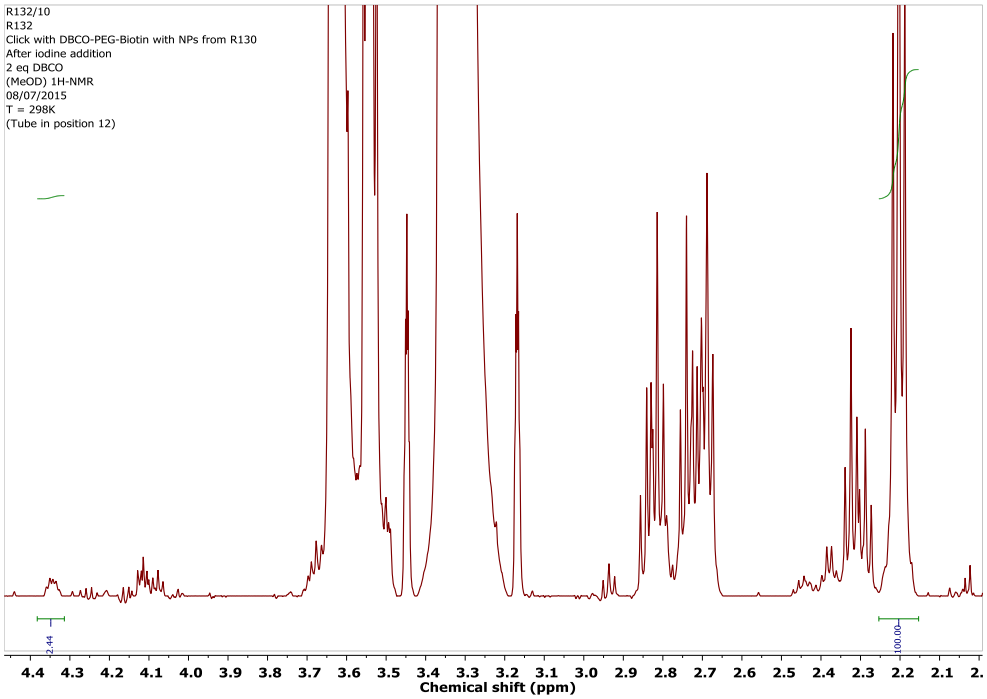

9 nm NPs – DBCO (TEG + AZ-6 5%) – 5 eq

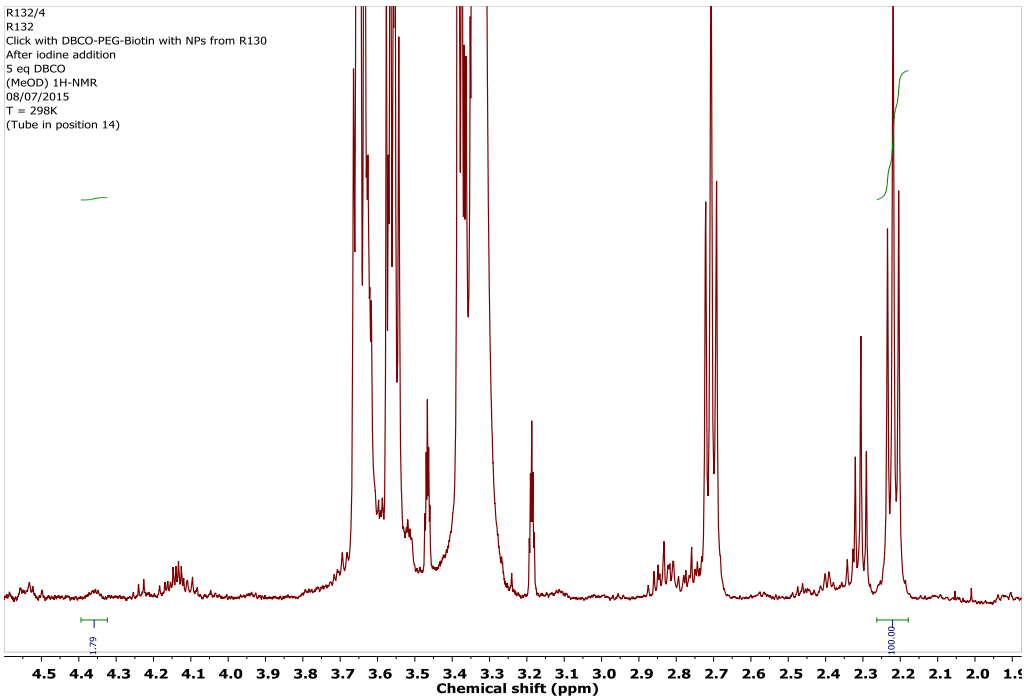

Comparison DBCO 5 eq (blue 9 nm / green 2 nm / red reference product DBCO-click)

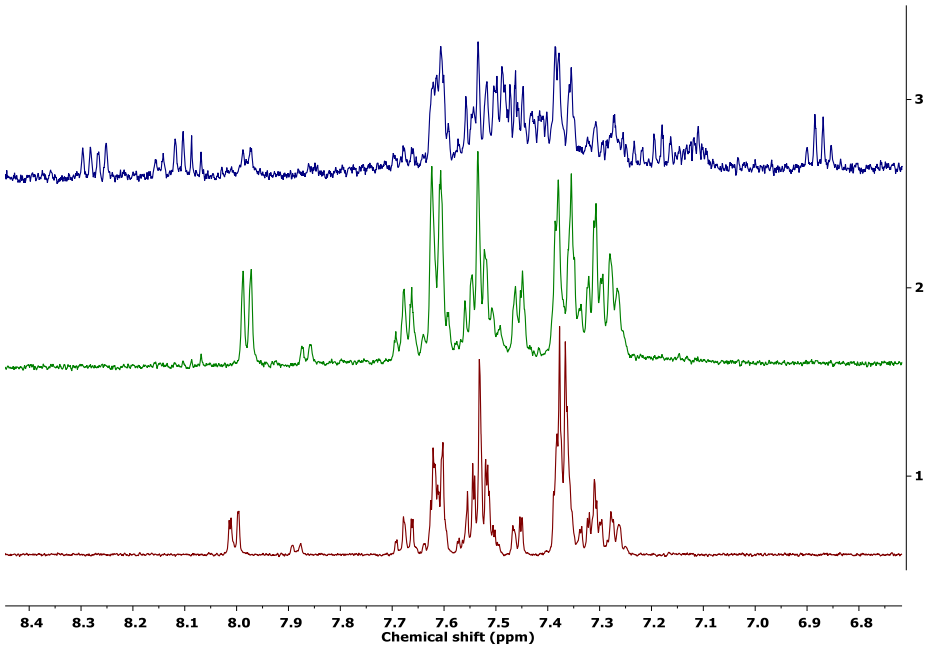

Comparison DBCO TEG (green 5 eq / red 2 eq)

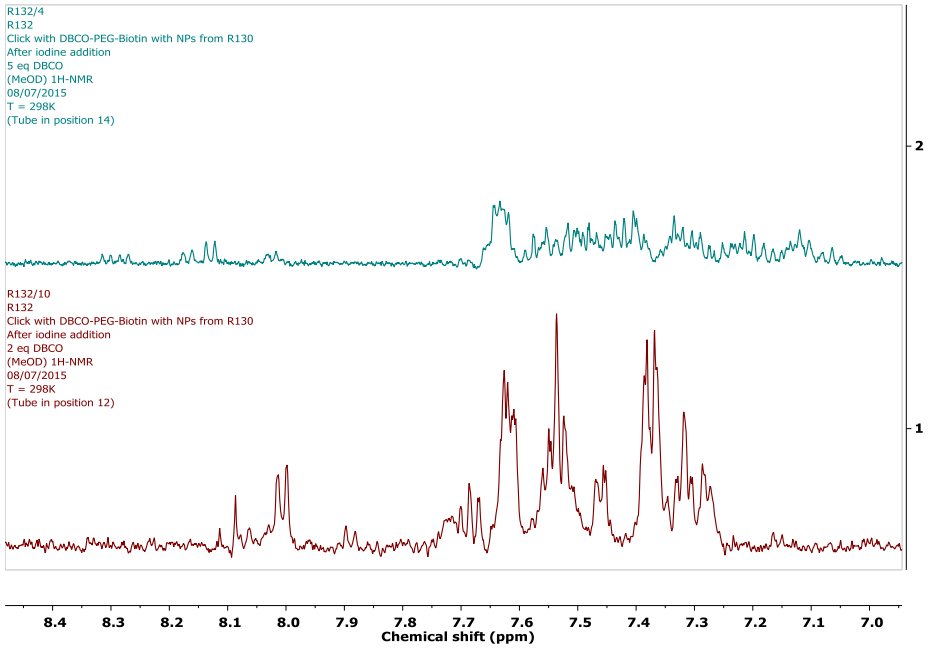

Appendix III – NMR Spectra of synthesised compounds

AZ-4 (2)

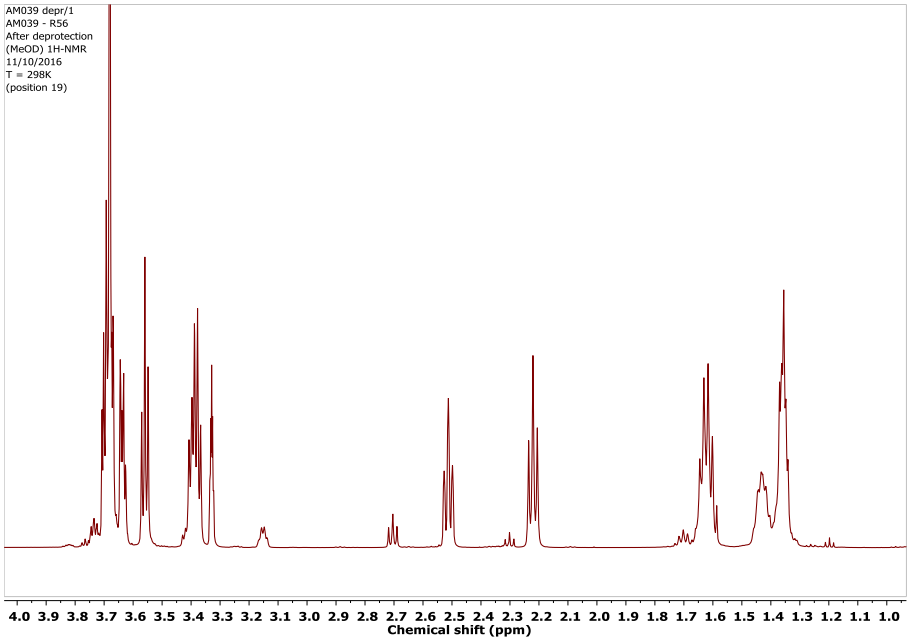

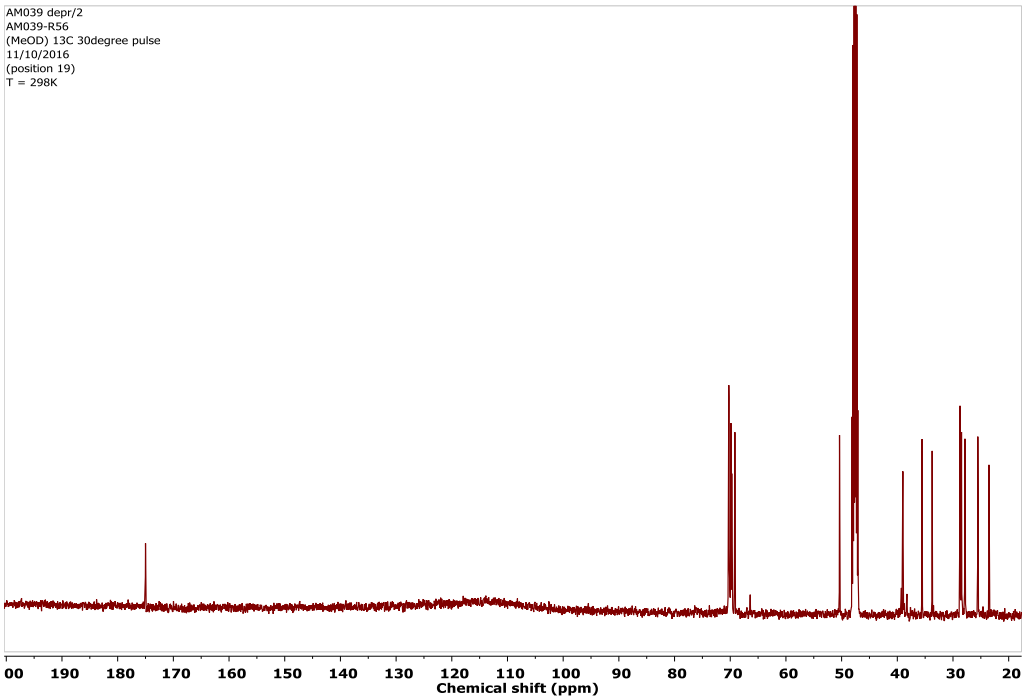

(2-Prot)

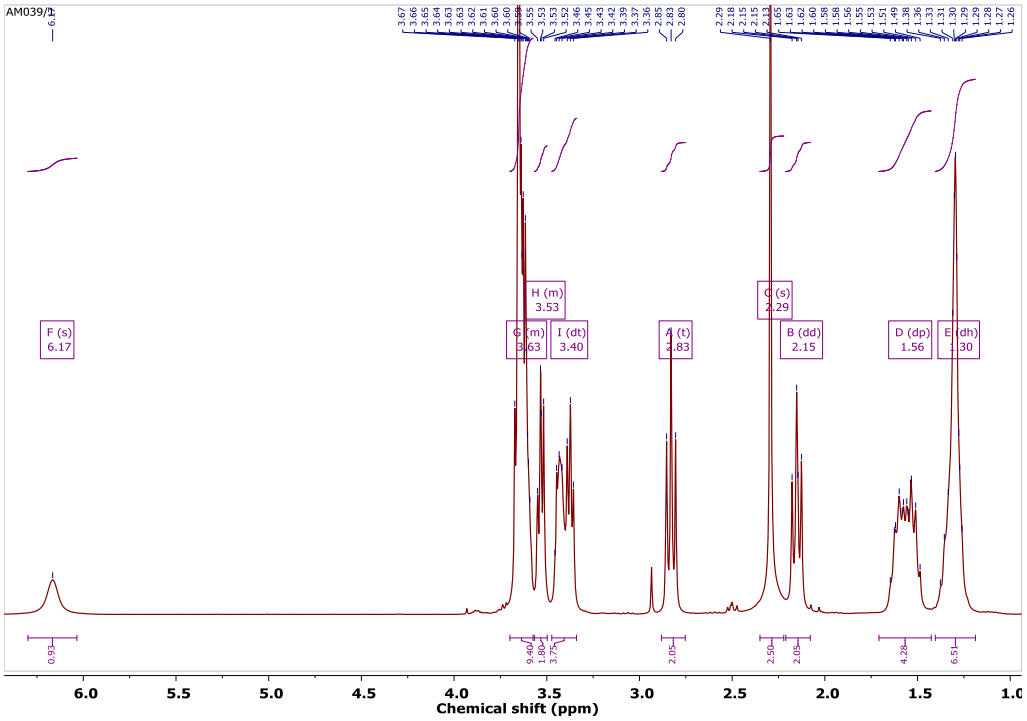
AM039/1
F (s)
6.17
H (m)
3.53
G (m)
3.63
I (dt)
3.40
A (t)
2.83
C (s)
2.29
B (dd)
2.15
D (dp)
1.56
E (dh)
1.30
Chemical shift (ppm)

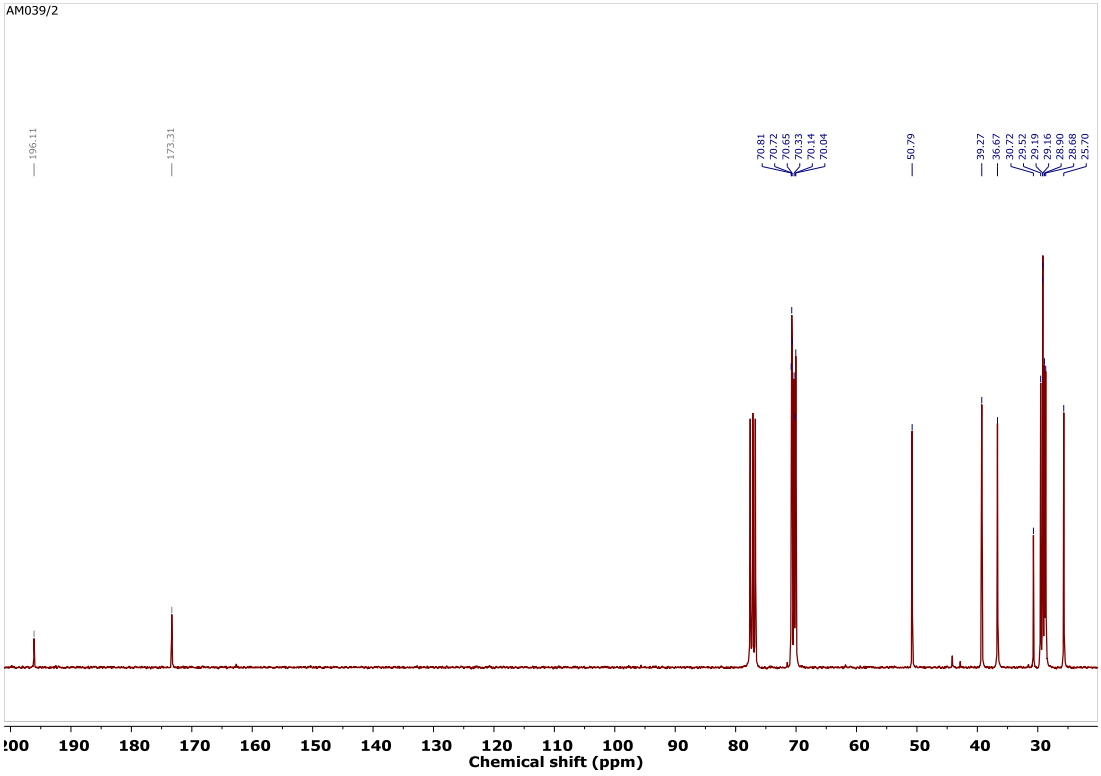
AM039/2
196.11
173.31
70.81
70.72
70.65
70.33
70.14
70.04
50.79
39.27
36.67
30.72
29.52
29.19
29.16
28.90
28.68
25.70
Chemical shift (ppm)

AZ-6 (3)

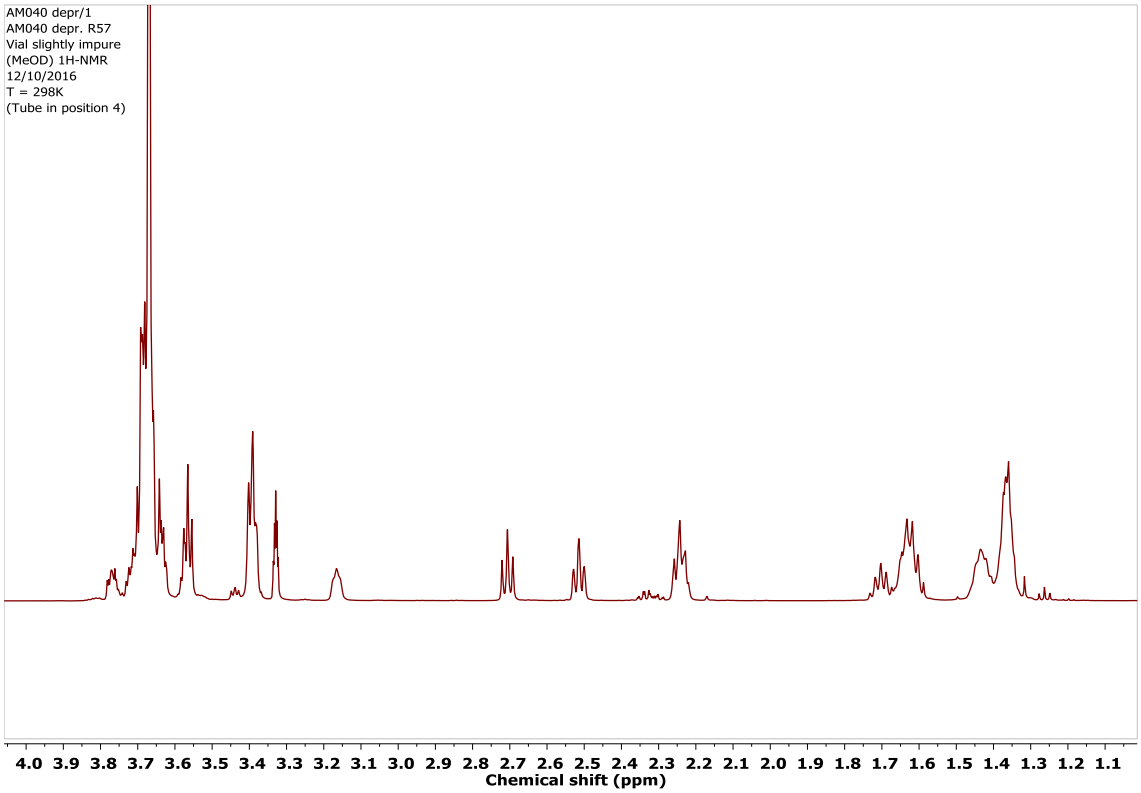
AM040 depr/1
AM040 depr. R57
Vial slightly impure
(MeOD) 1H-NMR
12/10/2016
T = 298K
(Tube in position 4)
4.0 3.9 3.8 3.7 3.6 3.5 3.4 3.3 3.2 3.1 3.0 2.9 2.8 2.7 2.6 2.5 2.4 2.3 2.2 2.1 2.0 1.9 1.8 1.7 1.6 1.5 1.4 1.3 1.2 1.1
Chemical shift (ppm)

3-Prot

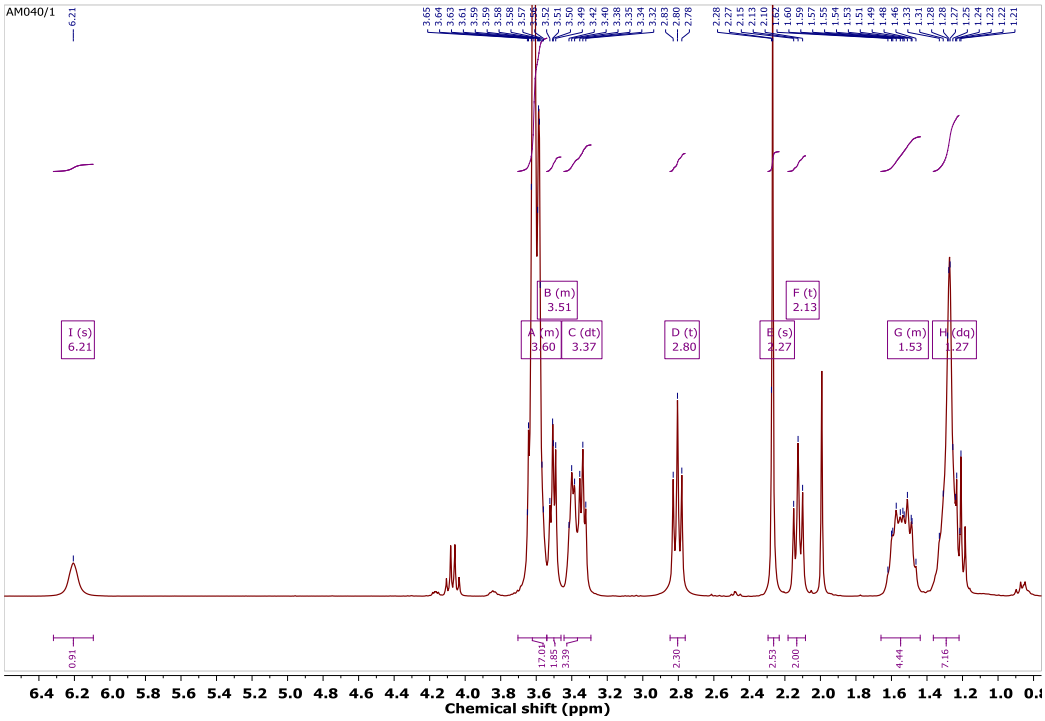
AM040/1
I (s) 6.21
B (m) 3.51
A (m) 3.60
C (dt) 3.37
D (t) 2.80
E (s) 2.27
F (t) 2.13
G (m) 1.53
H (dq) 1.27
Chemical shift (ppm)

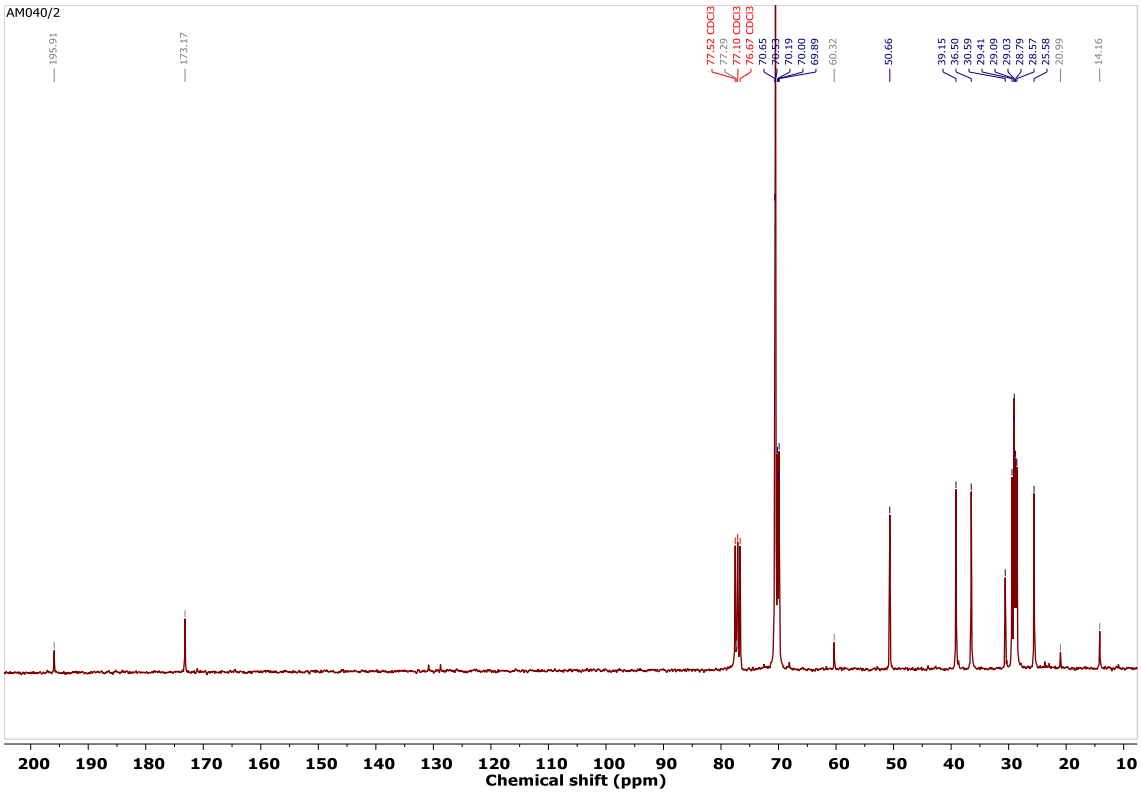
AM040/2
Chemical shift (ppm)

6 (Naprox)

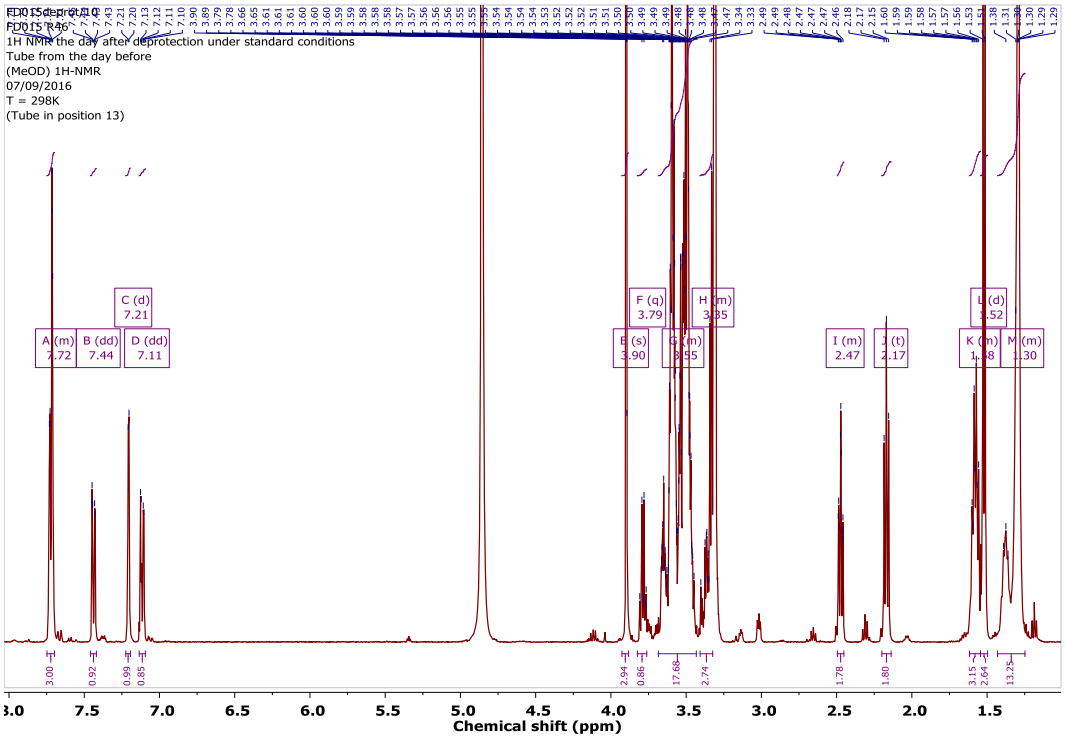
FD015deprot/10
FD015 R46
1H NMR the day after deprotection under standard conditions
Tube from the day before
(MeOD) 1H-NMR
07/09/2016
T = 298K
(Tube in position 13)
A (m) 7.72
B (dd) 7.44
C (d) 7.21
D (dd) 7.11
E (s) 3.90
F (q) 3.79
H (m) 3.35
I (m) 2.47
J (t) 2.17
K (m) 1.38
L (d) 1.52
M (m) 1.30
Chemical shift (ppm)

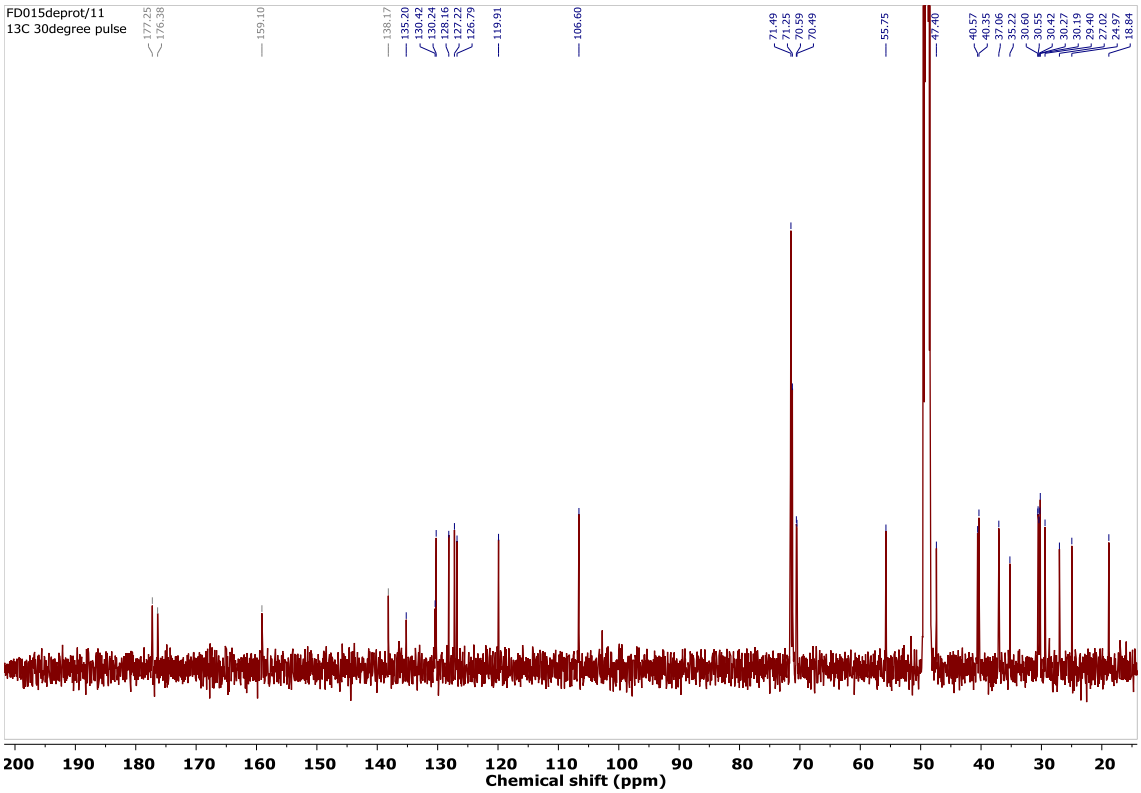
FD015deprot/11
13C 30degree pulse
Chemical shift (ppm)

6-Prot

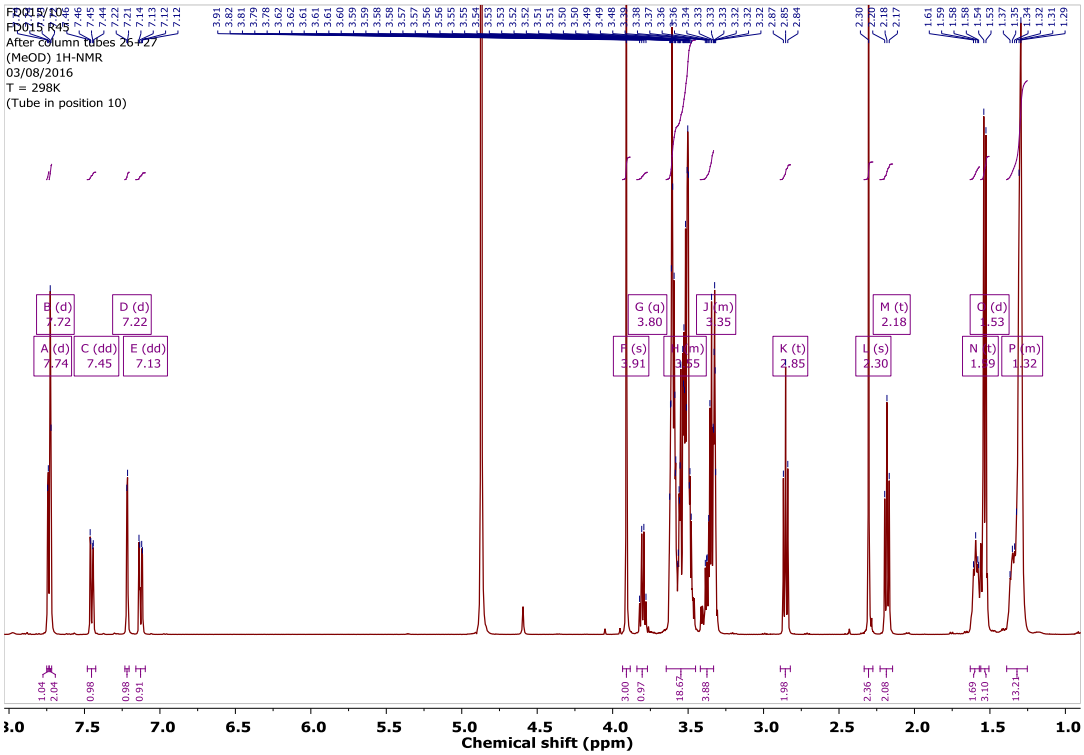
FD015/13
FD015 R45
After column tubes 26 +27
(MeOD) 1H-NMR
03/08/2016
T = 298K
(Tube in position 10)
A (d) 7.74
B (d) 7.72
C (dd) 7.45
D (d) 7.22
E (dd) 7.13
F (s) 3.91
G (q) 3.80
H (m) 3.65
J (m) 3.35
K (t) 2.85
L (s) 2.30
M (t) 2.18
N (t) 1.69
O (d) 1.53
P (m) 1.32
Chemical shift (ppm)

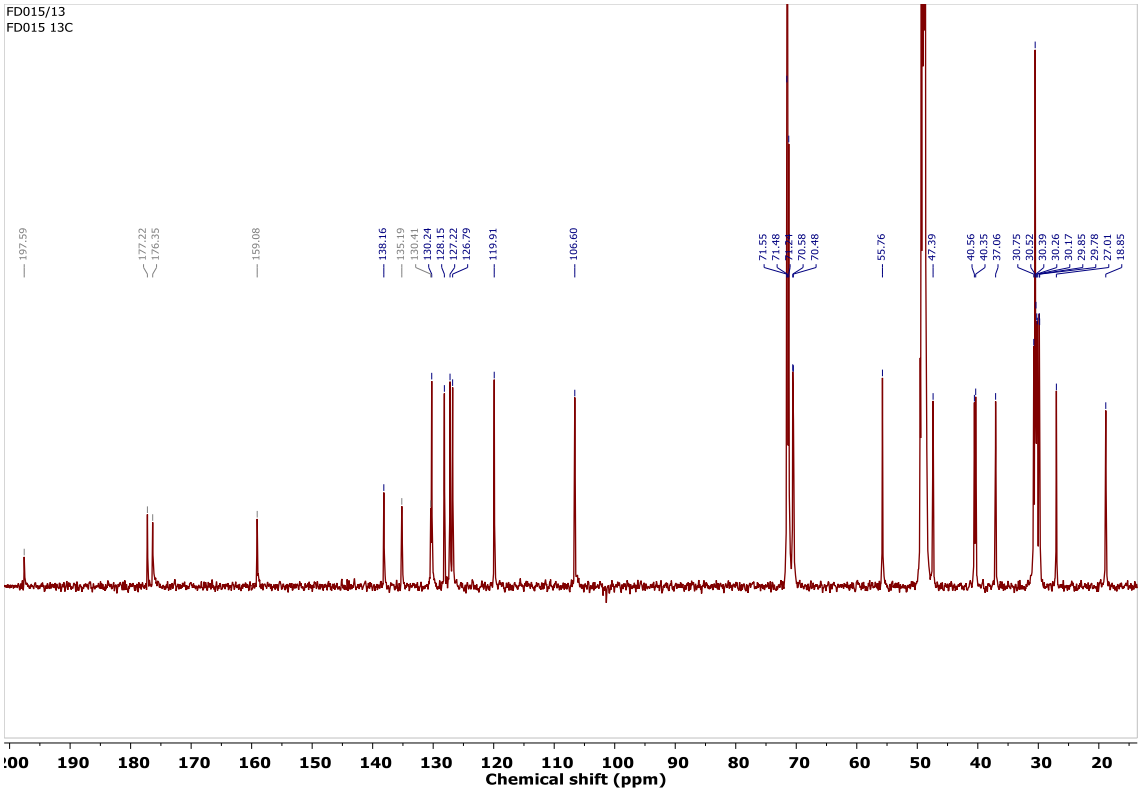
FD015/13
FD015 13C
Chemical shift (ppm)

7

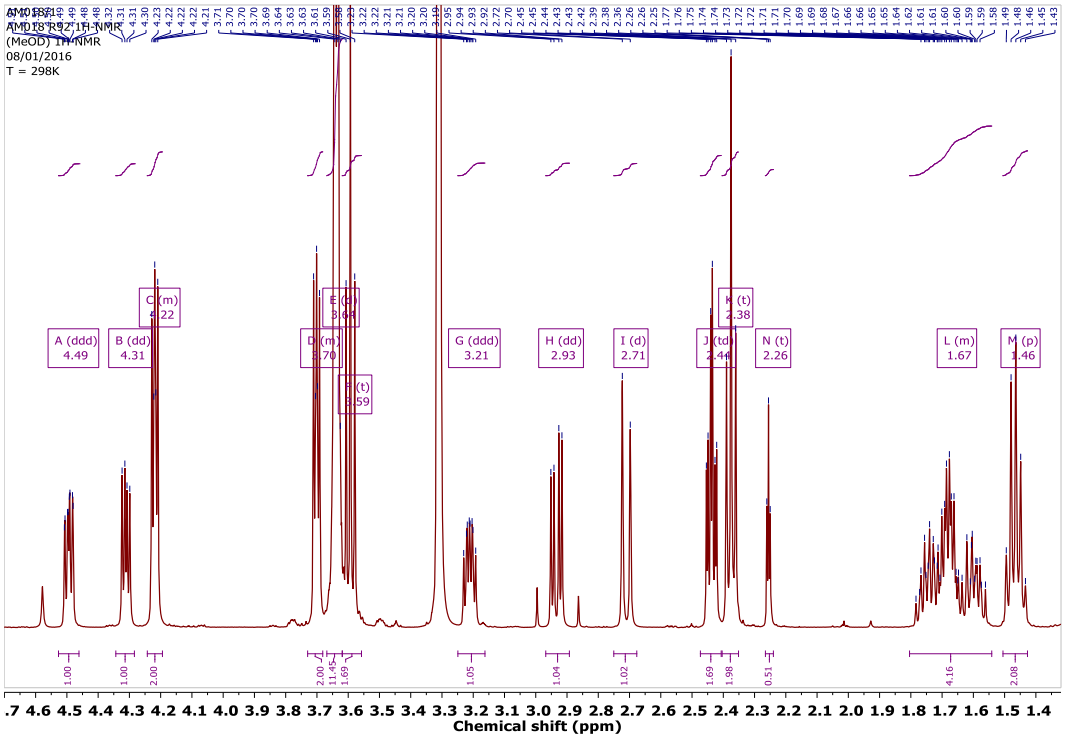
AM018/2
AM018 R92 1H-NMR
(MeOD) 1H-NMR
08/01/2016
T = 298K
A (ddd) 4.49
B (dd) 4.31
C (m) 4.22
D (m) 3.70
E (t) 3.63
F (t) 3.59
G (ddd) 3.21
H (dd) 2.93
I (d) 2.71
J (td) 2.44
K (t) 2.38
N (t) 2.26
L (m) 1.67
M (p) 1.46
Chemical shift (ppm)

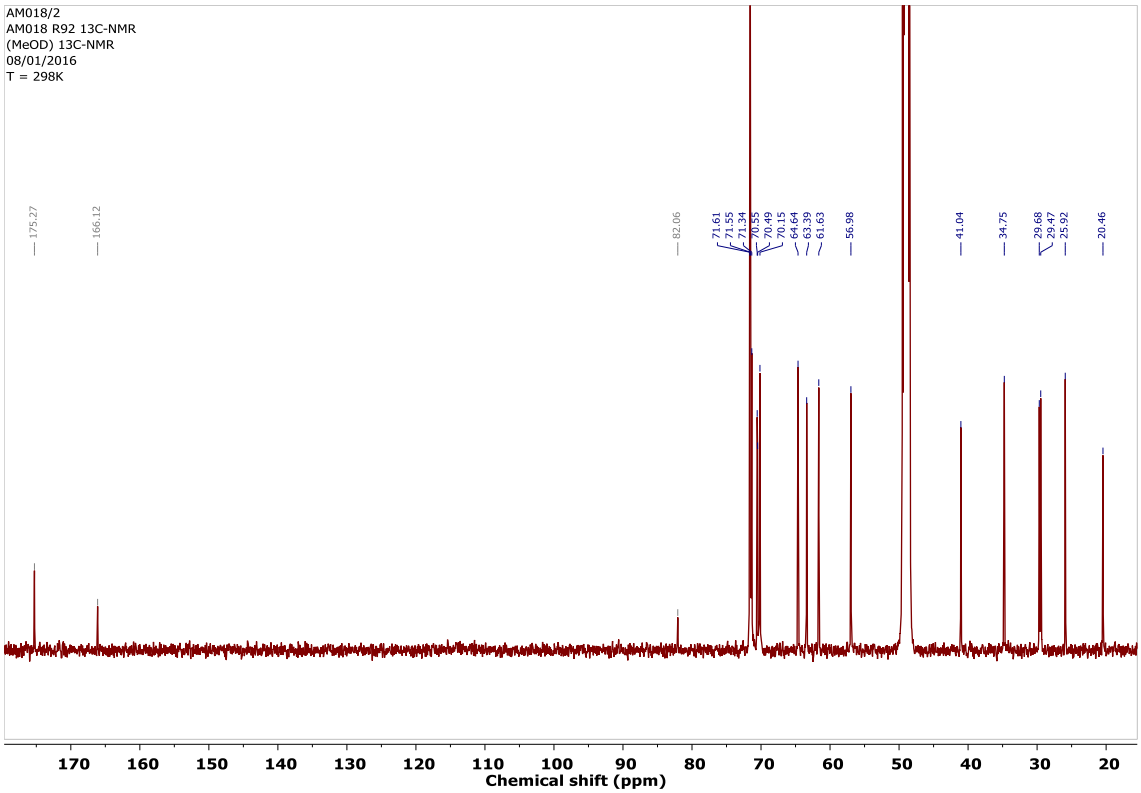
AM018/2
AM018 R92 13C-NMR
(MeOD) 13C-NMR
08/01/2016
T = 298K
175.27
166.12
82.06
71.61
71.55
71.34
70.55
70.49
70.15
64.64
63.39
61.63
56.98
41.04
34.75
29.68
29.47
25.92
20.46
Chemical shift (ppm)

Biot-4 (4)

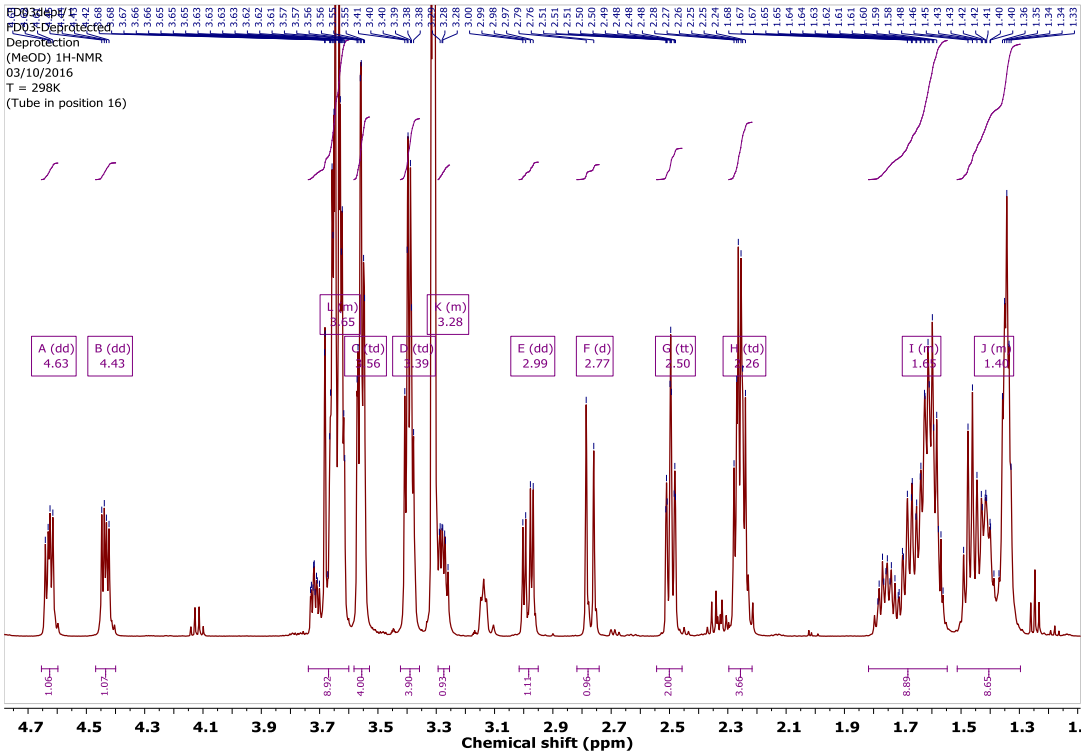
FD03depr/1
FD03-Deprotected
Deprotection
(MeOD) 1H-NMR
03/10/2016
T = 298K
(Tube in position 16)
A (dd) 4.63
B (dd) 4.43
K (m) 3.28
E (dd) 2.99
F (d) 2.77
G (tt) 2.50
H (td) 2.26
Chemical shift (ppm)

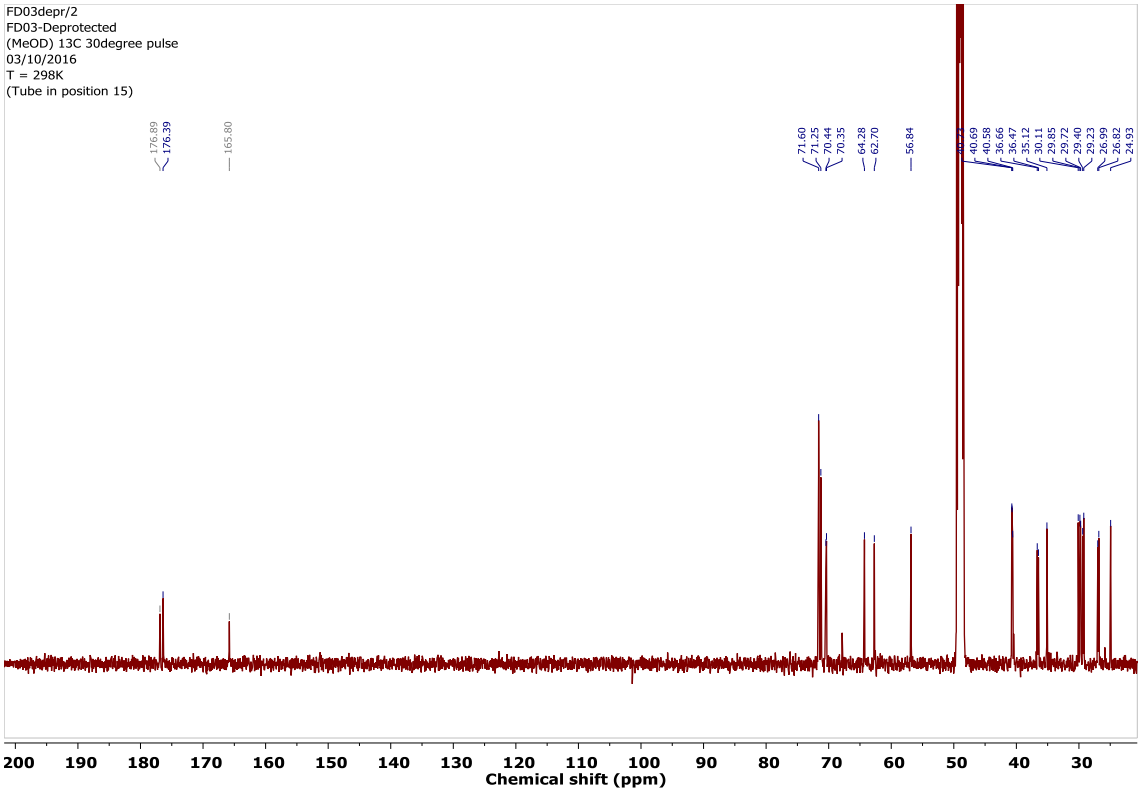
FD03depr/2
FD03-Deprotected
(MeOD) 13C 30degree pulse
03/10/2016
T = 298K
(Tube in position 15)
176.89
176.39
165.80
71.60
71.25
70.44
70.35
64.28
62.70
56.84
40.69
40.58
36.66
36.47
35.12
30.11
29.85
29.72
29.40
29.23
26.99
26.82
24.93
Chemical shift (ppm)

4-Prot

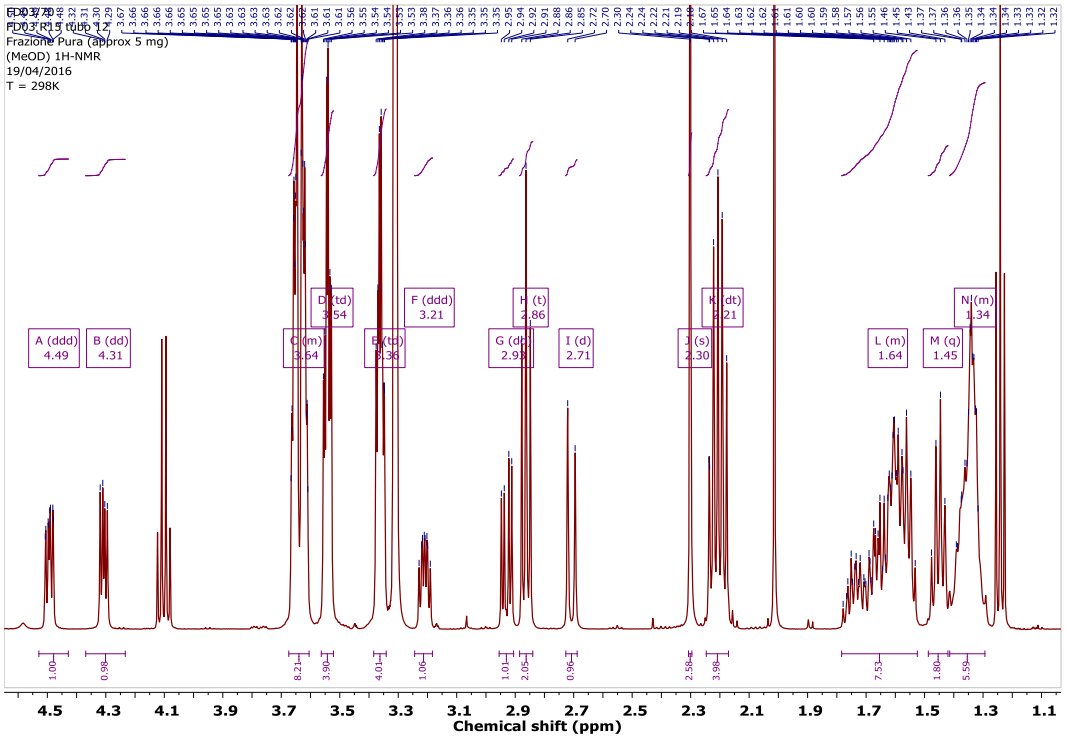
FD03/70
FD03 R15 tubo 12
Frazione Pura (approx 5 mg)
(MeOD) 1H-NMR
19/04/2016
T = 298K
A (ddd) 4.49
B (dd) 4.31
C (m) 3.54
D (td) 3.54
E (td) 3.36
F (ddd) 3.21
G (dd) 2.93
H (t) 2.86
I (d) 2.71
J (s) 2.30
K (dt) 2.21
L (m) 1.64
M (q) 1.45
N (m) 1.34
Chemical shift (ppm)

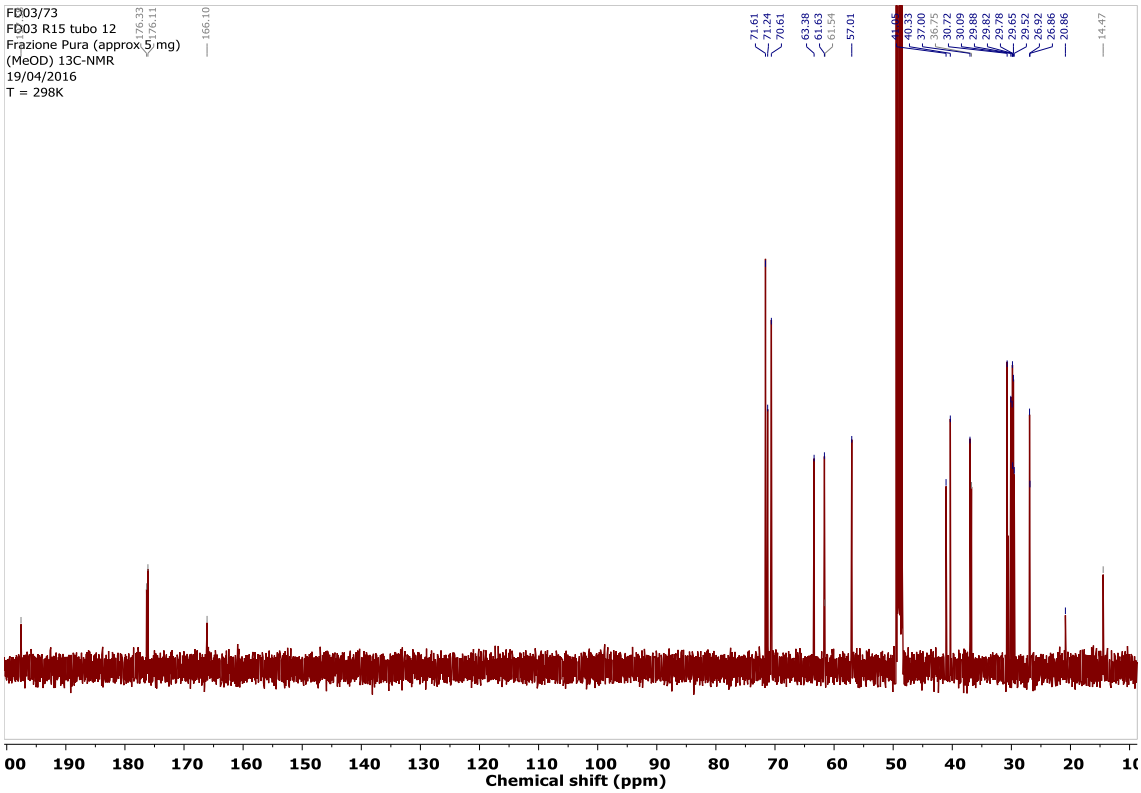
FD03/73
FD03 R15 tubo 12
Frazione Pura (approx 5 mg)
(MeOD) 13C-NMR
19/04/2016
T = 298K
Chemical shift (ppm)

Biot-6 (5)

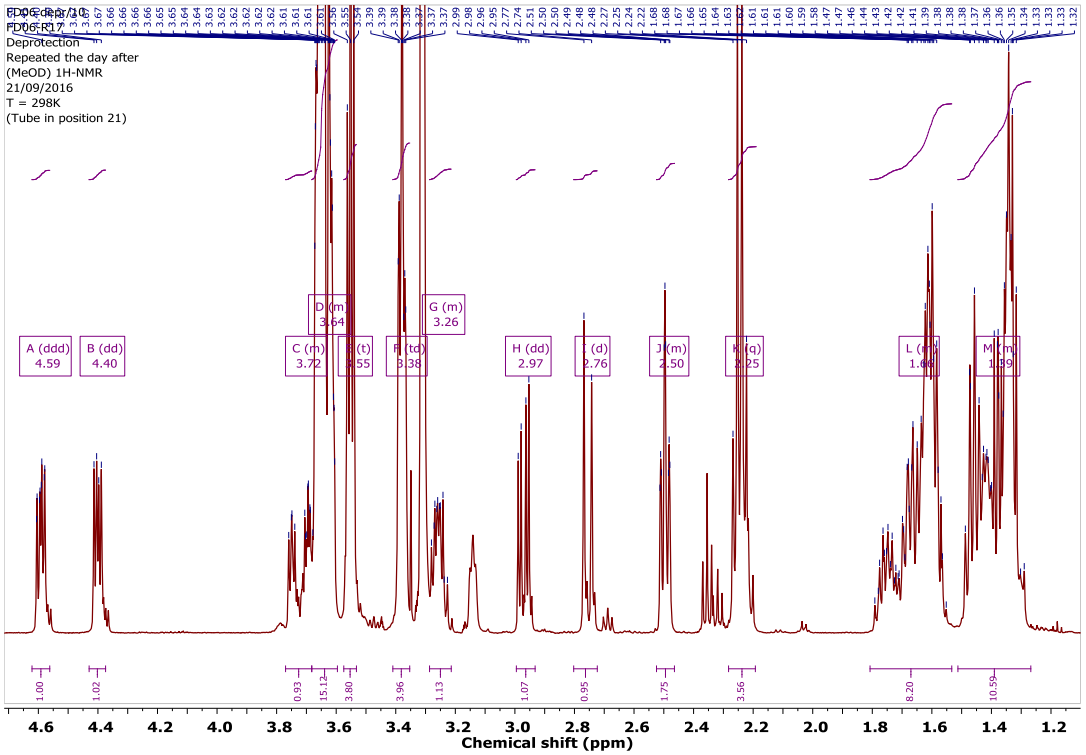
FD06 depr/1
FD06-R17
Deprotection
Repeated the day after
(MeOD) 1H-NMR
21/09/2016
T = 298K
(Tube in position 21)
A (ddd) 4.59
B (dd) 4.40
C (m) 3.72
D (m) 3.64
E (t) 3.55
F (tq) 3.38
G (m) 3.26
H (dd) 2.97
I (d) 2.76
J (m) 2.50
K (q) 2.25
L (m) 1.44
M (m) 1.39
Chemical shift (ppm)

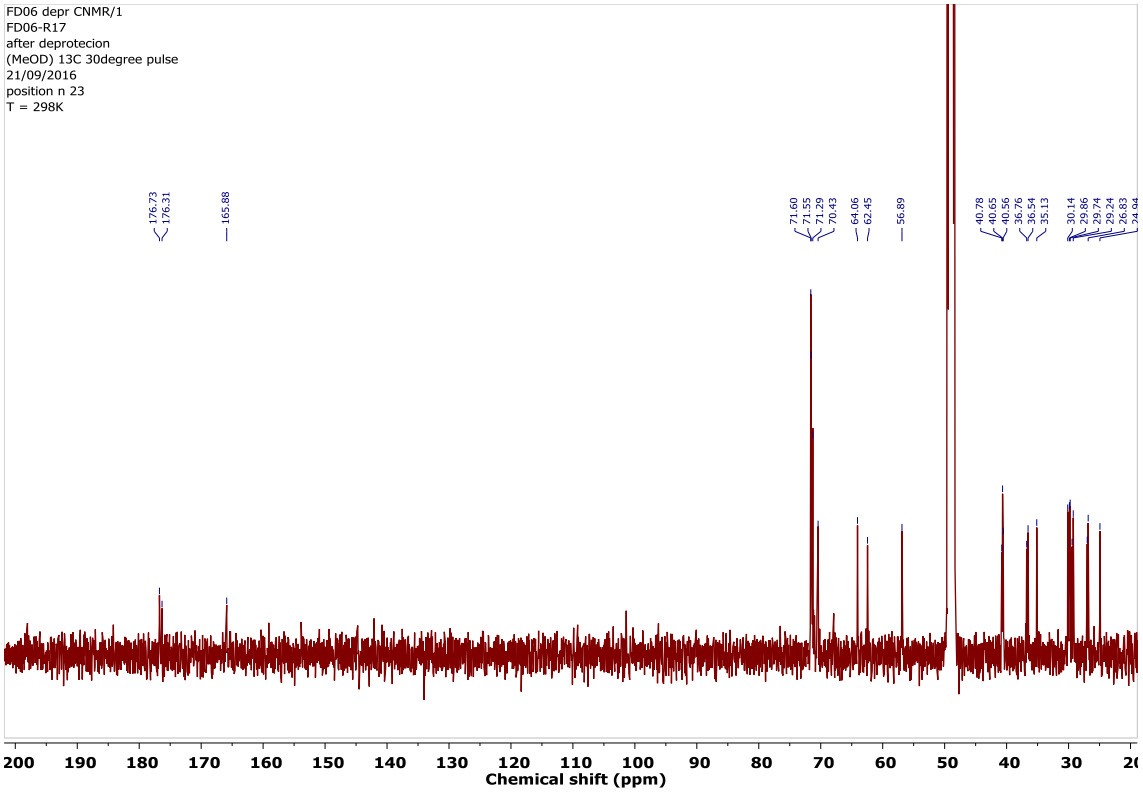
FD06 depr CNMR/1
FD06-R17
after deprotecion
(MeOD) 13C 30degree pulse
21/09/2016
position n 23
T = 298K
176.73
176.31
165.88
71.60
71.55
71.29
70.43
64.06
62.45
56.89
40.78
40.65
40.56
36.76
36.54
35.13
30.14
29.86
29.74
29.24
26.83
24.44
Chemical shift (ppm)

5-Prot

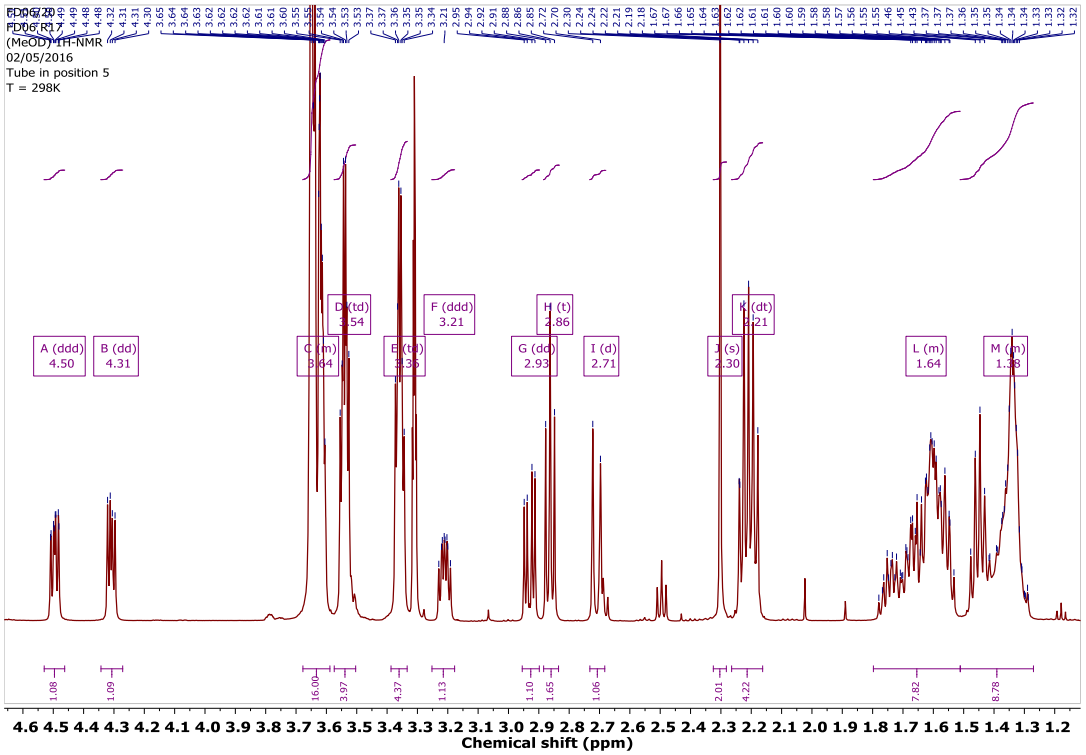
FD06/20
FD06 R17
(MeOD) 1H-NMR
02/05/2016
Tube in position 5
T = 298K
A (ddd) 4.50
B (dd) 4.31
C (m) 3.64
D (td) 3.54
E (td) 3.36
F (ddd) 3.21
G (dd) 2.93
H (t) 2.86
I (d) 2.71
J (s) 2.30
K (dt) 2.21
L (m) 1.64
M (m) 1.38
1.08
1.09
16.00
3.97
4.37
1.13
1.10
1.65
1.06
2.01
4.22
7.82
8.78
4.6 4.5 4.4 4.3 4.2 4.1 4.0 3.9 3.8 3.7 3.6 3.5 3.4 3.3 3.2 3.1 3.0 2.9 2.8 2.7 2.6 2.5 2.4 2.3 2.2 2.1 2.0 1.9 1.8 1.7 1.6 1.5 1.4 1.3 1.2
Chemical shift (ppm)

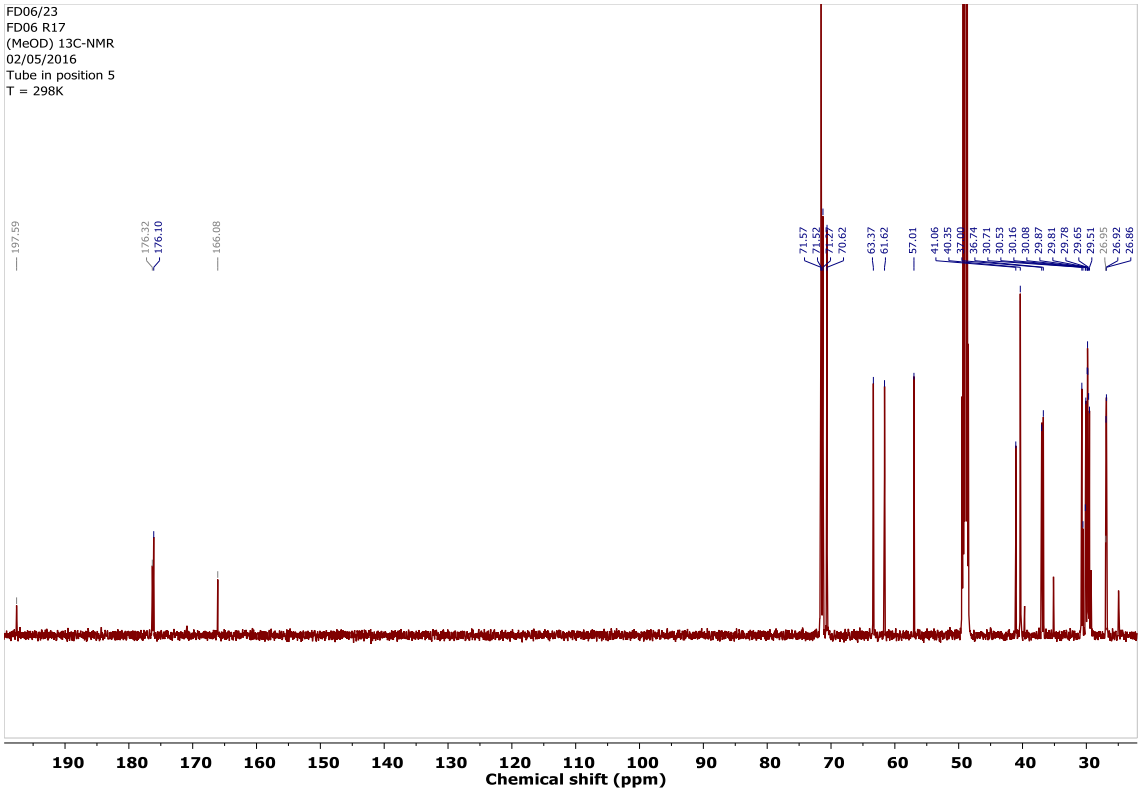
FD06/23
FD06 R17
(MeOD) 13C-NMR
02/05/2016
Tube in position 5
T = 298K
197.59
176.32
176.10
166.08
71.57
71.52
71.27
70.62
63.37
61.62
57.01
41.06
40.35
37.00
36.74
30.71
30.53
30.16
30.08
29.87
29.81
29.78
29.65
29.51
26.95
26.92
26.86
190 180 170 160 150 140 130 120 110 100 90 80 70 60 50 40 30
Chemical shift (ppm)

DBCO-Biot (20)

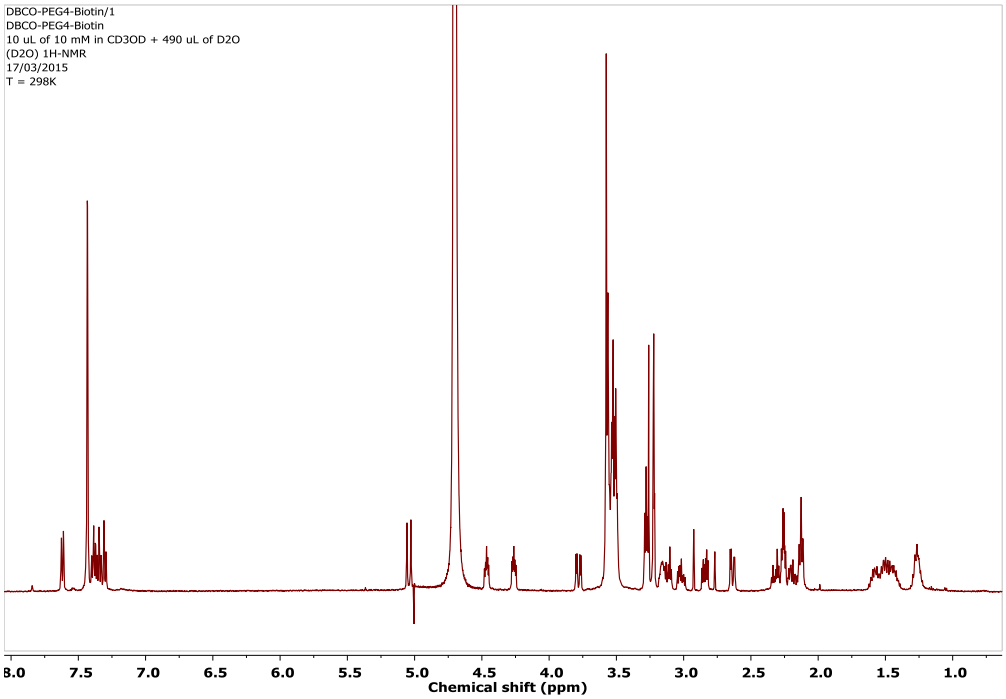

DBCO-click

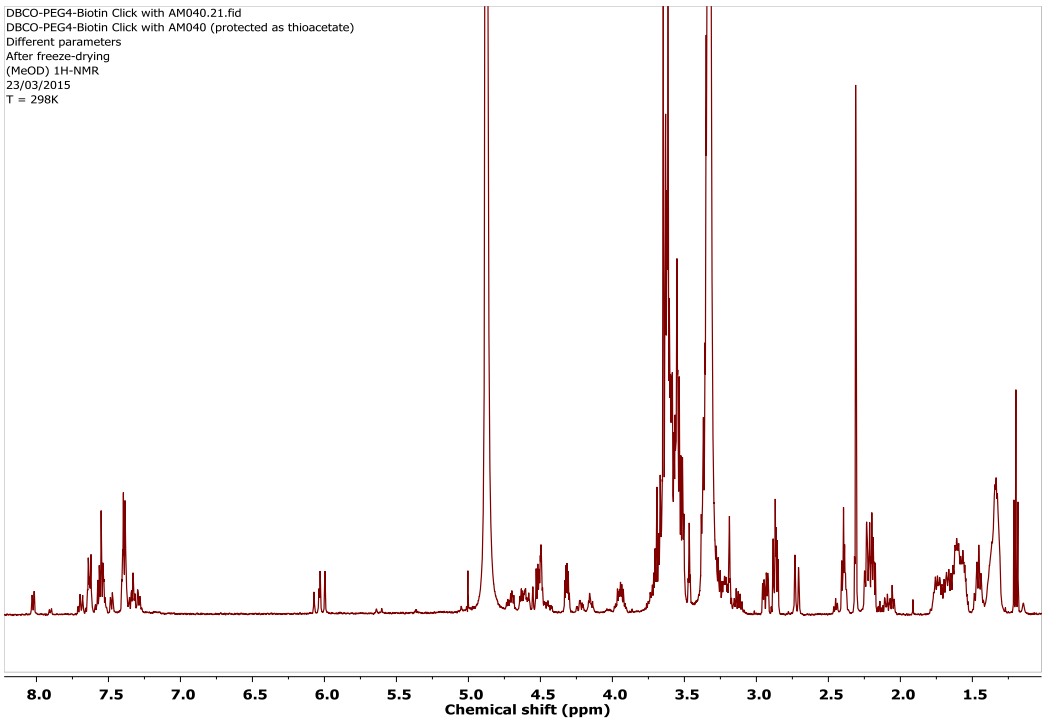

Intermediates:

IV

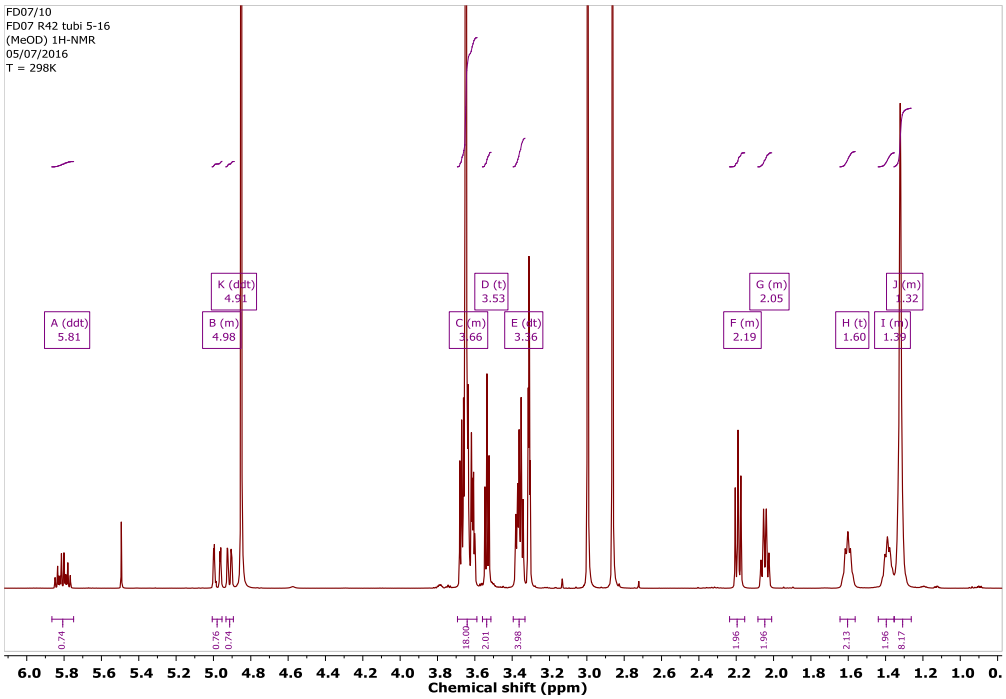

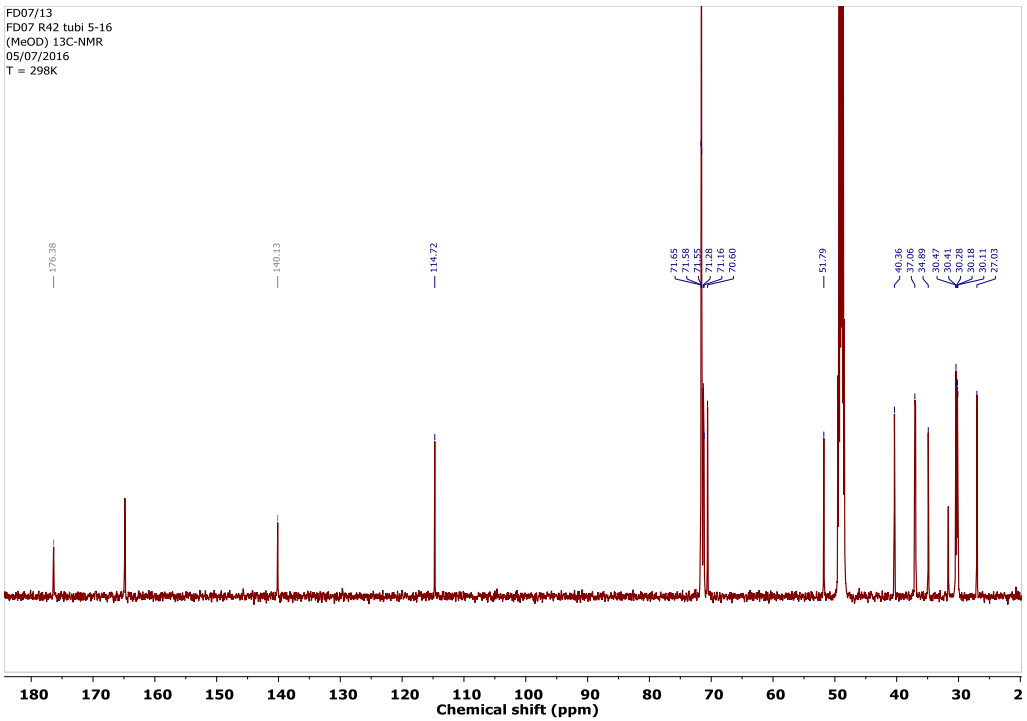

V

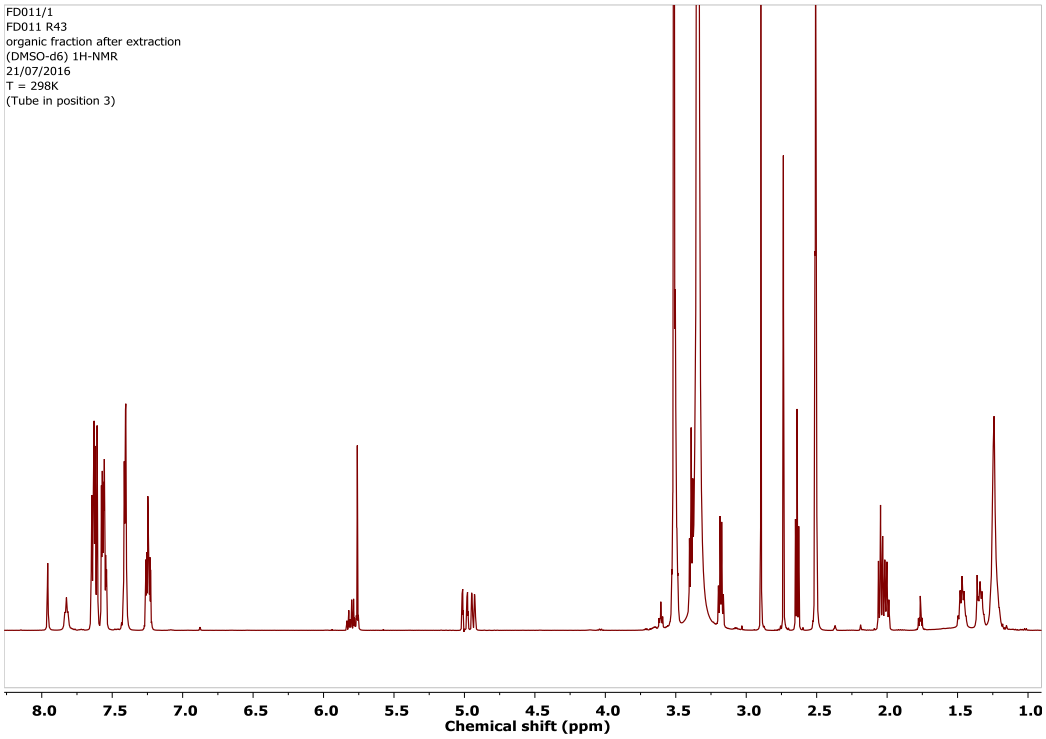
FD011/1
FD011 R43
organic fraction after extraction
(DMSO-d6) 1H-NMR
21/07/2016
T = 298K
(Tube in position 3)
8.0
7.5
7.0
6.5
6.0
5.5
5.0
4.5
4.0
3.5
3.0
2.5
2.0
1.5
1.0
Chemical shift (ppm)

XI

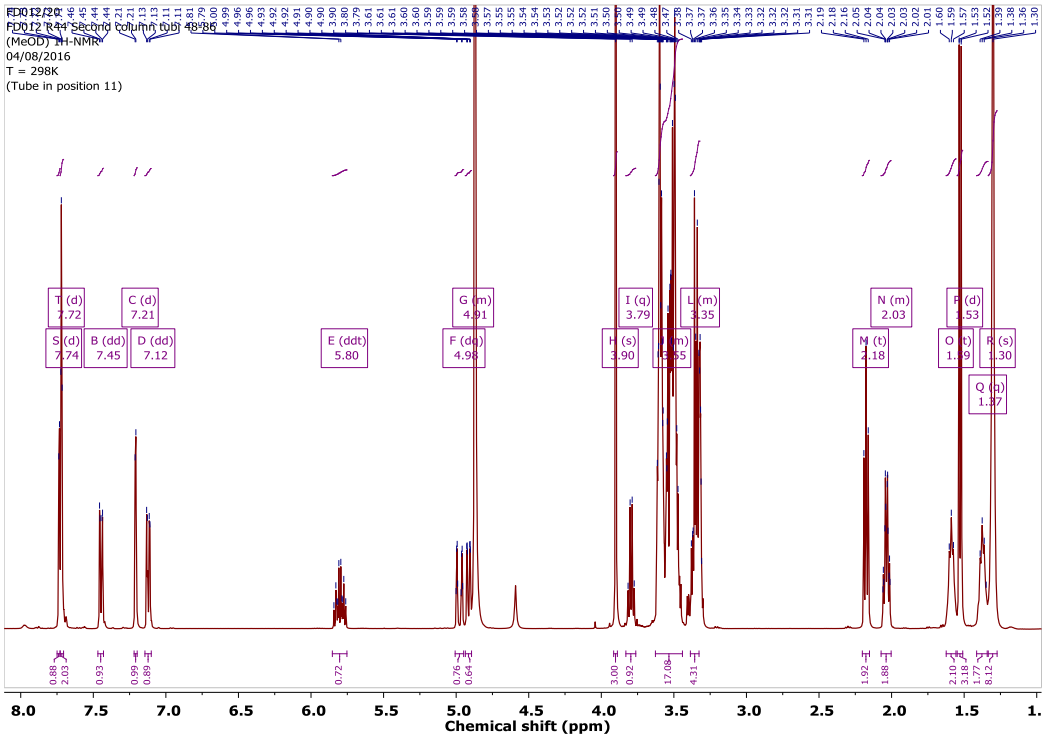
FD012/23
FD012 R44 Second column rubi 48-86
(MeOD) 1H-NMR
04/08/2016
T = 298K
(Tube in position 11)
T (d) 7.72
C (d) 7.21
G (m) 4.91
I (q) 3.79
L (m) 3.35
N (m) 2.03
P (d) 1.53
S (d) 7.74
B (dd) 7.45
D (dd) 7.12
E (ddt) 5.80
F (dd) 4.98
H (s) 3.90
M (t) 2.18
O (t) 1.39
R (s) 1.30
Q (q) 1.37
Chemical shift (ppm)

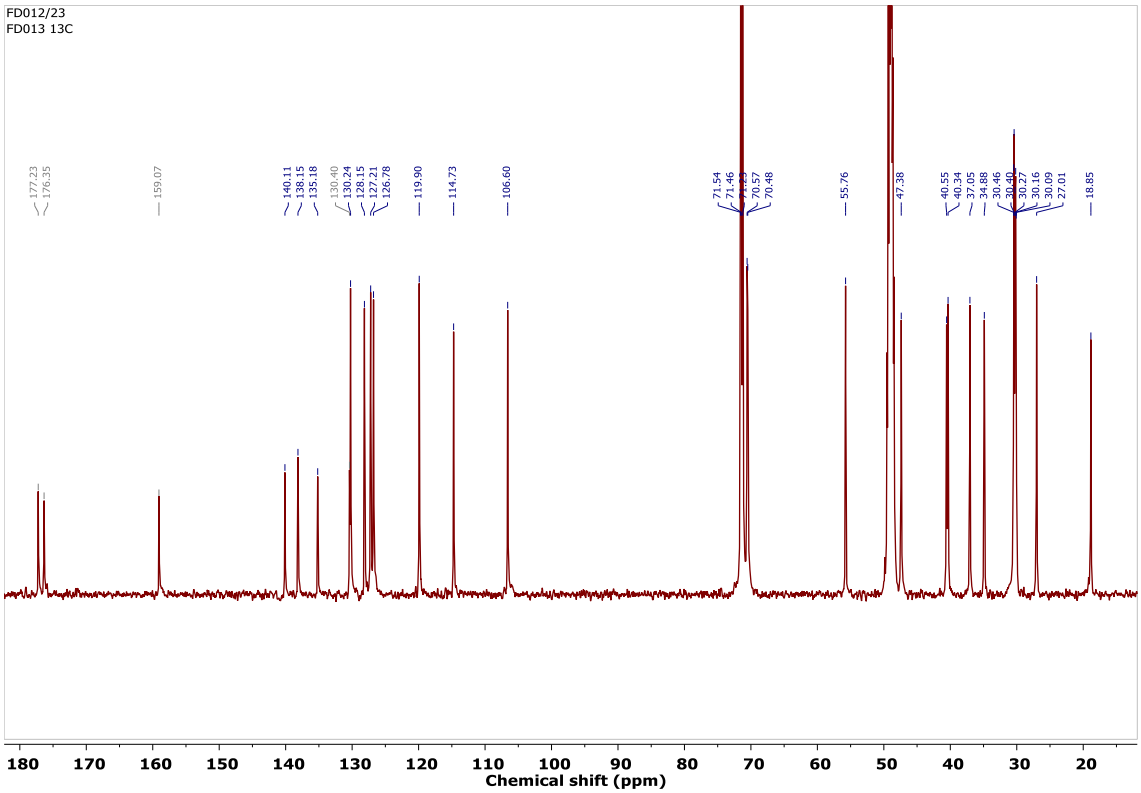
FD012/23
FD013 13C
177.23
176.35
159.07
140.11
138.15
135.18
130.40
130.24
128.15
127.21
126.78
119.90
114.73
106.60
71.54
71.46
70.57
70.48
55.76
47.38
40.55
40.34
37.05
34.88
30.46
30.40
30.27
30.16
30.09
27.01
18.85
Chemical shift (ppm)

IX-a

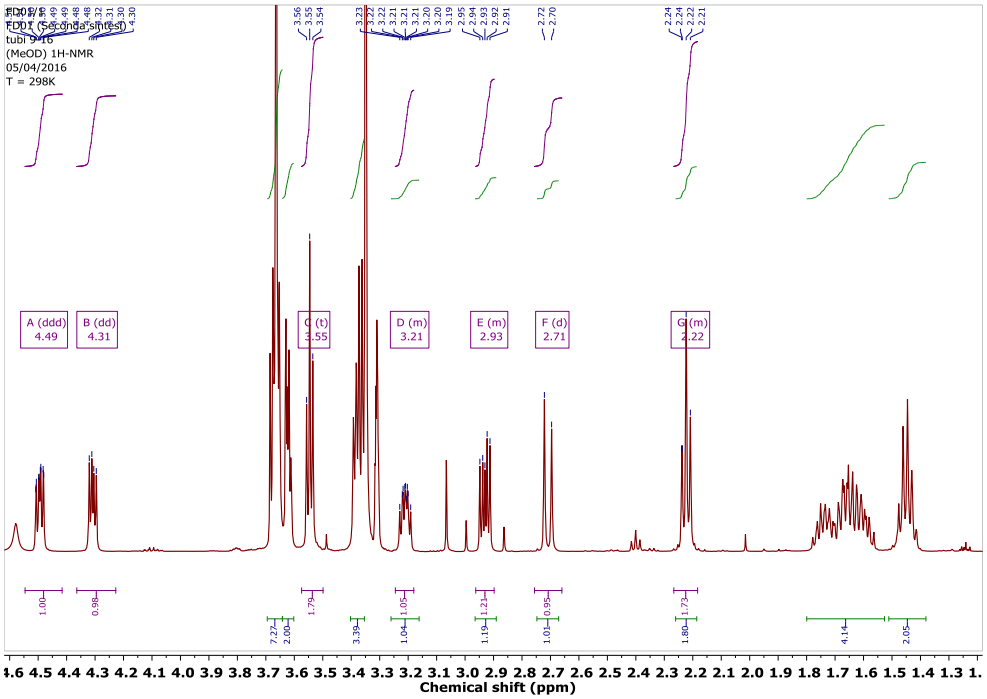
FD01 (Second sintesi)
tubi 9-16
(MeOD) 1H-NMR
05/04/2016
T = 298K
A (ddd) 4.49
B (dd) 4.31
D (m) 3.21
E (m) 2.93
F (d) 2.71
G (m) 2.22
Chemical shift (ppm)

X-a

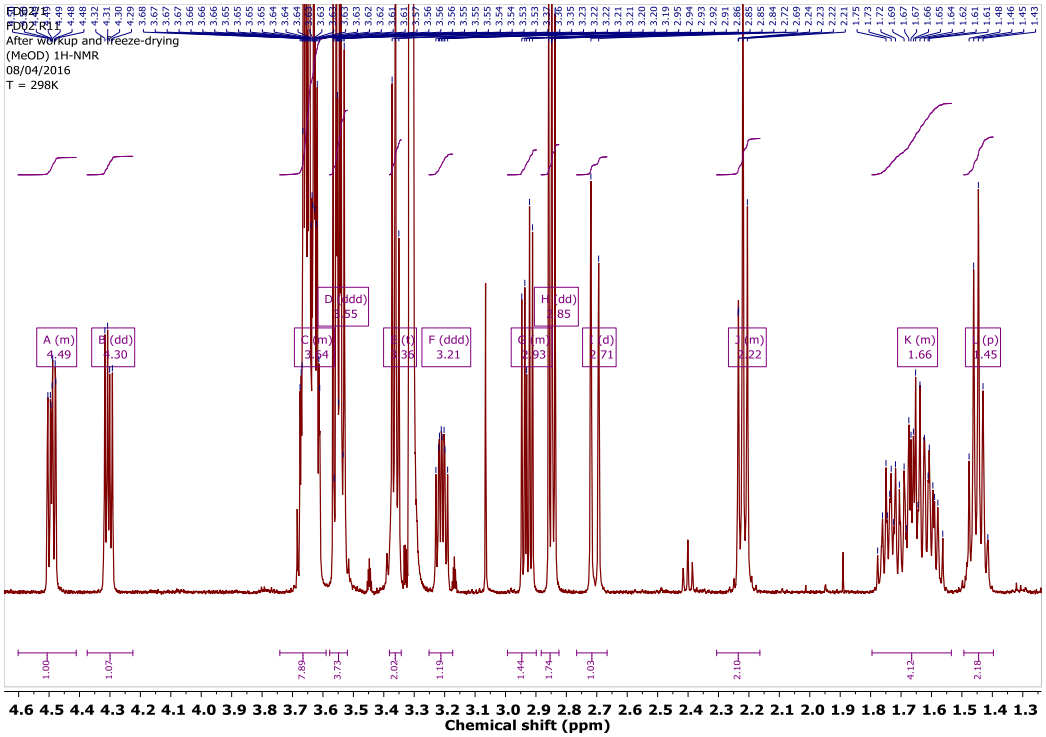
FD02 (1)
After workup and freeze-drying
(MeOD) 1H-NMR
08/04/2016
T = 298K
A (m) 4.49
B (dd) 4.30
F (ddd) 3.21
K (m) 1.66
Chemical shift (ppm)

IX-b

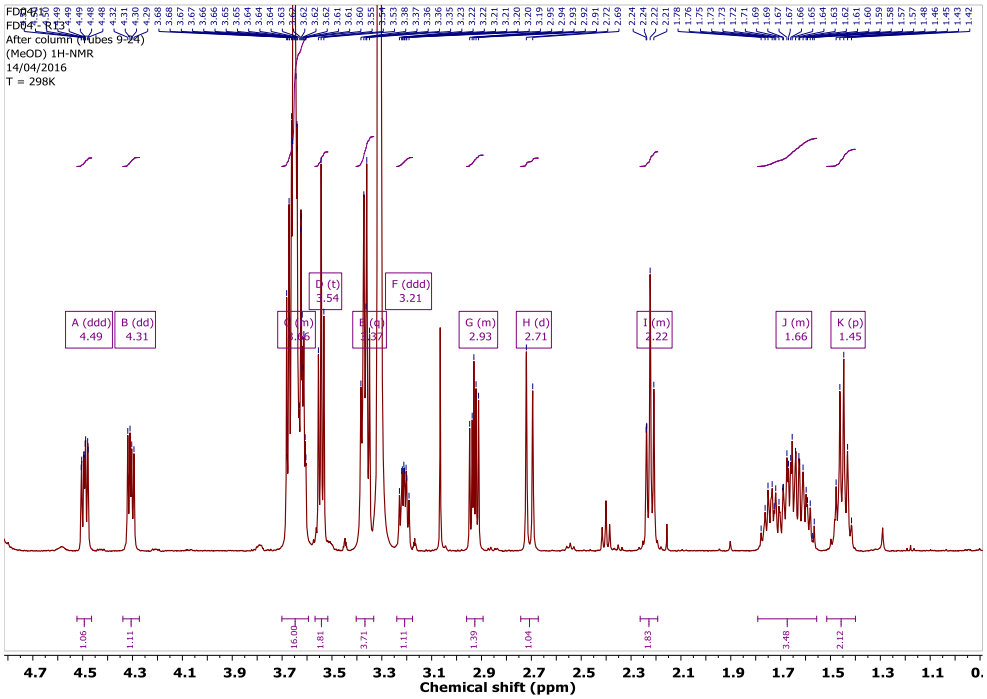
FD04_RT3*
After column (Tubes 9-24)
(MeOD) 1H-NMR
14/04/2016
T = 298K
A (ddd) 4.49
B (dd) 4.31
C (m) 3.66
D (t) 3.54
E (dd) 3.32
F (ddd) 3.21
G (m) 2.93
H (d) 2.71
I (m) 2.22
J (m) 1.66
K (p) 1.45
1.06
1.11
16.00
1.81
3.71
1.11
1.39
1.04
1.83
3.48
2.12
4.7 4.5 4.3 4.1 3.9 3.7 3.5 3.3 3.1 2.9 2.7 2.5 2.3 2.1 1.9 1.7 1.5 1.3 1.1
Chemical shift (ppm)

X-b

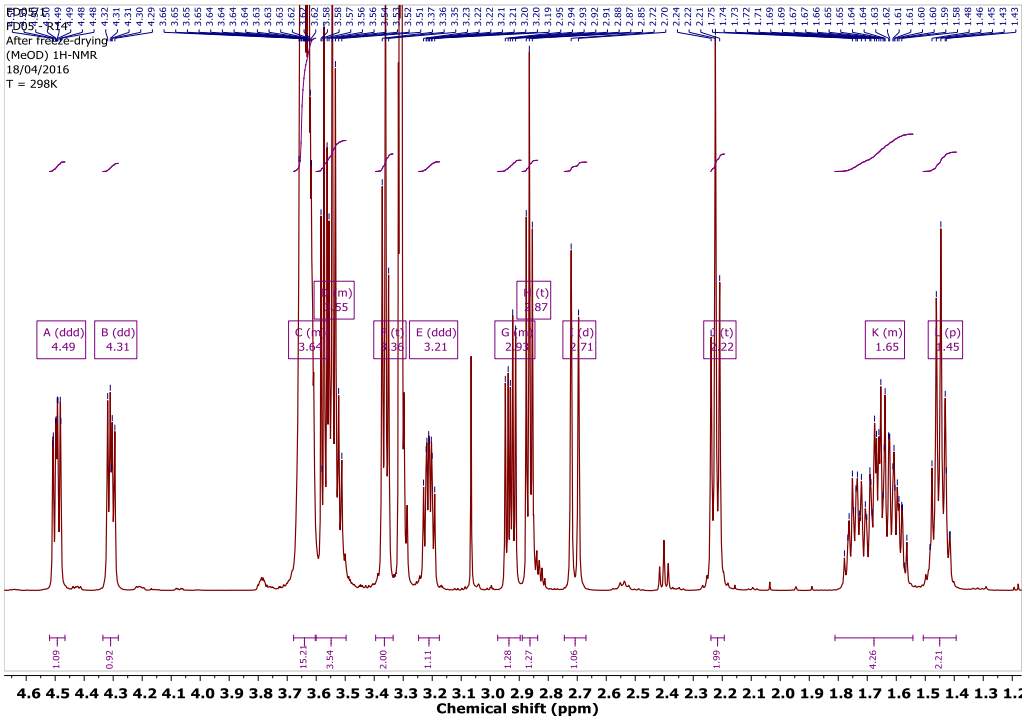
FD05/4
FD05 - R14
After freeze-drying
(MeOD) 1H-NMR
18/04/2016
T = 298K
A (ddd)
4.49
B (dd)
4.31
E (ddd)
3.21
K (m)
1.65
1.09
0.92
15.21
3.54
2.00
1.11
1.28
1.27
1.06
1.99
4.26
2.21
Chemical shift (ppm)

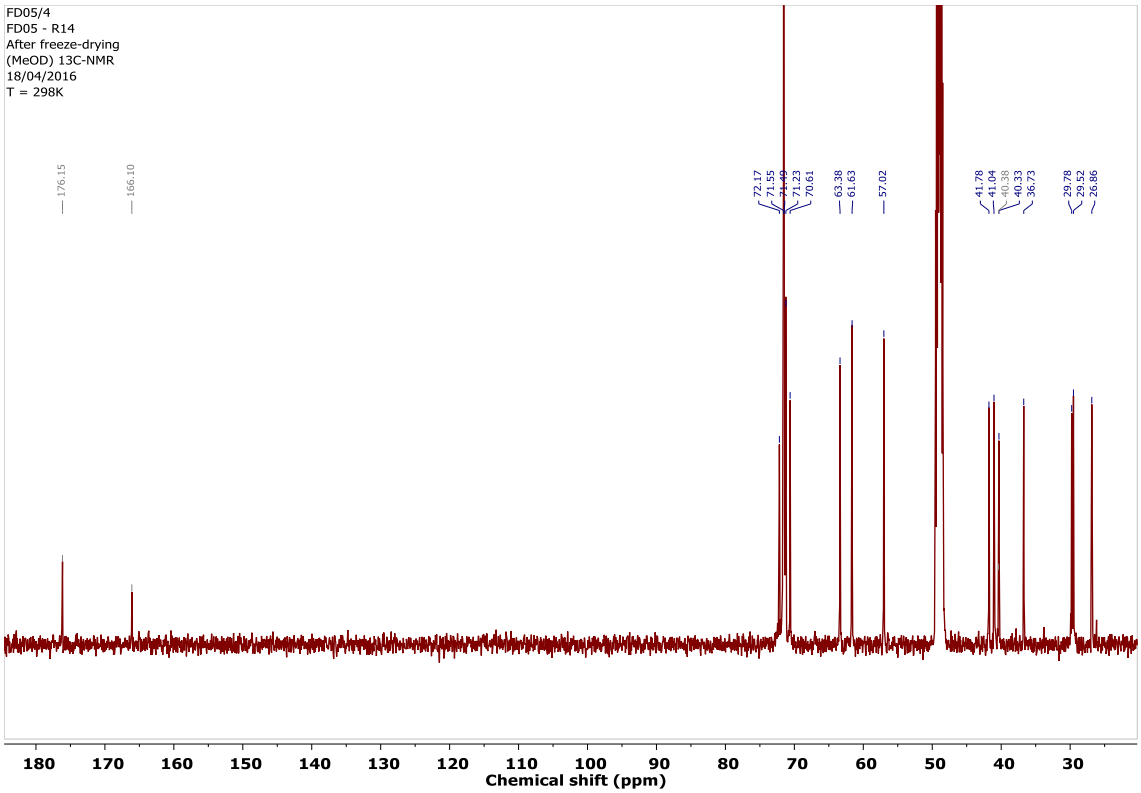
FD05/4
FD05 - R14
After freeze-drying
(MeOD) 13C-NMR
18/04/2016
T = 298K
176.15
166.10
72.17
71.55
71.49
71.23
70.61
63.38
61.63
57.02
41.78
41.04
40.38
40.33
36.73
29.78
29.52
26.86
Chemical shift (ppm)

II

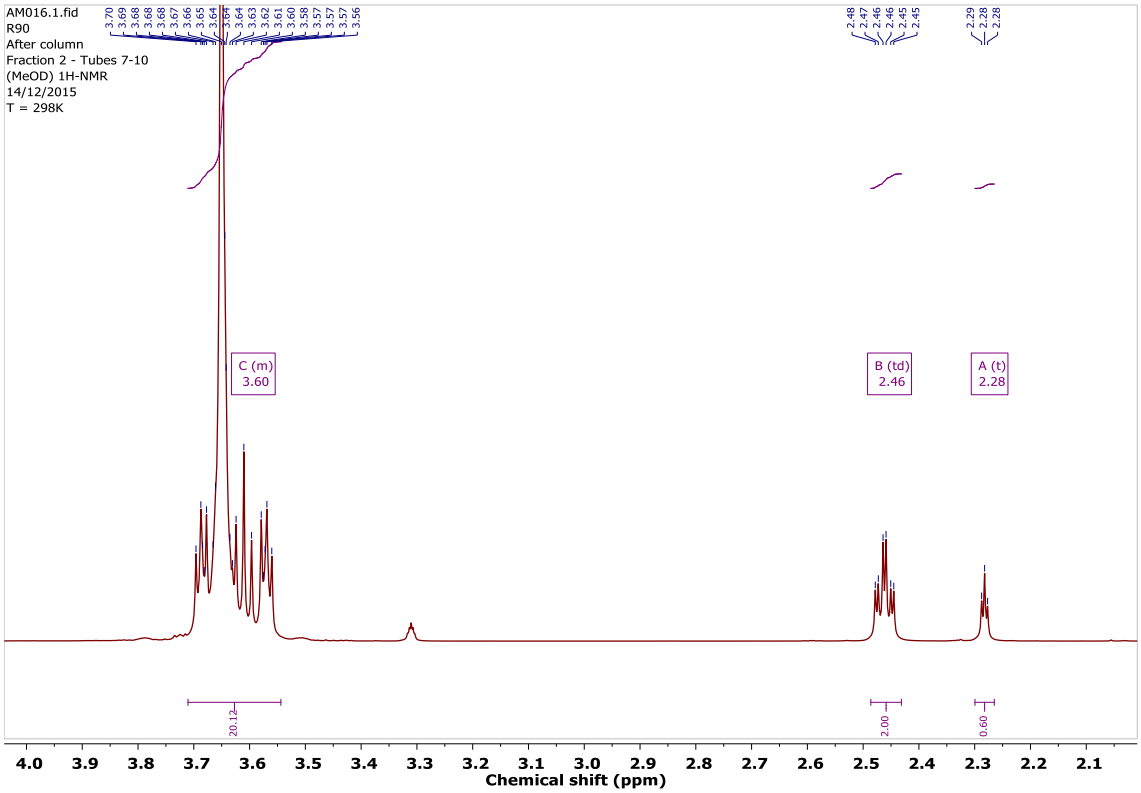
AM016.1.fid
R90
After column
Fraction 2 - Tubes 7-10
(MeOD) 1H-NMR
14/12/2015
T = 298K
C (m)
3.60
B (td)
2.46
A (t)
2.28
20.12
2.00
0.60
Chemical shift (ppm)